

AD-768 690

PROOF-OF-PRINCIPLE INVESTIGATION OF
300 W(E) STIRLING ENGINE PIEZOELECTRIC
(STEPZ) GENERATOR

M. A. White

McDonnell Douglas Astronautics Company

Prepared for:

Army Mobility Equipment Research and
Development Center

September 1973

DISTRIBUTED BY:



National Technical Information Service
U. S. DEPARTMENT OF COMMERCE
5285 Port Royal Road, Springfield Va. 22151

Best Available Copy

20050915082

UNCLASSIFIED

AD

REPORT MDC G4420

**PROOF-OF-PRINCIPLE INVESTIGATION OF
300 W(E) STIRLING ENGINE PIEZOELECTRIC
(STEPZ) GENERATOR**

Final Technical Report

by

M. A. White

September 1973

U.S. ARMY MOBILITY EQUIPMENT
RESEARCH AND DEVELOPMENT CENTER
FORT BELVOIR, VIRGINIA

CONTRACT NUMBER DAAK02-71-C-0405

DA Project No. 1G663702DG11-01

Donald W. Douglas Laboratories
Richland, Washington

MCDONNELL DOUGLAS ASTRONAUTICS COMPANY

UNCLASSIFIED

**Best
Available
Copy**

SUMMARY

The purpose of this work is to perform a proof-of-principle test of a unique concept for auxiliary electric power generation based on the use of a piezoelectric generator. The demonstration device consists of a modified Stirling-cycle engine which delivers pneumatic pressure pulses to a coupler consisting of an oscillating mercury column near ambient temperature. The coupler replaces the fly-wheel and mechanical coupling of a conventional engine-generator and drives a hydraulic load which simulates a piezoelectric generator.

The work is divided into two phases. Phase I includes piezoelectric generator tests and a system design based on computer simulation and requisite mechanical design analysis to develop complete system layout drawings. Preliminary piezoelectric generator tests performed by Physics International were inconclusive in certain areas. Subsequent testing at DWDL using an electrohydraulic materials loading system established the basic feasibility of the piezoelectric generator concept. Measurements at 60 Hz included power densities to 18 w/in.³, efficiency of 50% to 75% and continuous running time to 20 hours.

The final system design which includes substantial margins in several areas, is predicted to deliver 518 watts (mechanical) to the simulated load with an overall efficiency of 24%. When coupled with a piezoelectric generator, 419 watts (electrical) at 19% overall system efficiency is expected. Safety and operational problems with the mercury coupler, while not inhibiting a proof-of-principle demonstration of the concept, indicate the need for change in any prototype system.

The originally planned Phase II efforts consisted of detail design, fabrication, and testing of the engine-coupler-simulated load system, but later was redirected toward life testing of piezoelectric generators. Piezoelectric generator feasibility was demonstrated at ambient temperatures from -55° to +150°F. Operating times of more than 2000 hours at 9000 psi peak stress levels resulted in about 5% performance degradation.

Preceding page blank

FOREWORD

This report was prepared by the Donald W. Douglas Laboratories Richland, Washington, a Subdivision of the McDonnell Douglas ~~Astronautics~~ Company, under U. S. Department of the Army contract DAAK02-71-C-0405 to perform a proof-of-principle demonstration of a 300-w Stirling engine piezoelectric (STEP%) generator. The work was monitored by J. Harrison Daniel, Jr., Project Engineer, U. S. Army Mobility Equipment Research and Development Center, Fort Belvoir, Virginia.

This Final Technical Report covers the contract period from 30 June 1971 through 30 November 1971 for Phase I and from 26 January 1973 through 26 July 1973 for Phase II. Phase I consisted of developing layout drawings for the system and demonstrating practicability of the piezoelectric generator. Phase II was originally planned to include detail design, fabrication, and testing of a system utilizing a hydraulic load which simulates the piezoelectric generator, but later was redirected to provide 2000-hour piezoelectric generator life tests under varied environmental conditions.

The program was managed by M. A. White under the direction of Dr. W. R. Martini. Piezoelectric generator demonstrations at Physics International Company during Phase I were performed under the direction of P. Smiley.

Preceding page blank

CONTENTS

FIGURES	xi
TABLES	xv
Section 1 INTRODUCTION	1
1.1 Program Objectives	1
1.2 Phase I Piezoelectric Generator Testing	2
1.3 Layout Design of Proof-of-Principle System	5
1.4 Design Goal Concept	8
1.5 Piezoelectric Generator Life Tests	10
Section 2 INVESTIGATION AND DISCUSSION	13
2.1 Analytical Methods	13
2.1.1 Engine Analysis	13
2.1.2 Coupler Analysis	21
2.1.3 Piezoelectric Generator Analysis	24
2.2 Performance Analysis	38
2.2.1 Proof-of-Principle Test Device	38
2.2.2 Piezoelectric Generator	56
2.3 Mechanical Design	57
2.3.1 Engine	58
2.3.2 Coupler	70
2.3.3 Generator Simulator	72
2.4 Piezoelectric Generator Life Tests	73
2.4.1 Life Test Approach	73
2.4.2 Piezoelectric Disc and Contact Processing	87
2.4.3 Parametric Tests	94
2.4.4 Life Test Results	104
Section 3 CONCLUSIONS	111
Section 4 REFERENCES	113
Appendix A PHYSICS INTERNATIONAL REPORT PIEZOELECTRIC GENERATOR TESTS	115
Section 1 INTRODUCTION	117
Section 2 RESULTS	121
Section 3 DISCUSSION	123

Appendix B INDEPENDENT DEVELOPMENT OF PIEZOELECTRIC GENERATOR TECHNOLOGY USING CYCLE AVERAGED FORMALISM	159
Appendix C INDEPENDENT DEVELOPMENT OF PIEZOELECTRIC GENERATOR TECHNOLOGY USING TIME-STEP NUMERICAL INTEGRATION FORMALISM	173
Appendix D DETERMINATION OF HEAT TRANSFER COEFFICIENTS AND REGENERATOR PERFORMANCE IN THE STEP% ENGINE	195
Appendix E SAMPLE DESIGN OF A LINEAR ELECTROMAGNETIC DISPLACER ACTUATOR	201

FIGURES

1-1	Piezoelectric Generator General Arrangement	3
1-2	Measured PZ Generator Output	4
1-3	Piezoelectric Generator Test Results	5
1-4	Basic Concepts of the STEPZ Generator	6
1-5	Proof-of-Principle Test Setup	7
1-6	Assembly Drawing of Proof-of-Principle Device	9
2-1	Simplified Engine Schematic	14
2-2	Comparison of Computed Average Gas Temperature with Input Metal Temperatures	18
2-3	Free Displacer Simulation Terms	20
2-4	Fluid Coupler Arrangement	23
2-5	End Region Loss Coefficient Components	23
2-6	Equivalent Circuit for Piezoelectric Crystal Under Compression	29
2-7	Equivalent Circuit with Sinusoidal Compression and Resistive Load	29
2-8	Force-Displacement Diagrams	31
2-9	Continuous Power Load Simulator	36
2-10	P-V Characteristics of Continuous Power Load Simulator	36
2-11	Schematic of Pulsed Power Piezoelectric Generator Simulator	37
2-12	P-V Characteristics of Pulsed Power Load Simulator	37
2-13	Regenerator Clearance Tradeoff	43
2-14	Regenerator vs Heater - Cooler Tradeoff	44
2-15	Displacer and Power Piston Stroked Volume Performance Trades	45
2-16	Operating Frequency Tradeoff	46
2-17	Pressures and Temperatures as Functions of Time for the New Reference Design	47
2-18	Pressure - Volume Computer Plots for the New Reference Design	48

2-19	New Reference Design Performance Characteristics Versus Frequency	50
2-20	Transient and Stable Operation of Fully Self-Driven System	51
2-21	Engine Assembly	59
2-22	Displacer Drive System	60
2-23	Displacer and Supports	63
2-24	Displacer Upper Flexures	65
2-25	NHLI Displacer with Flexures	66
2-26	Displacer Drive Mechanism	67
2-27	Displacer Drive Forces vs Crank Position	69
2-28	Drive Shaft Seal	70
2-29	Coupler Assembly	71
2-30	Prototype Test Fixture Components	77
2-31	Prototype Test Fixture	77
2-32	Typical Contract Life Test Fixture Components	78
2-33	Load Frame Assembly Details	79
2-34	Preliminary Mechanical Assembly of Typical Test Fixture	80
2-35	Driver Stack Power Supply and Protection Circuit	82
2-36	Top of One Power Supply and Protection Circuit Module	83
2-37	Bottom of One Power Supply and Protection Circuit Module	83
2-38	Typical Generator Stack Electrical Load	84
2-39	Life Test Laboratory Showing Freezer and IRAD Stacks	85
2-40	Oven and Associated Test Equipment	86
2-41	Oven Stack Life Test Arrangement	86
2-42	Catastrophic Failure of Bonded and Potted Test Stack	87
2-43	Piezoelectric Discs in Ultrasonic Cleaner	89
2-44	Fully Processed Piezoelectric Discs and Copper Contact Assemblies	90
2-45	Copper Contacts in Vacuum Annealing Furnace	91
2-46	Stack Assembly in Pyrex Sleeve and Vee-Block	92
2-47	Stack Through Pyrex Sleeve	92
2-48	Damage Caused by Pyrex Sleeve	93
2-49	Parametric Test Setup	95
2-50	Ten-Disc Generator Stack in Place for Parametric Tests	96

2-51	Parametric Test Configuration	96
2-52	Performance Dependence on Load Resistance for Optically Lapped Stack	98
2-53	Performance Dependence on Load Inductance for Optically Lapped Stack	99
2-54	Performance Dependence Upon Load Resistance for Standard Lapped Stack	100
2-55	Performance Dependence Upon Load Inductance for Standard Lapped Stack	101
2-56	Performance Dependence Upon Load Resistance for Optically Lapped Stack	102
2-57	Performance Dependence on Load Inductance for Optically Lapped Stack	103
2-58	IRAD Stack Efficiency and Normalized Power Dependence on Elapsed Time	106
2-59	Stack No. 1 Efficiency and Normalized Power Dependence on Elapsed Time	107
2-60	Stack No. 2 Efficiency and Normalized Power Dependence on Elapsed Time	108
2-61	Stack No. 4 Efficiency and Normalized Power Dependence on Elapsed Time	109
(A)1	Equivalent Circuit of a Piezoelectric Generator with Matching Induction and Load Resistor	127
(A)2	Schematic of PZ Generator and Hydraulic Driving System	128
(A)3	Output Power of PZT-5H Generator, Volume of Material: 5 in. ³	129
(A)4	Output Power of LZT-1 Generator, Volume of Material: 0.8 in. ³	130
B-1	Mechanical and Electrical Equivalent Circuits	159
B-2	Simplified Electrical Equivalent Circuit	160
B-3	Simplified Electrical Equivalent Circuit with Inductance . .	162
B-4	Simplified Resonant Circuit with X_L , X_C	163
B-5	Mechanical and Electrical Equivalent Circuits	164
B-6	Mechanical and Electrical Equivalent Circuits	165
B-7	PZT-5H Stack Output Power Dependence Upon Stress . . .	168
B-8	PZT-5H Stack Output Power Dependence Upon Load	168
C-1	Piezoelectric Stack Equivalent Circuit	174
C-2	DWDL Analytical Correlation with Physics International LZT-1 Generator Performance	177

C-3	LTZ-1 Stack Output Power Dependence on Inductance	179
C-4	LTZ-1 Stack Output Dependence on Load Resistance	179
C-5	Apparatus for Testing Piezoelectric Stack	180
C-6	Piezoelectric Stack Test Fixture	182
C-7	Effective Capacitive Reactance of Piezoelectric Stack as a Function of Applied Stress	184
C-8	Test Results for Twenty-Disc Piezoelectric Stack	185
C-9	Dependence of Output Power Upon Inductance	186
C-10	Power Density Dependence Upon Load Resistance	187
C-11	Piezoelectric 20-Disc Test Stack	188
C-12	Typical Force-Displacement Experimental Curve for Twenty-Disc Piezoelectric Stack	189
C-13	Power Density Dependence Upon Inductance	191
C-14	Power Density Dependence Upon Load Resistance	191
C-15	Power Density Dependence on Load Resistance for 26-Disc Stack	192
D-1	Heat Exchanger Geometry	196
E-1	Displacer Actuator for STEP% Engine	201
E-2	Joule Heating as a Function of Magnet Gap Flux Density . .	205
E-3	Magnetic Circuit Configurations	205

TABLES

2-1	Materials Properties for High Power Piezoceramic Generators	26
2-2	Reference Design Performance and Specifications	41
2-3	Load Change Summary	55
2-4	Computer Piezoelectric Generator Characteristics ...	57
A-1	Properties of Piezoelectric Ceramics for High-Power Generators	131
B-1	Symbols Used in Sample Calculation	170
C-1	Definition of Symbols	175
C-2	Piezoelectric Tests Carried Out by DWDL	183
E-1	Weight Summary of Displacer Actuator Components...	206
E-2	Alnico 9 Displacer Actuator Characteristics.....	207

Section 1

INTRODUCTION

1.1 PROGRAM OBJECTIVES

The long-range objective of this program is to develop a long-life, high-efficiency, maintenance-free flame-fired engine-generator as a silent, portable, electric power source. The effort reported here encompasses layout design of a proof-of-principle system as well as performance and life testing of piezoelectric generators. Currently, in both civilian and military auxiliary power applications, gasoline or diesel engines operating rotating electromagnetic generators are almost universally used for portable auxiliary electric power. These units are reasonable in cost but are noisy, relatively unreliable, and require regular knowledgeable maintenance of the engine. Particularly in the Army, there is a need for something better at a reasonable price. Many applications in which reliability, low noise emission, and durability under rugged use conditions are important require continuous electric power in quantities larger than batteries can supply over long periods.

The STEPZ concept has the potential for satisfying these requirements, but it involves certain innovative and unconventional approaches. The initial objective of this program has accordingly been established as a proof-of-principle reduction to practice of the key components. Included are verification of (1) piezoelectric generator feasibility, (2) resonant operation of the coupler to obtain the required phase lag without mechanical linkages, and (3) adequate heat exchange capabilities for a simple displacer-regenerator engine with no extended heat transfer surfaces for use in the multihundred-watt(e) range.

In the Phase I effort, an experimental evaluation of the piezoelectric generator was conducted and a layout design of a proof-of-principle system was completed. The system consists of a modified Stirling engine, a simulated piezoelectric generator, and a mercury-filled hydraulic coupler to match engine output with generator input.

Basic feasibility of the piezoelectric generator concept was established in Phase I, but the question of long-term degradation led to a redirected Phase II effort. Test fixtures suitable for life testing piezoelectric generators was developed and applied to 2000-hour tests of four stacks under various environmental conditions. The life-test fixtures consist of a rigid load frame which encloses an 80-disc piezoelectric stack and associated force and displacement measuring instrumentation. Seventy

of the discs are operated as a driver stack from a high voltage ac power supply. The resultant stress fluctuation produces ac power in the 10-disc generator stack; power density and efficiency are measured. Long-term performance degradation was not severe.

4.2 PHASE I PIEZOELECTRIC GENERATOR TESTING

Piezoelectric generators are novel, partly because practical materials have only recently come into use. In addition, the generator requires pulsating mechanical power at high force and low displacement which is not a typical output characteristic for prime movers. A 97.5% efficient piezoelectric generator driven by a similar piezoelectric motor has recently been reported (Reference 1).

This generator, however, operates at very high frequencies and low stresses compared with the STEP% operating regime. Acknowledged experts in the piezoelectric materials field differ widely in their evaluation of practical operating stress levels and, therefore, power density.

Because of the relative uncertainty of piezoelectric generator feasibility compared with that of Stirling engines, the Phase-I effort included component testing of piezoelectric stacks. Testing of two considerably different piezoelectric materials was originally performed under subcontract to Physics International, (results reported in Appendix A), but limitations of the stack stressing equipment prevented extended operation as well as efficiency and temperature-rise measurements. These data have now been obtained at DWDL and are presented, along with supporting analysis, in Appendices B and C.

Piezoelectric generator operation is shown in Figure 1-1. The disks are made from a lead zirconate-titanate ceramic and metallized on both flat surfaces for electrical contact. Warm disks are polarized (analogous to magnetizing a permanent magnet) by applying a high voltage to align the dipoles. These are stacked with alternating polarity (electrically in parallel) with one side connected to the load, the other to ground. Compression of the stack produces charges delivered as load current in one direction, followed by a reversed polarity and current when compression is relaxed. Theory and experiment show that typically only about half the applied strain energy produces a charge. The balance is stored elastically, and in a real system, is utilized to effect the compression stroke on the engine. A portion of the generated power is dissipated in stack losses. This must be minimized to maintain an acceptable efficiency and maintain temperature rise in the stack within tolerable limits. Experiments confirm the feasibility of these objectives.

Preliminary experimental results obtained at Physics International are summarized in Figure 1-2 with measurements normalized to specific output power. Early stack stress fluctuations to 3500 psi were obtained using a piezoelectric driver. Extrapolation of these data is indicated as the original projection in Figure 1-2. The tests conducted as part of the Phase I effort used a rotary valve

and high-pressure hydraulic pump to apply stress fluctuations. Two types of piezoceramic materials were tested. PZT-5H is a piezoelectrically soft material with a high power density at a given stress level, but with relatively low stress limitations and high internal losses. As indicated in Figure 1-2, PZT-5H exhibited degradation with short-term tests near 5000 psi compressive stress. The other material tested was L71-1 (equivalent to PZT-4), a piezoelectrically hard material with basically opposite properties to those of PZT-5H. This stack also exhibited an apparent leveling off in power density around 9000 psi, but this was attributed to high pressure binding in the drive-piston seal.

Some of the pertinent data obtained at DWDL utilizing an electro-hydraulic materials-loading system are presented in Figure 1-3. These data were obtained using sinusoidal stressing at 60 Hz with a minimum compression of 1000 psi, and 7000 to 13,000 psi maximum compression.

Experimental power density follows the predicted curve closely to 8000-psi stress fluctuation, with decreased performance at higher levels. Following these measurements, a 20-hour continuous run at 12,000 psi stress fluctuation exhibited continuous and irreversible degradation at a decreasing rate. A similar continuous run at 6000 psi stress fluctuation three weeks later showed only an initial, reversible degradation while the hydraulic driver approached thermal equilibrium. Inductance was then used in the load circuit to compensate for capacitance inherent in the generator. Power density

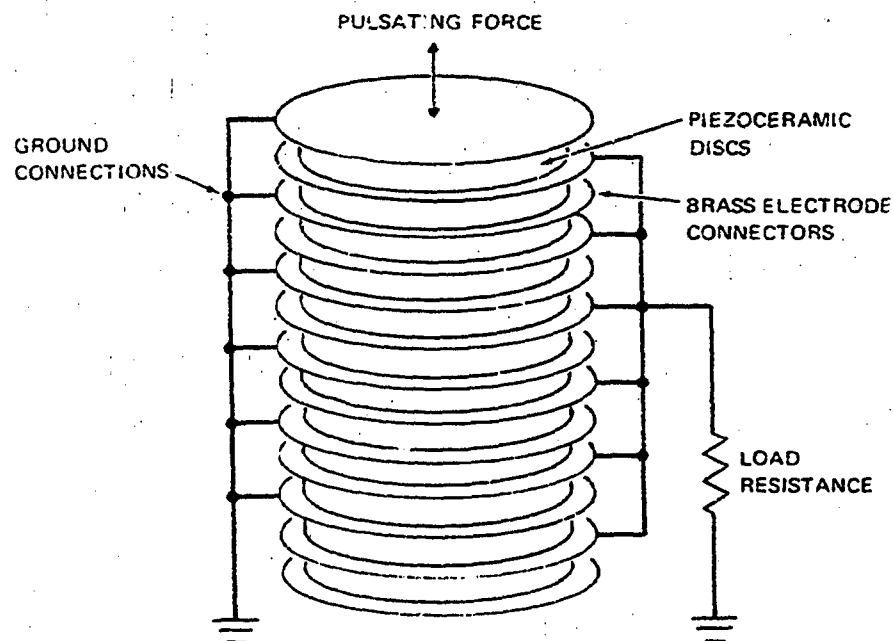


Figure 1-1. Piezoelectric Generator General Arrangement

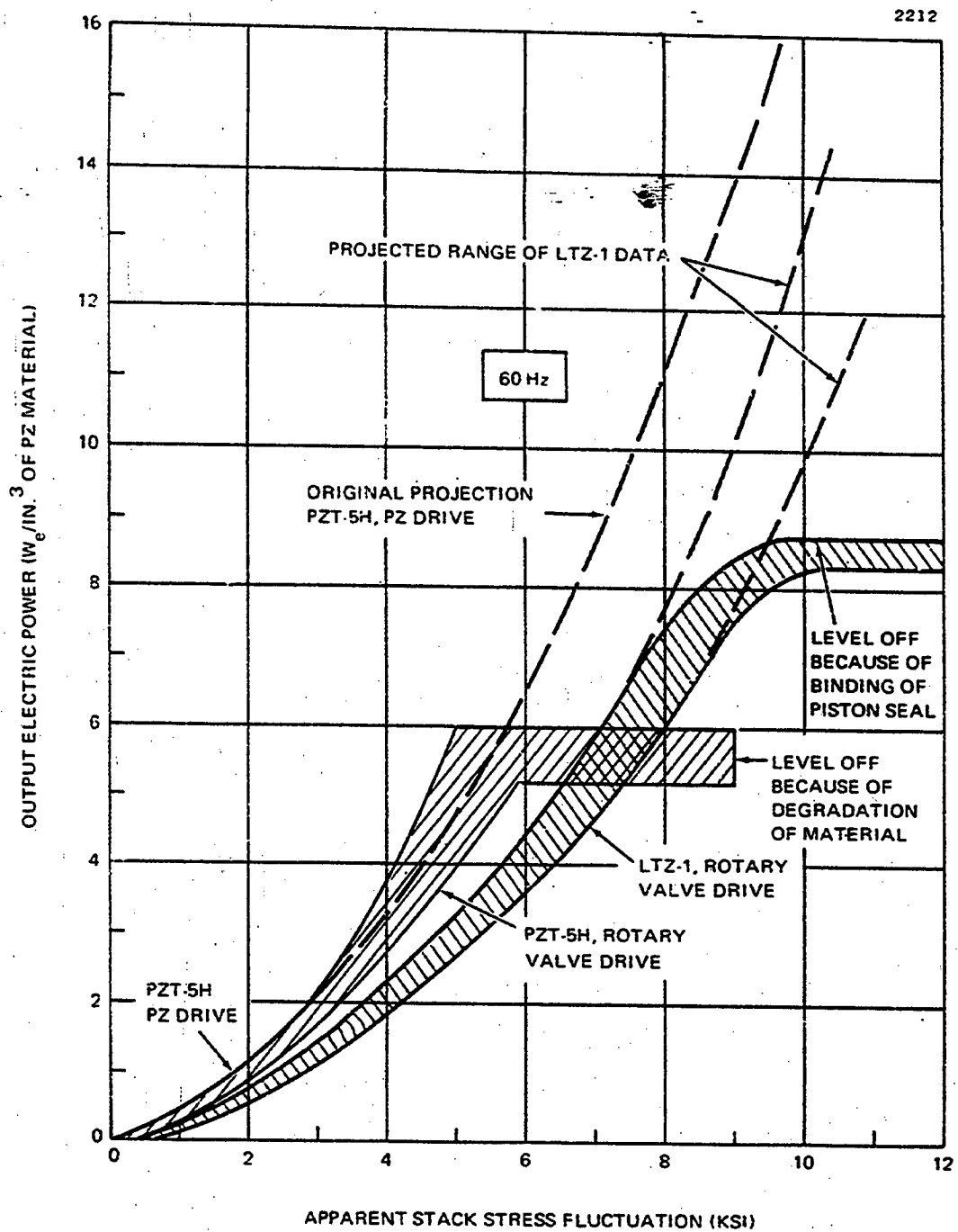


Figure 1-2. Measured PZ Generator Output

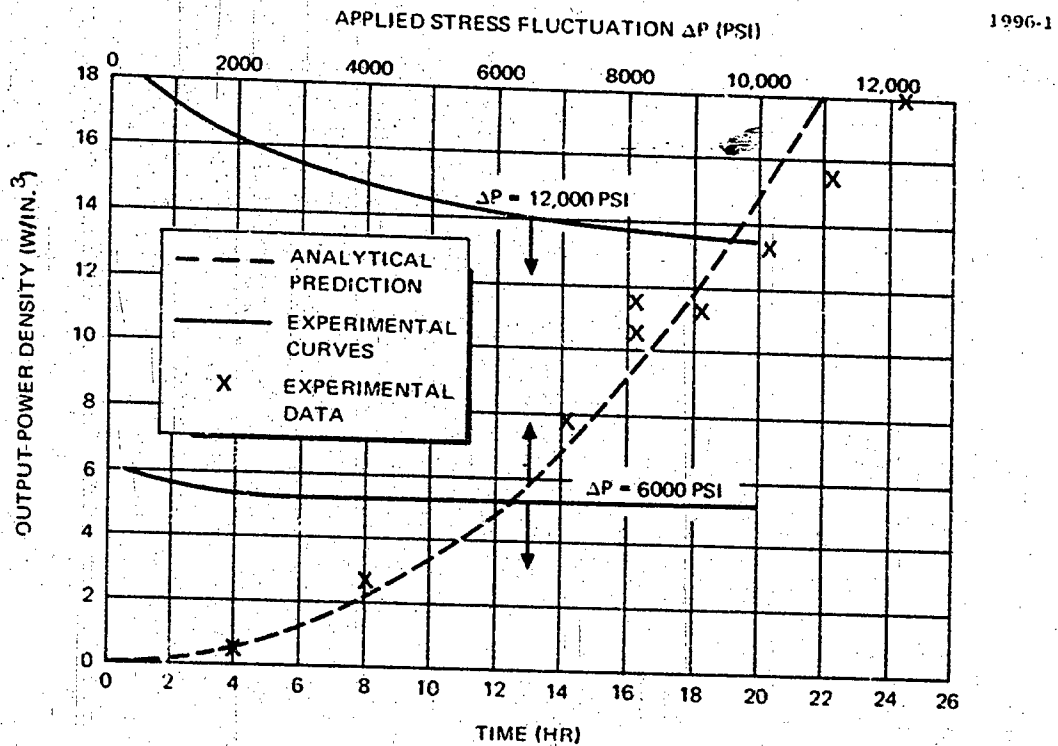


Figure 1-3. Piezoelectric Generator Test Results

increased by a factor of 2.5 as compared with a predicted value of 3.0. A piezoelectric generator efficiency of 67% was measured, with optimum inductance in the circuit at 6000 psi and a power density of 15 w/cu in.

These data show that an efficient piezoelectric generator with reasonable power density is possible. Excellent analytical correlations with experiment give confidence in designing generators for specific applications. Further experiments will eventually be required to determine the effect of disk geometry and surface finish on long-term operating properties and allowable stress levels.

1.3 LAYOUT DESIGN OF PROOF-OF-PRINCIPLE SYSTEM

The proof-of-principle system is designed to show that the basic concept shown in Figure 1-4 is feasible; the system utilizes a simulated piezoelectric generator. The Stirling engine produces pressure pulses from heat. After a phase shift by inertia in the coupler, these pressure pulses can be applied to a piezoelectric generator to produce electricity. Gas in the Stirling engine acts as a spring and a negative damper, one that produces instead of consuming power. The coupler acts as a mass, and the piezoelectric generator acts

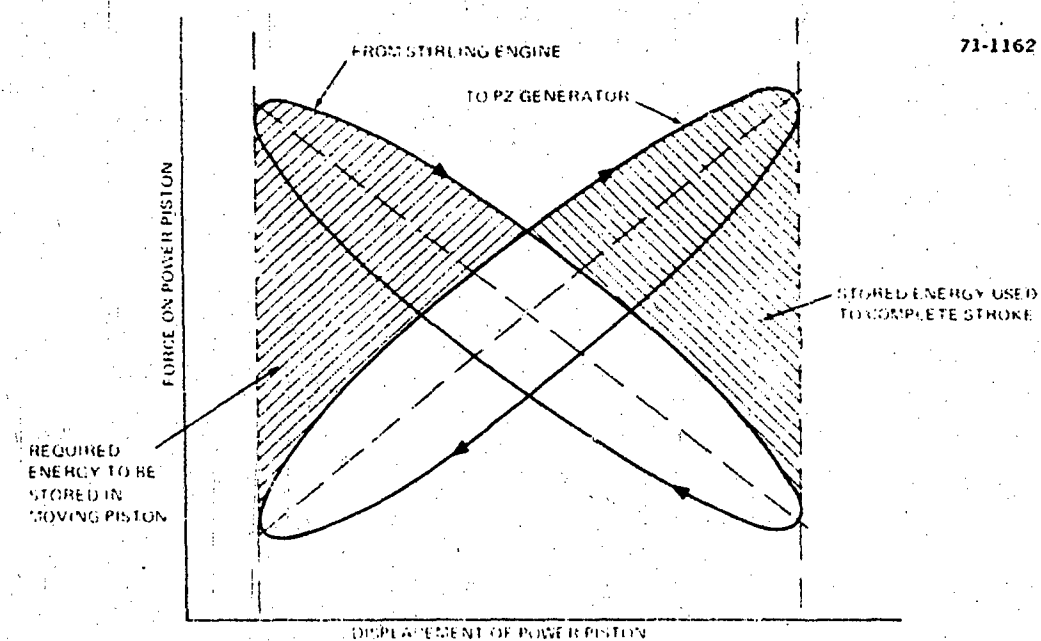
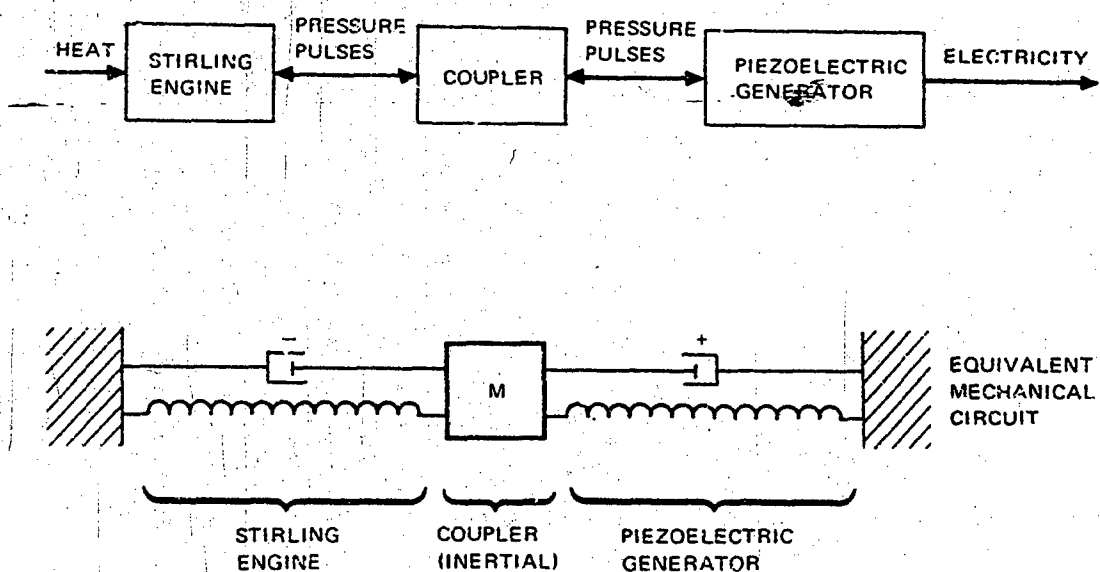


Figure 1-4. Basic Concepts of the STEPZ Generator

as another spring combined with a conventional damper. Figure 1-4 shows how forces from the engine and generator act on the coupler which serves as an inertial energy storage device analogous to the flywheel in a conventional engine. Figure 1-5 shows the principal features of the proof-of-principle system to demonstrate the basic concept.

The Stirling engine is similar to other silent, long-lived power sources developed and tested at DWDL. The engine consists of a lightweight displacer which oscillates inside the engine cylinder with a five-mil radial clearance between cylinder wall and displacer. This separation is maintained by a flexure at the hot end and a bearing (part of the displacer drive) at the cold end. This bearing may ultimately be replaced by a flexure. The gap acts as a gas heater, regenerator, and gas cooler. The use of this gap, instead of many small tubes manifolded into regenerator assemblies as in conventional Stirling engines, greatly simplifies the engine and significantly reduces cost for small Stirling engines. Oscillation of the displacer heats and cools the confined helium and creates the pressure pulses. An electric motor for startup and fine frequency control moves the displacer through a crank mechanism. These components will probably be replaced by an electromagnetic drive when prototype development is achieved. Once operating speed is reached, the gas pressure difference applied to the displacer drive piston varies over a cycle in such a way as to apply power to the displacer drive. If friction is not too great, the engine will run itself. The crank mechanism

71-1262

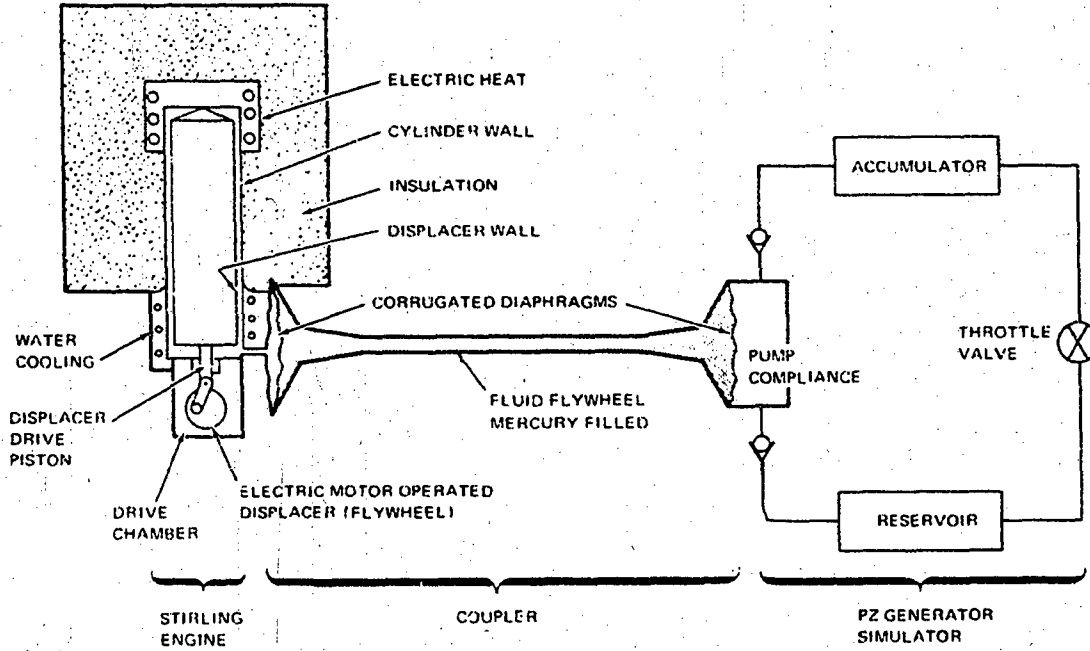


Figure 1-5. Proof-of-Principle Test Setup

is useful to control motion of the displacer to full stroke without danger of hitting the ends. A similar smaller engine operated at 20 Hz and 5 watts with a crank and flywheel for over 5000 hours at DWDL.

The coupler considered for the present study is a mercury-filled tube with diffusers at each end. A corrugated diaphragm separates the mercury from the engine gas at one end and from the hydraulic fluid in the generator simulator at the other. The necked-down configuration produces the effect of a much larger mass than is actually present (similar to a flywheel attached to a speed-increaser gear); therefore the name "fluid flywheel." For the reference design, the coupler is 96% efficient. One inconvenience in this test is the reaction forces of the coupler which require rigid anchoring for the test. In a practical system, imbalanced forces are eliminated by two opposing couplers or inertial members. A liquid coupler can also be coiled to reduce system dimensions. Another major change anticipated for a practical generator is in the displacer drive system. The present crank and flywheel mechanism and sliding seal will be replaced by a linear electromagnetic drive mechanism with full flexural support. A dynamic coil motor has been conceptually designed with 27% efficiency (Appendix E) at the one-watt level for a 50-wt STEP% generator. This approach has more basic simplicity, which is a fundamental objective of the STEP% effort, than does the proof-of-principle design.

The generator simulator is a liquid pump. Pump compliance and pressures in the accumulator and reservoir are chosen to simulate action of the piezoelectric generator. Power output of the simulator can be checked by measuring the steady flow and pressure drop at the throttle valve.

Figure 1-6 shows the proof-of-principle device based on current designs. The coupler is mounted vertically on a firmly anchored I-beam. The engine operates horizontally and is attached to the top of the beam. The simulated piezoelectric generator is on the side. The test system is about 39 in. high, 24 in. wide, and 24 in. deep.

1.4 DESIGN GOAL CONCEPT

The proof-of-principle device is not intended to be a prototype of a practical silent power source. Once the proof-of-principle is demonstrated, a number of changes and additions must be made to develop a practical prototype. These are expected to be:

1. A piezoelectric generator instead of the simulation.
2. A counterbalanced coupler to eliminate reaction forces.
3. A simplified displacer drive mechanism.

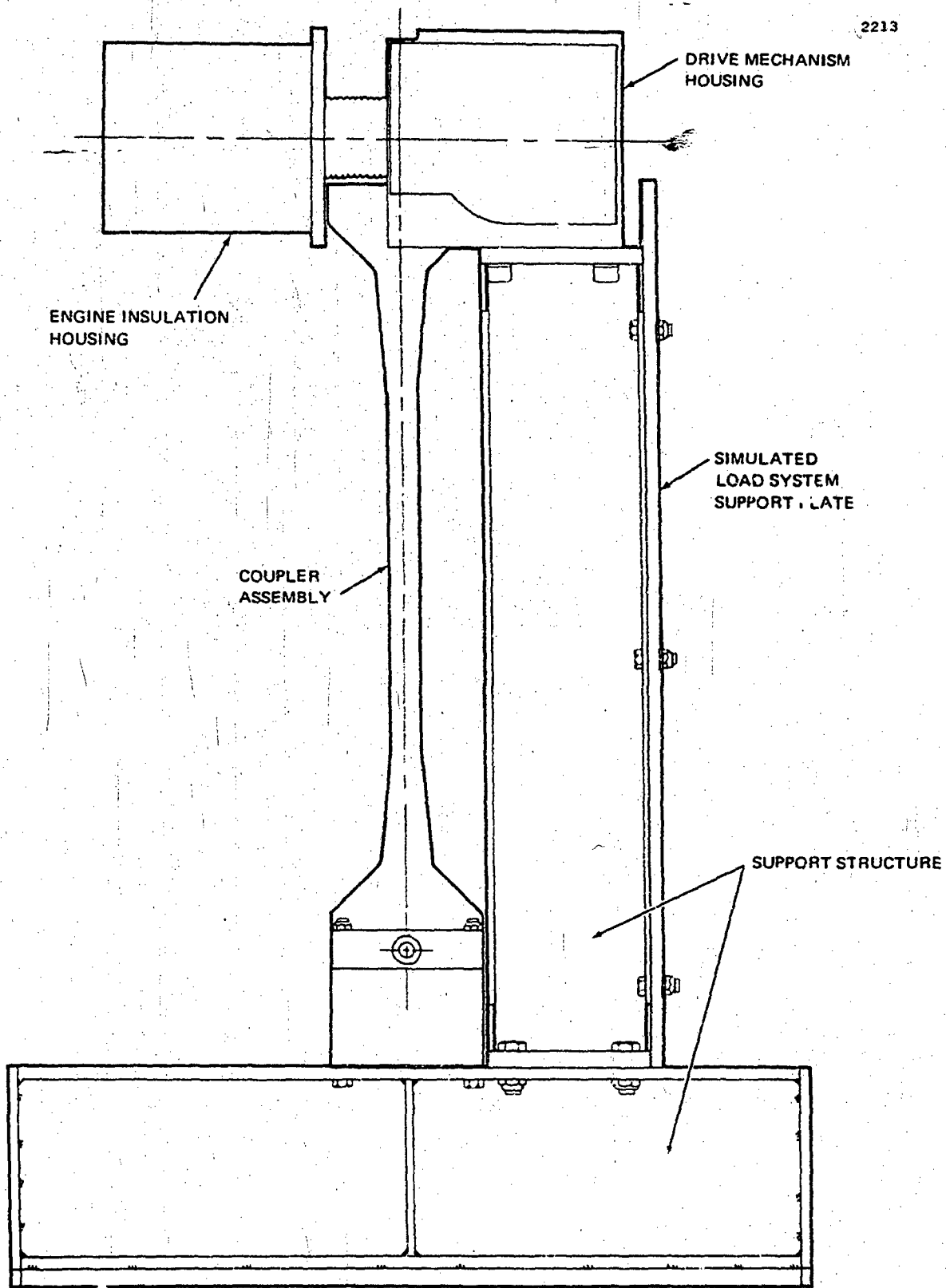


Figure 1-6. Assembly Drawing of Proof-of-Principle Device

4. Automatic control to give desired output voltage over the full power range.
5. Burner heat source.
6. Radiator heat exchanger.

1.5 PIEZOELECTRIC GENERATOR LIFE TESTS

Life tests were conducted to establish the effect of extended operation (2000-hour goal) on several piezoelectric stacks with different surface finishes at various environmental temperatures. Four life test assemblies were fabricated similar to an IRAD prototype system which was designed and built in the interim between Phase I and Phase II. Each test fixture consists of a stack of eighty 0.5-in. diameter by 0.040-in. thick piezoelectric discs, restrained within a rigid load frame, together with force and displacement measuring instrumentation. Electric excitation at 60 Hz is applied to 70 discs of each stack, which generates the driving force to excite the 10-disc generator stack. Specified test conditions for the four stacks are summarized in Table 1-1.

In addition, the IRAD prototype test fixture was reassembled in a new configuration and life tested concurrently with the contract stacks at room temperature. The IRAD stack is unique in that it utilizes a 60-disc driver stack and the generator stack is only 0.25 in. diameter. This enables the generator to experience the full desired stress swing

Table 1-1
SPECIFIED LIFE TEST CONDITIONS

Stack No.	Ambient Temp (°F)	Maximum Stress (psi)	Minimum Stress (psi)	Vendor Specified Disc Surface Finish**
1	<20*	9000	As low as possible	±0.0005 in. flatness (standard double lap)
2	<20	9000		±0.00005 in. flatness (optical lap)
3	Approx 70	9000		±0.0005 in.
4	Approx 150	9000		±0.0005 in.

*After 1000 hours of life testing at cold point of standard freezer, ambient test temperature will be reduced to ≤-25°F for 100 hours of operation. After this 100 hours, life test will continue at <20°F ambient.

**As specified in Gulton Industries, Inc. Quotation No. 1382, 12/15/71.

of 1000 to 9000 psi, in contrast to the contract stacks where the generator stress swing is typically around 5000 to 9000 psi as a result of excessive stack compliance.

All stacks have survived the life test with total times of 2300 to 3300 hours and are continuing to accumulate hours, with the exception of stack number 3 which suffered irreparable damage as a result of accidental overstressing during a preload operation. Several isolated discs in driver sections suffered electrical breakdown during the life test, but in each case, the appropriate 10-disc segment was removed from the circuit and operation continued. No breakdown or severe degradation occurred with any generator stack.

Quality control with commercially supplied piezoelectric discs is a practical problem. Standard lapped discs were microscopically reasonably smooth, but polarization after lapping caused warping with 0.002- to 0.004-in. deviation from flatness. The optically lapped discs were much better, but only about as smooth as the vendor specified finish for standard discs, and parallelism of the flat surfaces was poor. The warped discs flatten with a relatively small preload, but compliance of the standard discs was substantially higher than for the optically lapped discs. Those stacks received from the supplier in a permanently bonded state exhibited even higher compliance and were not used for life testing. High compliance is a severe problem for the driver stacks as used for life testing, but may actually be beneficial in a pure generator application. To maintain operating voltages at manageable levels, many relatively thin discs are used. The resultant large number of interfaces is the principal source of high compliance, with the result that much of the strain energy produced is not applied to the generator stack.

One result of nearly all stack testing, or even preloading to a substantial axial load, is that many of the discs crack into two or more pieces. Based on MTS tests using discs before and after cracking occurred, no apparent performance degradation results from this disturbing phenomenon. Some of the life test stacks were found to have cracked discs after assembly.

Through 7 September 1973, the IRAD stack had accumulated 3338 hours of excitation for a total of 0.721×10^9 cycles. Of the 3118 hours accumulated after the final load was established, the reduction in normalized output power was less than 5%, discounting occasional statistical or other variations. The normalization applied to the power output, based on theoretical expectations, was to divide the power density by the square of the applied stress swing. Efficiency data showed considerable scatter, especially about 900 to 1200 hours after life tests began, but the efficiency trend was basically constant.

In general, long-term operation of piezoelectric generators was demonstrated to be feasible, although many practical problems in integrating the generator into a practical power system remain to be resolved. Present costs of piezoelectric discs and assembly techniques may be prohibitive for most applications. Coupling reliably with the high-force low-displacement characteristic of piezoelectric generators presents significant problems as well. If successful application of Stirling engine piezoelectric generators is made, it may initially be at very small power levels where the piezoelectric generator is unique in maintaining a high efficiency.

Section 2

INVESTIGATION AND DISCUSSION

This section discusses the analytical methods applied to all the components of the system, how these methods were used to arrive at a reference design for the proof-of-principle test device, a piezo-electric generator design to meet the same requirements, and mechanical design considerations incorporated into the proof-of-principle test device.

2.1 ANALYTICAL METHODS

Concurrent with this work, a computer simulation has been developed for a Stirling engine, coupler, and simulated load system in an independent research and development program. Based on experience with this simulation, a reference design was chosen and the mechanical design layouts were completed.

2.1.1 Engine Analysis

Figure 2-1 shows a simplified schematic of the engine. The cylinder wall consists of discrete heater, cooler, and regenerator sections. Inner surfaces of the heater and cooler are held fixed at the heat source and sink temperatures, respectively. The regenerator section has an approximately linear temperature profile between the heater and cooler temperatures. As the displacer reciprocates in the cylinder, engine gas is shuttled between the hot and cold ends through the thin annular clearance. The power piston follows displacer motion with a phase lag near 90°. The expansion stroke occurs while the displacer moves from mid-stroke to bottom dead center and back to mid-stroke (while most of the engine gas is in the hot region). Conversely, power piston compression occurs while the displacer moves between mid-stroke and top dead center (gas mostly in the cold region). Because hot expansion work output is greater than cold compression work requirement, net power is delivered by the engine.

Various approaches to analyzing modified Stirling-cycle engines have been developed at DWDL over the past five years. The most extensively used is the isothermal analysis in which gas volumes in the engine are assumed to have a steady temperature throughout one cycle. This is an integrated approach in which all computations are time averaged over one cycle. All loss mechanisms are assumed to act independently so that the principle of superposition can be applied.

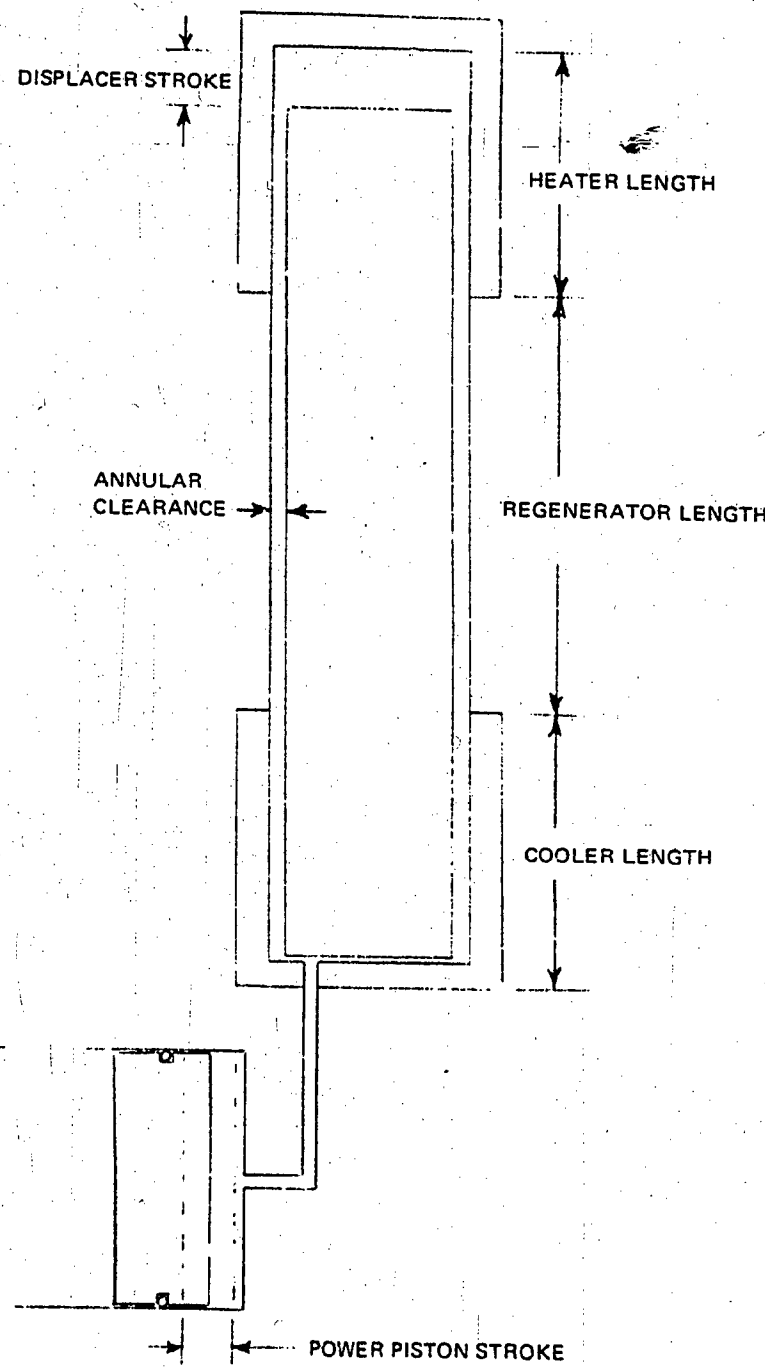


Figure 2-1. Simplified Engine Schematic

Analysis can be reduced to the solution of a set of algebraic equations. This approach has the advantage of short computation times and is well suited to parametric survey and optimization analyses. It has been used with good success in accurately analyzing engines for the National Heart and Lung Institute.

The other basic type of program is called nonisothermal because gas volumes in the engine have a changing temperature throughout one cycle. The computer program utilizes a time-step solution which models the system with simultaneous interactions and inherently includes nonisothermal heating and cooling effects caused by pressure changes. The accuracy of the results is limited only by the accuracy of the analytical model and the time step size, which can be arbitrarily small in principle. Computer running times are typically two or three orders of magnitude longer for the latter program because a full set of calculations must be made for each time step in a cycle and the solution must continue through several cycles to eliminate transients.

Computer programs representing both types of analytical models have been used in the design of the STEPZ proof-of-principle system. The isothermal program requires about seven seconds per case and is set up for running parametric surveys with minimum effort. It has proved to be satisfactory for optimizing all parameters except compression ratio. If the latter is restricted to values known by experience with the nonisothermal simulation to be reasonable, the isothermal program can be used with confidence to design new engine configurations, and in practice, is the only feasible means for so doing. The nonisothermal simulation includes dynamics of the entire system and provides the best available accuracy for predicting operation of a given system design. Comparisons are made in Section 2.2.1 between the isothermal and nonisothermal performance predictions.

The isothermal program was developed to operational status and used with extensive parametric surveys to establish the STEPZ engine geometry prior to initiation of this program. The simulation was then utilized during Phase I to verify the earlier engine design and to refine the operating parameters and performance specifications where necessary.

2.1.1.1 Isothermal Analysis

In this analysis, gas temperatures in a given region are assumed not to vary in temperature over one cycle. Average hot and cold gas temperatures are determined by an iterative process based on limited heat transfer. Power output is computed from the Schmidt equation (Reference 2) which is an analytical solution of the pressure-volume integral over one cycle. Sinusoidal motion of the regenerator and power piston with a specified fixed phase angle is assumed, which is very realistic for conventional Stirling engines with

mechanical phasing. In the STEP% system, both power piston and displacer move almost sinusoidally but the phase angle between the two is not fixed.

Heat transfer between metal and gas in the annular clearance is determined by assuming laminar gas flow. The heat transfer coefficient depends on annular clearance and not on gas velocity. The heat transfer calculational approach is given in some detail in Appendix D.

Imperfect heat transfer in the heat exchangers reduces the average hot gas temperature and increases the average cold gas temperature. The basic engine heat requirement (second law heat) is computed from output power by assuming the engine is an ideal heat engine with Carnot efficiency computed on the basis of average hot and cold gas temperatures. Another set of heat requirements (or losses), only one of which is significant in the STEP% engine, applies when the engine is running. Less-than-perfect heat transfer in the regenerator region (main reheat loss) contributes the primary loss mechanism in the STEP% engine. Main reheat loss results from not regeneratively supplying all the heat necessary to increase the gas temperature from the cold to hot values as gas flows through the regenerator. Heat which is not supplied regeneratively must be supplied by the heater. Calculation of main reheat loss is detailed in Appendix D. The rest of the thermal losses apply whether the engine is running or not. These include insulation loss, cylinder and displacer wall conduction, and gas conduction and radiation through the displacer.

In high power engines, mass flow around the regenerator is a critical parameter. In the isothermal analysis program, the maximum and minimum mass of gas in the hot and cold gas space is computed from a formula which considers the sinusoidal motion of both the displacer and the power piston, fixed gas temperatures, fixed total mass of gas, and an instantaneously uniform engine pressure. Mass flow calculated in this way is only approximate and leads to a significant error in main reheat. This does not have a major impact on the optimization capabilities, which represent the prime usage of this program. Windage power is based on the further approximate assumption that gas flows past the displacer sinusoidally, but windage calculations are nevertheless very accurate.

2.1.1.2 Nonisothermal Simulation

The nonisothermal dynamic simulation overcomes most of the basic limitations imposed by the isothermal model. Two basic versions of the simulation are available for specialized applications. The simpler version, like the isothermal program, calculates performance of the engine only. Power piston and displacer motion are specified as

sinusoidal with a fixed phase lag. This solution stabilizes most rapidly because only thermal processes are affected by transients. A more complete simulation includes an equation of motion for the displacer and coupler and a generator simulation. Because the displacer equation of motion includes flywheel torque, an externally driven displacer can be simulated by specifying a large moment of inertia for the flywheel. While the nonisothermal simulation is a substantial improvement over previous techniques, it remains incomplete in two general areas.

The major thermal inaccuracy involves specification of linear temperature profiles in the cylinder and displacer sidewalls. Calculations showed that, on the average, during the cycle, some portions of the cylinder and the displacer walls in the regenerator were losing more heat than they were receiving, and no provision was made for supplying this heat from the heat source. Other portions of the regenerator were gaining more heat than they were losing and no provision was made for conducting this heat to the heat sink. Figure 2-2 shows the average gas temperatures for the 10 nodes of the displacer in comparison with the assumed temperatures of the engine for the reference design. In the hot space, heater, cooler, and cold space, it is expected that the average gas temperatures will be different than the metal temperature because of the net heat flow through the engine. However, in the regenerator, it is assumed that there is no net heat flow between the gas and the walls. For the displacer this appears to be true. In the case of the cylinder wall, for the assumed temperatures to be true, additional heat must be supplied from the heater and be conducted along the cylinder wall to supply nodes 3 and 4. In the same way, additional cooling must be arranged for nodes 6 and 7. Under such conditions, an accurate heat balance was not possible. However, the effect on overall performance is very minor. In actual operation, experience with heat engines shows that an S-shaped wall temperature profile will result with minimal effect on engine thermal requirements. The basic heat requirement for the engine is determined by $\int pdV$ in the hot space plus a calculation of the main reheat loss. These do not depend on the computed heat transfer from and to the nodes. The problem could be remedied by adding nodes in the metal walls of the regenerator, each with an appropriate heat capacity and thermal conductance to adjacent nodes, but the simulation then would require reprogramming for a larger computer and become costly to run.

The other thermal inaccuracy concerns the uncertainty of heat transfer rate at the end walls in the hot and cold regions. A conservative assumption is now being used in both hot and cold spaces. It is assumed that no bulk mixing occurs, and heat transfer occurs through stagnant gas. Only with experimental data can this inaccuracy be assessed.

A unique method of computer simulation has been developed which allows a much larger time step than is stable for a conventional

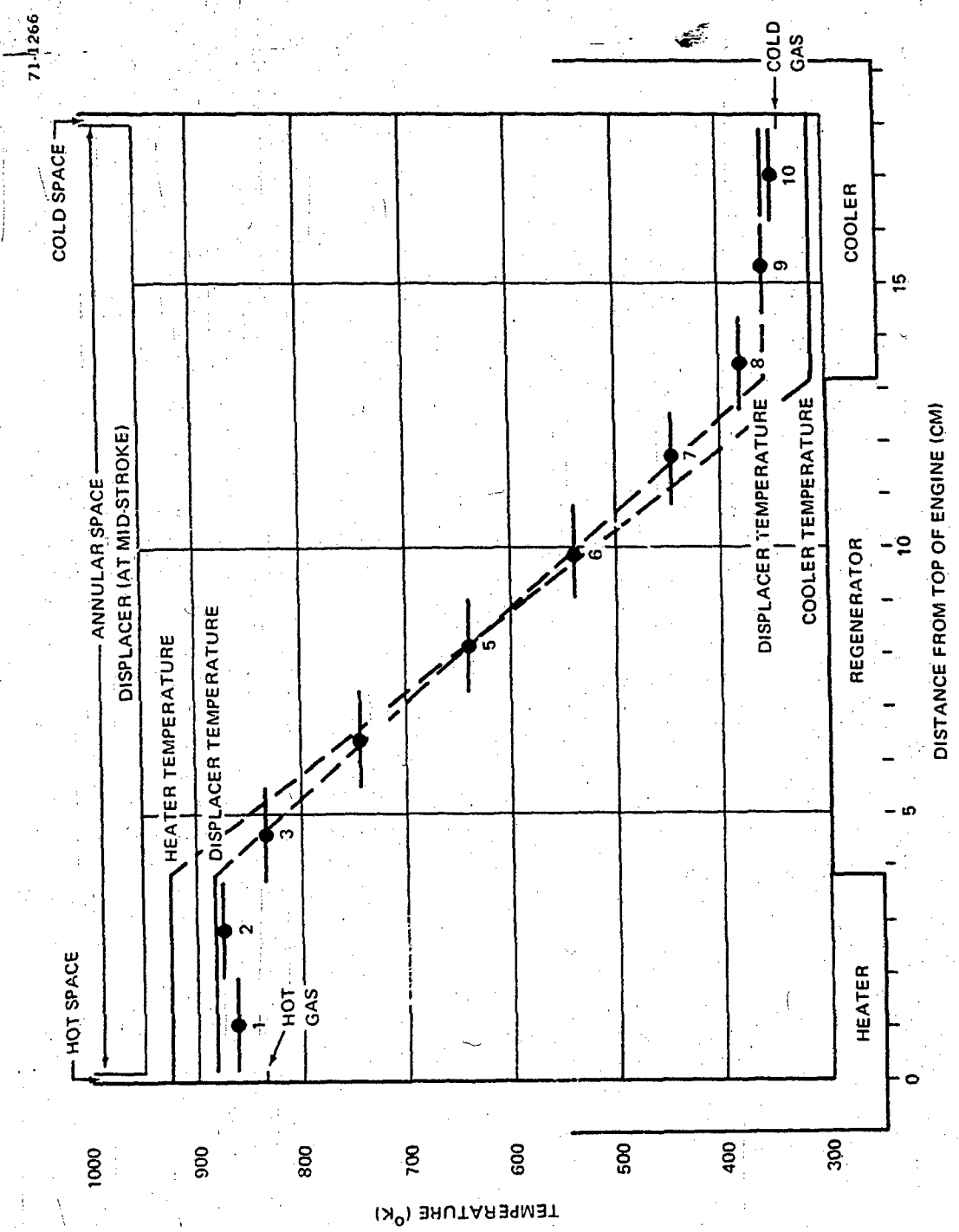


Figure 2-2. Comparison of Computed Average Gas Temperature with Input Metal Temperatures (Reference Design)

simulation scheme. This improvement has allowed limited use of nonisothermal parametric survey techniques for this report.

Some more subtle differences between the isothermal and nonisothermal simulations require discussion. In the isothermal simulation, second law heat input is determined by applying the Carnot equation to the time-averaged gas temperatures. This is only an approximation at best, because the nature of the temperature variations over one cycle have an impact on heat transfer. For example, in the STEP% reference design case using the nonisothermal simulation, hot gas temperature at one point reaches 60°C above the heat source temperature. This results in some heat flow from the gas to the heater which must be made up during other parts of the cycle. The net result is that most heat is transferred to the gas when it is at below-average temperatures. The effective temperature for determining second law heat input from the Carnot relationship is, therefore, below the time-averaged gas temperature, and, for this reason, the isothermal program gives a low value for second law heat input. However, the nonisothermal simulation can exactly determine the value by numerically integrating the pressure with respect to volume in the hot region over one cycle. Work output is similarly calculated by integrating cold region pressure with respect to total gas volume. Main reheat is determined by the same basic equations as in the isothermal program, except that it can be computed more accurately because it is based on instantaneous mass flow. This results in a significant increase in calculated main reheat, as discussed in Appendix D.

In the more complete engine simulation, displacer piston motion is determined by a force balance on the displacer which includes such effects as drive chamber pressure, flywheel torque, friction, windage, gravity, and spring forces. Flywheel torque is determined by solving a torque balance equation on the flywheel.

The equation for displacer dynamic force balance is (Figure 2-3).

$$P_H A_{DIS} - P_C (A_{DIS} - A_D) - P_D A_D - F_C \cos \phi \pm F_F$$

\pm Spring Forces - Gravity Force - $M_{DIS} \ddot{x}_{DIS}$

where

P_H = pressure in hot space

A_{DIS} = cross-sectional area of displacer

P_C = pressure in cold space

A_D = cross-sectional area of drive rod

P_D = drive chamber pressure

F_C = tension or compression force in connecting rod

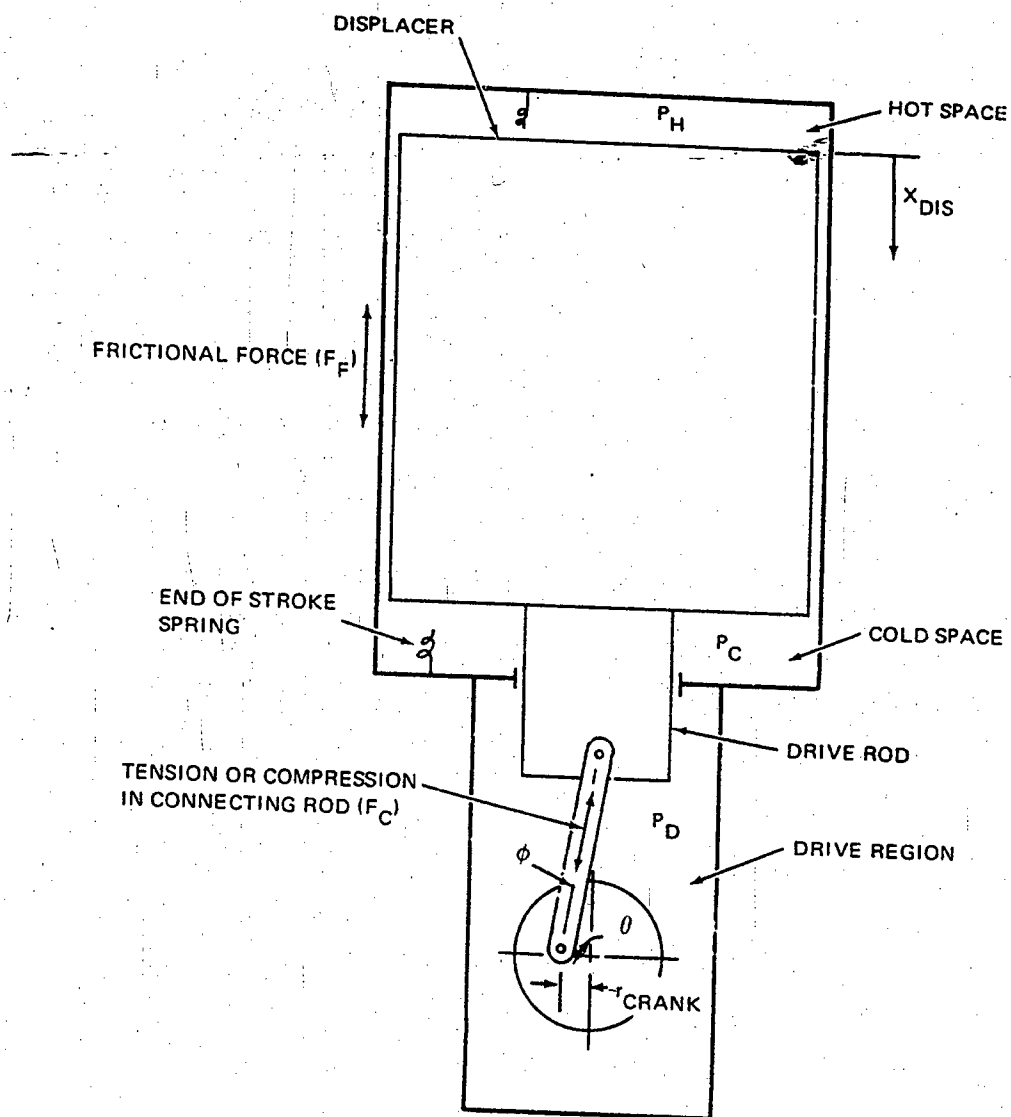


Figure 2-3. Free Displacer Simulation Terms

ϕ = angle between drive rod and connecting rod

F_F = frictional drag on drive rod

M_{DIS} = reciprocating mass of displacer

\ddot{X}_{DIS} = linear acceleration of displacer

The connecting rod force, F_C , is determined by a torque balance on the flywheel

$$F_C r_{crank} \sin(0 + \phi) - \text{Frictional Torque} + \text{External Torque} = I \ddot{\theta} \quad (2)$$

where

r_{crank} = crank arm radius

θ = angular displacement of connecting rod from top dead center

I = flywheel moment of inertia

$\ddot{\theta}$ = angular acceleration of the flywheel

Equation 1 is solved for displacer acceleration, \ddot{X}_{DIS} , at time t , and this value is used to determine the velocity, \dot{X}_{DIS} , and displacement from midpoint, X_{DIS} , at time $t + \Delta t$ by

$$\dot{X}_{DIS}(t + \Delta t) = \dot{X}_{DIS}(t) + \ddot{X}_{DIS}(t) \Delta t \quad (3)$$

$$X_{DIS}(t + \Delta t) = X_{DIS}(t) + \dot{X}_{DIS}(t) \Delta t + 1/2 \ddot{X}_{DIS}(t) \Delta t^2 \quad (4)$$

The external torque term in Equation 2 represents the torque applied by an electric motor. If this is zero, there is a net force balance on the displacer at any time which moves the displacer in some manner. It is desirable to have sinusoidal motion with the displacer leading the coupler by approximately 90°.

2.1.2 Coupler Analysis

Figure 2-4 shows the arrangement of the fluid coupler. The basic element is the fluid inertia column contained within the coupler tube. This inertia column permits optimum engine and load performance by eliminating the requirement of instantaneous engine and load pressure equality. This is made possible by the large pressure difference required to accelerate the liquid column at the velocities and displacements of interest.

The fluid is contained at each end of the coupler by relatively large diameter corrugated metal diaphragms. Diffusers are provided at each end to minimize coupler tube entrance and exit flow losses. The corrugated diaphragms are thin and cannot support a significant pressure difference. With reference to Figure 2-4, the equation of motion of the coupler is

$$P_E A_C - P_L A_C - \rho_C L_C A_C \dot{x}_C - 1/2 C_C A_C \rho_C \dot{x}_C^2 = 0 \quad (5)$$

where

P_E engine pressure

A_C coupler tube cross-sectional area

P_L load pressure

ρ_C coupler fluid density

L_C coupler tube length

\ddot{x}_C fluid acceleration in coupler tube

\dot{x}_C fluid velocity in coupler tube

C_C flow loss coefficient

The flow loss coefficient is given by

$$C_C = C_D + C_T \quad (6)$$

where

C_D diffuser coefficient

C_T coupler tube friction coefficient

The diffuser coefficient C_D includes friction and entrance and exit losses between the coupler throat and the corrugated diaphragms. It is a complex function of throat angle, throat length, and Reynold's number. As used here, it includes flow losses in the diffuser proper plus a full head loss assuming sudden expansion at the end of the diffuser. These two-loss components are plotted in Figure 2-5 as functions of the area ratio at the two ends of the diffuser. The two diffuser loss curves are experimental correlations from Reference 3 for loss coefficients at the specified upstream Reynold's numbers with an optimum total diffuser angle of 7.5°. These essentially

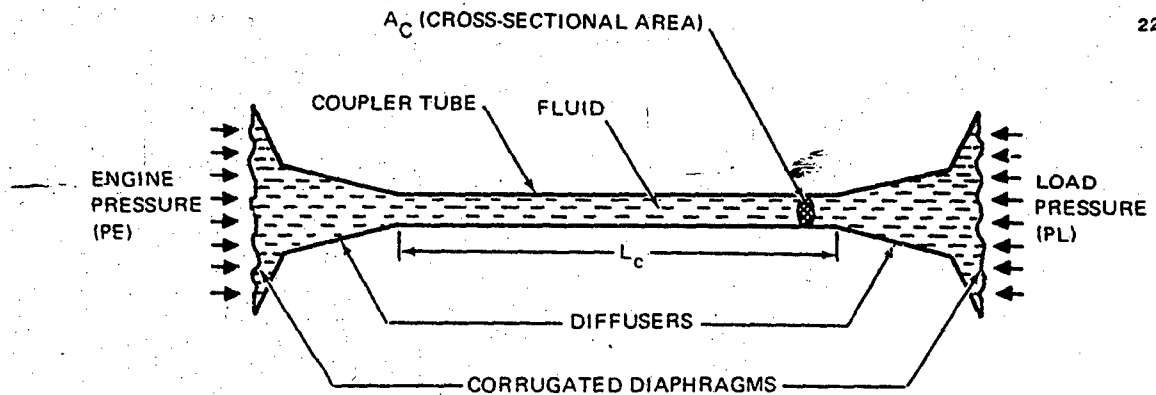


Figure 2-4. Fluid Coupler Arrangement

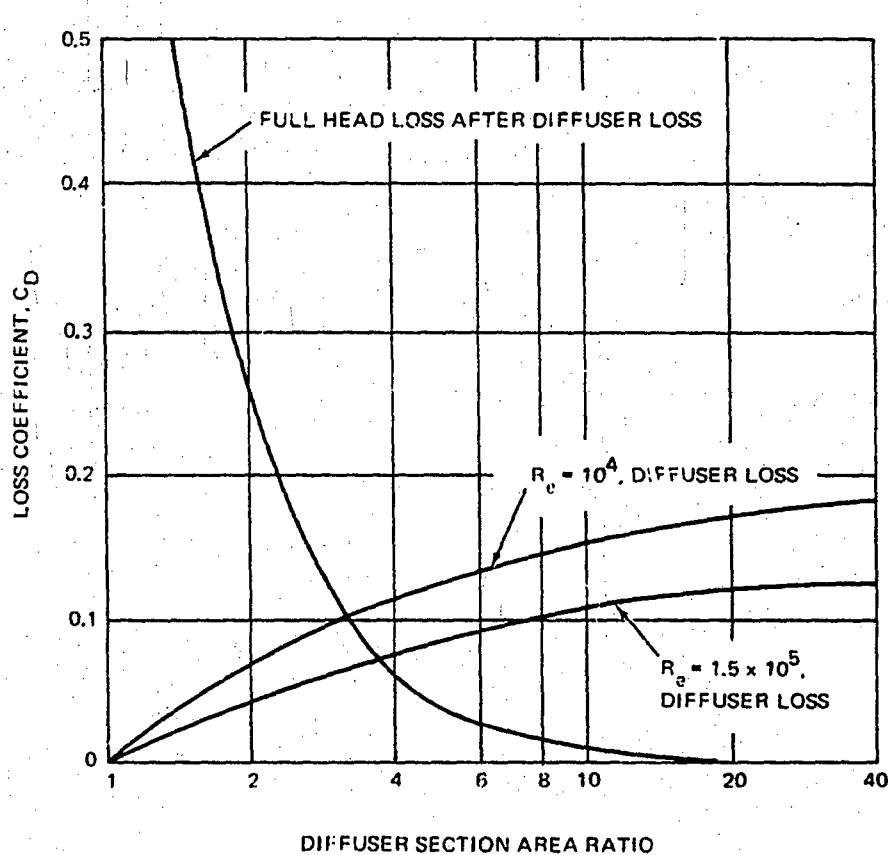


Figure 2-5. End Region Loss Coefficient Components

bracket the range of loss coefficient values. The third curve represents the total head loss for infinite expansion from the large end of the diffuser. The STEPZ coupler design has an area ratio of about 6 which gives a near optimum total loss coefficient of 0.12 to 0.16. A conservative value of 0.2 is used in the simulation. The coupler tube friction coefficient is expressed in general terms by the Blasius formula (Reference 4) for turbulent flow through smooth pipes and represents all friction losses in the necked down region of the coupler. It is expressed as

$$C_T = \frac{0.3164}{Re} \times \frac{L_C}{d} \quad (7)$$

where

Re = Reynolds number

L_C = coupler tube length

d = coupler tube diameter

C_T is typically 0.2 to 0.4 which is on the order of C_D .

2.1.3 Piezoelectric Generator Analysis

2.1.3.1 Material

The piezoelectric generator consists essentially of a stack of piezoelectric ceramic crystals which are subjected to compressive stress by the engine and coupler. While several naturally occurring crystals exhibit piezoelectric properties, in the last two decades work has centered on developing piezoelectric materials with improved electromechanical constants and better temperature and time (aging) stability.

Progress has centered on ferroelectric crystals with a perovskite structure. This structure is a cubic close-packed arrangement of oxide ions and the larger cations, with the smaller cations occupying octahedral interstices in an ordered pattern. Useful perovskite piezoelectric compositions of lead zirconate titanate (PZT) have been patented in the United States by the Clevite Corporation. Lead zirconate titanate compositions have 170° to 400° C. curie points (the temperature at which materials permanently lose their piezoelectric properties) which permit high operating temperatures. This characteristic, together with favorable piezoelectric electromechanical constants, enables power densities of at least 10 w/in.³ to be achieved.

Polycrystalline ceramic PZT material has an advantage of more stable polarization than single crystals and can be molded into

desired shapes before polarizing. Table 2-1 shows the pertinent properties of some important piezoceramic materials.

Appendix A describes the work performed by Physics International working with PZT-5H, a material capable of producing a high output power for a given stress, and LTZ-1 (similar to PZT-4), a material which produces a lower output power for the given stress, but which can withstand high compressive stresses without degrading its piezoelectric properties.

Appendix C describes the analytical techniques utilized at DWDL for predicting performance and correlating theory with experimental data. Included are correlations of the PZT-5H and LTZ-1 data with theory.

2.1.3.2 Power Output, Losses, and Efficiency

When the piezoelectric crystal is compressed, energy is stored both in mechanical and electrical form, typically about equal in magnitude. Electric energy is stored as the charge on an effective capacitance; the mechanical energy is stored as the potential energy of a compressed spring. The piezoelectric crystal may be connected to a load continuously or intermittently. In the latter case, the material functions as a voltage generator with a voltage proportional to the applied force. This energy can then be discharged periodically into a load.

For energy conversion, the fraction of energy stored as electrical energy is all that is available to the load; however, most of the stored mechanical energy is not lost; it is returned to the engine when the compressing force is relieved. This fraction of input mechanical energy, then, does not enter into an efficiency calculation for time-averaged power.

Both electrical and mechanical losses do occur and must be accommodated in any efficiency calculation. Electrical losses result from Joule heating and electrical hysteresis in the stack. Mechanical losses are both internal and interfacial and typically total a few percent of the output, with best performance occurring at resonance. Internal losses result from domain motion within the ceramic material and interfacial losses from relative motion of the ceramic with respect to electrodes and epoxy at the piezoelectric disc interfaces in the stack. The electrical losses are dependent on the electric field on the disc and on stress and load resistance. Mechanical losses depend on stress and piezoelectric stack geometry.

Superimposed on these dependencies is a temperature dependence. Temperature affects all piezoelectric properties. Furthermore, mechanical stresses occur with temperature changes at the disc interfaces because of differential expansion. Increases in stack temperature can result from internally generated heat associated with these

Table 2-1
MATERIALS PROPERTIES FOR HIGH POWER
PIEZOCERAMIC GENERATORS

Manufacturer	Designation	d_{31} (A)	M _r (Curie Temperature)	Allowable Stress (psi)	Density (g/cm ³)	(s)		(s)		(s)	
						Curie Voltage Coefficient	Charge Coefficient	Tan δ	Electrical Dissipation Factor	Relative Dielectric Constant	
		(V/m)	(N)	(M)	(V)						
Vernitron	PZT-4 (1)	12,000 at 25°C 6,000 at 100°C	7.5	>28	26.1 $\times 10^{-2}$	289 $\times 10^{-12}$	0.004	1300			
	PZT-5H (1)	2500 at 25°C 2090 at 109°C	7.5	193	19.7 $\times 10^{-3}$	593 $\times 10^{-12}$	0.02	3400			
Galton Industries Transducer Products	HTD-J1 (2)	10,000	7.6	>30	24 $\times 10^{-3}$	280 $\times 10^{-12}$	0.066	1300			
	LTZ-1 (3)		-7.5	550	24.2 $\times 10^{-3}$	284 $\times 10^{-12}$					

Notes: 1. Properties reported in Vernitron Catalog 695, "Piezoelectric Technology Data for Designers".

2. Properties reported in Gulton Catalog H-700, "Glenite Ceramics" except maximum allowable stress which was provided by T. Swanson, Gulton Industries.

3. Appendix A, Table A-1.

4. In practice, the operating temperature of the piezoelectric material must be kept significantly below the curie temperature.

5. Generally, these coefficients are shown with subscripts, e.g., d_{31} and d_{32} , which indicate the direction of the applied stress (e.g., in the Z direction) and the location of the electrodes (e.g., perpendicular to Z axis). In this report, the subscript j is understood to apply and all subscripts are omitted.

6. The values presented are for a crystal without mechanical constraint.

loss mechanisms or from increases in ambient temperature. Preliminary measurements suggest some reversible degradation in power output with an increase in temperature above ambient.

For large, high-power piezoelectric stacks, operating temperature must be maintained low enough that the maximum operating stress does not introduce permanent degradation. The higher the stack operating temperature, the lower is this allowable maximum operating stress. For PZT-4 material, the manufacturer's catalog (Reference 5) indicates this stress as 12,000 psi at 25°C but only 6000 psi at 100°C. For long-term stable operation, the allowable stress may be only 50% to 60% of these values according to some manufacturer representatives or may be much higher according to others. Only life testing of stacks under various stress and fabrication conditions can unequivocally answer the questions of maximum allowable stress for given requirements.

In the discussion which follows, the nomenclature involved in power output and power loss calculation is introduced. This enables discussion of performance expectations, parametric dependencies, assumptions, uncertainties, and relative merits of continuous operation versus pulsed operation.

The electric field gradient generated in a piezocrystal is proportional to the applied stress

$$E = \frac{V}{t} = g (F/A)$$

where the constant of proportionality, g , is called the piezoelectric voltage coefficient, E is the electric field, V the generated voltage, t the ceramic thickness, and F/A the stress or force applied per unit area. In this equation, the use of peak force results in peak voltage, and rms force results in rms voltage.

To determine the output power generated by a piezoelectric crystal, the dependence of force with time and the equivalent electric circuit must be established. At the relatively low frequencies (<500 Hz) being considered for compressing the piezoelectric material, the material is considered electrically as a voltage generator in series with a resistor and capacitor (Figure 2-6). In Appendix C, a more complete equivalent circuit involving series and shunt resistances is utilized as a basis for detailed analysis.

2.1.3.3 Continuous Operation

For continuous (non-pulsed) operation, the optimum load resistance for a nonreactive load equals the internal impedance of the stack plus the impedance of the leads. Because the capacitive reactance is so much greater than the stack and lead resistance at the frequencies being considered, these can be disregarded. Then, maximum power transferred is given by

$$W = \left(\frac{F_{\text{rms}}}{A} g t \right)^2 \frac{R_L}{(R_L^2 + X_c^2)}$$

where

$$X_c = R_L$$

For sinusoidal compression, this reduces to

$$W = \left(\frac{F_{\text{avg}}}{A} g t \right)^2 / 4X_c$$

where

$$X_c = 1/\omega C_0$$

with ω the angular frequency and C_0 the piezoelectric/ceramic capacitance $\epsilon_r A/t$

where ϵ_r is the relative dielectric constant of the material and ϵ_0 is the dielectric constant of free space (8.85×10^{-12} farads/meter).

Appendix A provides a stepwise derivation leading to

$$W = \frac{\omega}{16} d g \sigma^2 V_{\text{PZ}}$$

where

$$\sigma \text{ is the peak stress} = 2F_{\text{avg}}/A$$

$$V_{\text{PZ}} \text{ is the volume of piezoelectric material} = At$$

$$d \text{ is the piezoelectric charge coefficient} = \epsilon_r g$$

For this case, the equivalent circuit is shown in Figure 2-7.

Because no net energy is dissipated by the capacitor, essentially all power is applied to the load, and overall efficiency is near 100%. Losses are calculated using the electrical dissipation factor (D or $\tan \delta$) which equals the ratio of effective series resistance divided by X_c . Mechanical losses within the crystals are generally small compared to these electrical losses. Mechanical losses associated with stacking several crystals together and with coupling the stack to the compressing mechanism (e.g., piston) may be appreciable in practice. Electrical losses which do occur result from lead resistance and internal resistance of the piezoelectric stack, which were assumed in the first paragraph of this section to be much smaller than X_c and consequently much smaller than R_L also. Thus the Joule heating is much less in these resistances than in R_L which results in the high efficiency. While these losses must eventually be considered, additional work is required before a meaningful estimate can be made. In

2218

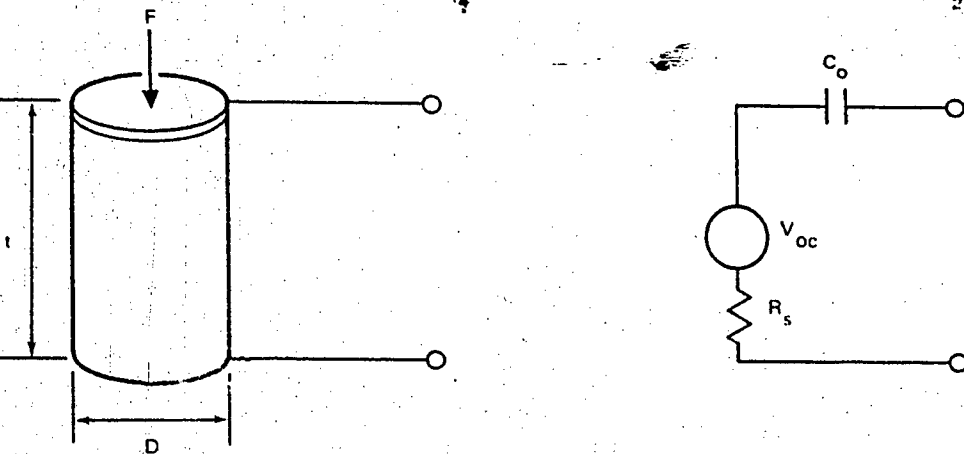


Figure 2-6. Equivalent Circuit for Piezoelectric Crystal Under Compression

2219

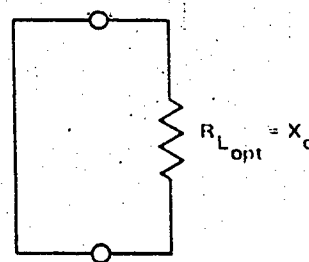


Figure 2-7. Equivalent Circuit with Sinusoidal Compression and Resistive Load

the literature, mechanical losses are considered as those effects that increase compliance of the stack. However, because stack spring-back is used, mechanical losses are only those frictional or hysteresis effects that result in heat.

Inductance can be added to the load circuit to reduce total reactance. When this is done, the optimum load resistance decreases, and maximum power available from a given stack increases as the inductive reactance approaches the capacitive reactance. At optimum, the inductive reactance equals the capacitive reactance, and stack and lead resistance are the only remaining components of impedance in the circuit with the load resistor. For the same load resistor ($R_L = X_C$) as gave maximum output power without inductance, adding inductance in this formulation permits four times as much power because the inductance has effectively cancelled half the circuit impedance, thereby doubling the current. Power to the load is $I^2 R$ and is therefore increased four times. The efficiency of the circuit is equal to the power delivered to the load divided by the power to the load plus power dissipated internally. When the internal resistance and its field dependence, inductor resistance, and frequency of operation are included as in Appendix C, this improvement in output power from adding inductance becomes a factor of two instead of four.

Maximum power transfer can be obtained by reducing the load resistor until it equals the sum of the stack, inductor, and lead resistances. The maximum power transfer is over four times greater than what was possible without the inductance. However, efficiency has decreased from nearly 100% to, at best, 50%, if mechanical losses are disregarded. Approximately half of the power is now dissipated in the stack and half is transferred to the load.

While this condition permits the smallest stack for a given output power, overall efficiency and stack overheating problems dictate operating at a load resistance well above the level for maximum power transfer. As the various power loss mechanisms within the stack are better understood, the design point can be optimized. Experimental measurements to date show that 60% of this maximum power transfer can be obtained with electrical losses in the stack reduced by more than half. Mathematical and experimental details of these results are presented in Appendices B and C.

The force-displacement diagram for the continuous connection (non-pulsed operation) is approximately as shown in Figure 2-8.

2.1.3.4 Pulsed Operation

Because energy stored in a capacitor is $E = 1/2 CV_{oc}^2$, stack energy becomes

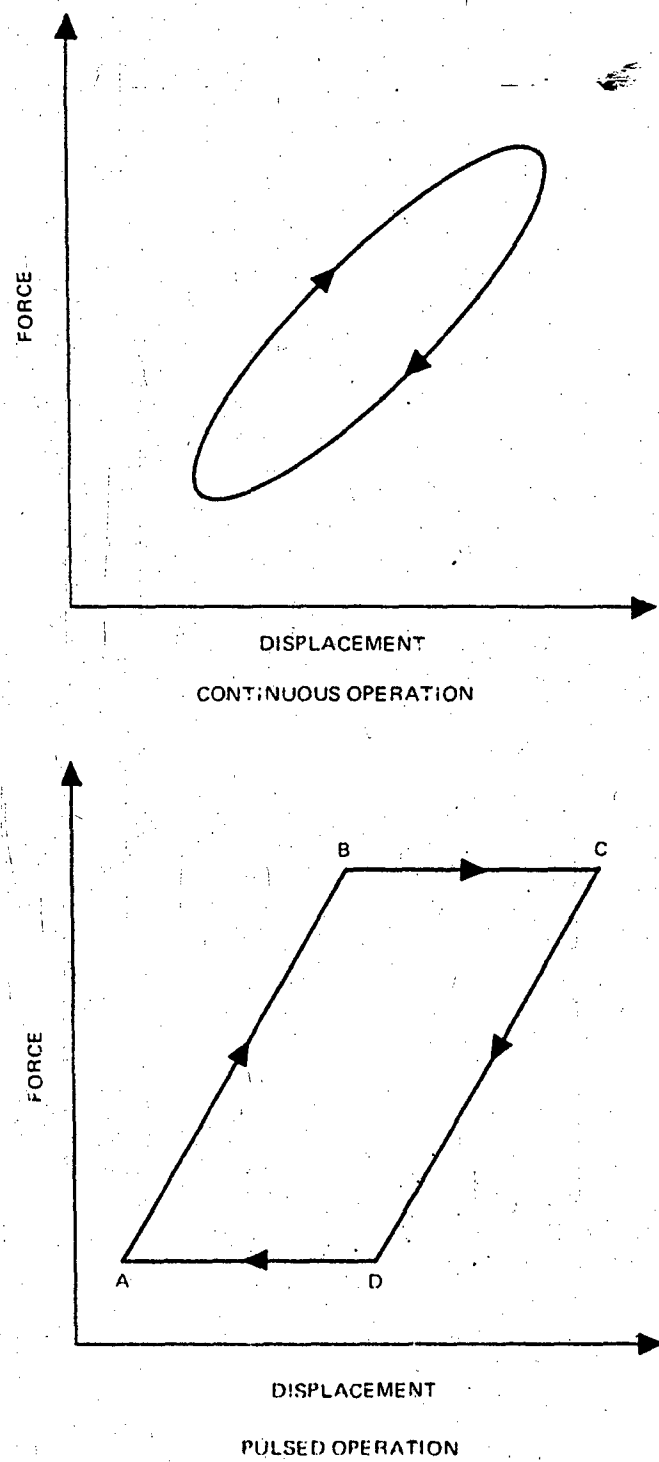


Figure 2-8. Force-Displacement Diagrams

$$E = 1/2 C_0 \left(\frac{F_{\text{peak}}}{A} g t \right)^2$$

where C_0 is the capacitance of the stack.

This energy is available each time the piezoelectric crystal is compressed or relaxed, or twice each cycle. Average power is then

$$W_{\text{po}} = \frac{2\pi}{2\pi} \sigma^2 d g V_{\text{PZ}}$$

The formulation of this equation and the mathematics of pulsed operation with only resistive or resistive and inductive loads are presented in Appendix B.

Average power during continuous operation (without inductance) can be compared with pulsed operation by

$$\frac{W_{\text{po}}}{W_{\text{co}}} = \frac{\frac{2\pi}{2\pi} \sigma^2 d g V_{\text{PZ}}}{\frac{8}{16} \sigma^2 d g V_{\text{PZ}}} = \frac{8}{\pi} = 2.55$$

This factor of 2.55 is reduced by various interactions of the system operating in the pulsed mode. For a given stack configuration, there is an optimum load resistor to which power is transferred. Energy discharges from the stack with a time constant proportional to the capacitance of the stack and resistance of the load. By the time the force is again applied, not all of the energy has been discharged; in fact, only a small fraction may be discharged before the stack is again recharging on the next cycle.

Another limitation on pulsed operation is the extent to which the piston supplying stress to the stack can maintain this stress when the stack is being discharged. This will be determined quantitatively by the interaction of the electrical discharge time constant and the mechanical displacement time constant of the piston. Analysis must be done on this time constant interaction and the use of an inductor in the load circuit to determine practical operating parameters. Such system analysis will provide better understanding of the relative merits of pulsed and continuous operation.

Qualitatively (disregarding time constants), the force-displacement diagram for pulsed operation may appear as shown in Figure 2-8. The stack is compressed from A to B on open circuit, discharged without relaxing the force (B to C), stress is released on open circuit (C to D), and the stack is again discharged with opposite polarity (D to A).

2. 1. 3. 5 Parametric Dependencies

Both continuous and pulsed power output depend on several classes of parameters. System variables include maximum stress level, stress wave-form, and frequency. Stack variables include ceramic diameter and thickness and piezoelectric material parameters. Pertinent load system characteristics are maximum allowable voltage, load resistance, and load inductance.

In general, for a given stress (force/area), output power increases with frequency and with the volume of piezoelectric material. Output is, therefore, proportional to the height of the stack and the square of stack diameter. Because the output voltage is proportional to ceramic thickness, the same output power can be delivered at a lower voltage by using many thinner ceramic discs instead of fewer thicker discs. This assumes negligible stacking losses at the crystal interfaces. To the extent that these losses occur, output power and efficiency will be decreased.

Associated with piezoelectric ceramic crystals of decreasing thickness is the cost of fabricating additional ceramic discs for a given output power. A 0.020-in. thick disc costs about 25% more than a 0.040-in. thick disc. Disregarding potential losses at the additional disc interfaces, twice as many discs are required to supply a given power; therefore, stack cost is about 2.5 times as much. Reducing the disc thickness to 0.003 in. (to supply 30 volts rms without a transformer), increases the cost by 3 to 7 times above the 0.020-in. thick disc. Further, 7 times as many discs are required for a total cost of 20 to 50 times as much as the stack using 0.020-in. thick discs.

Stacking is much more difficult and manufacturing reliability decreases as disc thickness is reduced below 0.020-in. However, the thicker the disc, the higher the voltage generated, and the higher the heat produced within a single disc. These factors limit maximum acceptable disc thickness. If stack potential is more than 500 volts rms, additional insulation must be added to the stepdown transformer winding to prevent breakdown. This results in no significant penalty until potentials of a few thousand volts are reached. The 0.040-in. thick disc design provides less than 400 volts rms at the transformer primary.

A more significant constraint is heat generated per disc and the ability of the system to remove this heat without the piezoelectric ceramic overheating and degrading. The brass interdisc electrical connectors also remove heat radially from the stack. Because brass has a thermal conductivity about 50 times that of the piezoelectric ceramic material, the brass thickness can be adjusted so that most of the thermal gradient in the piezoelectric disc occurs over the short distance between the brass and the midplane of the piezoelectric disc, thereby making the temperature increase proportional to the piezoelectric disc thickness.

To facilitate removal of heat from the stack, the diameter of the brass connectors can be larger than the piezoelectric ceramic discs. The brass connectors then serve as fins to dissipate heat. Further analysis and design studies are needed to determine a desirable brass connector configuration. These studies must consider stack geometry, power and efficiency, ambient conditions, and assembly constraints.

Other design uncertainties can only be resolved by testing the piezoelectric stacks under system operating conditions for extended periods. These uncertainties are primarily in requirements for stack preparation and limitations on stack operating conditions. The uncertainties in stack preparation include piezoelectric disc surface finish requirements, epoxy modulus, and joint thickness. Uncertainties in stack operating conditions include interaction of maximum operating stress, frequency, and temperature, as these variables promote and retard degradation.

2.1.3.6 Simulated Generator

Two generators were modeled and used with the dynamic simulation program. One represented continuous power extraction, the second pulsed power extraction from the piezoelectric generator. Initial simulation involved continuous power extraction because this was the operating mode utilized in the testing program. Early test results were disappointing from a power density standpoint, and alternate approaches were evaluated. The most promising concept was pulsed power extraction, which could be simulated by a hydraulic pump. Evaluation of this simulated load concept showed several advantages over that for continuous operation, and it was subsequently adopted for the reference design. Recent studies and test results discussed in Appendices B and C suggest that continuous power extraction may well be the best approach for the piezoelectric generator. Experience with the system simulation program has shown that the type of load has no significant impact on system performance at the desired operating point. For this reason and to avoid duplication of effort, the hydraulic load has been maintained in the reference design. The paragraphs which follow describe the two simulated load approaches.

In the complete nonisothermal simulation of the system, a force-displacement characteristic must be included for the piezoelectric generator. Displacement of the piston which compresses the stack is keyed to displacement of the power piston in the test setup because the coupler has very little compliance. However, force applied to the generator piston by compressing the piezoelectric stacks depends on the electrical interconnection of the stacks. A continuous-operation generator simulation test setup which utilizes hydraulic flow dissipation and pneumatic bounce chamber is shown in Figure 2-9. Pressure recovery is obtained at the generator end of the coupler by a

diffuser. This is the point at which work would be applied to the piezoelectric stack if a real generator were used. A metal diaphragm can be inserted at this point if different fluid properties are required in the coupler and load regions for the real or simulated load. In the simulated load, the fluid necks down to a variable flow restriction which is characterized by both linear and quadratic terms in flow velocity to represent any desired combination of laminar and turbulent flow. After passing through the load restriction, the load region fluid operates against a pneumatic bounce chamber acting as a spring. If there were no flow restriction, pressure volume changes (Figure 2-10) would move up and down the dashed line, with no work performed. The overall volume of the bounce chamber determines the stiffness and nonlinearity of this pneumatic spring characteristic. With a flow restriction, the generator side coupler pressure is higher as liquid moves to the right and compresses the bounce chamber. Conversely, this pressure is lower when liquid flow reverses. The resulting P-V diagram is shown by the solid curve in Figure 2-10. Work at the flow restriction is converted to heat and dissipated by the cooling coils.

The pulsed-operation generator simulation test setup selected for the proof-of-principle system is shown in Figure 2-11. This is a very close analog to a piezoelectric generator optimized for pulsed power extraction (Appendix B). The coupler works into the load diaphragm from the diffuser on the generator side of the coupler. The load diaphragm separates mercury in the coupler from hydraulic fluid in the compliance chamber, but does not sustain any pressure difference. With the diaphragm in its extreme left position and the compliance chamber at reservoir pressure P_L (Figure 2-12), as the mercury column and diaphragm move to the right, hydraulic fluid in the compliance chamber is pressurized to P_H (A to B). Sizing of the compliance chamber and compressibility of the hydraulic fluid determine the slope of A-B. At Point B, the high pressure check valve opens. As the load diaphragm continues to the right, hydraulic fluid is pumped into the high pressure accumulator at constant pressure. When the diaphragm reverses direction, pressure drops (C-D), and the low pressure check valve opens. Fluid is returned to the compliance chamber at reservoir pressure, P_L , as the diaphragm continues its leftward motion. At Point A, the cycle repeats.

The accumulators allow hydraulic fluid to bleed through the throttle valve at a constant rate, even though fluid is delivered in pulses. A throttle valve simulates work (Figure 2-11) by dissipating energy stored by the high pressure hydraulic fluid. Heat generated by flow loss in the throttle valve is dissipated by cooling coils. This system has the advantage of providing a ready measurement of simulated power delivered by measuring flow through the simulated load and pressure drop across it. It can also be readily converted to produce real work by replacing the throttle valve with a hydraulic motor.

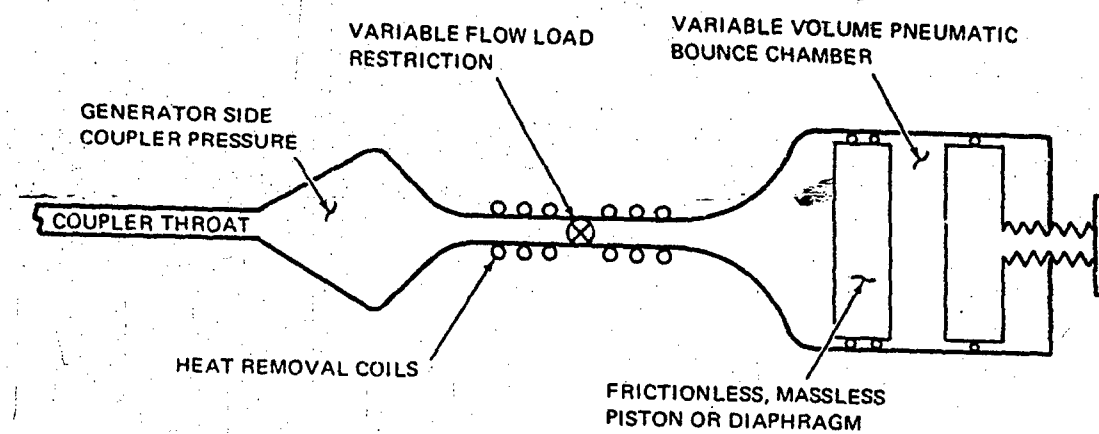


Figure 2-9. Continuous Power Load Simulator

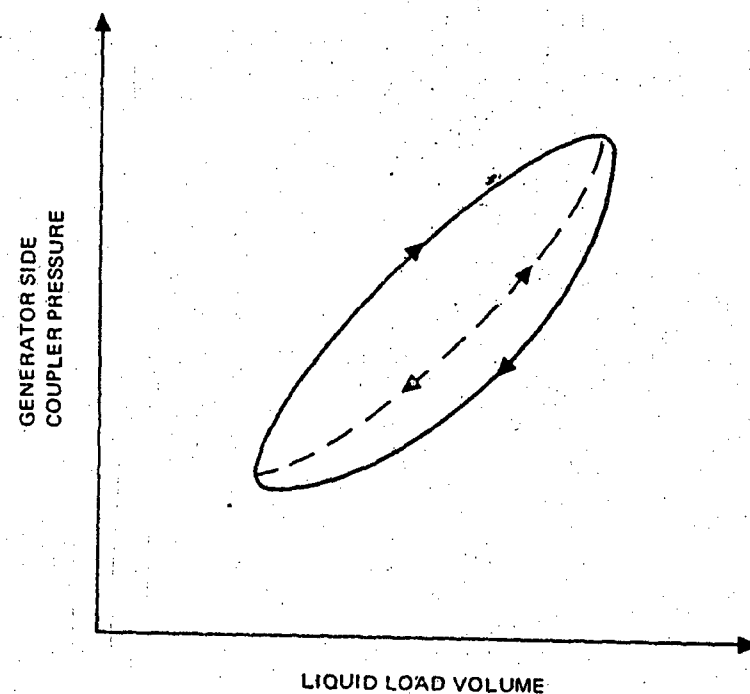


Figure 2-10. P-V Characteristics of Continuous Power Load Simulator

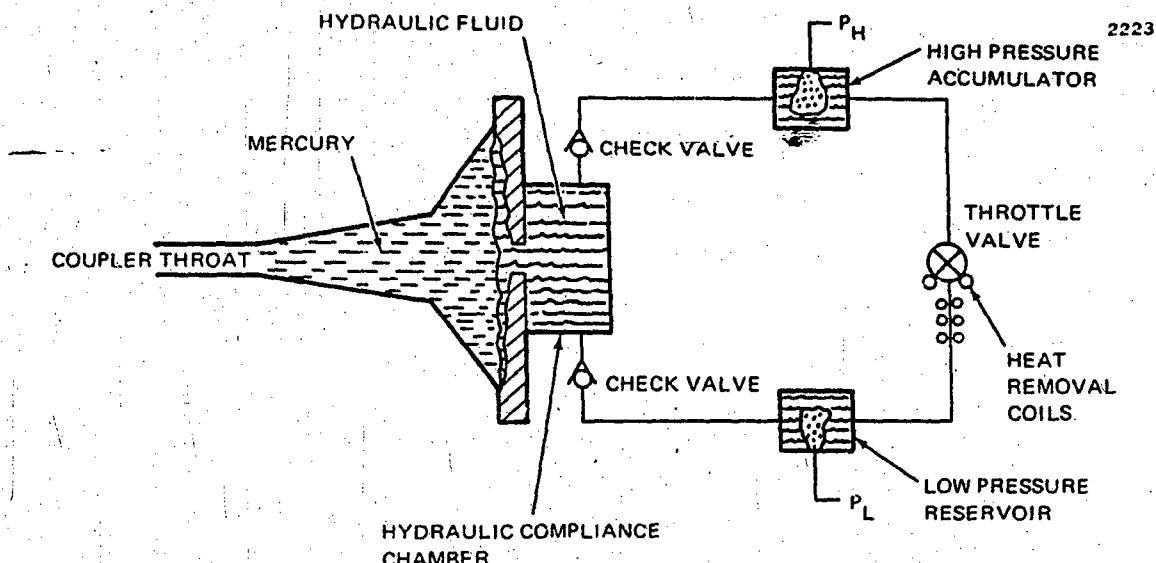


Figure 2-11. Schematic of Pulsed Power Piezoelectric Generator Simulator

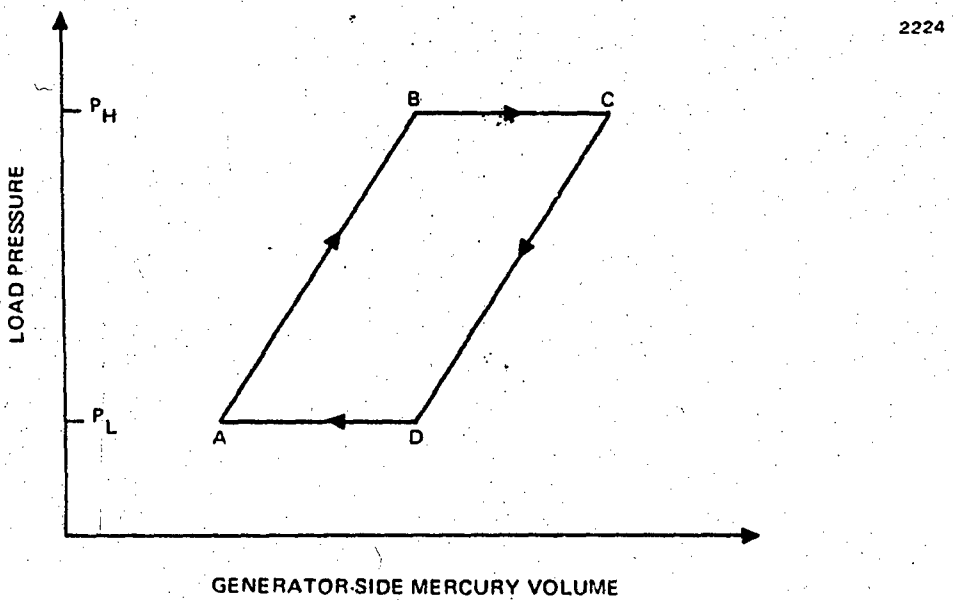


Figure 2-12. P-V Characteristic of Pulsed Power Load Simulator

Performance calculations with the two simulation models show virtually identical system performance at optimum, as a result of the large coupler inertia. The shape of the frequency response curve at off-optimum conditions differs in the two cases, but this does not affect the reference design system performance.

2.2 PERFORMANCE ANALYSIS

Using the analytical methods described in Section 2.1, performance of the proof-of-principle device and a suitable piezoelectric generator was computed.

2.2.1 Proof-of-Principle Test Device

Although the isothermal analysis was used to select the first reference design, real understanding of the problems came with the use of the nonisothermal simulation. Effects of nonlinear springs and the effect of displacer-power piston interaction were observed early.

The analysis which led to selection of the reference design is presented in this section. The design was selected using a very high moment of inertia for the displacer flywheel. This simulates a driven displacer which makes it much easier to achieve stable and consistent data for parametric studies. It was subsequently shown, as part of the startup and transient load change analysis, that a pneumatically self-driven free-running displacer is possible with a realistic flywheel inertia. It was also found that startup can be accomplished smoothly by cranking the displacer with an electric motor.

2.2.1.1 Effect of Nonlinear Springs

Some unexpected and apparently anomalous results emerged during development of the dynamic simulation. For example, coupler oscillation sometimes occurred at a frequency different from that of the displacer, typically in integral ratios, such as five power piston strokes for four displacer strokes. Bi-stable nodes were also observed, e.g., two cases with identical parameters and slightly different starting transients stabilized with vastly different operating conditions. These phenomena were at first attributed to the usual anomalies which appear in a complex new computer program. Evaluation of simplified nonlinear spring mass analogies to the STEPZ system showed, however, that these were real effects rather than computer idiosyncrasies.

The STEPZ system is highly resonant and has relatively little damping. This results from the large amount of inertial energy storage required by the coupler, as compared with the work output of the system. As a result, system performance is quite sensitive to operating conditions.

and design parameters. The coupler is analogous to a driven spring mass system, with the oscillating liquid column as the mass attached to the hydraulic load spring on one end and the pneumatic engine spring on the other. The problem is complicated by the fact that both springs and engine drive force are nonlinear. These nonlinearities are the direct cause of the bi-stable operating modes (Reference 6). Similarly, the differing displacer and coupler frequencies can be caused by either the nonlinearities or transient effects. These effects were greatly reduced in the final reference design as a result of reduced compression ratio.

2.2.1.2 Effect of Displacer and Power Piston Interaction

The sensitivities and dynamic interactions between the displacer and power piston caused enough problem in the simulation runs that an early decision was made to add an auxiliary electric motor drive for the displacer. This approach essentially removes one degree of freedom from the system and greatly simplifies control. The final reference design exhibited much less operating sensitivity than the initial design. This resulted primarily from reducing the compression ratio of the system, which effectively increases the ratio of work removed from the system to energy stored in the coupler. The system, nevertheless, remains highly resonant.

2.2.1.3 Compression Ratio Effects

The classic solution by Schmidt as refined by Goranson, et al. (Reference 2) is based on the assumption of isothermal conditions in the hot and cold gas regions. In the isothermal program, this assumption is carried through into thermal input computations. The primary factors which contribute to making this assumption unrealistic for the STEP% engine are pressure changes over one cycle and operating frequency. The combination of large pressure changes over one cycle with high cyclic rates results in rapid pressure changes with time. This tends to cause pressure changes to be more nearly adiabatic than isothermal, with large resultant temperature changes or nonisothermal effects over one cycle. The relative problem between engines for the artificial heart and the STEP% application is that the operating pressure ratio is increased from 1.2 to 1.9 and the frequency from 20 to 60 Hz. The problem is further augmented by an increased heat transfer requirement per unit heat exchanger area as discussed in Appendix D.

This problem was recognized early, but the isothermal program was the only means available to establish an initial reference design with which to begin the mechanical design effort. Early results with the nonisothermal program led to the conclusion that the compression ratio selected for the initial reference design was too high. The

stroked volume tradeoff studies with the nonisothermal simulation, as described in Section 2.2.1.4, were used to select a near-optimum compression ratio based on solid analytical foundation.

Compression ratio is conventionally defined as the ratio of working gas volume at the beginning of the compression stroke to that at the end. These points are difficult to determine exactly in the STEP% engine but are very closely approximated by the ratio of maximum to minimum working gas volume. Based on this definition, the compression ratio of the engine was reduced from 3.6 to 1.9 when the nonisothermal simulation was used to establish a new reference design. The resultant increase in displacer stroke caused performance reduction because of increased mass flow through the regenerator with attendant higher main reheat loss.

2.2.1.4 Design Trades and Predicted Performance of Reference Design

Two reference designs were used during this effort. The initial reference design was established prior to the start of contract work using the isothermal program. A summary of computer performance, operating conditions, and geometry is provided in Table 2-2 for this initial design (first column). Following completion of the nonisothermal simulation, it was used to establish a second reference design (center column). The last column in Table 2-2 shows performance of the second reference design, calculated using the isothermal program; this calculation is presented to contrast the results obtained with the two computer programs.

The major difference between the first and second designs is the compression ratio. The isothermal program, which was used to establish the initial design, predicts ever increasing performance with increasing compression ratio. A compression ratio of 3.6 was arbitrarily selected for the initial reference design as representing a practical upper limit. The compression ratio in the second reference design was reduced to 1.9 because of the nonisothermal heat transfer effects discussed in Section 2.1.1.2. This was accomplished by reducing coupler swept volume and increasing displacer stroke length.

In arriving at the new reference design, other geometric parameters were varied in a limited parametric survey using the simplified version of the nonisothermal simulation. No significant changes were indicated. However, minor changes were made for design convenience. For example, engine diameter was reduced from 1.50 to 1.44 in. so that previously designed displacer support flexures could be used directly. In the following paragraphs, some of the design tradeoffs and engine dynamic studies are discussed.

Table 2-2
REFERENCE DESIGN PERFORMANCE AND SPECIFICATIONS

Computed Performance Levels	Original/Isothermal Program	New/Non-Isothermal simul.	New/Isothermal Program
Power Output (w)			
Gross engine output	515	538	477
Windage	18	29	29
Drive power	—	31	—
Net engine output	497	540	449
Coupler loss	11 (15)*	22	22
Power delivered to simulated or real load	486 (338)*	518	427
Estimated mechanical loss in Pz stack driver (90% efficient)	49 (34)*	52	43
Electrical and mechanical losses in Pz stack	44 (30)*	47	38
Gross electrical power generated	393 (274)*	419	346
Power Input (w)			
Second law input	811	991	763
Main reheat loss	375	1108	633
Cylinder wall conduction loss	45	45	45
Displacer wall conduction loss	10	10	10
Displacer gas conduction and radiation loss	3	3	3
Insulation loss	20	20	20
Total	1264	2177	1474
Component and System Efficiency (%)			
Engine only	39.3	24.8	30.5
Engine and coupler	38.4 (26.7)*	23.8	29.0
Complete system	31.1 (21.7)*	19.2	23.5
Operating Conditions			
Power piston phase lag (°)	90	94 to 101	90
Operating frequency (Hz)	60	60	60
Maximum cycle pressure (psia)	2300	2642	2271
Minimum cycle pressure (psia)	816	1141	1306
Average cycle pressure (psia)	1384	1738	1738
Maximum load pressure (psia)	—	2070	—
Minimum load pressure (psia)	—	1392	—
Overall pressure ratio	2.8	2.3	1.7
Heat source temperature (°C)	650	650	650
Average hot gas temperature (°C)	627	561	634
Heat sink temperature (°C)	40 104°F	40	40
Average cold gas temperature (°C)	70	70	68
Coupler swept volume (cu in.)	0.424	0.244	0.214
Geometric Parameters			
Coupler:			
Throat diameter (in.)	0.37	0.3	0.3
Effective length at throat dia (in.)	10.2	10.2	10.2
Engine:			
Cylinder diameter (in.)	1.8	1.44	1.44
Displacer-cylinder radial clearance (in.)	0.005	0.005	0.005
Displacer stroke length (in.)	0.060	0.090	0.090
Displacer swept volume (cu in.)	0.106	0.147	0.147
Hot end clearance (in.)	0.010	0.010	0.010
Additional hot dead volume (cu in.)	0.0	0.013	0.013
Cold end clearance (in.)	0.019	0.005	0.005
Additional cold dead volume (cu in.)	0.018	0.057	0.057
Overall cylinder length (in.)	7.9	7.16	7.16
Heater length (in.)	1.0	1.82	1.82
Regenerator length (in.)	4.0	3.67	3.67
Cooler length (in.)	2.0	1.97	1.97
Drive piston diameter (in.)	0.0	0.25	0.0
Compression ratio	5.6	4.9	4.9

Principal values assume solid piston coupler as considered for original design.

(Parenthetical values relate to mercury coupler for direct comparison with other cases.)

The nature of the nonisothermal design trades and the relative performance sensitivities are shown in Figures 2-13 through 2-16. Figure 2-13 shows performance (engine power output and efficiency with no parasitic losses) as a function of displacer-cylinder radial clearance. This parameter has a stronger effect on performance than any other. Optimum performance occurs near 4 mils, but 5 mils was selected as the design point on the basis of practical fabrication limitations and maintenance of a reasonable windage value.

Figure 2-14 shows the effect of tradeoffs in the heat exchanger and regenerator lengths where the total cylinder length is held fixed at a practical limit of 7.0 in., which is also a little below optimum. The selected design point sacrifices some efficiency to permit enough cooler length for close coupling of the power piston diaphragm unit below the cold cylinder wall flange.

The effect of compression ratio, in terms of parametric variations between displacer stroke and piston pumped volume, is shown in Figure 2-15. The original isothermal reference design is far off-optimum with the nonisothermal analysis. Some efficiency compromise was made in the new design to raise the power level above 500 w. This reflects a power density limitation for the simple annular regenerator, at a reduced compression ratio, which could not be observed with the isothermal program. This effect is emphasized in Figure 2-16 which shows performance of the new reference design as a function of frequency. At 20 Hz, power has decreased to 200 w, but the efficiency has increased beyond 40%. Parasitic losses were not included in these calculations, but their effect would be to decrease efficiency at 20 Hz to about 36% with a sharp drop to zero efficiency at zero frequency.

In Figure 2-16, it is assumed that the charge pressure remains fixed. This means that coupler length must be increased as frequency is reduced. The proof-of-principle system will, however, be capable of demonstrating increased efficiency at reduced power levels by operating at an appropriate combination of reduced frequency and charge pressure.

After final selection of the basic geometry and operating conditions with the simple version of the nonisothermal simulation, the more complete version was used for additional refinements. With the driven displacer and free coupler motion, fine adjustments were made with load pressures, gas charge, and coupler length to achieve stable resonant operation at 60 Hz with the engine diaphragm nearly bottoming out on the support plate for minimal dead volume.

Selected computer plots in Figures 2-17 and 2-18 show resonant operation of the system. Figure 2-17 shows hot and cold end region gas temperatures and load and engine pressures as functions of time over one cycle. The significance of nonisothermal effects is apparent, even at the low compression ratio of this system. Hot gas temperature

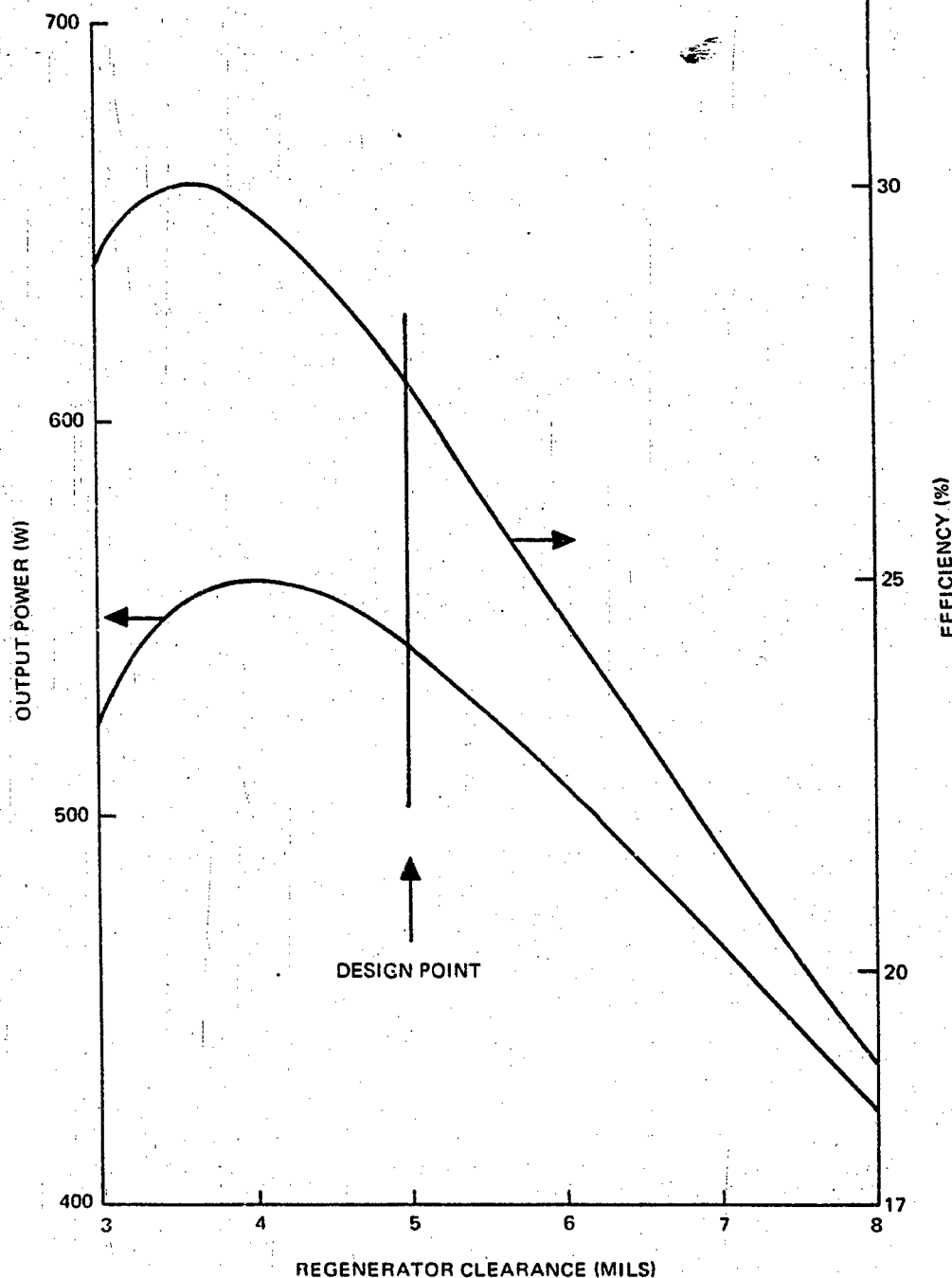


Figure 2-13. Regenerator Clearance Tradeoff

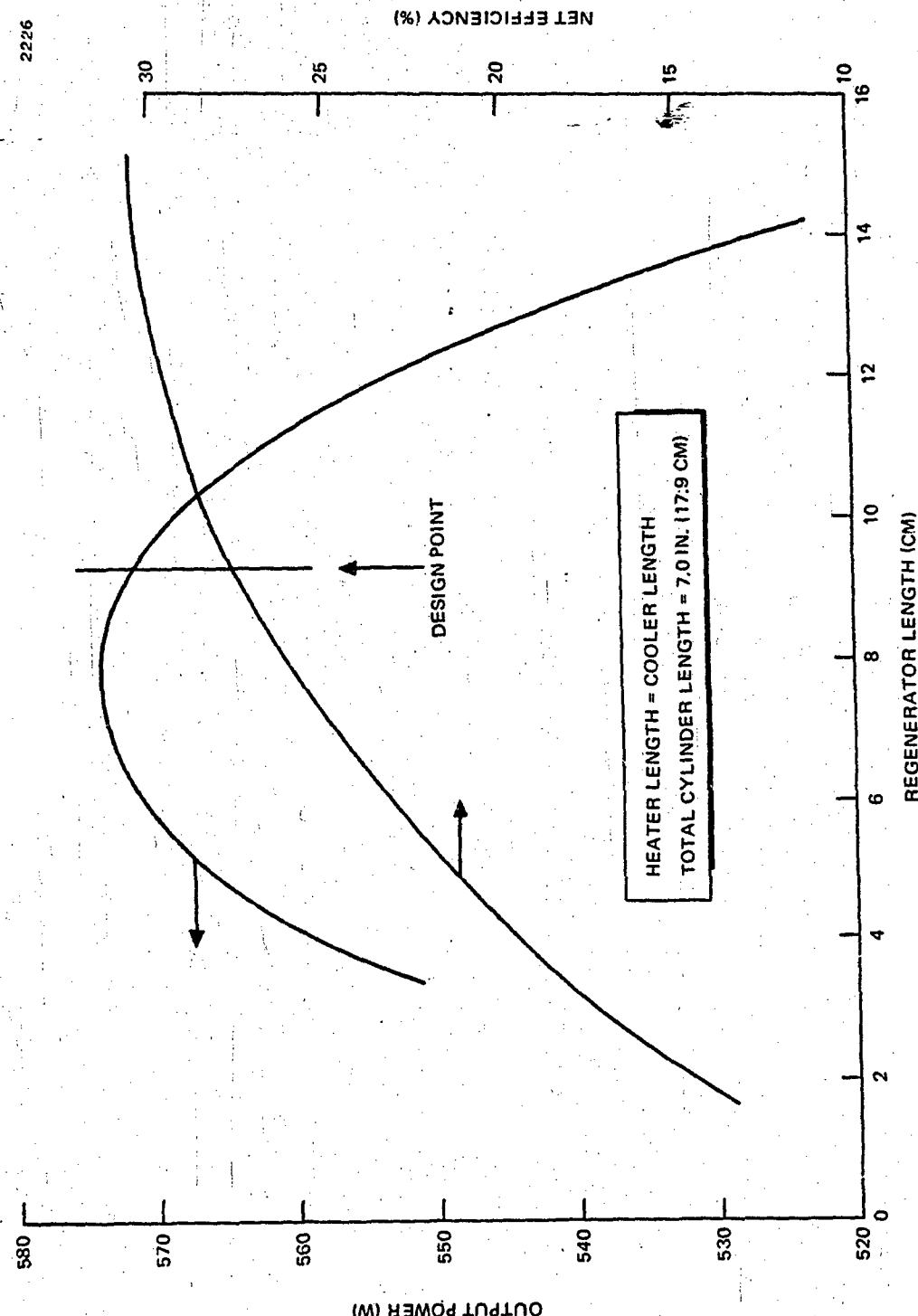


Figure 2-14. Regenerator vs Heater - Cooler Tradeoff

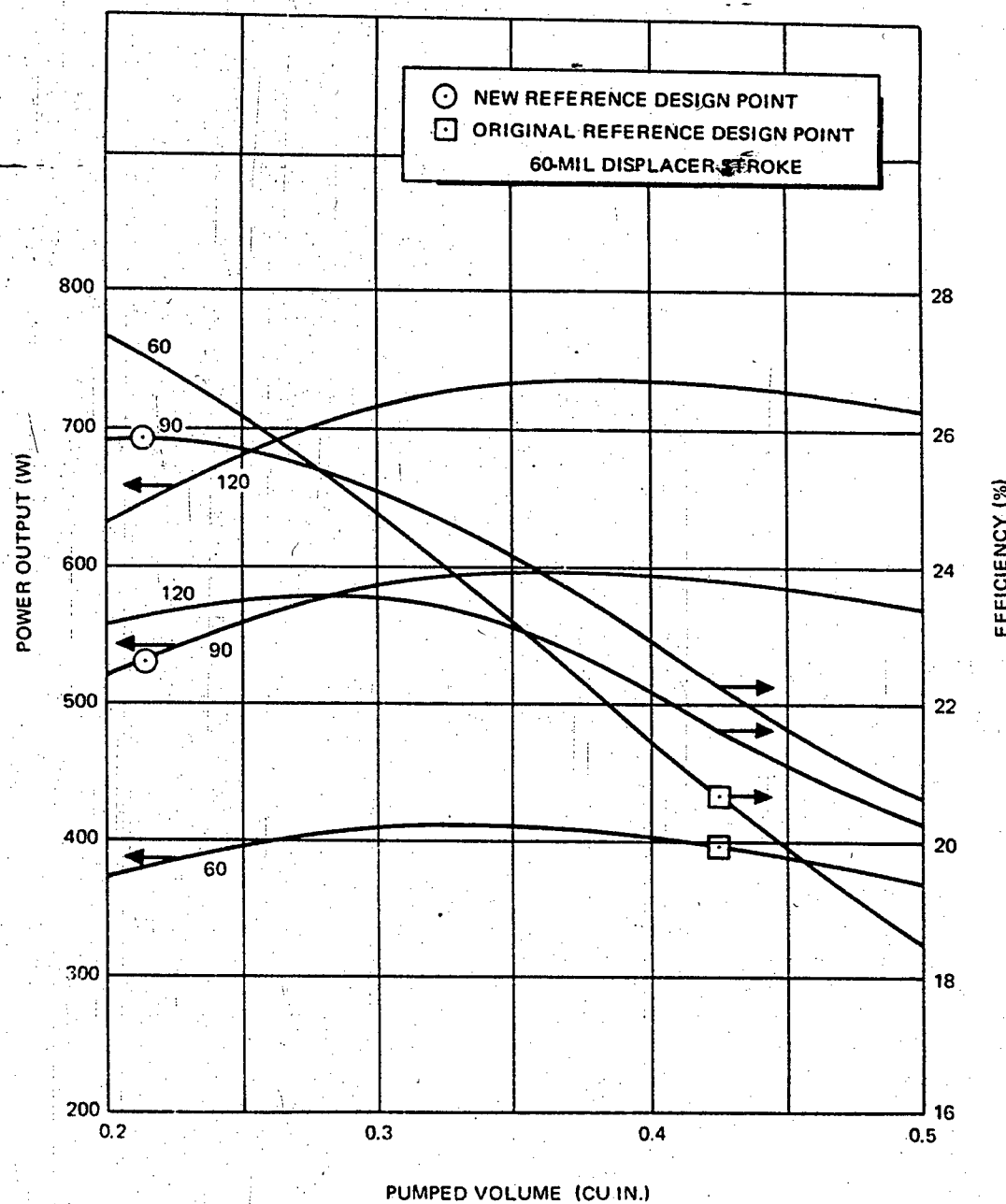


Figure 2-15. Displacer and Power Piston Stroked Volume Performance Trades

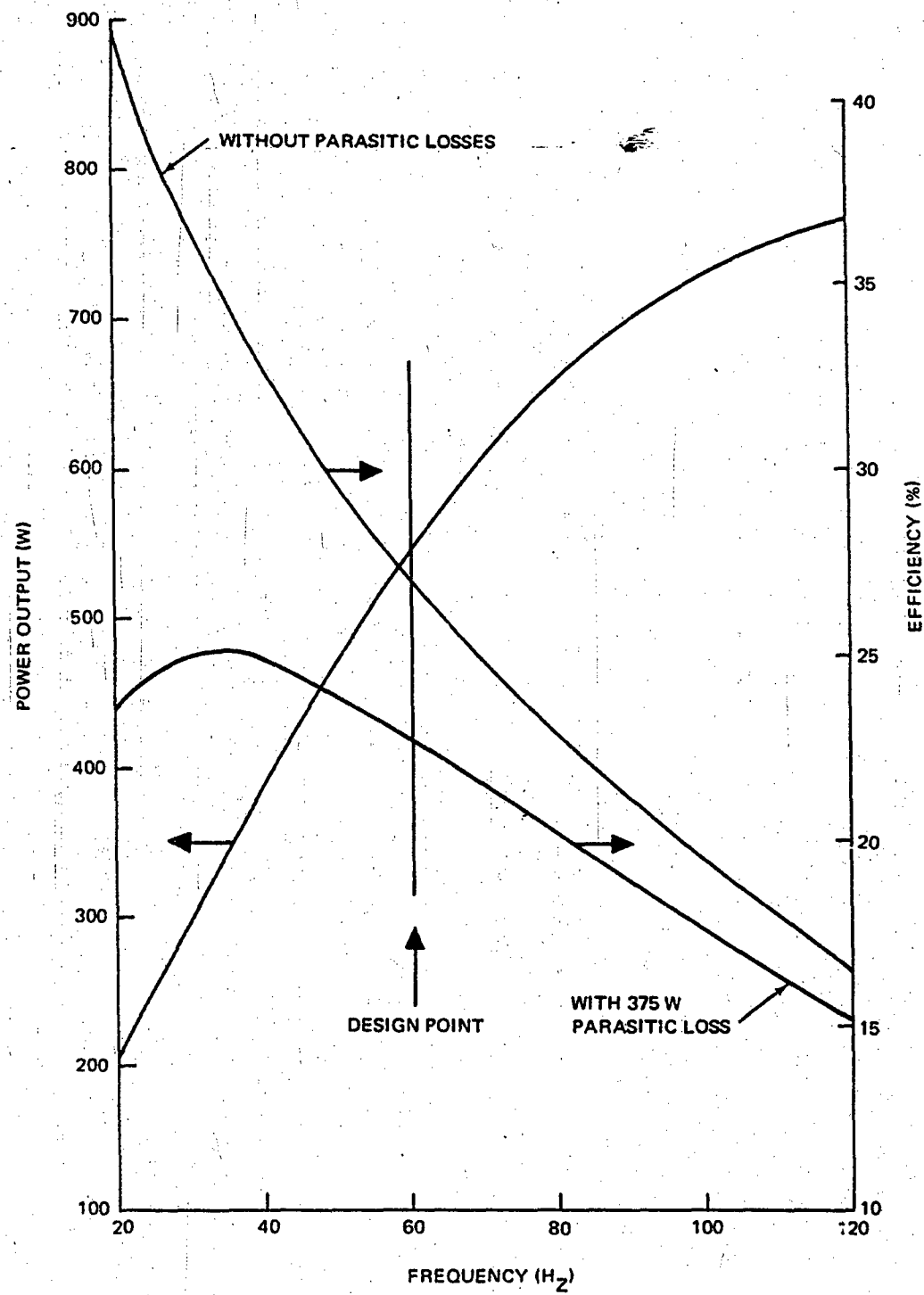


Figure 2-16. Operating Frequency Tradeoff

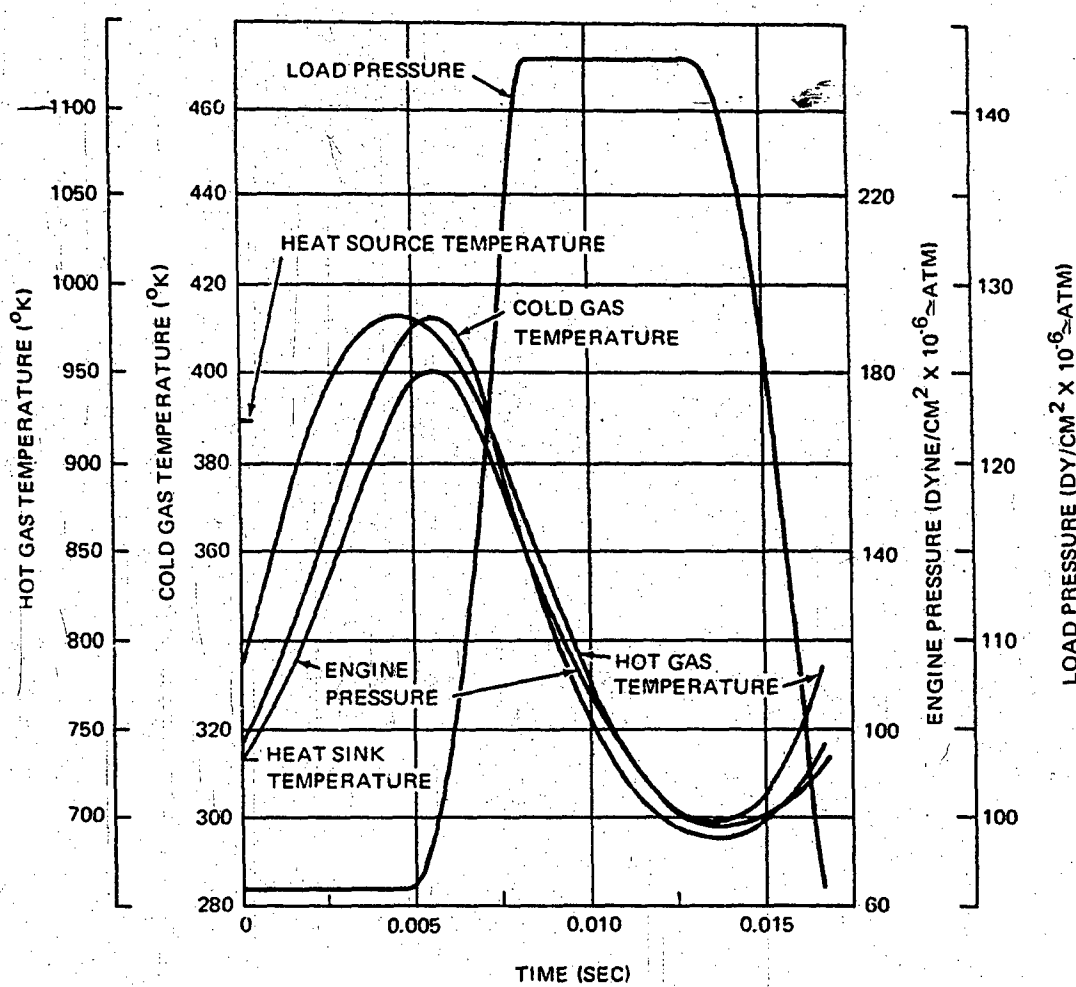


Figure 2-17. Pressures and Temperatures as Functions of Time for the New Reference Design

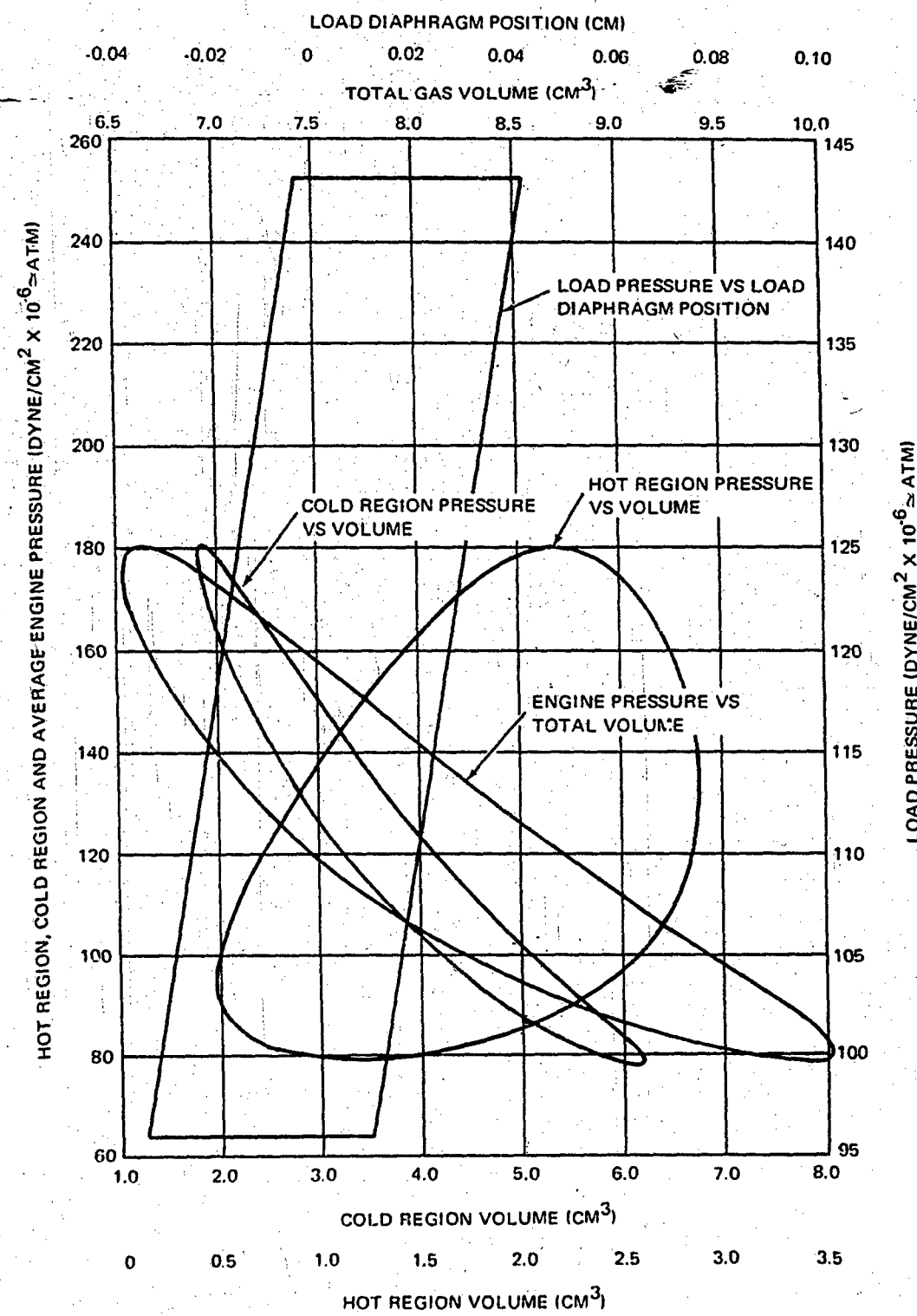


Figure 2-18. Pressure - Volume Computer Plots for the New Reference Design

varies from 60°C above the heat source temperature to 226°C below it. Similarly, the cold gas drops 18°C below the heat sink temperature and rises to 99°C above it. Load pressure exhibits relatively steep rise and fall characteristics with most of the time spent with intake and discharge. The engine pressure trace is considerably broader on the low pressure portion of the cycle, with the arithmetic average pressure of 1876 psia at 138 psi above the time average pressure of 1738 psia. One pressure-displacement and three pressure-volume diagrams are shown in Figure 2-18. The area enclosed by the hot and cold region diagrams respectively represents second law heat addition to and rejection from the system. The area of engine pressure versus total working gas volume diagram, gives the cyclic work output of the engine. The area of the load diagram, multiplied by the effective diaphragm area of 45.7 cm², gives the work delivered to the load.

The displacer was driven at a series of frequencies around resonance to develop a frequency response curve for the system. Results are plotted in Figure 2-19. Power peaks with a fairly flat characteristic right at 60 Hz. Power drops off steeply below the resonance frequency, but comparatively slowly with increasing frequency. This characteristic is the most pronounced effect of using the pulse power generator simulation as opposed to continuous-connection piezoelectric generator simulation. With the latter, the falloff from resonance is sharper on the high frequency side and shallower as lower frequencies are approached. This results from the differing characteristics of the nonlinearities. The resonant point shows virtually the same performance, however. Efficiency shows a much sharper peak than power density, which reflects greater efficiencies possible at lower power densities. The phase lag of the power piston behind the displacer is near zero at frequencies much below resonance. Phase lag increases sharply toward the resonance value of about 90°, then asymptotically approaches 180° with increasing frequency.

2.2.1.5 Free Running Displacer

All computer runs discussed utilized an extremely large moment of inertia for the displacer flywheel to effectively drive the displacer at a fixed frequency equal to its initial value. The effect of a realistic flywheel inertia is consequently of interest. An inertia of 450 g-cm², equal to that of the system design, was used, and the system was started from equilibrium resonant conditions. The result is shown in Figure 2-20, which plots angular velocity of the flywheel as a function of time. After a slowing transient which lasted for about 5 cycles, the system was run for 15 additional cycles (only 5 shown) and stabilized nicely. Because of non-uniform drive forces, angular velocity varies from about 350 to 407 radians per second over one cycle. This represents fully self driven operation with the drive motor coasting and all windage forces overcome with the pneumatic drive power, if bearing and seal friction on the displacer drive shaft are disregarded.

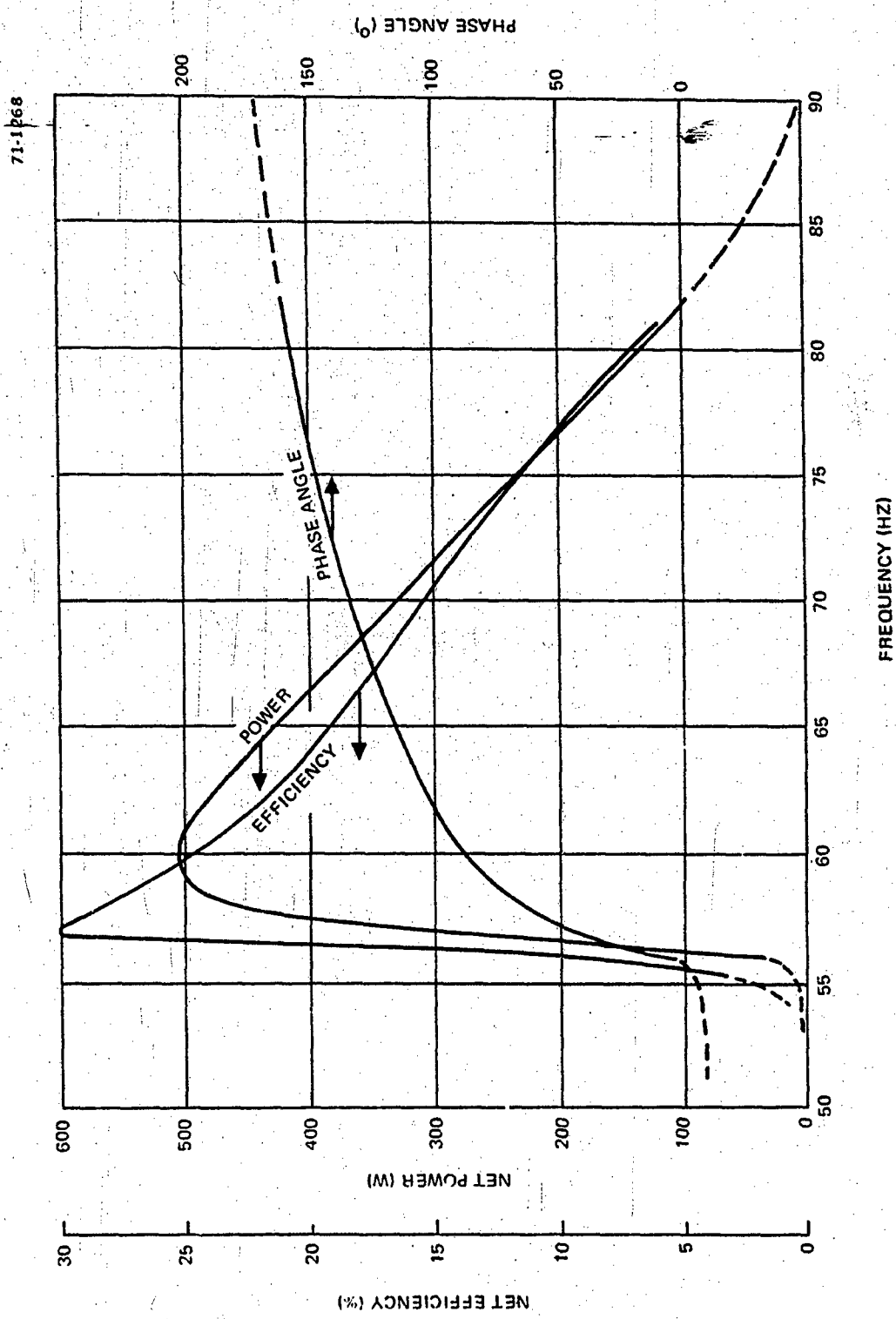


Figure 2-19. New Reference Design Performance Characteristics Versus Frequency

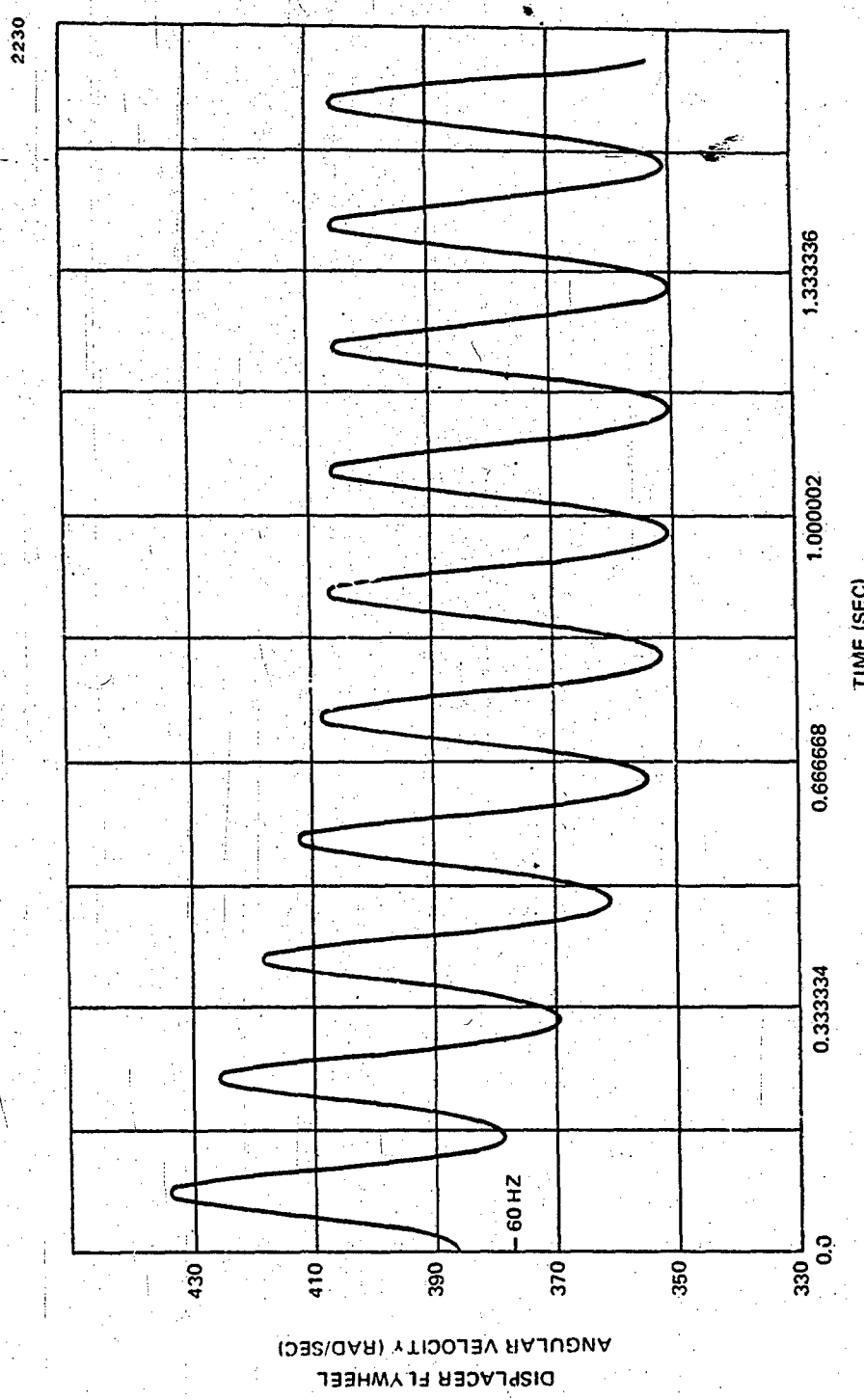


Figure 2.20. Transient and Stable Operation of Fully Self Driven System

2.2.1.6 Startup, Shutdown, and Transient Load Change Characteristics

Several studies were made with the nonisothermal simulation to investigate startup, shutdown, and transient load change dynamics.

Startup and Shutdown Characteristics

Two types of startup were investigated. These include (1) an increase in displacer frequency from 0 to slightly above the design value with the heater and cooler temperatures held constant, and (2) an increase in heater temperature from cooler temperature (40°C) to the reference design heater temperature with the cooler temperature and displacer frequency held constant.

The increasing frequency startup simulates a condition where heat has been applied and operating temperature has been achieved; at that time, displacer motion is started. During the initial heatup before the displacer is started, pressure in the engine increases; this moves the engine power diaphragm from its initial position to a new equilibrium position which depends on the displacer position (i.e. the distribution of gas between the hot and cold regions). These are the starting positions for displacer and engine diaphragm when displacer motion is started. During heatup or cooldown, a condition is never reached in which either diaphragm bottoms out against its backup plate as a result of static pressures.

In the increasing frequency simulation, a forcing function was applied to the displacer to increase its angular velocity from 0 to 400 rad/sec (equivalent to 63.66 Hz) in three seconds of real time. Because effects near each end of the speed range are of primary interest, the forcing function was

$$\dot{\theta} = 200 [1 - \cos(1.0472t)]$$

where $\dot{\theta}$ is the displacer flywheel angular velocity in rad/sec and t is time in sec. This function causes the displacer to start with zero frequency and acceleration and increase speed slowly at first. Maximum acceleration is at an angular velocity of 200 rad/sec, which is reached 1.50 sec after start. The speed then continues to increase to 400 rad/sec at 3.00 sec while acceleration is decreasing to zero. The first full cycle takes 0.56 sec as contrasted with the final cycle of 0.016 sec. A hot shutdown case is simulated by this same plot with a reversal of the time scale or 63.66 Hz at zero time decreasing to zero Hz at 3.00 seconds.

Starting with the reference design conditions (except for frequency), the computer simulation required 15 hours to determine system response to this forcing function. Power piston (diaphragm) position was plotted as a function of time on a plot about 13 ft long, to achieve

reasonable resolution of the high frequency oscillations. The length of this plot makes it impractical to include in this report, because photo reduction to a practical size would destroy essential detail. A similar run was made with the connecting rod force (F , Equation 2 of Section 2.1.1.2) as the plotted variable. This showed that instantaneous forces during startup never exceeded the design bearing loads. Highest loads were experienced at frequencies above resonance. These plots are furnished separately for MERDC review.

One unexpected but readily explained result emerged from the first run. A low-to-moderate-amplitude 75-Hz oscillation of the mercury column, about a central point directly proportional to power piston position, started almost immediately. This oscillation continued until the displacer reached about 50 Hz, after which the power piston synchronized with the displacer frequency. In normal resonant operation, the effective spring constant of the load is proportional to the slope of line A-B, Figure 2-12, during compression of the fluid in the hydraulic chamber. During expulsion of the hydraulic fluid into the high pressure accumulator from B to C, the spring constant of the load is zero. The net effective value of the spring constant is, therefore, proportional to the slope of a line from A to C. The system has been sized to produce 60 Hz operation with this effective spring constant. When the frequency is appreciably below resonance, however, the power piston is not moving far enough to expel any fluid, so the system oscillates along a portion of A-B. This effective spring constant, together with that of the engine, is such that the coupler oscillates at the observed value of 75 Hz. This oscillation occurs with a minimal driving force, because the only dissipation mechanism is from flow losses in the coupler.

The envelope of the power piston oscillations follows displacer motion, with no phase lag, to about 25 Hz, where an irregular beating between the driving frequency and the 75-Hz coupler frequency begins and continues to 47 Hz where the frequencies synchronize. Starting at 56 Hz, the power piston amplitude increases rapidly to its resonance value at 60 Hz, then decreases almost imperceptibly at the maximum frequency of 63.66 Hz. All observations are consistent with previously observed or calculated phenomena.

The increasing temperature case simulates a situation where the displacer is brought to the driven frequency of 60 Hz, and heat is then applied. The simulation starts with the entire engine at a temperature of 40°C and increases heater temperature linearly to 650°C in three seconds of real time. This simulation also requires 15 hours of computer time and results in a very lengthy plot of power piston (diaphragm) position versus time, which is also furnished separately.

This type of startup yielded a beating effect attributable to a starting transient. Amplitude varies as well as frequency during this starting transient. These transient effects decay gradually and have almost completely disappeared after 100 cycles (1.67 seconds of real time):

after this point, amplitude gradually increases uniformly. At the end of 3 seconds, heater temperature is 923°K and the linear temperature increase is stopped; the heater is then held at a constant temperature. When the heater temperature increase is removed, the average position of the power piston moves toward the engine; all variables (power piston position, pressure, temperature, etc.) rapidly stabilize to the reference design values. The work output and efficiency are also equal to the reference design values. This curve also simulates loss of the heat source with the displacer driven at 60 Hz by reversing direction of the time scale.

The most significant result of these startup runs and the static analysis is that no undesirable effects, such as a large amplitude transient, is expected during startup.

Load Change Characteristics

The basic load characteristic for simulated pulsed load operation of a piezoelectric stack (as in Appendix B, Case IV) is in the form of a parallelogram shown in Figure 2-12. The slope of the sides is determined by simulated stack compliance and minimum and maximum pressures, P_{\min} and P_{\max} , can be set to any desired value. For the reference design, $P_{\min} = 96 \times 10^6$ dyne/cm² and $P_{\max} = 143 \times 10^6$ dyne/cm².

The effect of a load change was investigated by step changes in the values of P_{\min} and P_{\max} , after stabilized reference design operation had been achieved, such that the average pressure remained the same. This is analogous to changing the load resistance, or the voltage level at which power is dumped to the load in pulsed operation. A summary of these load changes and results is presented in Table 2-3.

In all cases, a run was started with the reference load, the load was changed and then permitted to run until stabilization occurred or until it became apparent that stabilization would not occur for a long period; at this point, the load conditions were changed to the reference values again until stable operation resulted. Cases 1 through 4 were run to 50 cycles; the reference cases were terminated after 10 cycles. The resultant plots of power piston position for these cases were necessarily long, and are included separately and appropriately annotated.

Cases 1 and 3 had the effect of decreasing the height and increasing the width of the parallelogram. Therefore, the effective spring constant of the load (proportional to the slope of the line from A to C in Figure 2-12) is decreased. These runs achieved a stable operating condition even though power output was low. Cases 2 and 4 had the effect of increasing the height and decreasing the width of the load parallelogram, with a consequent increase in effective spring constant. These cases never stabilized (power piston position did not follow a regular sinusoidal motion of constant amplitude and frequency); the diaphragm hits the end stop at low velocity in these cases, but the overpressure accumulators prevent damage.

Table 2-3
LOAD CHANGE SUMMARY

Case	P_{\min} (10^6 dyne/cm 2)	P_{\max} (10^6 dyne/cm 2)	Output Power (w)	Efficiency (%)	Stable Operation	Simulated Piezoelectric Generator Condition	
						Condition	Reduced load resistance
Reference 1	96 116	143 123	520 30.6	24.7 1.8	Yes Yes		
Reference 2	96 70	143 169	520 0	24.7 0	Yes No		
Reference 3	96 119.5	143 119.5	520 0	24.7 0	Yes Yes		
Reference 4	96 10	143 300	520 0	24.7 0	Yes No		
Reference	96	143	520	24.7	Yes	Increased load resistance	short circuit
							open circuit

These stability phenomena are consistent with the engine frequency response curve (Figure 2-19). An increase in spring constant moves the peak of the curve to the right, thereby placing the operating frequency of 60 Hz in a region of rapidly changing response (the slope of the power and therefore the amplitude curve is very steep in approaching the peak from the left). In such a region of rapidly changing characteristics, unstable operation might be expected, especially in a nonlinear system such as this simulation represents. A decrease in spring constant places the operating frequency to the right of the peak; this region has much more gradual frequency response characteristics, and the system should be considerably more stable.

The power output and efficiency associated with any of the load changes is very low and would not be a desirable operating point, but the most important result of these runs is that no large amplitude transients or other potentially destructive effects occurred as the result of change from load to no load or partial load.

These load-change results emphasize the highly resonant nature of the STEP% system. In the moderate load change cases, stabilized operation is possible if the system is tuned to the new operating conditions by changing frequency or other parameters. The most likely operating mode, based on present limited knowledge, is to utilize a variable parasitic load to maintain fixed output voltage at the generator terminals.

2.2.2 Piezoelectric Generator

An analytical formalism has been developed which accurately predicts the electrical output characteristics for a given piezoelectric stack. Appendix C describes this formalism and analyzes data gathered at DWDL using this approach. Both analysis and experiment show that an attractive generator can be designed using property values and limitations of the piezoelectric material given by the suppliers. Table 2-4 gives the results of DWDL calculations for a typical 300 w(e) generator together with calculations and measured performance for a smaller stack operating under similar stress and load conditions. These measurements verify the feasibility of piezoelectric stacks operating at a power density of 15 watts/in.³ of piezoelectric ceramic and a stack efficiency near 70%.

Currently, the formalism includes only electrical losses. The difference between predicted and measured efficiencies is substantial. This difference is attributable to mechanical losses not accounted for, and electrical losses incompletely or inaccurately predicted. Nevertheless, a piezoelectric generator with reasonable power density and efficiency can be built, based on analytical and experimental results reported in Appendix C.

Table 2-4
COMPUTED PIEZOELECTRIC GENERATOR CHARACTERISTICS

Stress limit: 1000 to 7000 psi
Frequency: 120 Hz
Material: P.Z.T-4 or equivalent

Characteristic	Calculated 300 w(e) Generator Module*	Experi- mental Measure- ments	Calculations Corresponding to Experimental Conditions
Disc diameter, in.	1.00	0.50	0.50
thickness (in.)	0.04	0.10	0.10
Number of discs	160	26	26
Length of stack (in.)**	6.4	2.6	2.6
Output power (w)	76	7.67	7.67
Output voltage (v)	336	678	678
Power Density (w/in. ³)	15.0	15.0	15.0
Load Resistance (Ω)	1500	60	60
Load Inductance (h)	1.55	30	30
Efficiency (%)	92	67	93

* 4 modules required

** Disregarding copper or brass interdisc leads and any epoxy

2.3 MECHANICAL DESIGN

The three major components of the design are the engine, coupler, and load. This concept is identical to hardware systems previously produced at DWDL, except for the addition of the fluid coupler which replaces the flywheel and mechanical coupling of a conventional engine-generator. When the coupler operates in the resonant mode with about 90° phase lag, the work diagram is nearly identical with one for a conventional Stirling engine. This increases power output by about a factor of seven compared with the non-inertial operating mode of the artificial heart engine. Increased efficiency also results because parasitic and reheat losses change little between the two operating modes. Compared with

the heart engine, the STEP% engine operates with about 10 times the charge pressure, 3 times the frequency, and one-half the displacer stroke. Because these factors are essentially proportional to power output, the STEP% engine power level can be scaled from the 5-watt heart engine as $5 \text{ watts} \times 7 \times 10 \times 3 \times 1/2 = 525 \text{ watts}$, which is very close to the actual value.

These differences in operating conditions have a significant effect on mechanical design stresses and loads. Hardware design of the engine and simulated load is based primarily on extrapolating existing and proven hardware approaches to the required operating conditions and accomodating system sensitivities introduced by the coupler.

Major components of the proof-of-principle generator are attached to an I-beam (Figure 1-6) which is the basic support structure for the system. The overall design approach emphasizes engineering judgment and economy in the use of proven and low-risk hardware approaches.

2.3.1 Engine (Figure 2-21)

The engine includes the following components.

1. Cylinder
2. Displacer and supports
3. Displacer drive mechanism and housing
4. Thermal insulation housing

The drive housing is the basic structure to which major engine components attach. The engine cylinder mounts to the drive housing with a bolted flange connection for ease of construction, assembly, and disassembly. The power piston diaphragm is attached to the side of the housing. The driveshaft crosshead is supported in bearings which are mounted in the housing. The insulation housing attaches to the upper flange of the cooler section of the engine cylinder. The crankshaft and electric startup and drive motor are assembled into the spindle housing which is bolted to the main housing (Figure 2-22).

2.3.1.1 Cylinder

The engine cylinder consists of the heater and cooler section and a central section to which the heater and cooler section are connected with flanged joints. This three-piece construction allows the use of high-thermal-conductance materials in the heater and cooler ends of the cylinder and low-conductance material in the central portion to minimize cylinder sidewall parasitic heat loss.

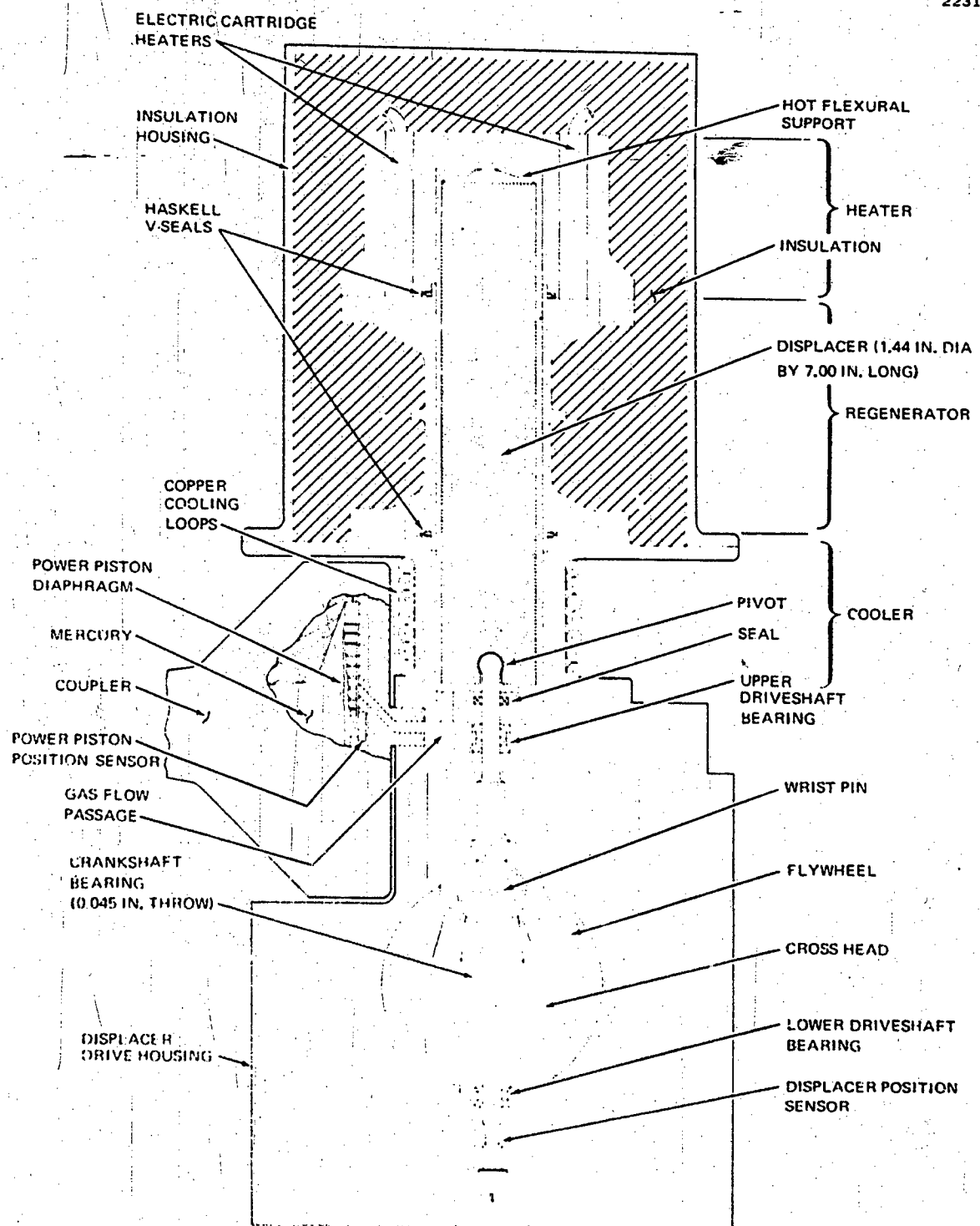


Figure 2-21. Engine Assembly

2232

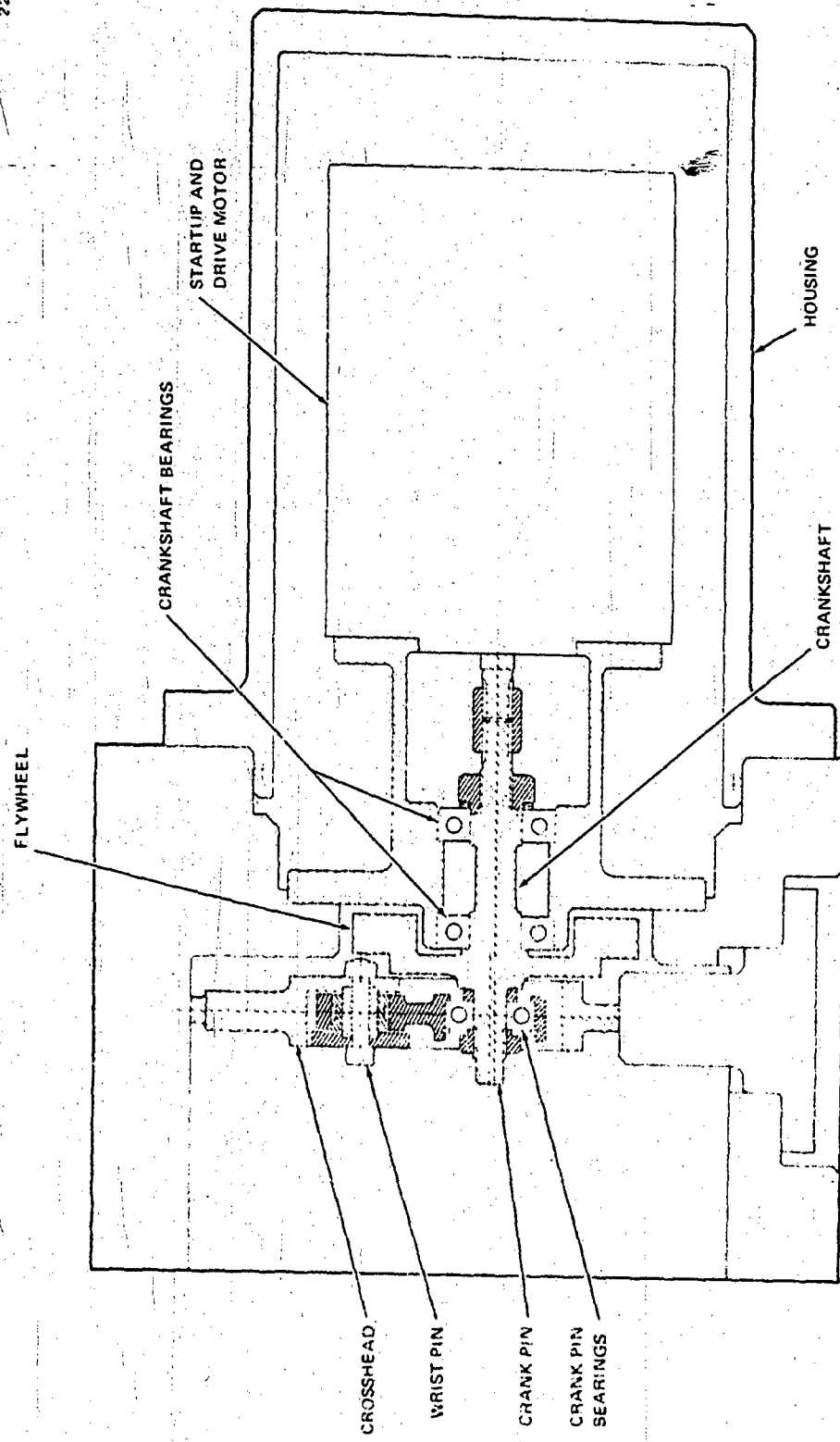


Figure 2-22. Displacer Drive System

This approach is used in the proof-of-principle design to avoid electric heater burnout problems and simplify the design and fabrication of the cold heat exchanger. In a flame heated system, the entire cylinder could be fabricated in one piece from a single high-strength, low-conductance alloy.

The central portion of the engine cylinder is Inconel 625, selected for relatively good machinability. A production version of the device is likely to use Rene' 41 for the cylinder material because of its higher strength at temperature. The ID is 1.437 in. nominal with a 0.150-in. wall thickness, and operates at a hoop stress of 14,000 psi at 2600 psi max operating pressure. This stress is a factor of two below the Inconel 625 value of 29,000 psi for 0.001% creep in 1000 hours. At the 29,000-psi level, creep per year is less than one mil in length and about 1/10 mil in diameter. The cylinder will be proof tested at 1.5 times operating pressure to ensure integrity of the structure. Side wall heat loss is 45 watts.

The heater section is coupled to the central portion of the cylinder with a flanged joint using a Haskell HV3-29 V-type high-temperature self-energizing seal. This seal, which has proved satisfactory in other DWDL engines, is gold-plated Rene' 41 operating with a 0.003-in. preset. The flange has eighteen 0.25 in. diameter Waspalloy high-temperature bolts preloaded to 900 lb. With an effective cross-sectional area of 0.0355 sq in. for each threaded bolt, the 900-lb preload yields an operating stress of 25,400 psi which is well below acceptable limits. The maximum operating pressure in the engine is 2600 psi, which for the 1.44 in. diameter engine, results in an axial force of 4200 psi. This is transmitted as about 235 lb force on each of the 18 bolts. Because this is well below the preload value, cycling stress does not strain the bolts and no fatigue occurs. The 10,000-hr 0.5% creep stress value for Waspalloy is 60,000 psi, which provides more than a factor of two margin above the actual stress levels.

The heater block is constructed of chromium copper because of its high heat transfer characteristics. It is brazed to an Inconel 625 jacket to ensure dimensional stability and carry the required loads. Twelve 350-w cartridge heaters are used, resulting in a 4200-w heating capability, well above the expected nominal requirement of 2200-w. The maximum allowable heater element temperature is 1600°F, which represents 1400°F at the cartridge surface. Therefore, the cartridges are silver soldered to the copper block to minimize thermal contact resistance. With 1200°F at the cylinder surface of the copper block, the maximum heater cartridge surface temperature under nominal operating conditions is 1240°F. Heaters can be replaced by drilling out and rebraze, which is standard operating procedure at DWDL for this type of construction.

The cold-end heat exchanger is coupled to the central cylinder section through a flange using eleven 5/16-in. diameter high strength bolts prestressed to 26,000 psi. Chromium copper is again used for combined high strength and thermal conductivity along with the V-type Haskell seal as used in the flange adjacent to the hot heat exchanger. The wall thickness is 0.312 in., yielding a maximum hoop stress in operation of 11,500 psi compared to a room temperature yield stress of 42,000 psi. The lower flange of the cooler section is bolted to the drive housing and sealed with a Viton O-ring.

Heat is removed from the system using water circulated through a simple cooling loop consisting of 3/16 OD x 1/8 in. ID copper tubing coiled around and brazed to the periphery of the cold heat exchanger. The pressure drop through this single-pass cooling loop at the design flow of one gallon per minute is 15 psi. The sensible temperature rise of the water passing through the cooler is 15°F. The film temperature drop is 43°F and the solid material temperature drop in the cold heat exchanger is 30°F. A maximum rise of 88°F above cooling water source temperature or about 150°F would therefore be expected at the gas-metal interface in the cooler.

2.3.1.2 Displacer and Supports (Figure 2-23)

The displacer is a thin shell made of Inconel 625 with a wall thickness of 0.052 in. It is pressurized internally with argon to 900 psi at room temperature which increases to 1900 psi at the arithmetic mean operating temperature of 343°C. This reduces the pressure differential experienced by the cylinder and minimizes the regenerator wall thickness required for the cylinder buckling failure mode. Hoop stress from internal pressure is 10,100 psi maximum during operation of the engine. The critical buckling pressure is 4430 psi. Eight radiation shields are mounted internally to reduce radiation heat loss to less than 3 watts. Gas conduction heat loss is only 0.1 watt, so the sidewall heat leak of 10 watts makes a total displacer axial heat leak of 13 watts.

The operating clearance between the displacer and cylinder wall is 0.005 in. which is maintained by supporting the displacer at both ends. It is supported at the hot end by flexures and is mounted to the drive shaft at the cold end by a spherical joint which accommodates initial misalignments and eliminates spurious side loads at the flexures. This support system was subjected to 3.56×10^8 cycles at operating temperature during life testing of a NH11 engine (Reference 8) without evidence of degradation under a microscopic examination, following a crankshaft bearing failure.

The spherical joint at the drive shaft uses a standard 0.5-in. diameter steel ball. The upper seat is Inconel 625 impregnated with molybdenum disulfide dry lubricant; the lower seat is bearing bronze. Maximum operating bearing stress is a negligible 120 psi. Precision in this joint is expected to result in 0.0005-in. maximum lost motion. The

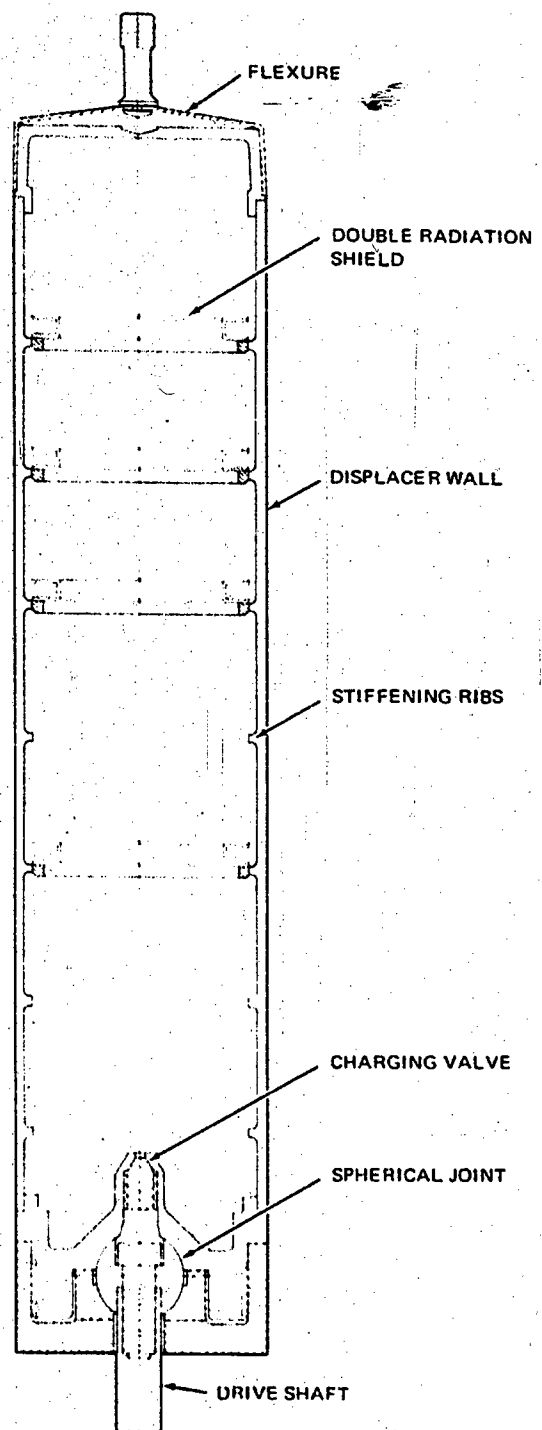


Figure 2-23. Displacer and Supports

displacer separates from the drive shaft at this joint so that the cylinder and displacer can be removed from the assembly without interfering with the drive mechanism. This enhances ease of checkout and minimizes turnaround time during the development phase of the system.

The flexures used to support the upper end of the displacer are shown in Figure 2-24. The deflection mode of the flexure as the displacer reciprocates is shown at A and B. A pair of flexures is used as shown at C. D and E show how lateral loads are reacted by the flexure pair. Each flexure resists lateral components in one direction resulting in a flexural system of high lateral rigidity yet high axial compliance.

Figure 2-25 shows a pair of flexures installed in the hot end of the NHLI Engine 5 displacer. These flexures were deflected from the relaxed position 0.080 in. upward and 0.108 in. downward during life test operation of the NHLI engine. The STEP% flexure is identical except for a material thickness of 0.004 in. instead of 0.005 in. (used in Engine 5 because of stock availability). The STEP% flexure is deflected 0.090 in. upward only, to utilize existing tooling and simplify displacer hot end machining. Use of thinner stock reduces stress concentrations in the flexure to safe levels.

2.3.1.3 Displacer Drive Mechanism (Figure 2-22)

The purpose of the displacer drive mechanism is to provide startup and operation of the displacer at 3600 rpm against the forces of bearing and rod seal friction, inertia, and windage. Seal friction is about 6 watts and bearing friction 2 watts, based on manufacturers' specifications for the seal drag and bearing loads encountered in normal operation. The windage of 29 watts was determined directly from the computer simulation. The total displacer drive power dissipation is, therefore, 37 watts under nominal operating conditions. Of this, nominally 31 watts are supplied by pneumatic drive power and 6 watts by the drive motor. At off-optimum operating conditions, friction power varies directly with operating frequency, and windage varies with frequency squared. Drive power is proportional to output power and is only appreciable near resonance. The maximum load on the drive motor, therefore, occurs during startup, shortly before the resonant frequency is reached, and amounts to about 30 watts. The drive system is shown in Figure 2-26. In summary, the electric drive motor is included in the proof-of-principle system to (1) provide starting and trimming torque, (2) act as a regulator to maintain constant speed, and (3) permit investigations at off-design conditions.

The basic linkage system is a conventional overhanging crank pin driving a connecting rod. The connecting rod reciprocates the drive shaft which kinematically acts as the crosshead in a conventional system. The drive mechanism is sized to withstand all startup and steady state operating loads as determined by the startup simulation described in Section 2.2.1.6. Bearings have a 90% probability of surviving

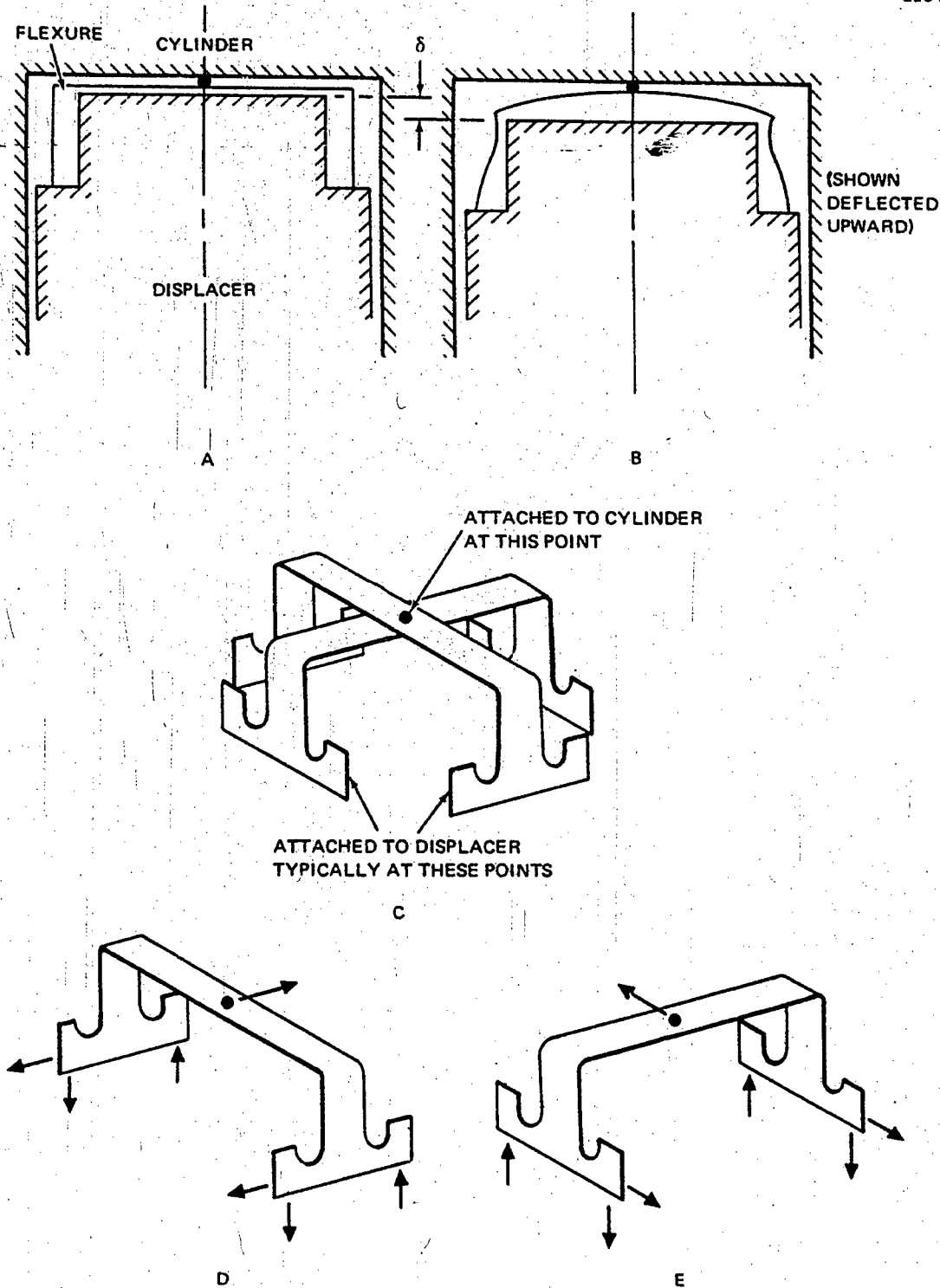


Figure 2-24. Displacer Upper Flexures

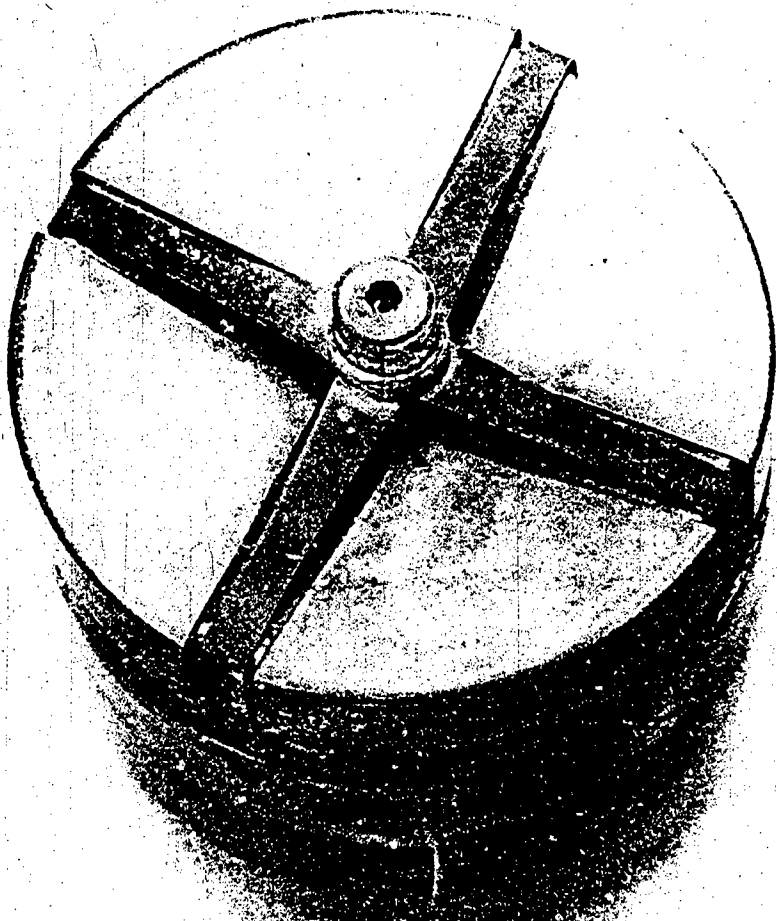


Figure 2-25. NHLI Displacer with Flexures

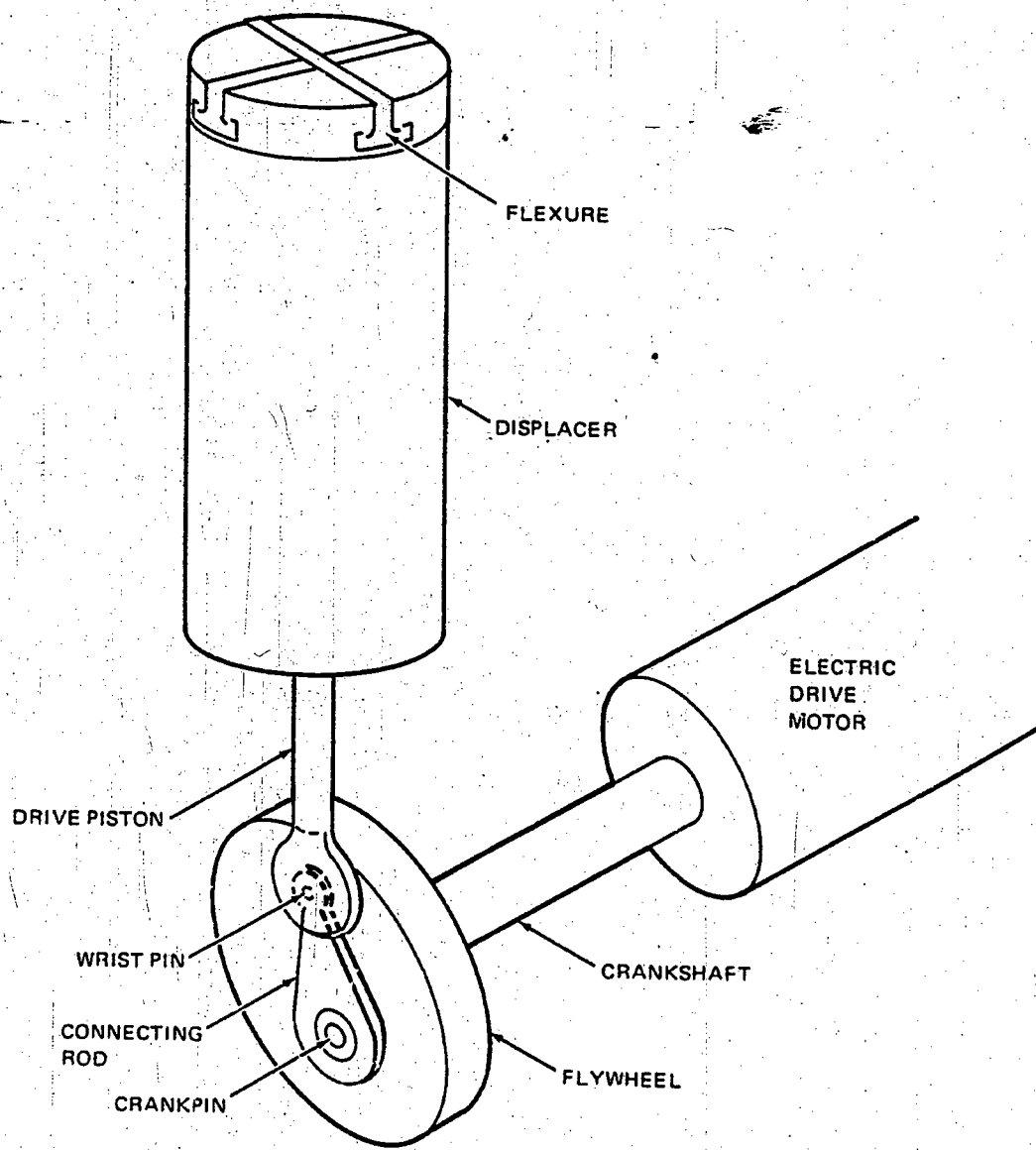


Figure 2-26. Displacer Drive Mechanism

10,000 hours of operation at or below the resonant frequency. Figure 2-27 shows the steady state loads obtained from the computer simulation based on a maximum operating pressure of 2710 psia, a reciprocating mass of 0.025 slug, and an engine speed of 3600 rpm. The flywheel is sized to allow a maximum cyclic angular velocity variation corresponding to 12.4 rpm resulting from instantaneous unbalance of drive and energy absorption forces.

The crank pin and main crankshaft bearings are prelubricated precision ball bearings. The wrist pin is a hardened 0.164-in. diameter pin operating in an aluminum bronze bushing. The support bearings for the drive shaft are of sintered oil impregnated bearing bronze. The critical bearing is at the crank pin and has an estimated life of 18,500 hours based on data furnished by the supplier. Although the loads for this engine are significantly higher, resulting in more rugged members and larger bearings, the basic approach is identical to the NHEI Engine 5 which operated continuously for more than 5000 hours without degradation in performance.

The drive shaft seal separates the engine cylinder working gas, which fluctuates in pressure, from the drive chamber at constant pressure. This seal must have low friction and minimum leakage across a pressure difference of several hundred psi. The high pressure difference eliminates from consideration the low friction hermetic seal provided by a convoluted metal bellows. A labyrinth seal also had excessive leakage at design conditions. However, two seals proposed by the piston ring and seal department of Koppers Company, Baltimore, Md., were investigated and are satisfactory for this application.

The Koppers seal chosen (Figure 2-28) is a 0.250 ID x 0.390 in. OD split piston ring of glass-filled Teflon with an 0.062 in. wall, split outer stainless steel compression ring to apply pressure for initial sealing. The split inner ring has a lapped joint to minimize leakage. The frictional drag of the seal is about 5.0 lb, and leakage is calculated as 0.013 cu in. over one-half of an engine cycle, both of which are satisfactory values.

A hysteresis synchronous motor has been selected for use with the displacer drive mechanism. The motor is inside the pressurized drive housing and provides added inertia to promote stability. This motor has the advantage of speed/torque independence and avoids the brush/commutator assembly. An appropriate signal generator and power amplifier will power this motor which is capable of delivering 56 watts, or about a factor of two higher than the expected transient startup values.

A dc motor was rejected for this application because the manufacturer could not guarantee performance and life of the brush/commutator systems in a high-pressure helium atmosphere. An induction motor was rejected because of uncertainties in the electronic speed control requirement in the resonant range of the STEPZ engine.

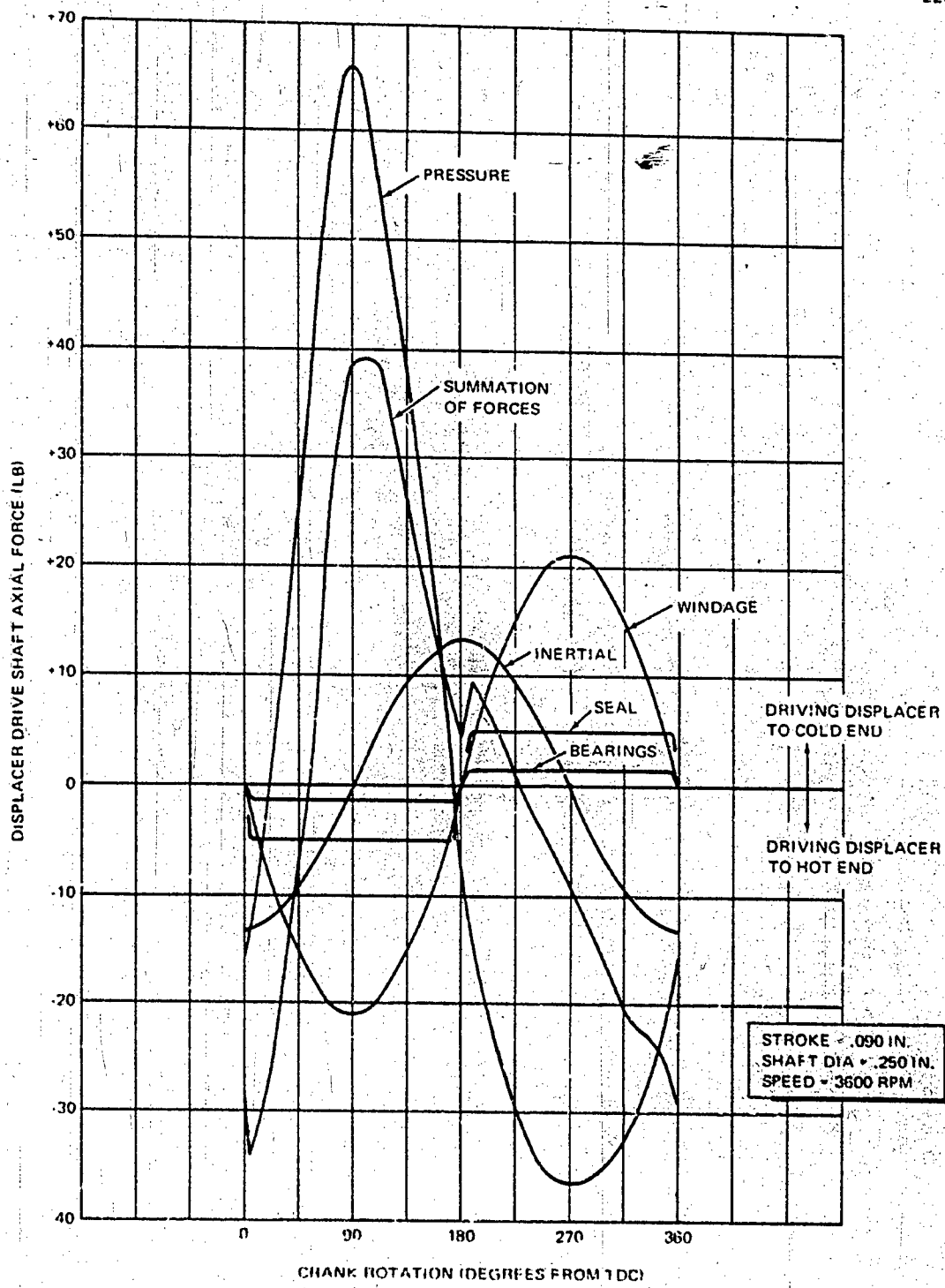


Figure 2-27. Displacer Drive Forces vs Crank Position

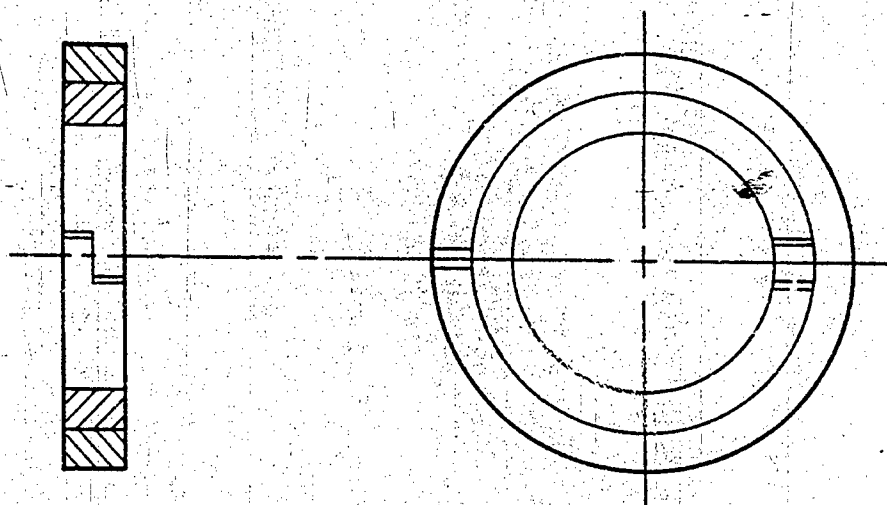


Figure 2-28. Drive Shaft Seal

2.3.1.4 Thermal Insulation Housing

The insulation housing is a 4.62-in. dia aluminum can which attaches to the upper flange of the cooler block. This flange also serves as a feedthrough plate for electric power and instrumentation leads. The insulating material is Min-K 2000 machined into segments to accommodate irregularities in the external surfaces of the cylinder and the power and instrumentation leads. The insulation housing is slipped over the insulation blocks after these are set in place. The insulation heat leak is about 20 w.

2.3.2 Coupler (Figure 2-29)

The coupler function in the proof-of-principle generator is provided by a mercury inertia column contained by a metal tube with diffusers at each end. Corrugated metal diaphragms separate the mercury from the helium in the engine and from the oil in the generator system. Mercury fill and trim valves are provided at each end of the coupler along with overpressure relief accumulators. The coupler is designed as a unit so that it can be removed for filling or servicing. Weight minimization was not a goal for this proof-of-principle design.

Mercury was selected as the coupler fluid primarily because of its high density and low compressibility. High density minimizes the size of the inertia column; low compressibility minimizes lost motion.

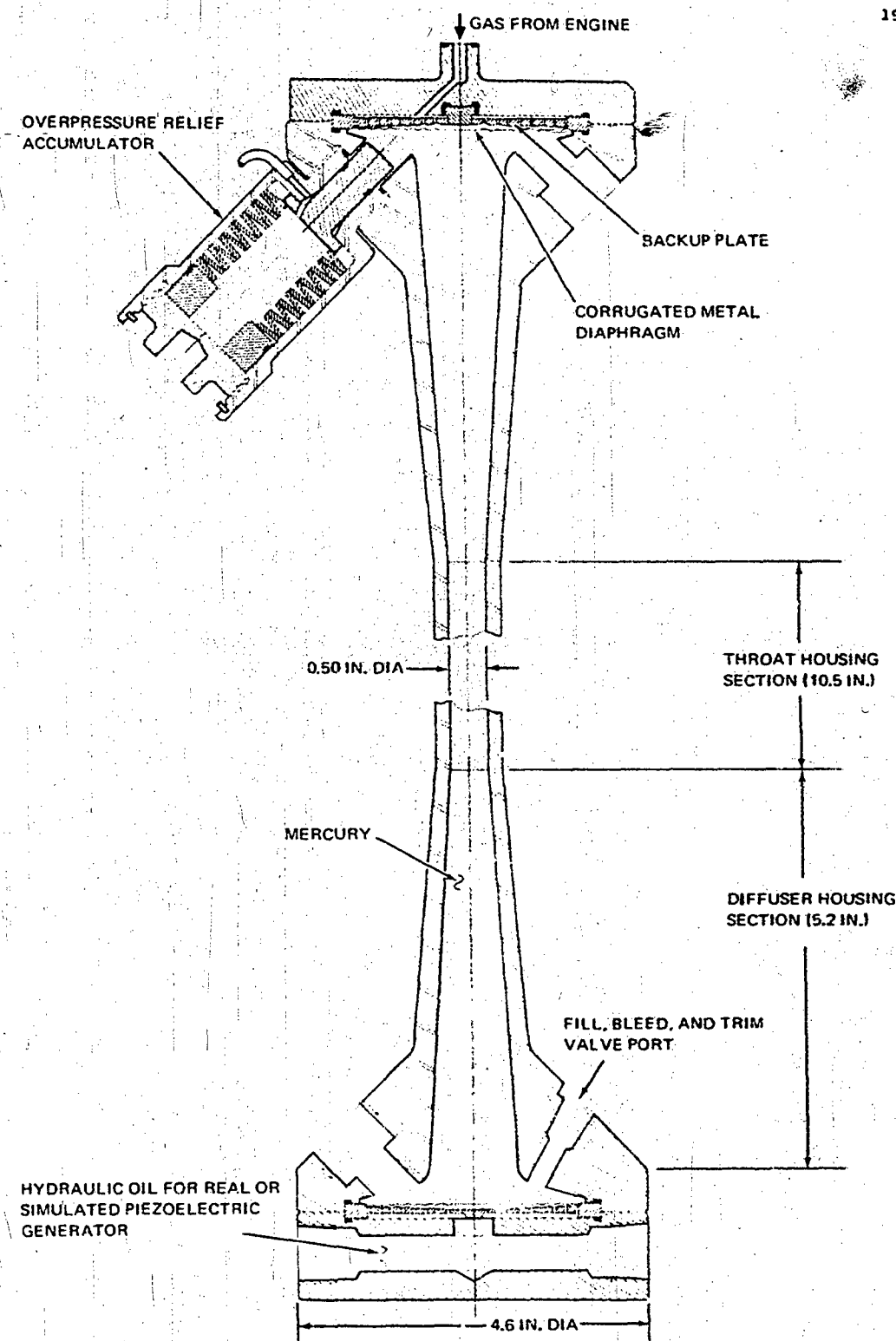


Figure 2-29. Coupler Assembly

The coupler housing is made of 300-series austenitic stainless steel. The 10.5-in. long coupler tube is standard 0.5-in. ID tubing with a 0.188-in. wall thickness. Hoop stresses are approximately 4000 psi at hydraulic pressures of 3000 psi. A 5.6-in. long diffuser with a 7.5-degree half-angle is provided at each end of the coupler tube to minimize flow losses. End flanges with eight 3/8-in. diameter high strength bolts prestressed to 38,000 psi provide attachment to the diaphragm support structure at each end. The mercury inventory in the coupler is 11.5 cu in.

Both corrugated diaphragms are 0.0015-in. thick AM 350 stainless steel. These have eight convolutions with a peak-to-peak height of 0.024 in. and a pitch of 0.15 in. The diaphragms are capable of operating through a swept volume ± 0.2 cu in. from the central unstressed position to their extreme deflected position with a maximum tangential stress of 31,000 psi. The design point swept volume totals 0.21 cu in., or about one-half the allowable value.

Each diaphragm has a 7075-T6 aluminum backup plate to limit its travel. At the engine/coupler interface, the backup plate is on the gas side of the diaphragm. Gas must be distributed over the surface of the diaphragm while minimizing gas dead volume. Eight radial channels are provided behind the backup plate, each connected to eight 0.015-in. diameter holes which vent gas to the diaphragm. The diaphragm is capable of supporting a 1060-psi pressure differential across this hole area with a maximum of 20,000-psi flexural stress when bottomed against the backup plate. The total dead gas volume between the diaphragm and the engine cold plate is 0.04 cu in.; the pressure drop in the manifolding is 8 psi. The position of the diaphragm is sensed by a proximity transducer which has a maximum linear range of 0.13 in. compared to the limiting diaphragm midpoint deflection of 0.142 in. and the nominal design deflection of 0.075 in.

At the load/coupler interface, the backup plate is on the oil side of the diaphragm. The vent holes and radial channels are larger than at the engine/coupler interface because entrained fluid volume is unimportant, and pressure drops would otherwise be too high.

To protect the diaphragms from overpressurization when against the backup plates, an overpressure relief accumulator is provided at each end of the mercury column. These are piston-type accumulators with the pistons springs loaded to accept fluid at a preset value to prevent damage to the diaphragm. Fill, bleed, and trim valves are located at each end of the coupler for charging and providing the proper amount of mercury.

2.3.3 Generator Simulator

The function of this component in the proof-of-principle device is provided by a hydraulic circuit designed to simulate characteristics of a piezoelectric generator. Primary elements of the load system as

designed but not fabricated under the present contract are (1) inlet and outlet power check valves, (2) a liquid compliance chamber, (3) a low pressure reservoir, (4) a high-pressure accumulator, and (5) an adjustable main load valve (Figure 1-3). In addition, appropriate shutoff valves are provided. The load system will be breadboarded using standard components wherever possible.

Power valves are standard poppet type check valves. The pressure drop across each valve at maximum flow is 15 psi; total flow loss for both valves is 1% of generator power output.

The accumulator and reservoir are standard 10 cu in. bladder-type accumulators. Cyclic pressure variation with a 10 cu in. gas volume is limited to 2%.

Design flow through the primary load valve is approximately 6 cu in. / sec, corresponding to a power dissipation of 500 w. A 0.25-in. needle valve with a maximum flow capacity of 27 cu in. per sec has been selected. The outlet line from the valve passes through a water-cooled heat exchanger to remove heat generated by the power dissipation (flow loss) in the valve. All components will be connected with 0.5-in. diameter lines to minimize flow losses elsewhere in the setup.

2.4 PIEZOELECTRIC GENERATOR LIFE TESTS

This section describes the Phase II effort which consisted of life testing four piezoelectric generator stacks under varied environmental conditions. Test results from a fifth stack, independently developed as a prototype unit between Phase I and Phase II, are also included. Widely divergent opinions of piezoelectric materials experts and the absence of published test data concerning long-term stability of a piezoelectric generator operating at high stress levels made life testing a key element in establishing feasibility of the STEPZ concept. The Phase II effort was accordingly directed toward accumulation of such test data for up to 2000 hours. The life test fixtures and associated hardware are discussed, followed by a description of the techniques utilized in processing the 0.040-in. thick by 0.50-in. diameter HDT-31 (PZT-4 equivalent) piezoelectric discs and interleaving copper contacts. Test results include both the parametric tests performed on the MTS system and actual life tests.

2.4.1 Life Test Approach

2.4.1.1 Evaluation of Alternate Concepts

Three basic approaches for executing the desired long-term testing were independently evaluated in the interim between the conclusion of Phase I and the initiation of Phase II. These included an electro-hydraulic system such as used for the Phase I generator tests by DWDL,

variations of a mechanical actuation device, and using a piezoelectric motor or driver stack to stress a similar generator stack. A fourth approach utilizing a mechanically driven rotary hydraulic valve as used by Physics International and described in Appendix A was not seriously considered. Drawbacks with the latter approach were undesirable putting stress application to the piezoelectric stack, high friction in the rotary valve with attendant heat generation and high pressure start-up problems, system leaks, and excessive but undetermined seal friction on the stack driver piston. While none of these appeared insurmountable, the required engineering design effort and questionable likelihood of success led to the decision not to evaluate this approach.

Two possible approaches utilizing the electrohydraulic loading technique used in Phase I were seriously considered. High costs together with basic limitations on the number of stacks which could be tested and the attainable operating temperatures led to abandonment of this approach.

The mechanical actuation device which was carried through layout design utilized an oscillating lever actuated by an electric motor driven cam. Both needle bearings and tension flexures were considered for the fulcrum support of the driving lever, and alternatives for compression loading of the piezoelectric stack were a spherical-ended pushrod and a compression flexure. Factors which influenced the decision not to pursue this approach were (1) the relatively high cost, to complete the detail design and fabricate four test units (2) the requirement for regular maintenance and compensation for wear associated with some elements, and (3) the difficulties associated with ensuring that the piezoelectric stack is stressed axially with no lateral components of applied force.

Within the constraints of the Phase II program, the only practical approach for long-term stressing of piezoelectric generator stacks appeared to be with a similar coaxial piezoelectric driver stack constrained by a rigid load frame. This approach was considered during Phase I, but rejected on the basis that the driver stack must have a much larger volume than the generator stack. This can, however, be used to advantage where a small generator stack is acceptable. The driver stack experiences the same stress cycle as the generator, but is subjected to somewhat higher electric fields and, therefore, more stringent operating conditions. Conservatively, such a driver-generator stack which survives a given life test has demonstrated survival of a generator stack the size of the full stack.

A crude mockup of a piezoelectric driver-generator stack was established by stacking 24 piezoelectric discs 0.5-in. diameter by 0.1-in. thick with a load cell and proximitron in a 12-ton hydraulic press. Up to 215 volts ac was applied to 12 or 23 discs in parallel, under various preloads, with voltage output measured for the remaining discs. Substantial displacements but very low forces and generated voltages were measured. These results were attributed to compliance in the load cell and frame members, which was corroborated by analysis of component compliances. This experiment established the necessity of a

very-rigid load frame with no high-compliance elements in the system. Such a load frame was designed and fabricated as an IRAD prototype to verify performance prior to initiation of the Phase II effort.

Figures 2-30 and 2-31 show the prototype test fixture, both disassembled and assembled. Components include a Kistler Model 901A low compliance load cell for measuring instantaneous stack stress, a fixed-position reference plate, the short generator stack, a holder for two Bently Nevada Model 324L6 proximitor position sensors which measure generator stack displacement with respect to the position reference plate, and the piezoelectric driver stack enclosed by a slotted Pyrex sleeve. The quartz load cell operates on the piezoelectric principle, which is the only available type with sufficiently small compliance. The disadvantage with using this type of load cell is that output is not referenced to an absolute base, and therefore, long-term drift must be accommodated by periodically reducing the preload to zero to provide a temporary known reference point.

2.4.1.2 Independent Compliance Reduction Efforts

High compliance that is not dissipative is not a significant problem for a piezoelectric generator and may even be beneficial in reducing the required swept volume transformation between engine and generator. When using the stack as a driver, however, excess compliance results in more displacement swing with less stress fluctuations developed. Substantial independent compliance reduction efforts between Phase I and Phase II met with only limited success, and Phase II was initiated on the basis of accepting reduced stress fluctuation, but maintaining planned peak stresses.

First assembly of the IRAD prototype stack gave results which still indicated substantial compliance, and high-voltage dc excitation was applied to the stack. Electronic dial indicators capable of measuring in microinches were used to measure relative displacement at various locations. These measurements showed that structural members exhibited compliances very close to the predicted values, and that excess compliance (or low compressive modulus) was restricted to the stack itself.

A series of stress-strain measurements was made for a variety of stack assembly procedures including brass and copper electrical contacts with varying degrees of hardness. Best results were obtained using indium solder which was melted while maintaining axial compression on the stack. Practical problems included voids in the interfaces and indium squeezed out on the sides. The most reasonable compromise was judged to be the use of fully annealed copper contacts with no bonding agent. This technique produced moduli of around 3.3×10^6 psi compared with 5.3×10^6 psi for the indium bonded stacks and 9.4×10^6 psi for the ideal piezoelectric material for the short-circuited condition, and slightly higher than this for practical operating conditions. It increases to 18.4×10^6 psi under open-circuit conditions. A modulus

of at least 7×10^6 psi under normal operation would have been required to achieve a full 1000 to 9000 psi stress swing with the 55 volts/mil excitation voltage used for life testing.

2.4.1.3 Test Fixture Assemblies

The life test fixtures consist of a rigid load frame which encloses the piezoelectric stack with a means for applying uniform torque-free axial preload to the stack. Other elements mechanically in series with the stack include a quartz load cell, centering pins, and two proximitors which measure axial displacement across the generator stack. These elements for the IRAD prototype load frame (Figure 2-31) and included in a typical contract assembly (Figure 2-32). The IRAD prototype load frame was engineered during the interim between Phase I and Phase II, and was modified slightly during Phase II to incorporate improvements based on initial operating experience. The primary change was an increase in the load frame opening for better assembly accessibility with only a slight increase in compliance. A single large diameter thread was also used for the preload adjusting screw to simplify fabrication and assembly and reduce galling.

Assembly of the life test fixtures is indicated in Figure 2-33. The lower jam nut retains the locating plug which is held concentric with the load frame on its outer diameter and locks the bottom load pad into position with a pin. The load pad is followed by a 0.005-in. thick mica disc for electrical isolation, a fully annealed ETP copper compliance pad, and the piezoelectric driver stack consisting of seventy 0.5 in. diameter by 0.040-in. thick HDT-31 (PZT-4 equivalent) discs with interleaved copper contacts 0.002 in. thick. The assembly continues with a compliance pad, mica disc load pad, and proximitator mounting plate which uses a locating pin to mate with adjacent load pads. This is followed by a similar stack buildup for the 10-disc generator section. The assembly is topped with the proximitator reference plate, load cell, spacer, and torque isolation yoke, which are all located by the preload adjusting screw. The arms of the torque isolation yoke fit closely into grooves in the load frame, which enables the preload to be varied without applying rotational components to the stack. Precision bore slotted Pyrex tubes were used to maintain stack concentricity during assembly, and then broken away on a previously scribed mark after establishing the preload. This tube also locates up to the load pad on each end of the stack, which is in turn located by the central pin. A typical contract stack is shown in Figure 2-34 after mechanical assembly, but prior to completing electrical and instrumentation connections. The Pyrex alignment tube sections are still in place, and the edges can be seen on both sides of the copper contact terminals.

The fully annealed copper contacts, and especially the compliance pads, serve to compensate for surface irregularities and any tilting that does occur in the final assembly. These pads yield at about 9000 psi compressive stress, and generally conform well to nonuniform loading

2347

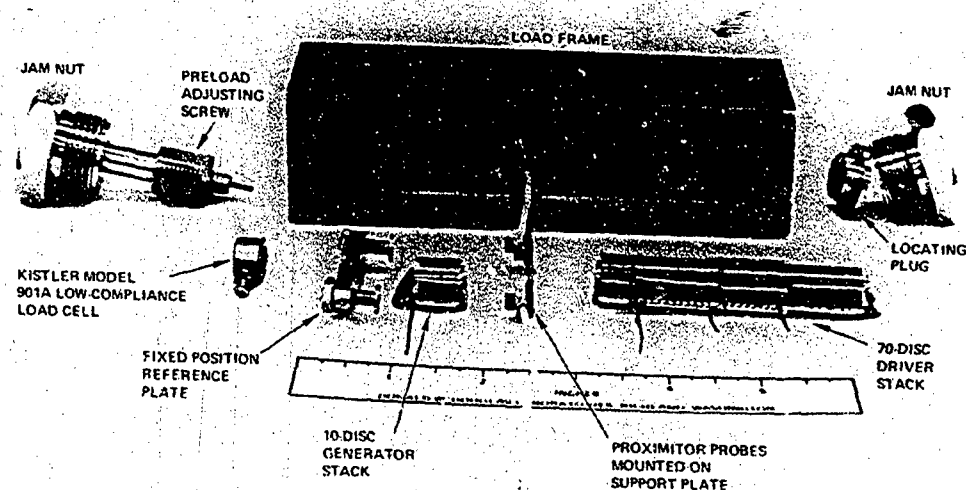


Figure 2-30. Prototype Test Fixture Components

2348

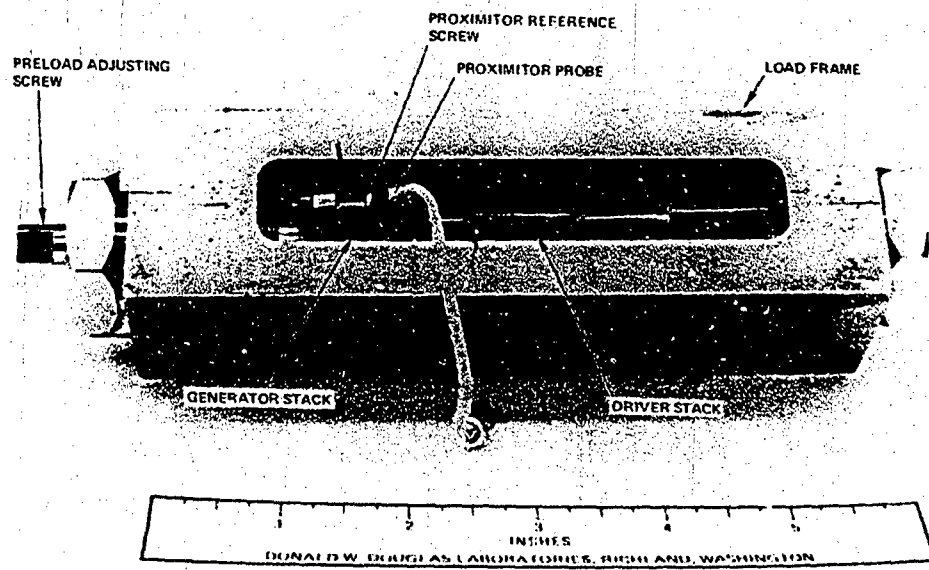


Figure 2-31. Prototype Test Fixture

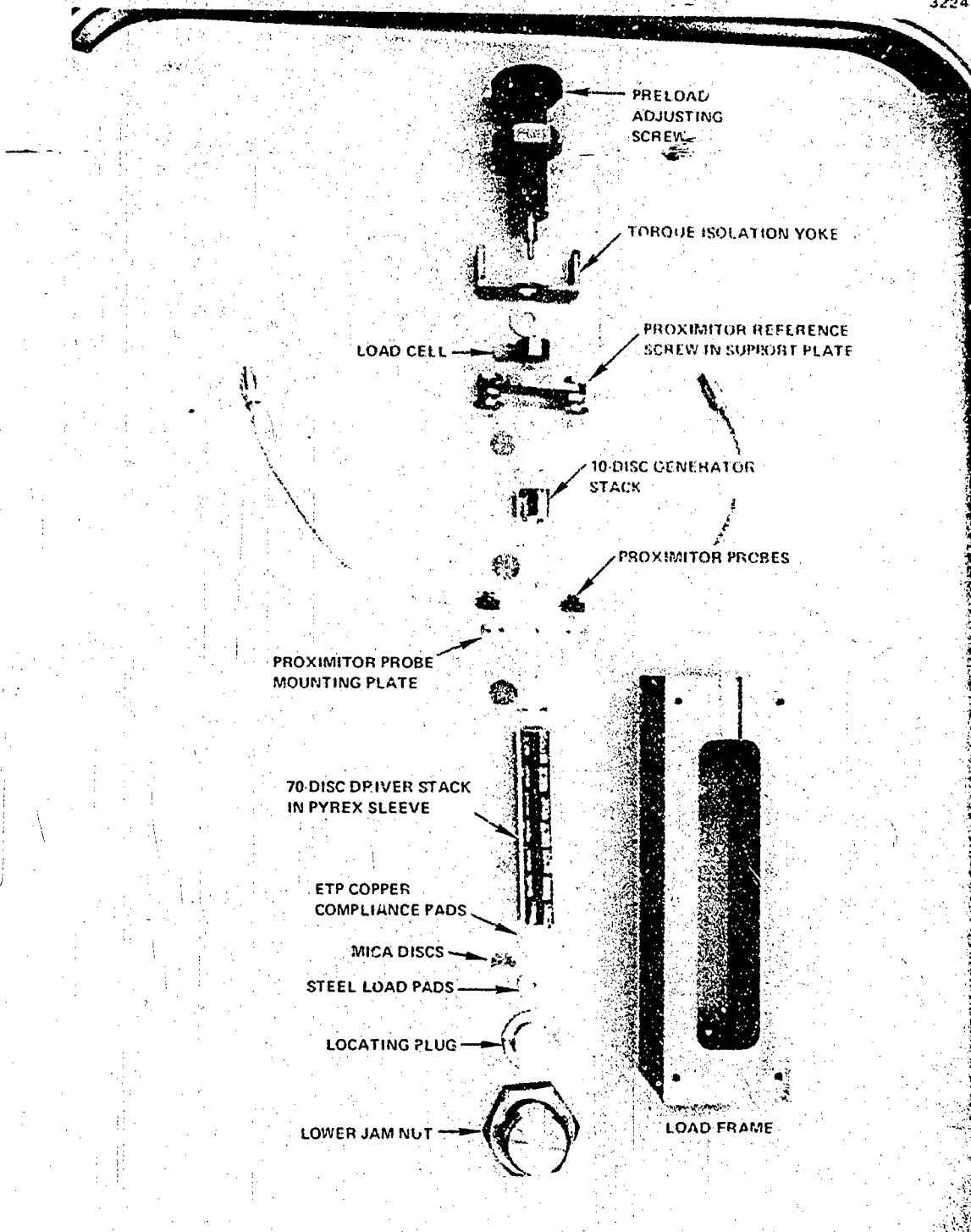


Figure 2-32. Typical Contract Life Test Fixture Components

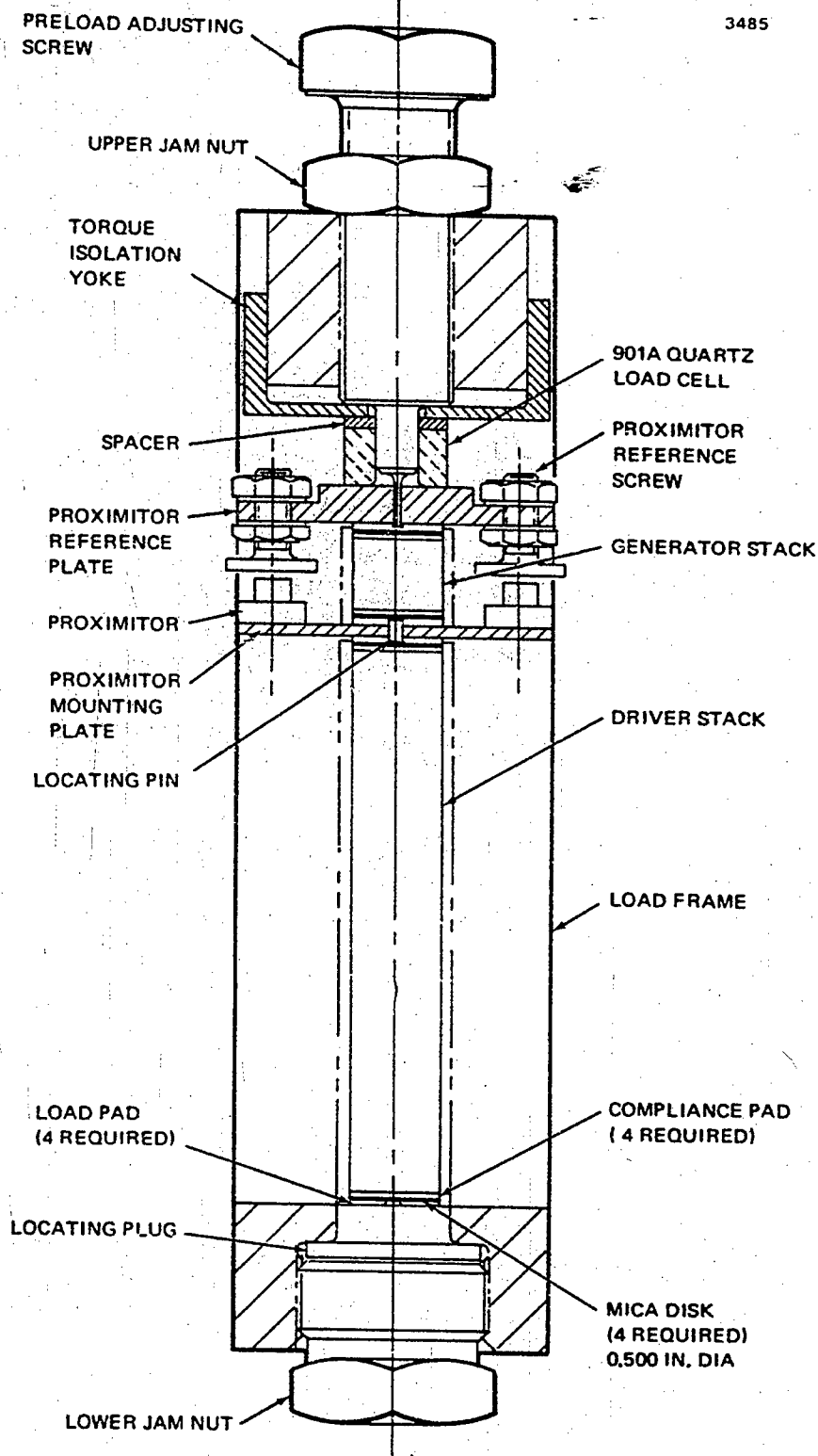


Figure 2-33. Load Frame Assembly Details

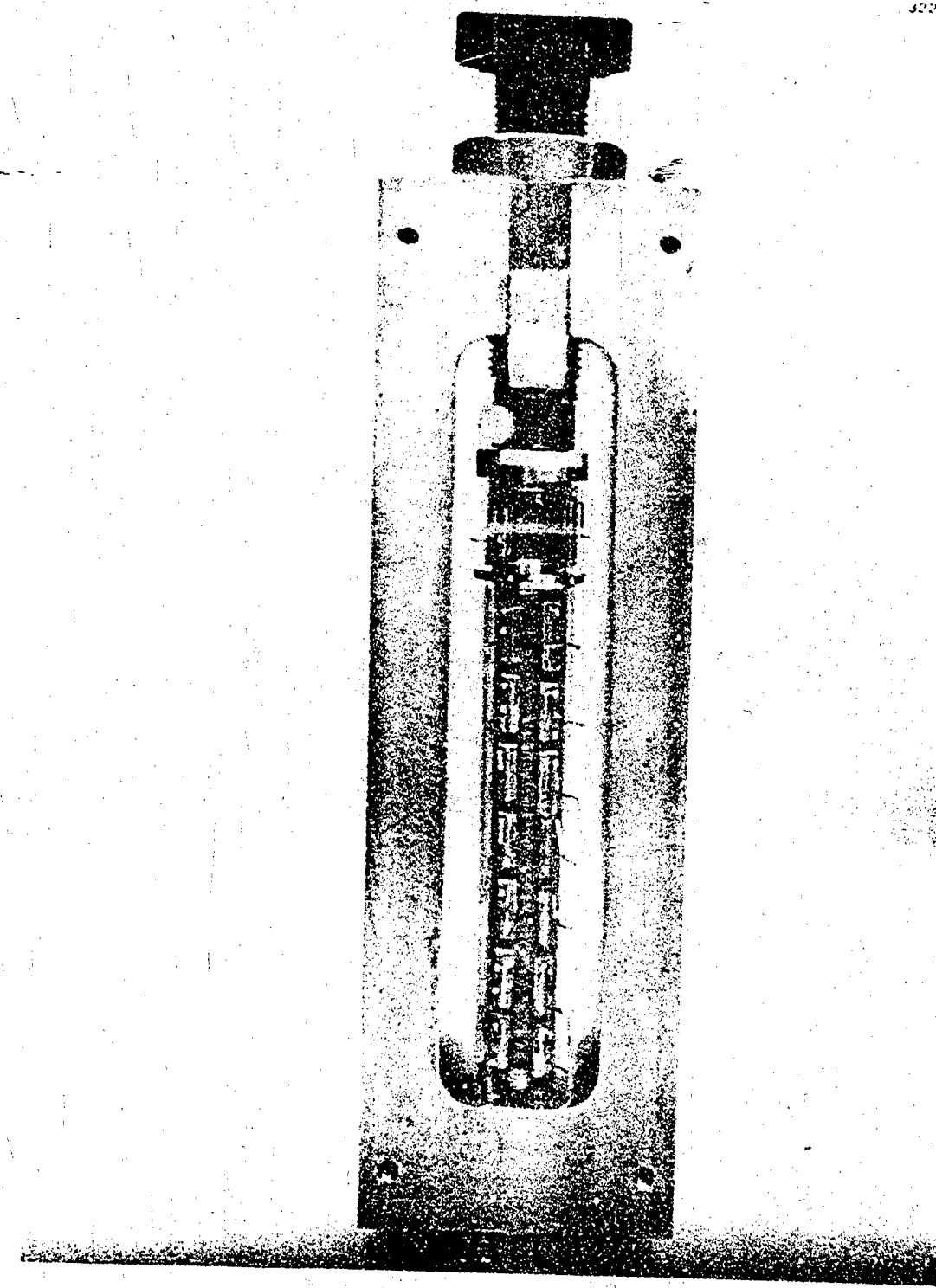


Figure 2-34. Preliminary Mechanical Assembly of Typical Test Fixture

where the localized stresses can reach higher levels than the initial average preload of 12,000 psi used to seal in the stacks. This preload significantly reduces as stack elements relax and is repeated several times during initial assembly until yielding essentially stops, as indicated by load cell stress remaining high for several minutes. Once this condition is achieved, the preload is never fully relaxed until the high-dielectric strength potting compound is hardened in place to effectively maintain all relative locations, with or without preload. The encapsulating technique is described more fully below in Section 2.4.2.2.

2.4.1.4 Driver Stack Power Supply and Protection Circuit

The best means for achieving a large voltage swing on the piezoelectric driver circuit is to allow the supply voltage to swing partly negative. This reduces the highest absolute potential experienced by the stack. Based on vendor recommendations (Reference 5), a negative swing of 10 volts/mil or 400 volts is acceptable before depolarization is initiated. The 55 volts/mil or 2200 volt peak-to-peak power supply (Figure 2-35), was therefore normally operated with a 700 volt dc bias and an 1100 volt ac amplitude to produce voltage swings from -400 to +1800 volts. Two such circuits were used; one was designed to handle three stacks in parallel, while the other drives two stacks in parallel. Ac line power is applied through a variable autotransformer to the primary of a 30 to 1 step-up transformer. Because the dc power supply does not pass reverse current, a low impedance ac shunt is provided by the high-voltage 1.6 μ f capacitor.

The 70-disc piezoelectric driver stacks are connected as seven 10-disc segments, each of which is represented by a capacitance C_s . Any segment can be easily removed from the circuit in case of individual failure. Protection against high current surges from complete voltage breakdown across a disc is provided by resistors R_p . The value of R_p is 125K for the 10-disc segments of the contract stacks and 75K for the 20-disc segments of the IRAD driver stack. The variable resistor was included in only one power supply circuit which used a step-change dc power supply to limit voltage buildup rates across C_s during dc supply changes. The resistance was decreased to zero before applying ac excitation so that essentially the entire dc voltage drop appears across C_s . The two power supply and protection circuit modules (not including the dc supply) are shown respectively in Figures 2-36 and 2-37.

2.4.1.5 Generator Stack Electrical Load and Instrumentation System

A piezoelectric generator may be schematically represented by a voltage source in series with an internal resistance and capacitance. For both the parametric tests and life tests, generator output was applied to a resistance load with a series inductance used to compensate for generator capacitance by resonantly tuning the circuit (Figure 2-38).

Generator output is determined as V_L^2/R_L where V_L is the voltage measured across the load resistance R_L . Maximum power to the load is achieved when the load resistance R_L is equal to the generator stack internal resistance R_s . As with any generator, this is an undesirable operating condition because half the generated power is dissipated in heating the generator, and a maximum of 50% efficiency can be achieved (if mechanical stack losses are negligible). To achieve a reasonable compromise in the tradeoff between power output and efficiency, load resistances of 120K (three times the value for maximum power transfer) were used for the contract life test stacks. The smaller-diameter IRAD generator stack had a maximum power load of 200K, and 540-K resistors were used during the life tests.

Optimum inductance (to give maximum power transfer with the operating load resistance) for the contract stacks ranged from 115 to 135 henries during the parametric tests, but was measured at 175 henries for the actual operating conditions of the life tests. An optimum value of 840 henries was experimentally determined for the smaller-diameter IRAD generator stack.

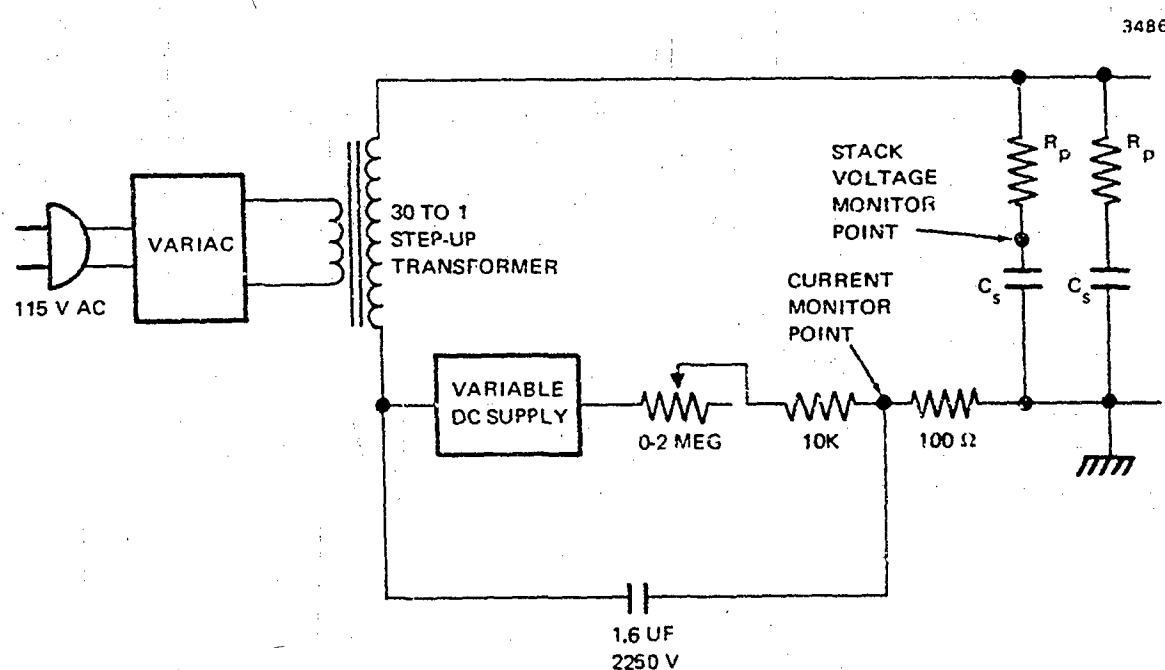


Figure 2-35. Driver Stack Power Supply and Protection Circuit

3336

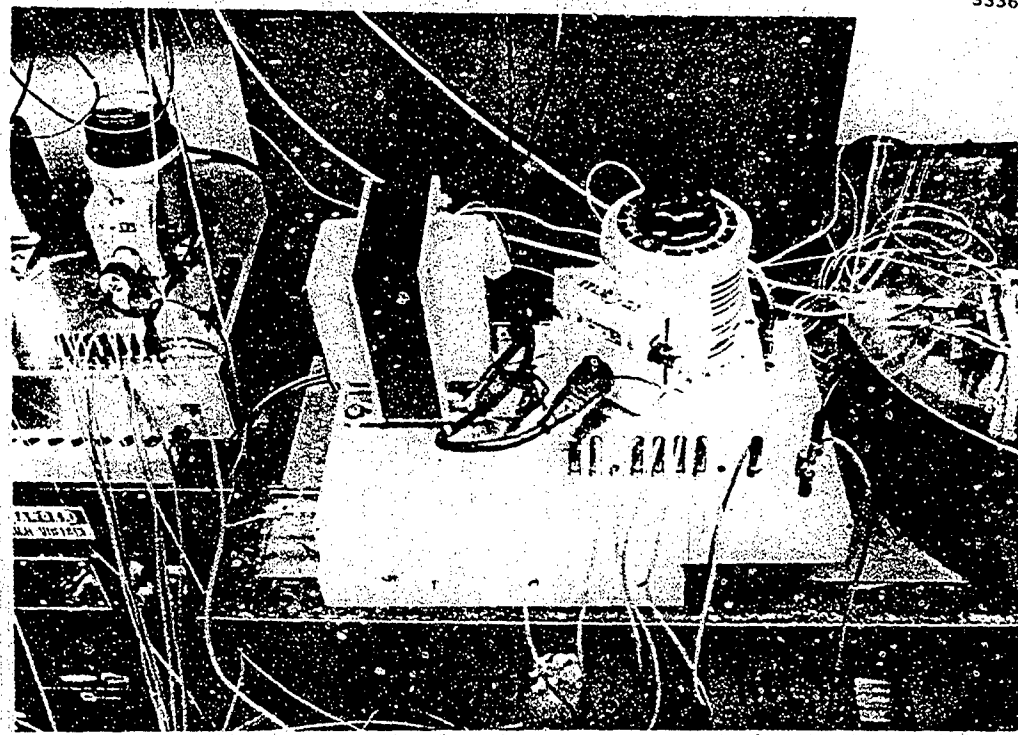


Figure 2-36. Top of One Power Supply and Protection Circuit Module

3337

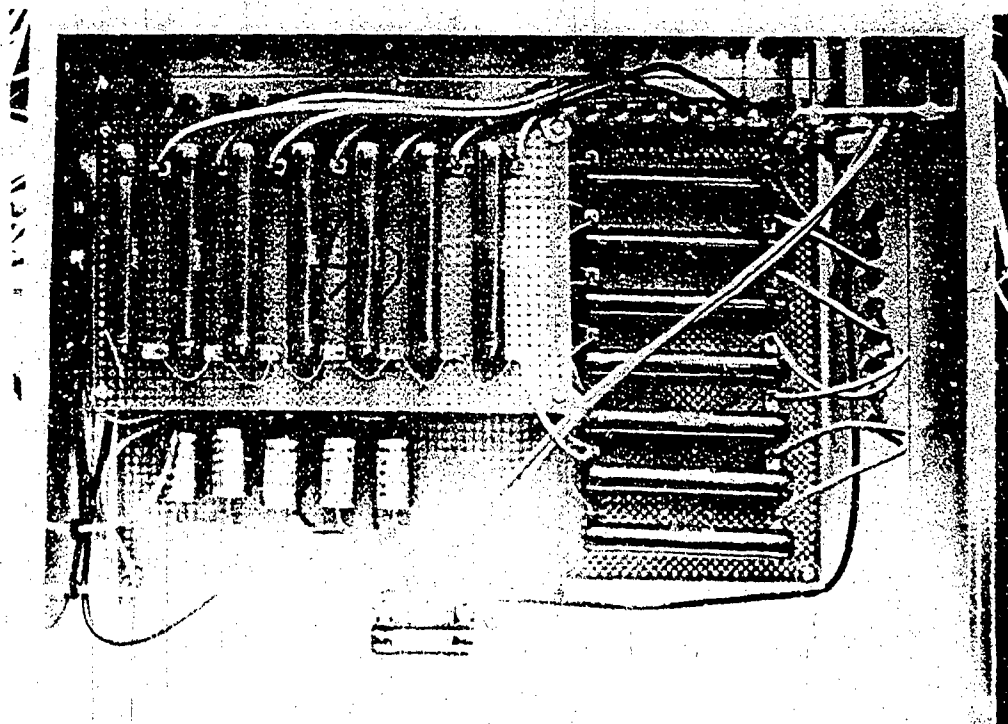


Figure 2-37. Bottom of One Power Supply and Protection Circuit Module

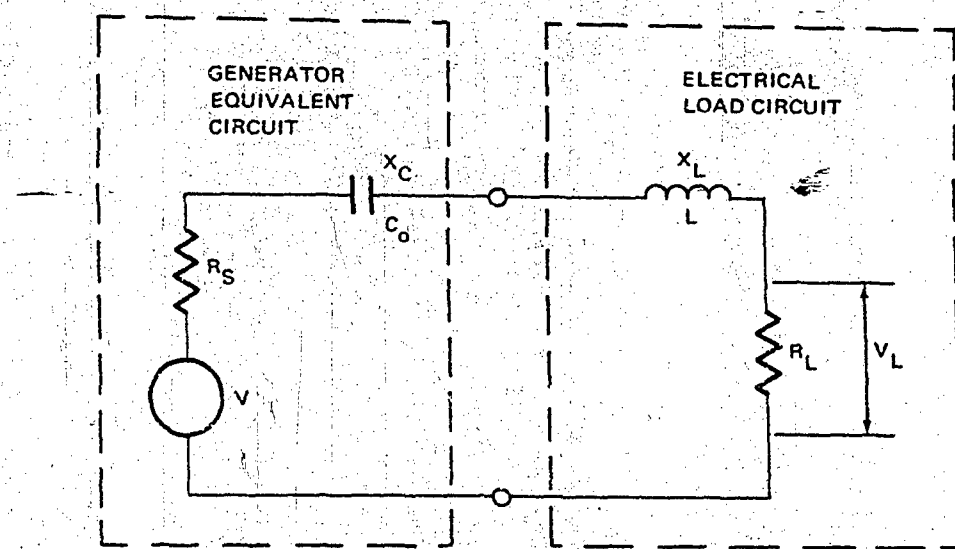


Figure 2-38. Typical Generator Stack Electrical Load.

Instrumentation to monitor stack performance included Tektronix Model P6013 1000x attenuator probe with a 100 megohm input impedance used in conjunction with a Tektronix Model 545A oscilloscope to measure voltage applied to the driver stack and output at the terminals of the generator stack. This not only reduced the measured voltages to manageable levels, but was the only device available with sufficiently high input impedance to avoid loading the circuits being monitored. The load voltage across R_L only was measured with a Ballantine Model 355 digital voltmeter.

Output from the Kistler Model 901A quartz load cell mechanically in series with the stack was fed through a Kistler Model 566 or 504D (depending on the stack) charge amplifier into another Ballantine Model 355 digital voltmeter. Output is directly proportional to axial force and therefore also to stack stress.

The strain for each generator stack was measured with two Bently-Nevada proximitron probes connected to Model 3601 proximitrons. Physical relationships between the proximitron probes and metal reference surfaces are shown in Figure 2-33. The proximitrons were calibrated prior to assembly using a Pratt and Whitney Model G-2100 Supermicrometer.

Cyclic work input was determined by connecting the proximitron and charge amplifier outputs, respectively to the x- and y-axes of a Tektronix Model RM503 x-y oscilloscope. This produced a force-displacement diagram for the generator stack which was recorded photographically and the enclosed area was later determined to quantify mechanical input to the generator stack. The measured electrical output divided by this mechanical input produces an efficiency measurement for the generator stack.

The life test equipment and instrumentation are shown in Figures 2-39 to 2-41. Figure 2-39 includes the right side of the test facility including the low temperature stacks inside the freezer, dual beam oscilloscope, IRAD test fixture on the benchtop, Kepco Model 1250B dc power supply, and one power supply and protection circuit system. The left side of the laboratory (Figure 2-40) includes the Fluke Model 412B dc power supply on top of the 150° F oven, two digital voltmeters on the x-y oscilloscope, and both power supply and protection circuit systems. Figure 2-41 shows the oven interior with the high-temperature stack.

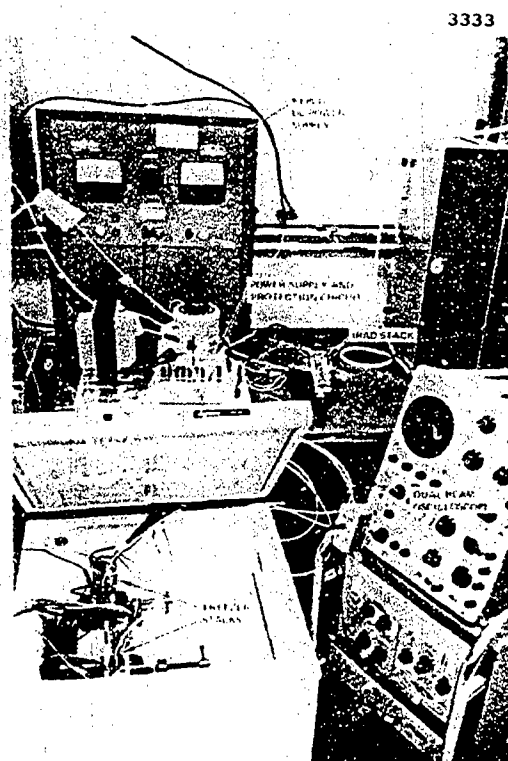


Figure 2-39. Life Test Laboratory Showing Freezer and IRAD Stacks

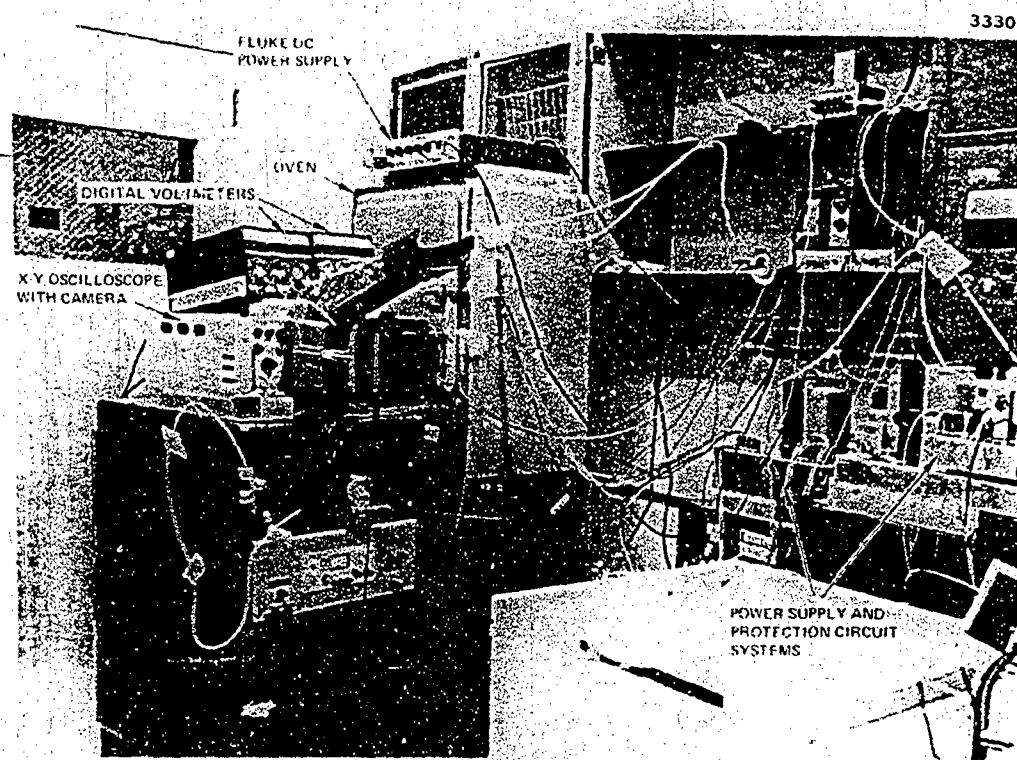


Figure 2-40. Oven and Associated Test Equipment

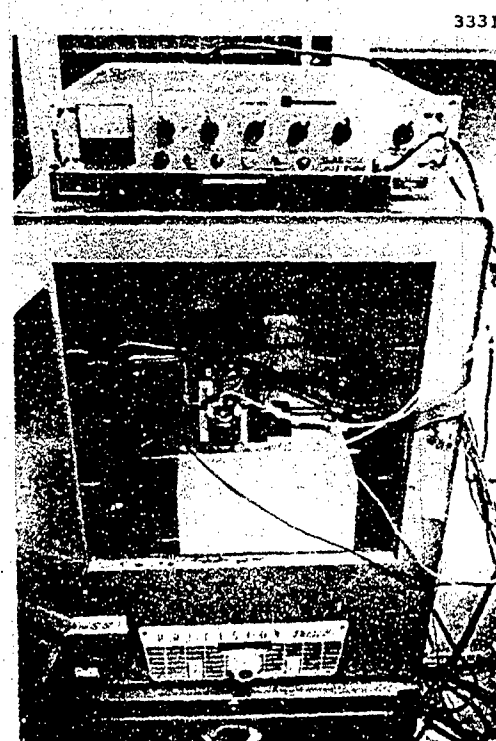


Figure 2-41. Oven Stack Life Test Arrangement

2.4.2 Piezoelectric Disc and Contact Processing

Elaborate cleaning and processing was used for the piezoelectric discs and copper contacts for the life test assemblies. This action was based on results reported by Physics International (Reference 7) for their piezoelectric motor driven artificial heart system and on earlier failures experienced by DWDL. The primary objective of the procedures is to eliminate contaminants and sharp points which may initiate electric discharges that produce carbon tracks and eventually lead to complete breakdown. Another secondary effect of foreign particles between discs and contacts or of hard, non-annealed copper contacts is to increase system compliance which reduces the potential stress swing.

An example of catastrophic piezoelectric disc failure is shown in Figure 2-42. Fused ceramic and carbon deposits are visible where the encapsulant has been removed. This failure occurred in a stack with the same size and type of discs as used for the life test assemblies. It was, however, received from the supplier as a bonded assembly, then cleaned and potted with the silastic used as the secondary encapsulant for the life test stacks. The stack was operated under no load for about 20 hours at peak-to-peak voltage swings up to 2000 v. Inductance was used in the driver circuit, which stored sufficient energy to cause even the ceramic to melt in the discharge area. A similar breakdown occurred in the first assembly of the IRAD prototype stack.



Figure 2-42. Catastrophic Failure of Bonded and Potted Test Stack

These components had been thoroughly cleaned and degreased, assembled in a laminar flow bench, and the assembly operated submerged in high-dielectric transformer oil. This unit operated only on an intermittent basis with numerous minor audible discharges culminating in catastrophic failure when voltage swings reached 1500 volts peak-to-peak. Failure was attributed to foreign particles from the oil, because some such particles were removed from adjacent parts of the stack prior to final failure. Improvement was obviously needed to achieve a 2000-hour life test with peak-to-peak voltages of 2200 volts or 55 volts per mil.

2.4.2.1 Processing and Assembly of Life Test Stacks

The processing procedure actually used for the life test stacks was an extensively modified version of that developed by Physics International (Reference 7). Many steps developed at DWDL for processing of thermionic diode components were incorporated. This procedure was first applied to the third assembly of the IRAD prototype stack for proof testing, although schedule commitments required completion of the contract disc and contact processing prior to actual operation of the IRAD stack. This procedure represents extreme precaution to provide maximum confidence in successful life testing. It is likely that considerably simpler procedures would prove satisfactory. The sequence for the piezoelectric discs is summarized as follows.

1. Discs are stacked and clamped with flat surfaces together for surface protection, sandblasted on the edges with 20-micron aluminum-oxide grit, and flushed with tap water. This removes metallizing left from electric contact deposition and other contaminants from the edges.
2. Warm water and Alconox wash in ultrasonic cleaner with solution being recirculated and filtered (15 minutes).
3. Continuous flow flushing rinse with tap water in ultrasonic cleaner (30 minutes).
4. Distilled water rinse in ultrasonic cleaner with water being recirculated and filtered (15 minutes). Figure 2-43 shows some of the discs at this stage of processing. The black marks on the discs indicate polarity.
5. Trichloroethylene rinse in ultrasonic cleaner (10 minutes).
6. Reagent alcohol rinse in ultrasonic cleaner with fluid being recirculated and filtered (15 minutes).
7. Freon rinse in ultrasonic cleaner with fluid being recirculated and filtered (15 minutes).

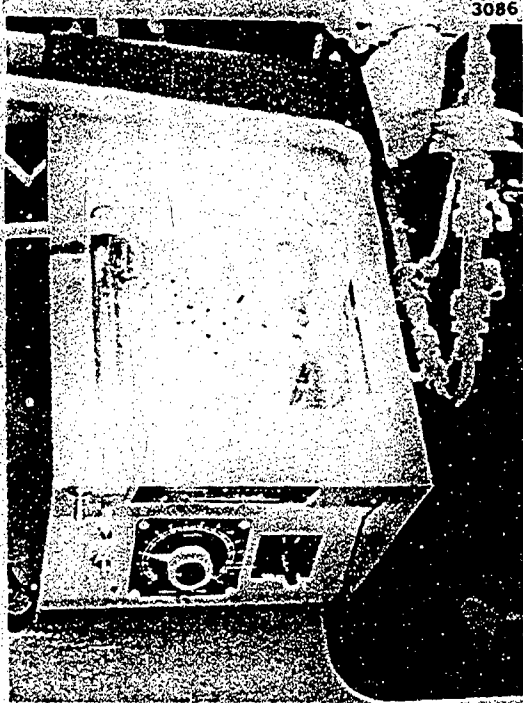


Figure 2-43. Piezoelectric Discs in Ultrasonic Cleaner

8. Vapor degrease with trichloroethylene (1 hour).
9. Freon rinse in ultrasonic cleaner with fluid being recirculated and filtered (15 minutes). Repeat with fresh fluid (15 minutes).
10. Vacuum bake at 150°F with discs shorted (overnight).
11. Recheck polarity as required by loss of identifying marks during processing.
12. Store in clean Petri dishes until assembly. Examples of this for both discs and completed copper contacts are shown in Figure 2-44.

Preparation of 0.002-in thick copper contacts is directed toward minimizing both electrical breakdown probability and stack compliance. The copper contacts are put through the following operations.

1. Freon rinse in ultrasonic cleaner with fluid being recirculated and filtered (15 minutes).
2. Discs are rolled flat on granite surface plate.
3. Deburr in kitchen cleanser and water slurry using ultrasonic cleaner with mixture being recirculated (5 hours).

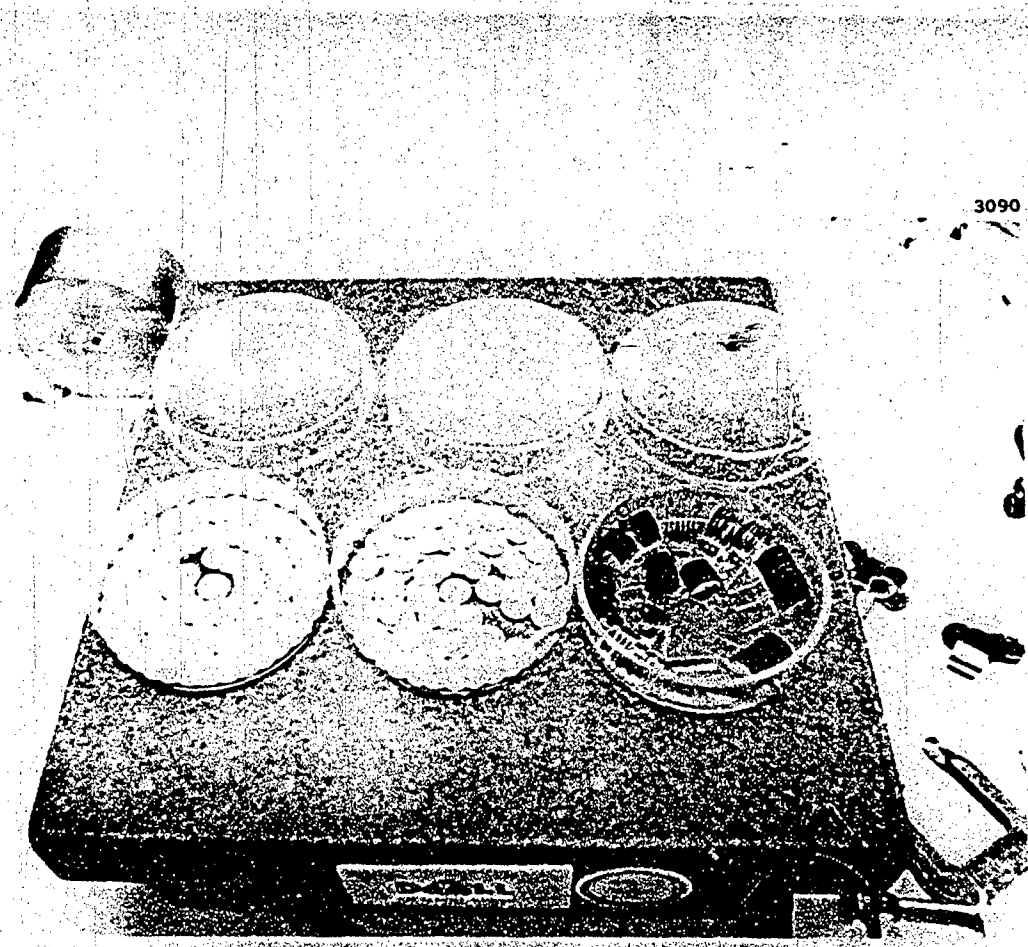


Figure 2-44. Fully Processed Piezoelectric Discs and Copper Contact Assemblies

4. Continuous flushing rinse with tap water in ultrasonic cleaner (45 minutes).
5. Flush with distilled water, reagent grade alcohol, and Freon (as required).
6. Rinse with Freon in ultrasonic cleaner with fluid being recirculated and filtered (2 hours).
7. Rinse with reagent alcohol (as required).
8. Rinse with Freon in ultrasonic cleaner with fluid being recirculated and filtered (15 minutes).
9. Rinse with reagent alcohol and ethyl alcohol (as required).
10. Outgas with mechanical vacuum pump and liquid nitrogen cold tap (overnight).
11. Anneal in 10^{-6} torr vacuum at 700°C (5 minutes). Contacts are shown in the vacuum furnace just prior to annealing in Figure 2-45.
12. Solder contact tabs together in groups of five.

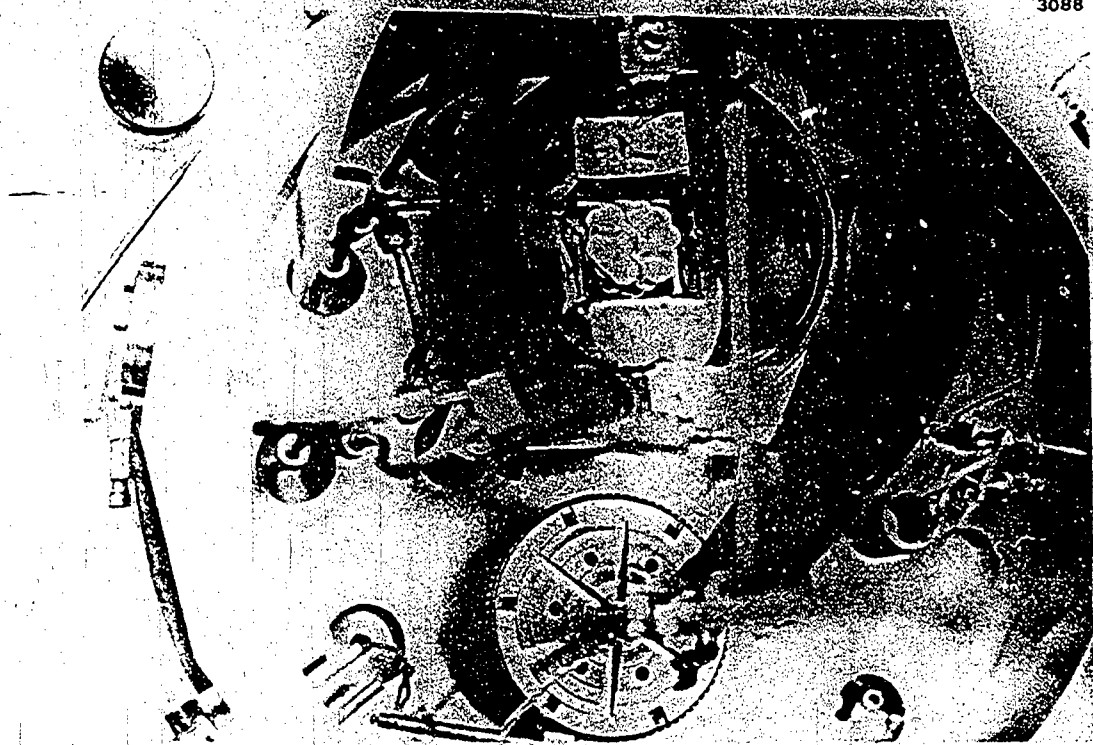


Figure 2-45. Copper Components in Vacuum Annealing Furnace

13. Remove residual acid flux with boiling distilled water, assisted by a camel hair brush, while clamped in assembly fixture.
14. Flush with distilled water, alcohol, and Freon (as required).
15. Remove from assembly fixture and store in Petri dish until final assembly.

The piezoelectric stacks are assembled electrically in parallel by placing discs on edge with alternating polarity and interleaving the copper contact subassemblies to form seven 10-disc segments. Initial buildup is accomplished in a semicylindrical section of precision-bore Pyrex tubing. The 10-disc generator stack or 70-disc driver stack is then transferred to a slotted Pyrex-tube handling fixture which encloses about two-thirds of the stack circumference by placing the Pyrex sections end to end in a steel vee-block and sliding the stack assembly from one to the other (Figure 2-46). The copper contact tabs for all seven sections of one polarity have been soldered together; the sections on the other side are independently connected to the power supply and circuit protection equipment.

A closer view of the reverse side of the stack through the glass sleeve is shown in Figure 2-47. Surface irregularities in the disc edges and slight misalignments are visible. In two or three cases, copper con-

3218



Figure 2-46. Stack Assembly in Pyrex Sleeve and Vee-Block

3222

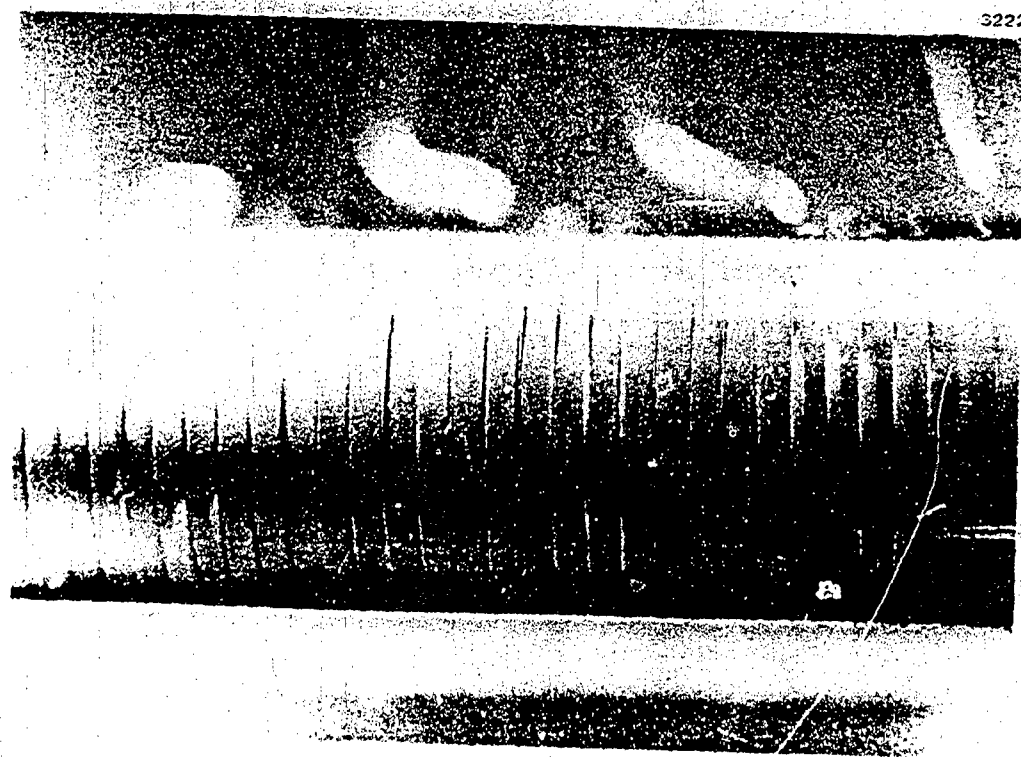


Figure 2-47. Stack Through Pyrex Sleeve

2.4.2.2 Dielectric Environment for Life Test Stacks

It is imperative that a high dielectric strength environment be provided around the stack, because voltage gradients are much higher than those needed to ionize air and initiate an electrical discharge. Oil is typically used for this type of application, and was used by DWDL for early work, including the first assembly for operational testing of the IRAD prototype stack. Problems associated with using oil in the present application include the following.

1. High dielectric oils are typically somewhat hygroscopic, and probably accumulate an unacceptable amount of moisture over a 2000-hour open atmosphere test.
2. Tools used for preload adjustments during data taking, and other aspects of practical operation, make contamination of oil with foreign matter difficult to avoid.
3. Most importantly, use of the piezoelectric load cells requires reducing stack preload to zero, for an absolute reference point each time data are taken. Stack slippage is possible where it is not externally held in place.

These considerations led to an attempt to find an inert high-dielectric-strength potting compound with sufficient flexibility to accommodate stack vibrations and rigid enough to maintain relative positions of components with or without the preload screw in place. The basic encapsulant selected was Dow Corning Sylgard 184 with a dielectric strength of 500 volts/mil. Encapsulation of a test stack, however, resulted in a poor bond between the stack and Sylgard. Accordingly, a 5- to 10-mil thick layer of Dow Corning QR-4-3117 circuit board coating with a dielectric strength of 2000 volts/mil and excellent adherence to copper and ceramic was used as the primary encapsulant with Sylgard 184 applied for final encapsulation. This combination of encapsulants tested with smooth metal spheres exhibited no breakdown when 20,000 volts were applied with a 10-mil separation. Some microscopic bubbles were observed in the primary encapsulant applied to the stacks. Improved potting techniques reduced the problem with later stacks, but it is possible that some of the observed breakdowns in driver segments might have resulted from a series of such bubbles. Results of this encapsulating approach have been basically good and definitely superior to oil.

2.4.3 Parametric Tests

The primary purpose of the parametric testing was to establish baseline generator stack performance characteristics and optimum load values for one standard and one optically lapped stack using equipment with known and controllable stress application. These objectives were

acts appear to protrude slightly beyond the adjacent discs and are bent downward. This condition occurred only in the contract stacks. For assembly of the prototype stack, the entrance end of the glass tube was beveled for easier insertion. This was one of several minor operations which were modified or eliminated to expedite assembly of the contract load frames, and which generally achieved the desired effect. In this instance however, the result was an unacceptable condition where some of the copper contacts had portions severed off and smeared onto the edge of the piezoelectric discs. The extent of damage is shown in Figure 2-48 in the region at one edge of the Pyrex sleeve where most problems occurred.

After considering several rework alternatives, the damaged stacks were assembled into the load frames, preloaded to 12,000 psi, alignment sleeves removed, and sandblasted locally to remove debris. Subsequent microscopic examination indicated removal of copper (and substantial ceramic) from the disc edges, but some sand particles remained wedged between disc interfaces. Such sharp edges are sources of localized electric field concentration, but the ultimate dielectric environment was expected to be capable of sustaining such fields without breakdown.

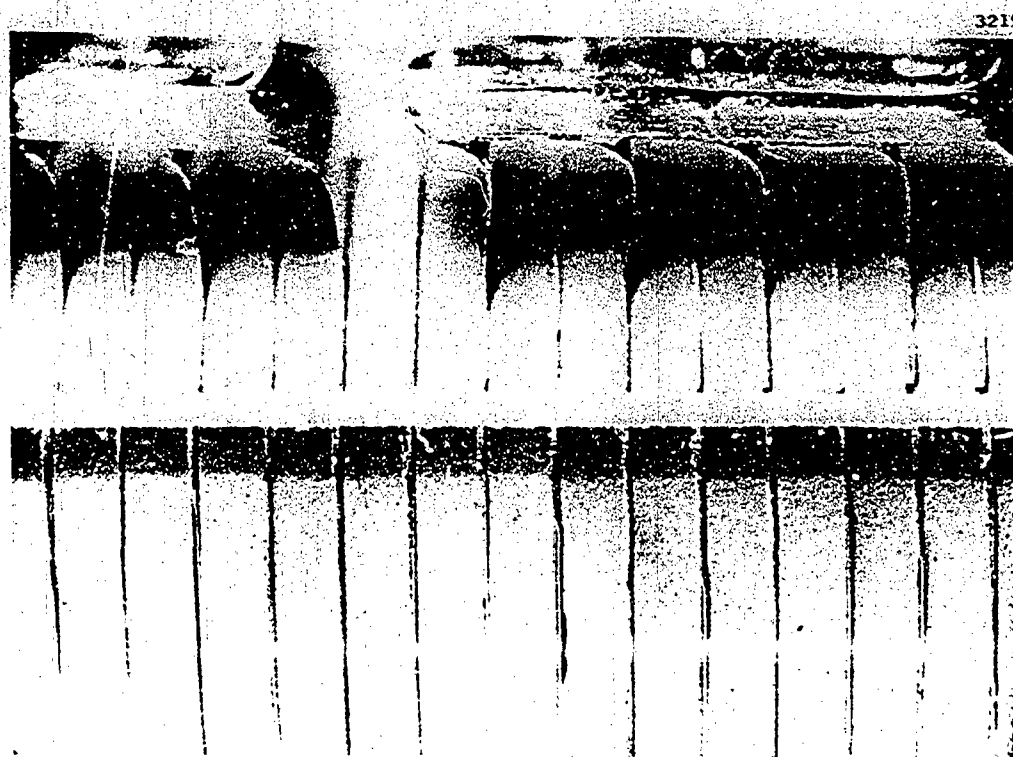


Figure 2-48. Damage Caused by Pyrex Sleeve

accomplished on schedule. Original intentions were to repeat the parametric tests on surviving generator stacks following life testing. After technical problems delayed the initiation of life tests, however, completion of the final parametric tests would have required premature destructive termination of the life tests to meet the schedule. This task was accordingly deleted by mutual agreement to accumulate more time in life testing.

2.4.3.1 Electrohydraulic Test Equipment

The electrohydraulic materials loading system used for the parametric tests was leased from Battelle Pacific Northwest Laboratories in Richland, Washington. Details of the test equipment and associated instrumentation are described in Appendix C. The test configuration used for the parametric tests is shown in Figures 2-49, 2-50, and 2-51. Figure 2-49 shows the load system with electrical leads from the test stack and proximitors leading to the electrical load and instrumentation racks. The test stack in place appears in Figure 2-51; electric connectors from the 10-disc generator stack obscure the proximeters used for displacement measurements across the stack. These are more clearly shown in Figure 2-51 showing the opposite side of the test stack.

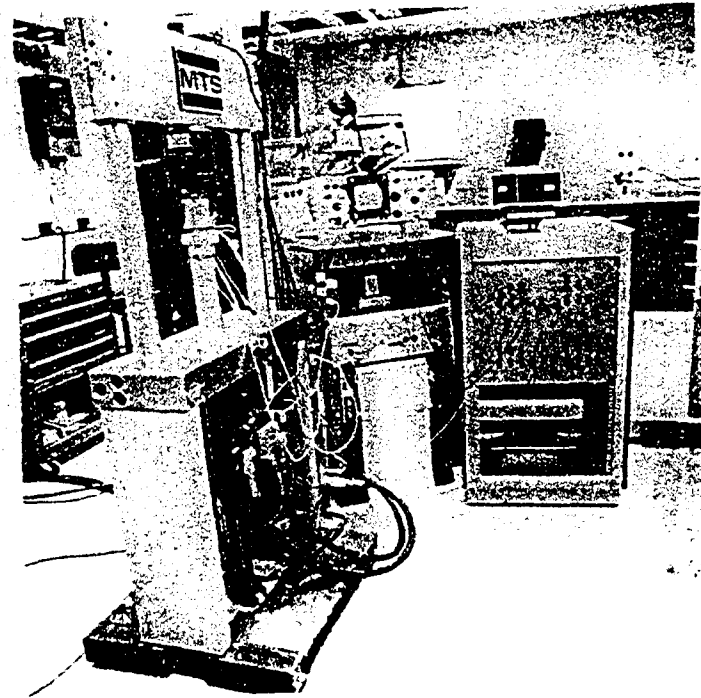


Figure 2-49. Parametric Test Setup

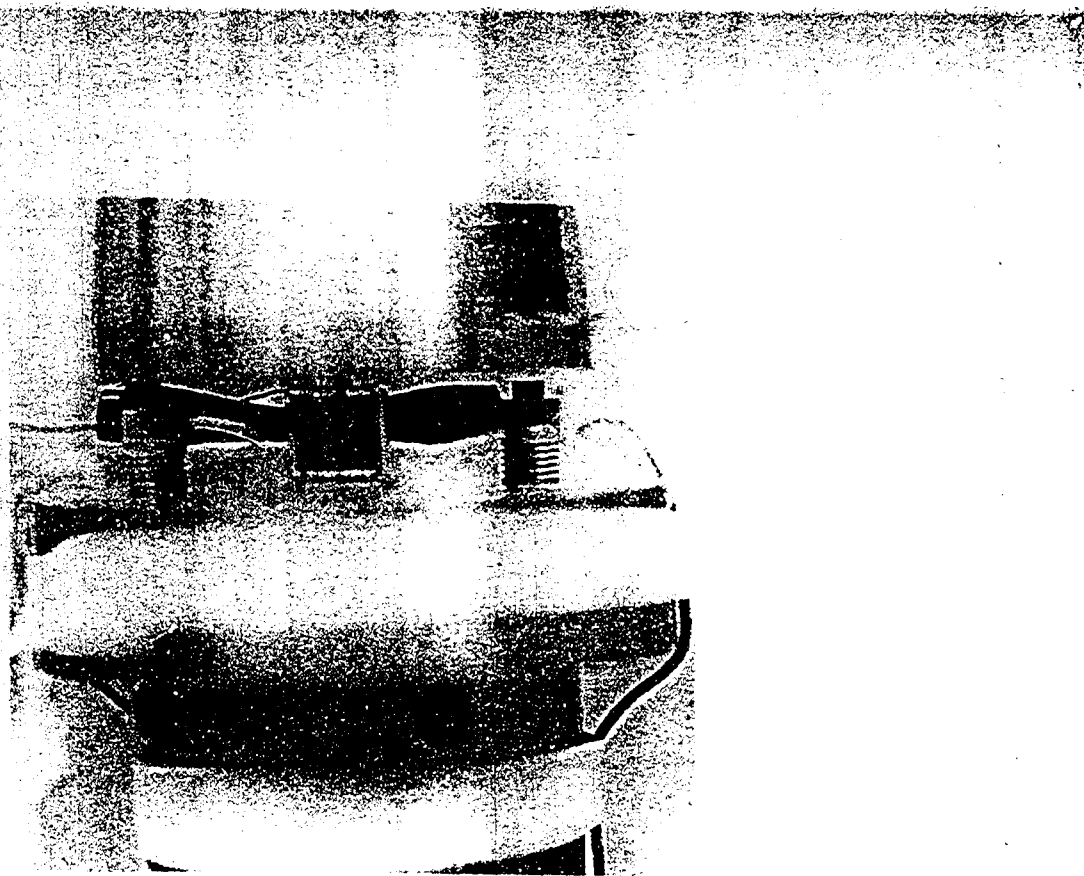


Figure 2-50. Ten-Disc Generator Stack in Place for Parametric Tests

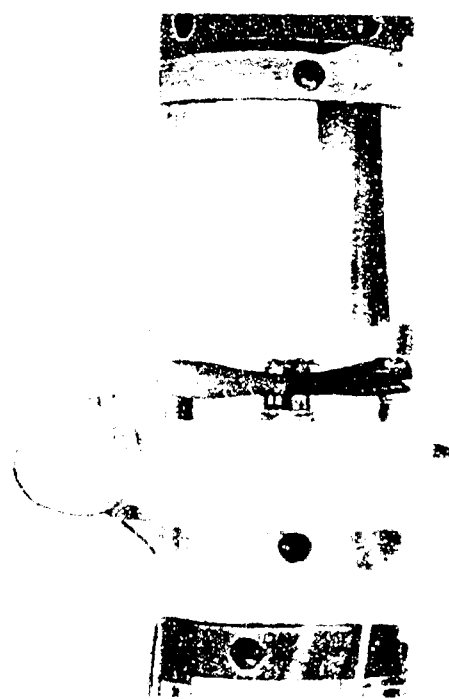


Figure 2-51. Parametric Test Rig Configuration

2.4.3.2 Parametric Test Results

All parametric tests were run with peak stress levels of 9000 psi, and were preloaded to achieve minimum stress levels of 5000, 3000, and 1000 psi. These varied conditions resulted in respective stress swings of 4000, 6000, and 8000 psi. Load resistances were varied over a wide range and inductance was varied around the expected optimum. Highlights of the test results are summarized in Table 2-5. The data in Table 2-5 is for operation at the optimum load inductance for each stack and load resistances of 60K and 80K as noted. This improves efficiency substantially above the maximum power transfer condition at a load resistance of 40K. The effects of varying load resistance and inductance on power density and efficiency for the different stress swings are shown in Figures 2-53 through 2-57. Efficiency of the optically lapped stack was very close to 50% in each case where the power output reached a maximum value, or the load resistance was equal to the internal resistance of the stack. The breadth of the maximum power peak and amount of data prevent an accurate assessment of exactly where the peak occurs, but the efficiency is clearly not far below 50%, which shows there are only small mechanical losses within discs and at interfaces. For the standard lapped stack in Figure 2-54, peak power occurs for a load resistance of 20K to 30K. The efficiency in this range varies from 32% to 40%. Since the electrical efficiency at this operating point is 50%, the reduced efficiency is caused by mechanical losses within the stack.

Table 2-5
SUMMARY OF PARAMETRIC TEST RESULTS AT 60 HZ WITH
OPTIMUM LOAD INDUCTANCE

Stack Type	Peak Stress (psi)	Stress Swing (psi)	Load Voltage (volts)	Load Current (ma)	Stack Temp (°F)	Stack Temp (°C)	Effective Modulus (psi)	Efficiency (%)	Power Density (w/in. ³)
Standard	9000	4000	141	1.76			5.22×10^6		3.08
Lap	9000	6000	205	2.56			4.99×10^6		6.52
L 115 H	9000	8000	273	3.41	95.0/69.6	4.41	4.41×10^6	53	11.3
R _L 80K									
Optical	9000	4000	168	2.10			4.98×10^6	81	4.39
Lap	9000	6000	211	3.52			6.67×10^6		9.23
L 135 H	9000	8000	314	3.93	95.2/69.8	5.18	5.18×10^6	74	15.3
R _L 80K									

*R_L = 60K

**Ideal material modulus = 9.35×10^6 psia at Short Circuit
Ideal material modulus = 18.4×10^6 psia at Open Circuit

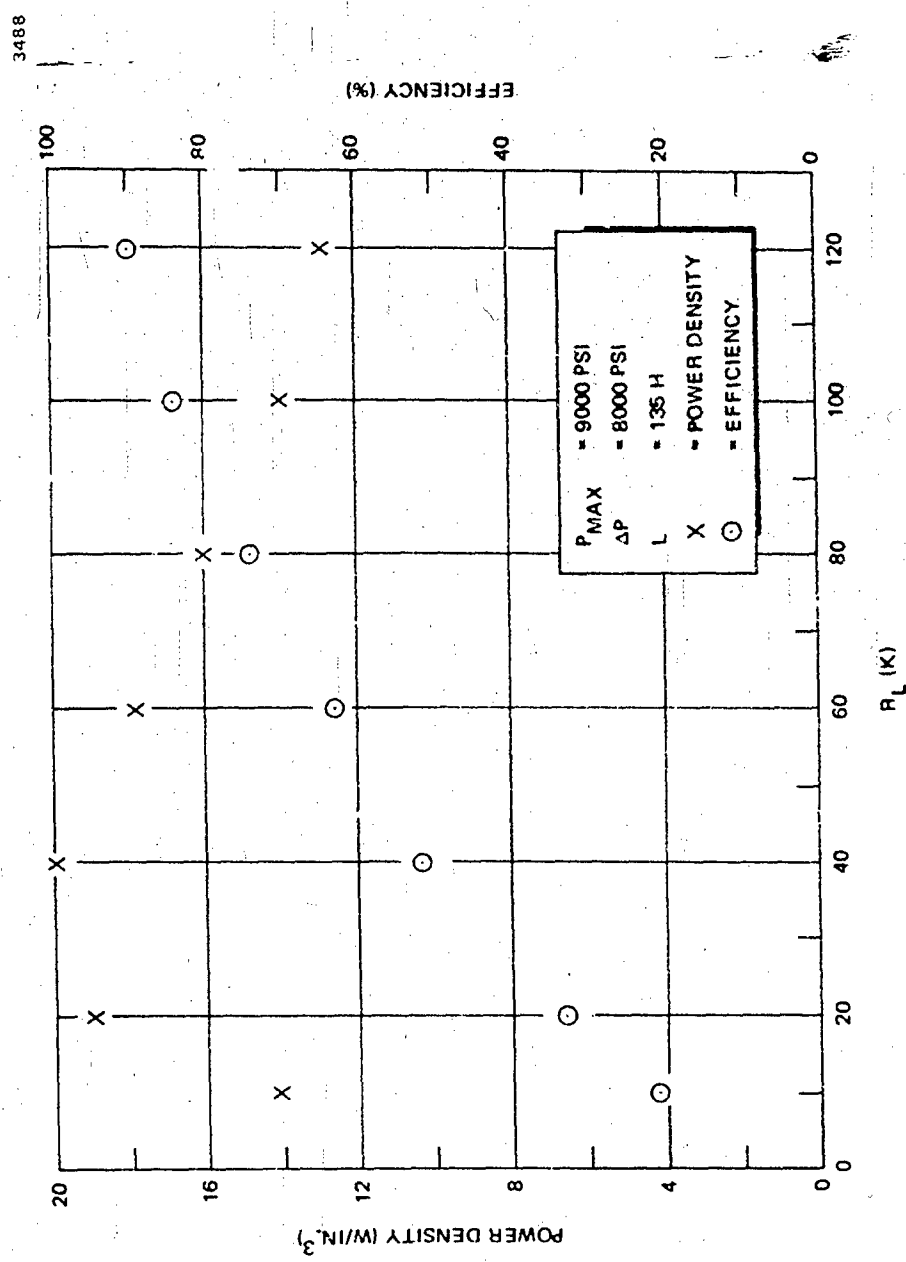


Figure 2-52. Performance Dependence on Load Resistance for Optically Lapped Stack

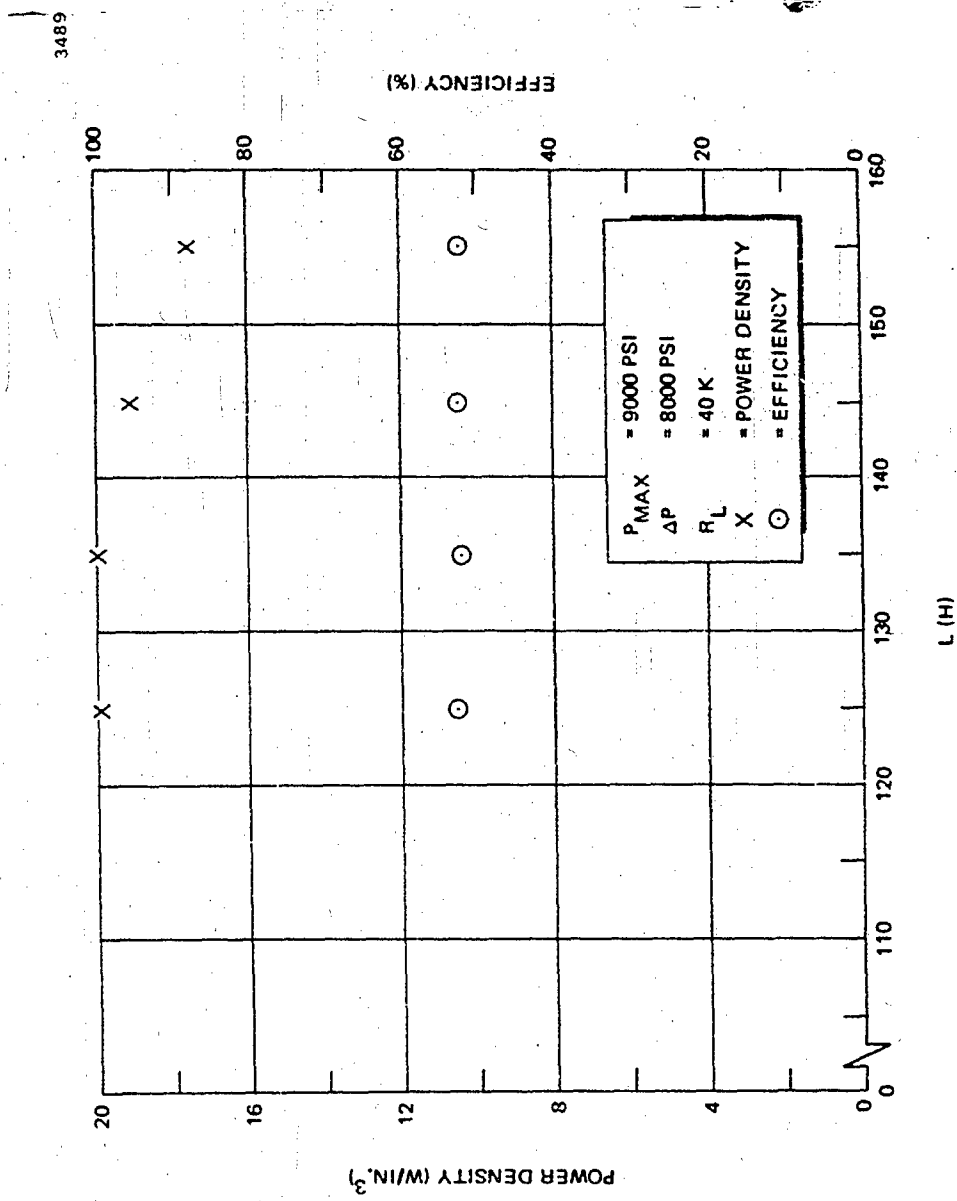


Figure 2-53. Performance Dependence on Load Inductance for Optically Lapped Stack

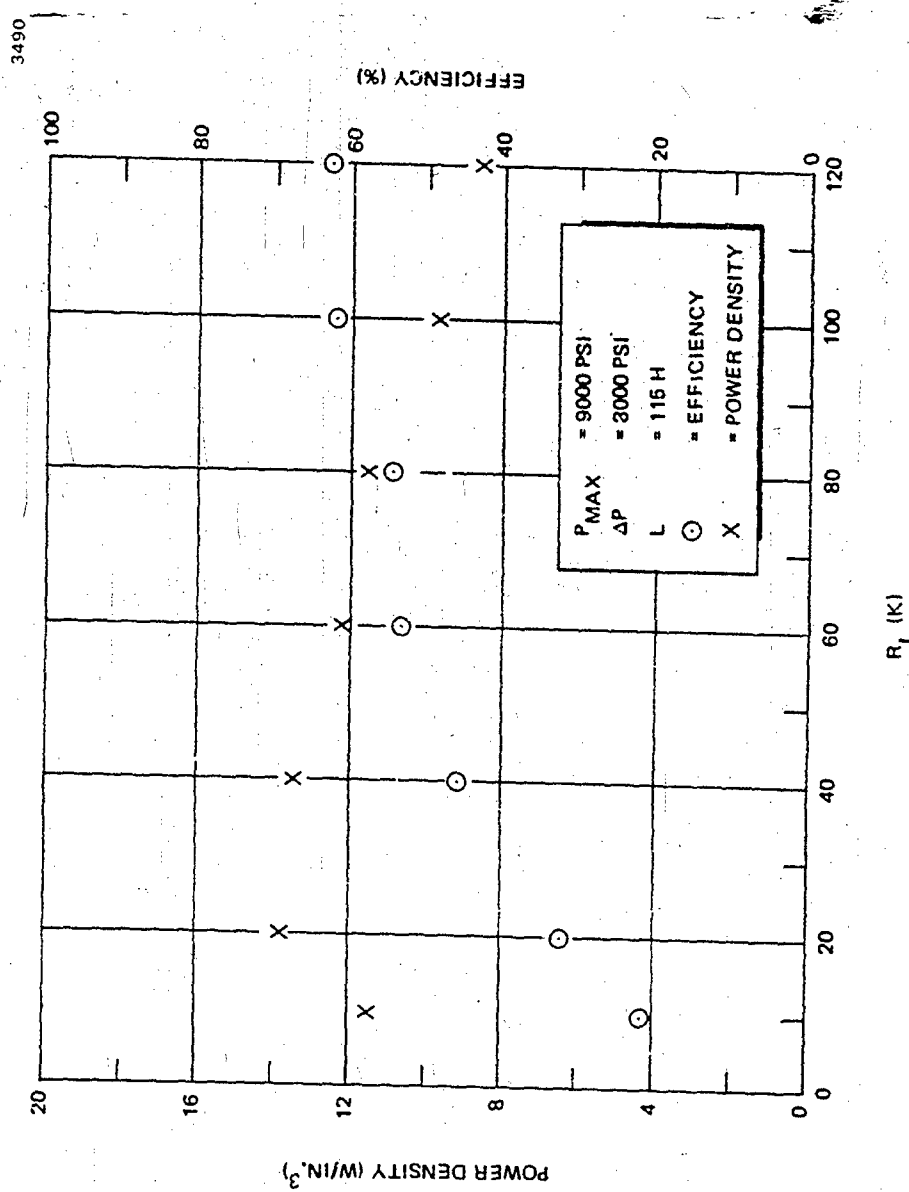


Figure 2-54. Performance Dependence Upon Load Resistance for Standard Lapped Stack

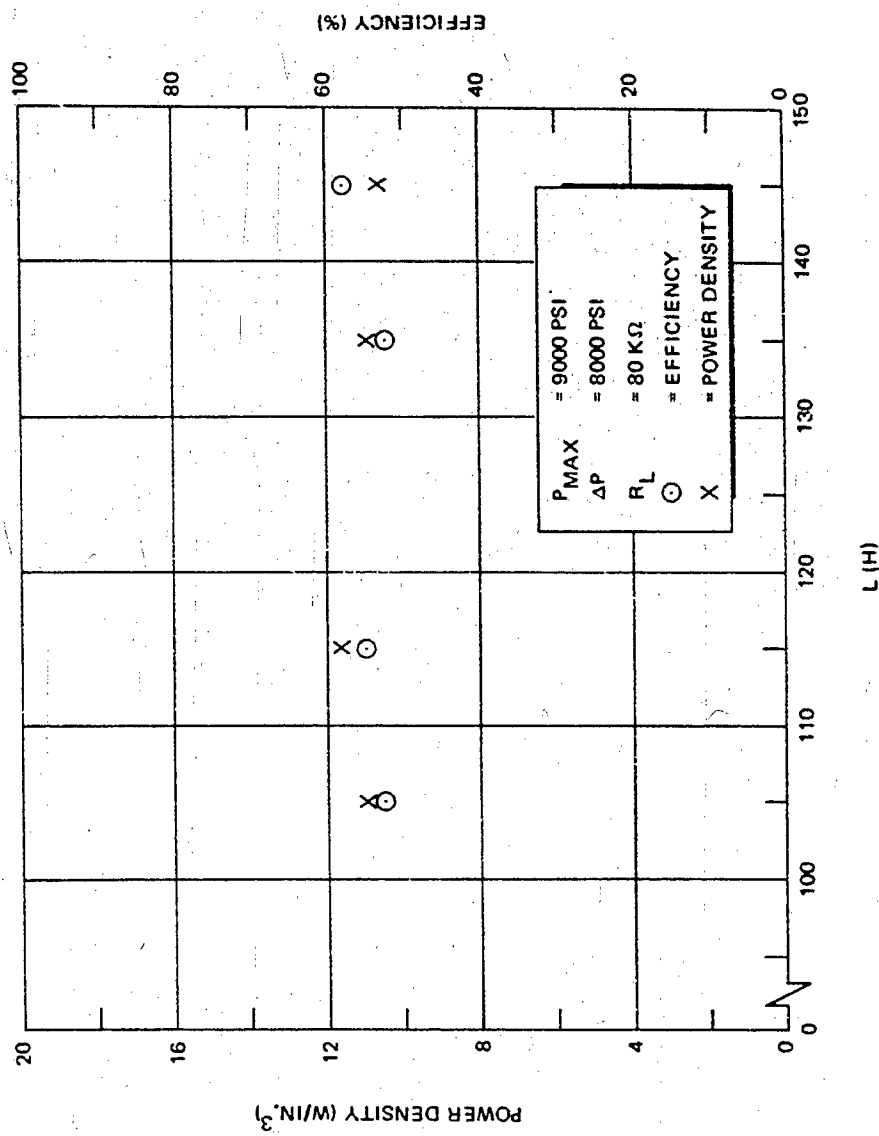


Figure 2-55. Performance Dependence Upon Load Inductance for Standard Lapped Stack

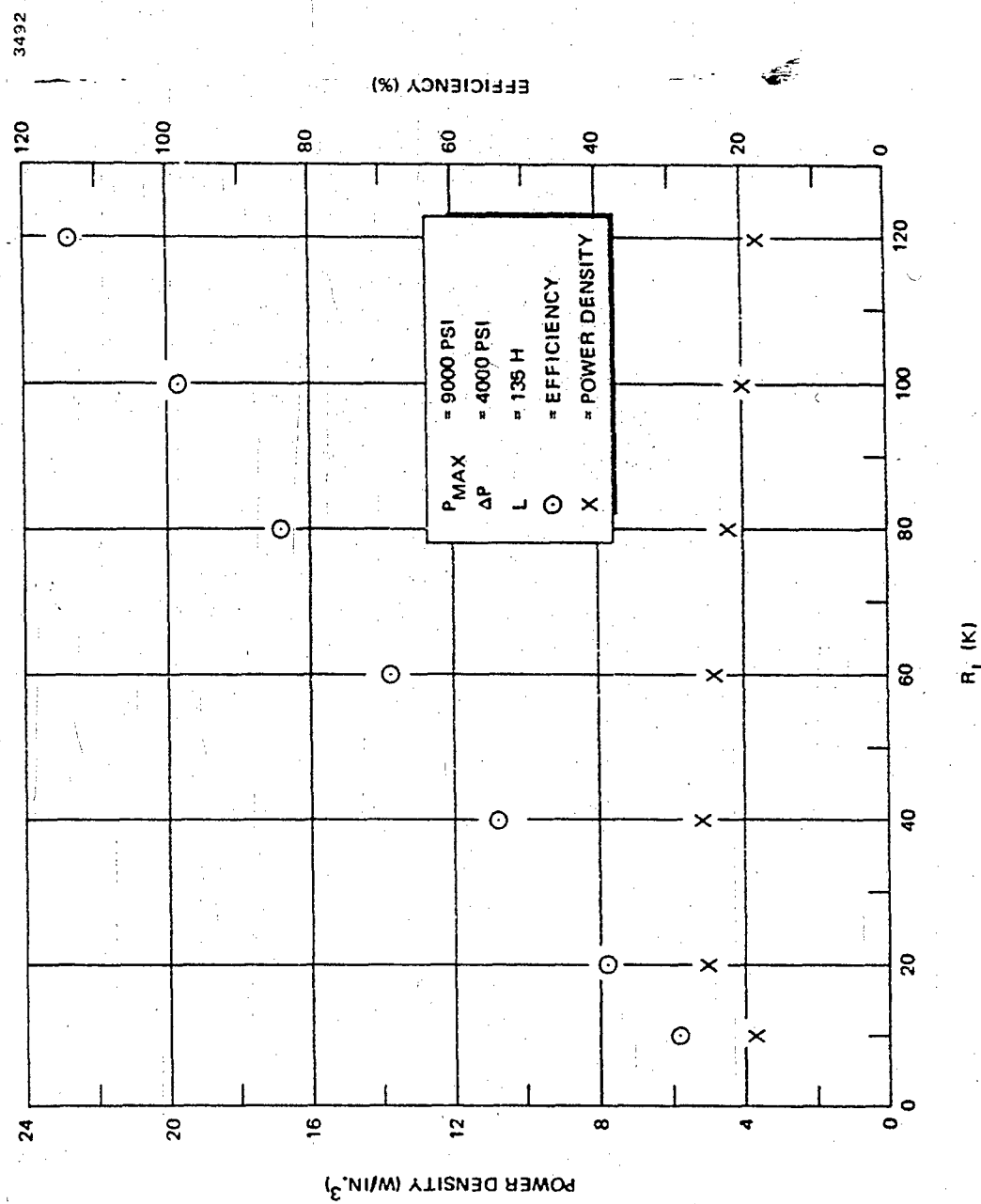


Figure 2-56. Performance Dependence Upon Load Resistance for Optically Lapped Stack

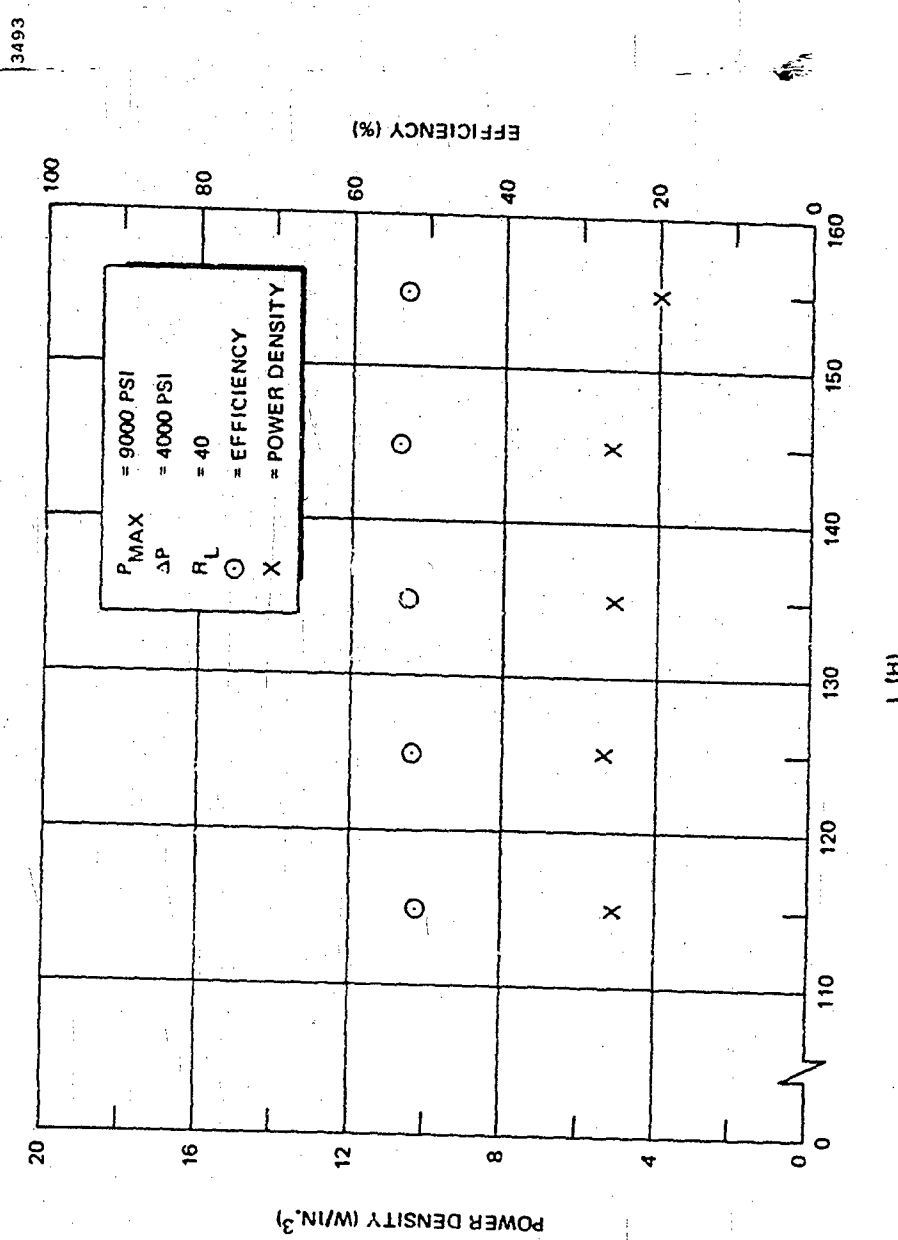


Figure 2-57. Performance Dependence on Load Inductance for Optically Lapped Stack

The efficiency range of 32% to 40% means that mechanical losses are between 50% and 112% of the electrical power actually delivered to the load. It is these substantial mechanical interface losses which cause the maximum measured efficiency of 63% in Figure 2-54 to be near the asymptotic limit.

2.4.4 Life Test Results

Life test conditions and test results are summarized in this section.

2.4.4.1 Operating Conditions

Electric excitation of the life test fixtures was initiated as each assembly was completed. Varying amounts of time were spent at relatively low input voltages to provide stack conditioning. Emphasis was on initiating life testing of all units as early as possible, and complete instrumentation was not added to all units until some had accumulated several hundred hours. A brief summary of accumulated times at various conditions is reported for each stack in Table 2-6.

Normalized power density and efficiency are plotted for the operational times of the life test, as appropriate to each stack, in Figures 2-58 through 2-61. Life test hours do not necessarily agree with total accumulated hours in Table 2-6, since the life test hours were only counted from the time when full stress was applied to the stack at the specified environmental condition. No life test plot is shown for stack No. 3 because it was physically damaged prior to installation of full instrumentation for making efficiency measurements. The normalization factor used in this data presentation was to divide output power density by the square of the developed stress swing. This accounts for variations in applied stress swing as a result of different driver voltages or reducing the number of driven stack segments when short circuits developed. The quadratic dependence corresponds to the simple theory in Appendix B, and correlates well with measurements over a wide range of conditions.

Both power density and efficiency of the IRAD stack exhibit erratic behavior over the period from about 900 to 1200 hours into the life test (Figure 2-58), including some efficiency measurements above 100%. The actual variations in power density over this period are only on the order of 7%, although these are somewhat magnified by the use of an expanded scale. The efficiency variations are much more severe, however, and suggest a temporary error in instrumentation calibration or utilization. The circles and triangles represent efficiency as measured by the two proximitors on both sides of the stack. Except for the erratic data, the correlation between the two proximitors was generally good, indicating very little tipping of the proximitor mounting plate or reference plate. The long-term trend in normalized power density for the IRAD stack shows less than a 5% reduction. The efficiency trend was essentially flat.

Table 2-6
SUMMARY OF LIFE TEST RESULTS THROUGH 7 SEPTEMBER 1973

Stack No.	Environmental Condition	Power Density (w/in. ³)	Operating Time (hr.)	Driver Stack Peak to Peak Voltage (v)	Peak Stress Level	Stress Swing	No. of Cycles (millions)
1	Ambient	2.86	360	400-2200	5370-6749	554-3312	77.8
	16° F	0.645-1.52	2523	2000-2200	8671-9206	2880-3279	318.0
	10° F	0.168-0.326 ⁴	120	600-1400	8424-9928	717-1091	25.2
	<-25° F	1.28-1.44	299	2200	8990-28029	2571-3109	21.4
2	Ambient	2.86	138	200-1600	8562-9000	354-3111	29.8
	16° F	2.23-2.82	1986	2000-2200	8697-9104	3475-4112	429.0
	<-25° F	2.82-3.04	99	2200	8010-8447	4081-4159	21.4
	150° F	1.77-2.48	349	2200	8670	341-5343	75.4
3	Ambient	2.86	360	400-2200	5370-6749	554-3312	77.8
	16° F	0.645-1.52	2523	2000-2200	8671-9206	2880-3279	318.0
	10° F	0.168-0.326 ⁴	120	600-1400	8424-9928	717-1091	25.2
	<-25° F	1.28-1.44	299	2200	8990-28029	2571-3109	21.4
4	Ambient	1.288	138	200-1600	8308-9699	278-2279	29.8
	150° F	0.22-0.37	2028	1800-2200	8787-9100	1624-1758	438.0
	150° F	0.71-0.77	172	2200	8804-8855	2683-2741	37.2
	Ambient	1.288	2338	1800-2200	8534-9187	6024-7577	505.0
IRAD	Ambient	6.66-10.1	2792	1800-2200	8534-9187	6024-7577	693.1
	Ambient	4.87-6.46	326	1200-1800	8672-8847	4016-5898	70.4
	Ambient	2.18 ⁵	220	400-1000	8804-8956	1120-3489	17.5
44	Ambient	1.288	338	1800-2200	8534-9187	6024-7577	721.0

Contract generator stacks connected to loads of $L_1 = 175$ H and $R_L = 120$ k Ω except as noted.

IRAD generator stack connected to load of $L_1 = 840$ H and $R_L = 540$ k Ω except as noted.

⁴ At 455 H, $R_L = 278$ k Ω ; or $L_1 = 980$ H, $R_L = 258$ k Ω .

⁵ Generator stack shorted.

44. $L_1 = 210$ H, $R_L = 270$ k Ω .

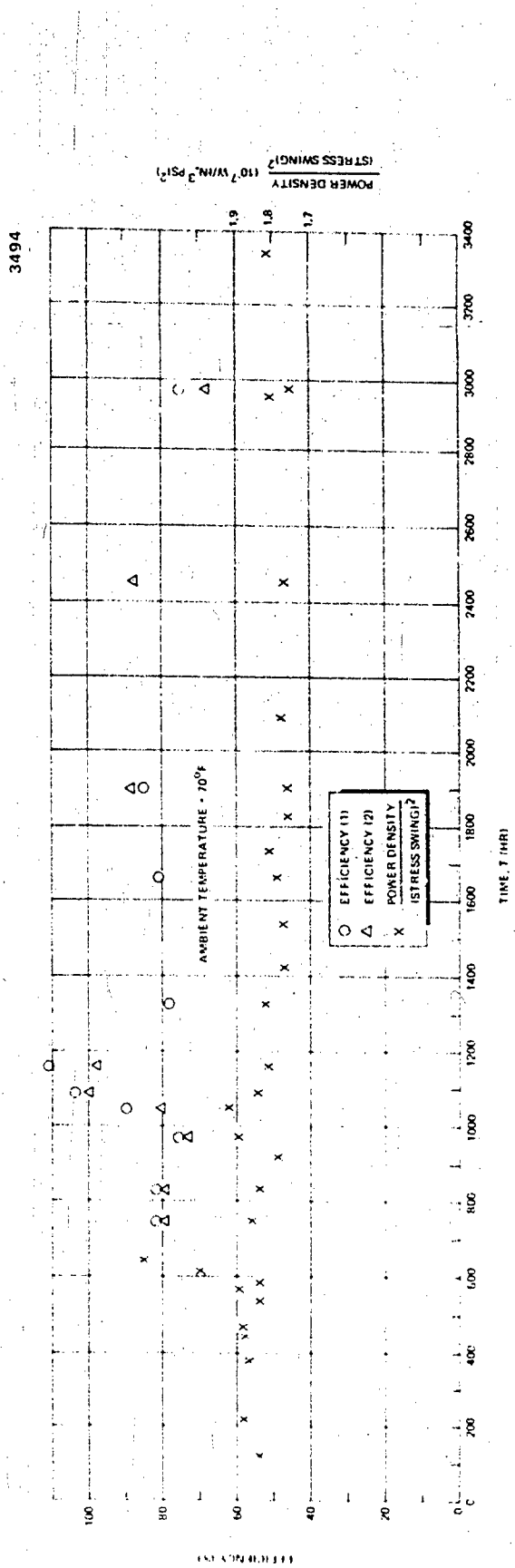


Figure 2-58. IRAD Stack Efficiency and Normalized Power Dependence on Elapsed Time

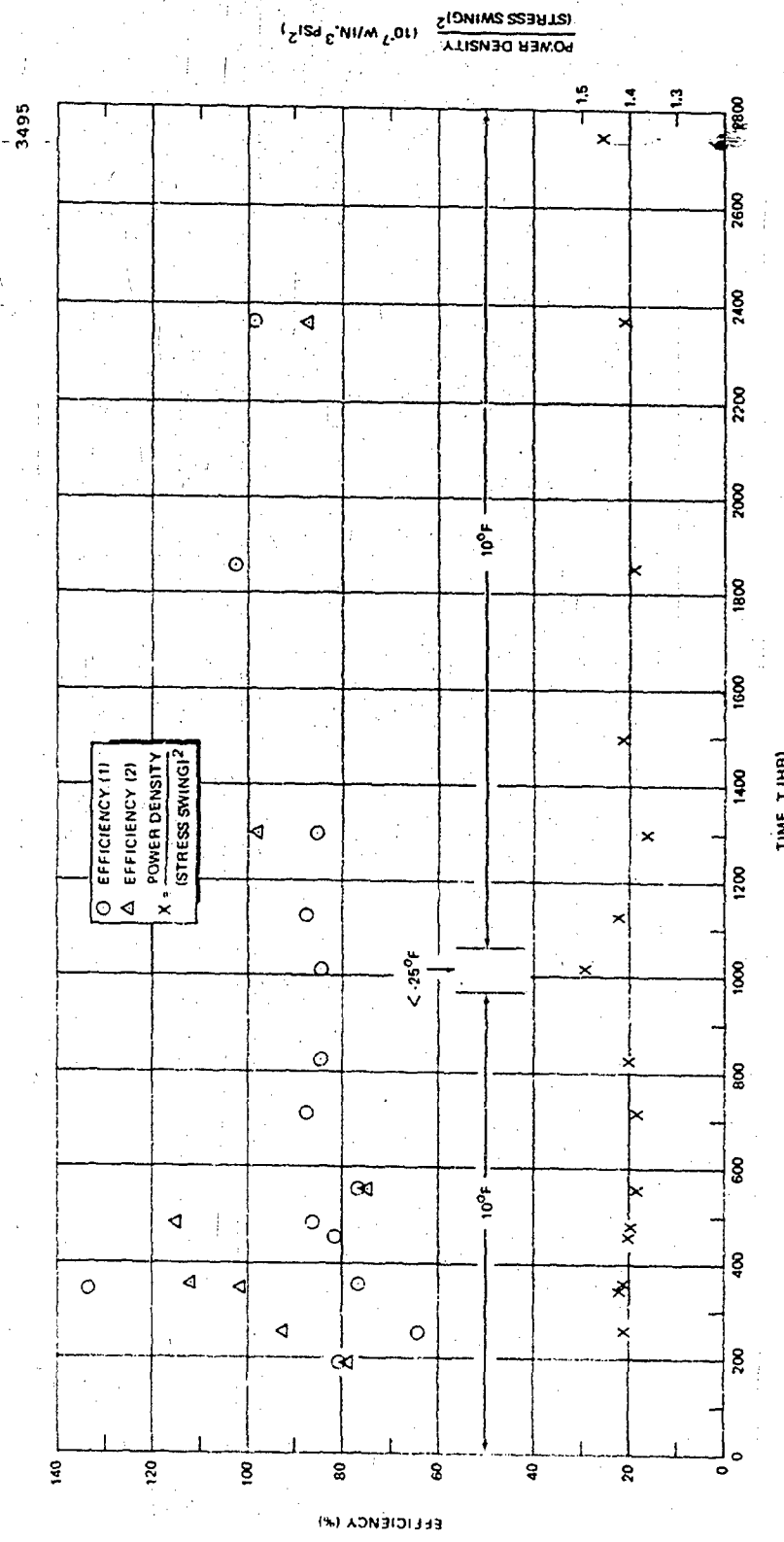


Figure 2-59. Stack No. 1 Efficiency and Normalized Power Dependence on Elapsed Time

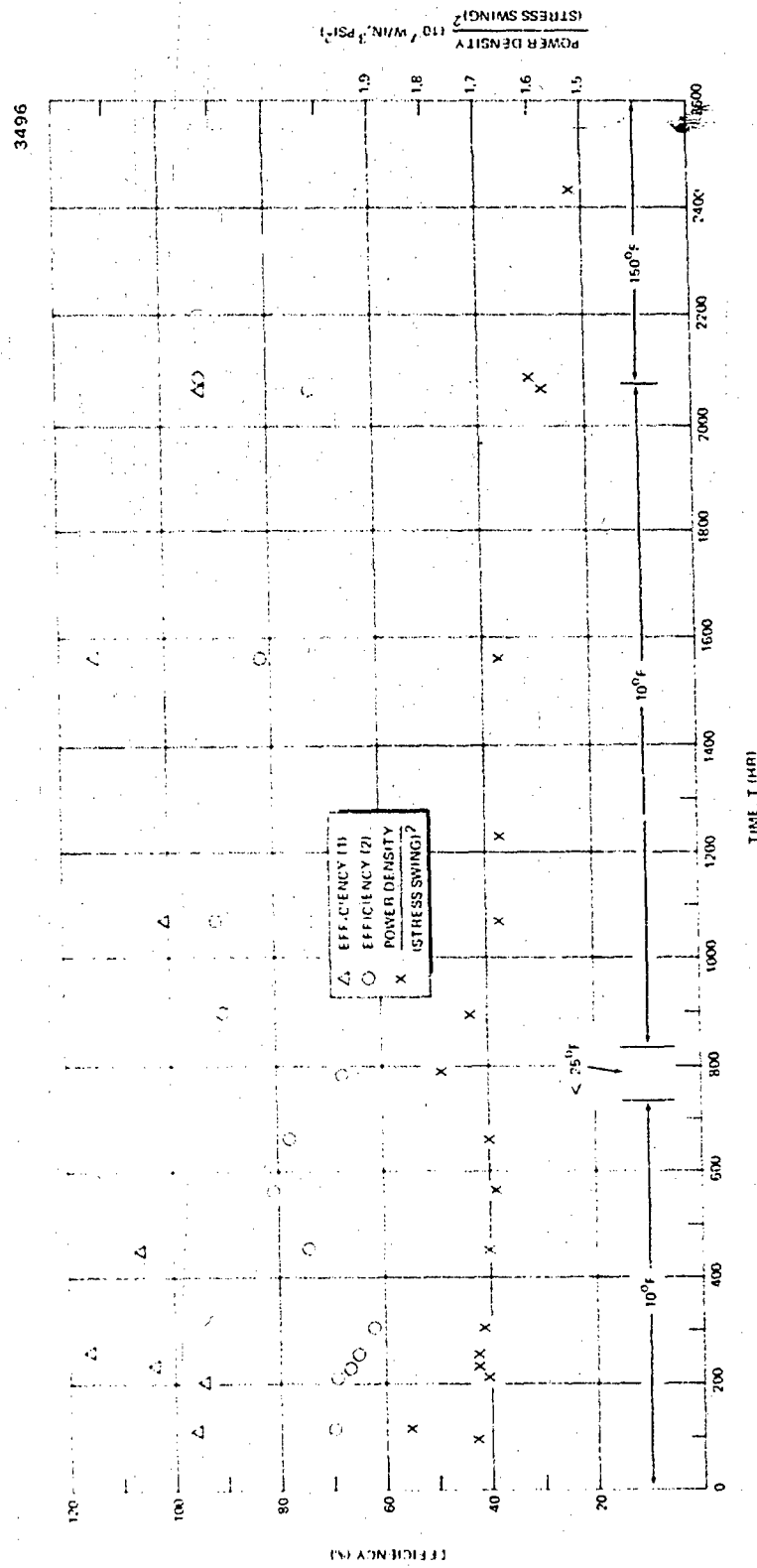


Figure 2-60. Stack No. 2 Efficiency and Normalized Power Dependence on Elapsed Time

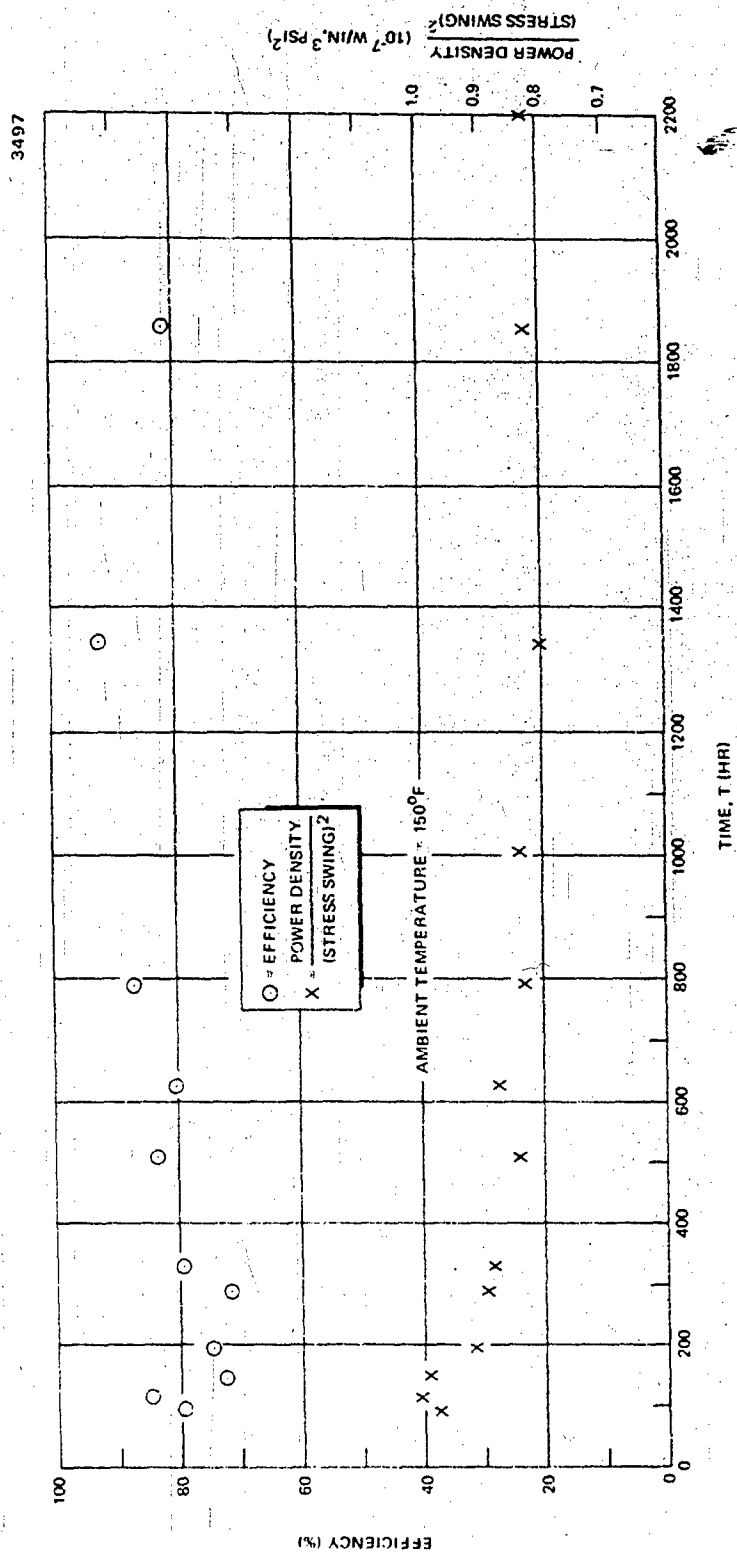


Figure 2-61. Stack No. 4 Efficiency and Normalized Power Dependence on Elapsed Time

Freezer Stacks No. 1 and 2 (Figures 2-59 and 2-61, respectively) again showed quite stable power output, with scatter in the efficiency data. The increased power density at about 1000 hours for Stack No. 1 and 800 hours for Stack No. 2 are real effects associated with decreasing the ambient temperature below -25°F. The normalized power density for the lapped stack is about 23% greater than that for the standard stack. Power density in Figure 2-61 again shows about a 35% decrease for the standard oven stack as compared with the standard freezer stack, verifying the power density trend indicated by subcooling the freezer stacks. As an additional check on temperature sensitivity, Stack No. 2 was transferred to the oven after 2085 hours in the freezer. Power density decreased rapidly for the first few hours of operation at 150°F, then stabilized. The overall reduction in power density was about 35% after 340 hours in the oven, although a reduced stress swing resulted in only a 10% reduction in normalized power density. No electrical breakdown was observed, substantiating the theses that the breakdowns which occurred during initial operation of Stack No. 4 at 150°F were a result of specific stack processing problems rather than a function of the elevated temperature. A significant trend toward power density degradation is shown for the oven stack (Figure 2-61) where the normalized power density decreased about 15% in 800 hours, then remained essentially constant.

The scatter of efficiency data (Figures 2-59 and 2-60) for the two proximitors indicates that, in contrast to the IRAD stack, considerable tipping of the mounting plate for the proximitors or reference screws was occurring. Similar relationships between the two proximitors on each stack were usually maintained, but in some instances the tipping effect appeared to reverse. This could have been caused by minor position changes occurring when the preload was reduced for data collection. The general efficiency trends (Figures 2-59 to 2-61) range from essentially constant to a modest increase in efficiency with accumulated operating lifetime.

Section 3 CONCLUSIONS

As a result of the testing, analysis, and mechanical design effort during the contract period, the following conclusions can be derived with respect to the STEP% concept.

1. Piezoelectric generator life tests demonstrated a power density of 10 watts/in.³ with 80% efficiency at about 7500-psi stress fluctuation, at which level less than 5% degradation occurred during 3000 hours of operation at 60 Hz. Successful operation was demonstrated at temperatures from -55°F to +150°F. Significantly better performance was achieved with optically lapped piezoelectric discs than with standard discs. Extensive processing and clean room handling of discs was used in the life test assemblies, but the degree of cleanliness required for successful operation was not firmly established.
2. Development of a sophisticated dynamic simulation detailing the STEP% system with more realism than previous computer programs, used successfully by DWDL for modeling actual engines, leads to a high degree of confidence in the analytical projections. Projected performance is, in general, encouraging although the highly resonant operation makes the system sensitive to load changes. A nearly constant net load will probably be required.
3. Extrapolations of successful hardware approaches to higher operating pressures and bearing loads involve reliable engineering design techniques. This provides confidence in the soundness of the mechanical design of this engine. The mercury coupler is straightforward in concept, but does utilize unique features. Recent related experience with corrugated metal diaphragms in a conceptually similar system has revealed operational problems which raise questions with regard to system safety for the mercury coupler.

Section 4
REFERENCES

1. H. Minchenko. High-Power Piezoelectric Transducer Design. IEEE Transactions on Sonics and Ultrasonics, Vol SU-16 No. 3, July 1969, Sonic Power Laboratory, Department of Welding Engineering, Ohio State University, Columbus, Ohio.
2. R. B. Goranson, et al., Development of a Simplified Stirling Engine to Power Circulatory Assist devices. Third Intersociety Energy Conversion Conference Proceedings, p. 733, August 1968.
3. M. L. Albertson, J. R. Barton, and D. B. Simons. Fluid Mechanics for Engineers. Prentice Hall, Inc., 1960, p 288.
4. H. Schlichting. Boundary Layer Theory. McGraw-Hill, Inc., New York, 1960, p 503.
5. Clevite Catalog No. 695. Piezoelectric Technology Data for Designers. Clevite Piezoelectric Division, Bedford, Ohio, 1965.
6. S. Timoshenko. Vibration Problems in Engineering. Third Edition, 1955, D. Van Nostrand Company, pp 158-163.
7. P. Smiley. Development of a Piezoelectric Driver for a Ventricular Assist Device. National Heart and Lung Institute Report No. Ph43-67-1115-1, October 1972, pp. 39-40.
8. L. V. Feigenbutz et. al. A Stirling Engine Approach to an Implantable Heart-Assist System. Eighth Intersociety Energy Conversion Conference Proceedings pp. 441-448, August 1973.

Preceding page blank

Appendix A
PHYSICS INTERNATIONAL REPORT
PIEZOELECTRIC GENERATOR TESTS

ABOUT THIS APPENDIX

Appendix A consists of two reports submitted by Physics International Company to document their efforts on the sub-cont. a to test piezoelectric generator performance. The original report discusses results and conclusions of the tests with an electrical circuit analysis of piezoelectric generator operation. The supplementary report provides additional background information, analysis, and a tabulation of test data. Certain areas of analysis and conclusions are based on preliminary and incomplete information, but are included here without comment. More extensive testing and analytical development has since been performed by DWDL and is reported in Appendices B and C.

Preceding page blank

SUMMARY AND CONCLUSIONS

Two piezoelectric generators (stacks of piezoceramic discs) were tested by driving them hydraulically up to 12,400 psi compressive stress at fluctuations of 60 Hz. The first generator consisted of 5 cubic inches of PZT 5-H material, a ferroelectrically "soft" ceramic; the second consisted of 0.8 cubic inches of LTZ-1, a ferroelectrically "hard" ceramic.

The PZT 5-H generator produced electrical power as predicted up to stresses of 5000 psi, but the piezoelectric properties were degraded when the stresses exceeded 5000 psi. The output at 5000 psi was 6 watts per cubic inch of PZ material.

The LTZ-1 generator produced approximately 9 watts per cubic inch at 9700 psi.

Data above 9700 psi was invalid because of excessive friction in the hydraulic seal.

It is concluded that 16 to 20 watts of electrical power per cubic inch of PZ material can be extracted with greater than 90-percent efficiency. This estimate is made by a small extrapolation from 9700 psi to 12,000 to 14,000 psi.

SECTION 1

INTRODUCTION

This report covers the experimental work performed to determine power-density limitations of a piezoelectric power generator driven hydraulically at low frequency (60 Hz).

The tasks to be performed were:

1. Design and fabricate a hydraulic system capable of driving a stack of 100 PZ discs, each 1.25 inch in diameter by 0.040 inch thick, with pressure pulses of 60 pulses/min. at zero to 14,000 psi compressive stress.
2. Build a stack of 100 PZT 5-H discs and install into an existing housing.
3. Test PZT 5-H generator up to 14,000 psi or to its limiting stress.
4. If PZT 5-H is not satisfactory up to the required stress, test a second material with a higher stress rating.

1.1 CHOICE OF PZ MATERIALS

Table 1 shows piezoelectric properties for several PZ materials from various manufacturers. The power output for a PZ generator with a pure resistance load matched for maximum power transfer is given by

$$W = \frac{\omega}{16} d_{33} g_{33} \sigma^2 v_{pz}$$

—where: W = electrical power, watts

ω = frequency, radians per second

d_{33} = PZ charge coefficient, $10^{-12} \frac{\text{coul/M}^2}{\text{N/M}^2}$

g_{33} = PZ voltage coefficient, $\frac{\text{volts/M}}{\text{N/M}^2}$

σ^2 = compressive stress N/M^2

v_{pz} = volume of PZ material, M^3

This expression is derived in the appendix.

In Table 1, the product of $d_{33} g_{33}$ is used as a figure of merit for PZ materials with respect to power output. Note that PZT 5-H and LTZ 2-H have the highest output coefficient. However, stability of the piezoelectric properties of a material in the operating environment is also important. The Curie temperature and the coercive field have a bearing on this stability. PZ properties become unstable as the temperature approaches this Curie point. The coercive field, E_c , is the electric field that will cause the material to reverse its polarization. Thus it is more difficult to change the polarization of a material with a high E_c than one with a low E_c . Vernitron, Inc., recommended a maximum compressive stress (cycled) parallel to the polar axis for each of its materials. Note that the rated stress for PZT 5-H is 2500 psi, compared to 12,000 psi for PZT-4. Note also that the internal losses, are lower for PZT-4.

From Table 1 it can be concluded that of the commercially available PZ materials, the ferroelectrically "soft" materials such as PZT 5-H and LTZ 2-H give the highest output at a given value of stress fluctuation; and the ferroelectrically "hard" materials will withstand higher compressive stresses without their piezoelectric properties being degraded. The hard materials are also less lossy than the soft materials. Physics International has fabricated experimental piezoelectric materials that appear to have high output, high Curie temperature, and high coercive field. These materials have not yet been fully characterized, but would be worth testing in a generator.

Power transfer is greater when the capacitive impedance is balanced by an inductive impedance rather than a pure resistance load as shown below (referring to Figure 1):

$$W = \frac{E_q^2}{Z^2} R_L$$

or, when

$$W = \frac{E_q^2 R_L}{(Z_C - Z_L)^2 + (R_S + R_L)^2}$$

the power, W , is maximum when Z is minimum or when $Z_C = Z_L$.

1.2 EXPERIMENTAL APPARATUS

A schematic of the hydraulic system and PZ generator is shown in Figure 2. Basically, the PZ generator is alternately

connected to a hydraulic pressure source and to a vent with every half rotation of the rotary valve. The system was designed to use on-hand hydraulic components wherever possible. The rotary valve, however, was fabricated for the test. A Vickers axial piston pump with a displacement of 0.065 cubic inches per revolution was driven at 3450 rpm to supply hydraulic pressure. The pressure in the generator was monitored with a Kistler 607L pressure transducer. Hydraulic fluid was stored in an accumulator close to the rotary valve to provide fast pressurization of the generator. The schematic of the generator equivalent circuit and the output circuit is shown in Figure 1. The inductor is used to match the impedance of the generator's capacitive impedance. Electrical power output was determined by measuring voltage across the load resistors.

SECTION 2

RESULTS

2.1 PZT 5-H MATERIAL

The data plotted in Figure 3 show the hydraulic power as a function of compressive-stress fluctuation on the PZT 5-H stack. The numbers indicate consecutive runs. Power output generally decreased with each run.

After run 5, the stack was repolarized with 2-kV pulsed dc at 2 pulses per second. Run 6 showed a higher output than run 5, but the output was still lower than run 1. The power reached 30 watts at 6600 psi and then dropped to 26 watts as the stress fluctuation was raised to 9300 psi. When the stress fluctuation was reduced to 4400 psi, the power was 13 watts, compared to 20 watts for the same stress fluctuation at the start of the run.

The projected curve was obtained by extrapolation from earlier tests at stresses up to 3500 psi on a similar stack. The power output exceeds the projected curve for stress fluctuations up to a stress level of 5000 psi. For stresses above 5000 psi, power dropped below the projected curve. Data taken after the stack had been driven above 5000 psi showed lower power output. Power output could be raised by repolarizing the stack with dc voltage.

— 2.2 LTZ-1 MATERIAL

A second generator was built with 10 discs of LTZ-1 (1.25-inches in diameter by 0.040 inch thick), a material with more resistance to depolarization but with theoretically lower output at a given stress. A 0.125-inch-thick disc of the same material was placed at each end of the stack to reduce shear stresses produced by the Poisson's ratio effect of the steel parts at the ends of the stack.

Power output of the LTZ-1 generator is shown as a function of applied stress fluctuation (Figure 4). Data points are shown for seven runs. The last data point taken was 7 watts at 9700 psi. Two curves are drawn through the data points to cover the spread of the data. The curves are extrapolated to 12,000 psi. The data is discussed in Section 3.

SECTION 3

DISCUSSION

3.1 PZT 5-H MATERIAL

Figure 3 indicates that PZT 5-H and probably other ferroelectrically "soft" materials cannot be driven to the stress considered for the STEPZ generator. This material did perform as predicted for short periods up to 5000 psi, which is twice its rated stress. Even at low-stress levels it was necessary to cool the stack with a cooling coil in the insulating oil. This material may be suitable for applications that require a short-duty cycle or one-shot power from a small package.

Notice that there is some scatter in the data that increased with increasing stress. There was a 0.013-inch-diameter clearance between the piston and housing. The O-ring seal tended to extrude into this gap even though there was a nylon backup ring. This could cause enough friction between the seal and the housing to explain the scatter, since all of the hydraulic force on the piston was not transmitted to the stack.

3.2 LTZ-1 MATERIAL

The LTZ-1 material (similar to PZT-4) showed no signs of losing its piezoelectric properties. Several runs were made, showing that the power output repeated after the material had been driven to high stresses. The data points in run 6 are numbered to show the order in which they were taken.

The following evidence supports the theory that the deviation of the data from the exponential power curve at stresses above 10,000 psi was due to a defect in the test apparatus rather than to degradation of PZ properties.

1. Marks on the piston and the housing indicated that the O-ring had extruded past the nylon backup ring into the 0.013-inch-diameter gap between the housing and piston.
2. During run 5 the output power shifted from the upper exponential curve, 6 watts at 7200 psi, down to 3.1 watts at 8800 psi. The subsequent four data points formed a distinct curve significantly lower than the exponential curves. However, the data in run 6, taken the following day, generally fall between the two exponential curves up to 9700 psi. The data above 9700 psi are lower and scattered. The last data point taken lies on the lower exponential curve, 7 watts at 9700 psi.

It is concluded that the lower power curve determined in run 6 is the result of the O-ring extruding into the gap between the piston and housing, causing the actual load on the stack to be significantly lower than that indicated by the hydraulic pressure on the piston. The scatter in run 5 is due to varied degrees of high friction caused by the extruding O-ring.

Assuming that the scatter in the data is due to seal friction, the output power at 12,000 psi, the maximum recommended stress for this material, would be 13 watts for 0.8 cubic inches of material. Thirty-eight percent of this material was in the two 0.125-inch-thick end discs. It is probable that the output would be greater if all the material were in 0.040-inch-thick discs. It is also probable that the material could be driven at higher stress than 12,000 psi. Therefore, it is estimated that 80 to 100 watts of power can be extracted from 5 cubic inches of LTZ-1 material.

3.3 GENERATOR EFFICIENCY

The efficiency of the PZT 5-H generator had been determined in an earlier experiment to be 70 percent. The power loss is considered to be divided into three mechanisms:

1. Electrical and mechanical losses in the material.
2. Losses due to friction between the PZ stack and the steel end pieces from radial expansion (Poisson's ratio effect).
3. Seal friction.

The PZ material loss is about 5 percent for PZT 5-H and about 1 percent for LTZ-1. It is estimated that seal friction is the greatest of the other losses. Therefore, it is estimated that generator efficiency greater than 90 percent can be achieved by replacing the O-ring with a metal diaphragm.

3.4 TEST APPARATUS

The rotary valve was designed and fabricated to drive the PZ generator for testing purposes. It became apparent during testing that the system had several limitations. The pressure applied to the stack was pulsatile rather than sinusoidal. At high pressures the system required a higher flow rate than the pump would produce. Therefore, a large air/hydraulic accumulator was necessary so that hydraulic energy could be stored for short runs. Also, the rotary valve became hard to start at hydraulic pressures above 2800 psi.

3.5 RECOMMENDATIONS

It is recommended that small stacks of Physics International's own materials be tested to assess their applicability in a PZ generator. It is also recommended that a longer stack of LTZ-1 material be tested in such a way that the limitations of the test apparatus do not effect the results.

A piezoelectric driver is quite satisfactory at low stresses, but at 14,000 psi the driver stack would have to be 3.5 times as long and twice the diameter of the driven stack.

It is also recommended that the hydraulic driving system be modified to overcome the difficulties encountered in this program. These modifications would include:

1. Using with a low-friction seal or metal diaphragm, a larger piston so that the required hydraulic pressure and seal friction are lower.
2. Modifying the ports in the rotary valve so that the pressure pulses would more closely represent a sine wave.

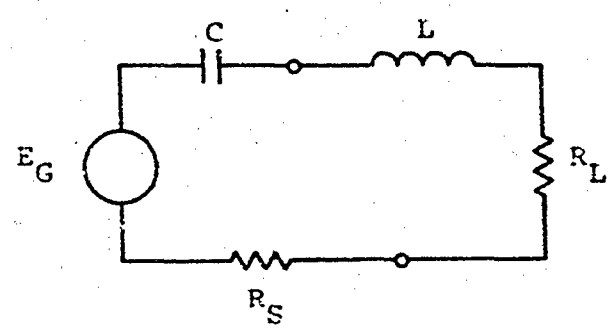


Figure 1 Equivalent circuit of a piezoelectric generator with matching induction and load resistor.

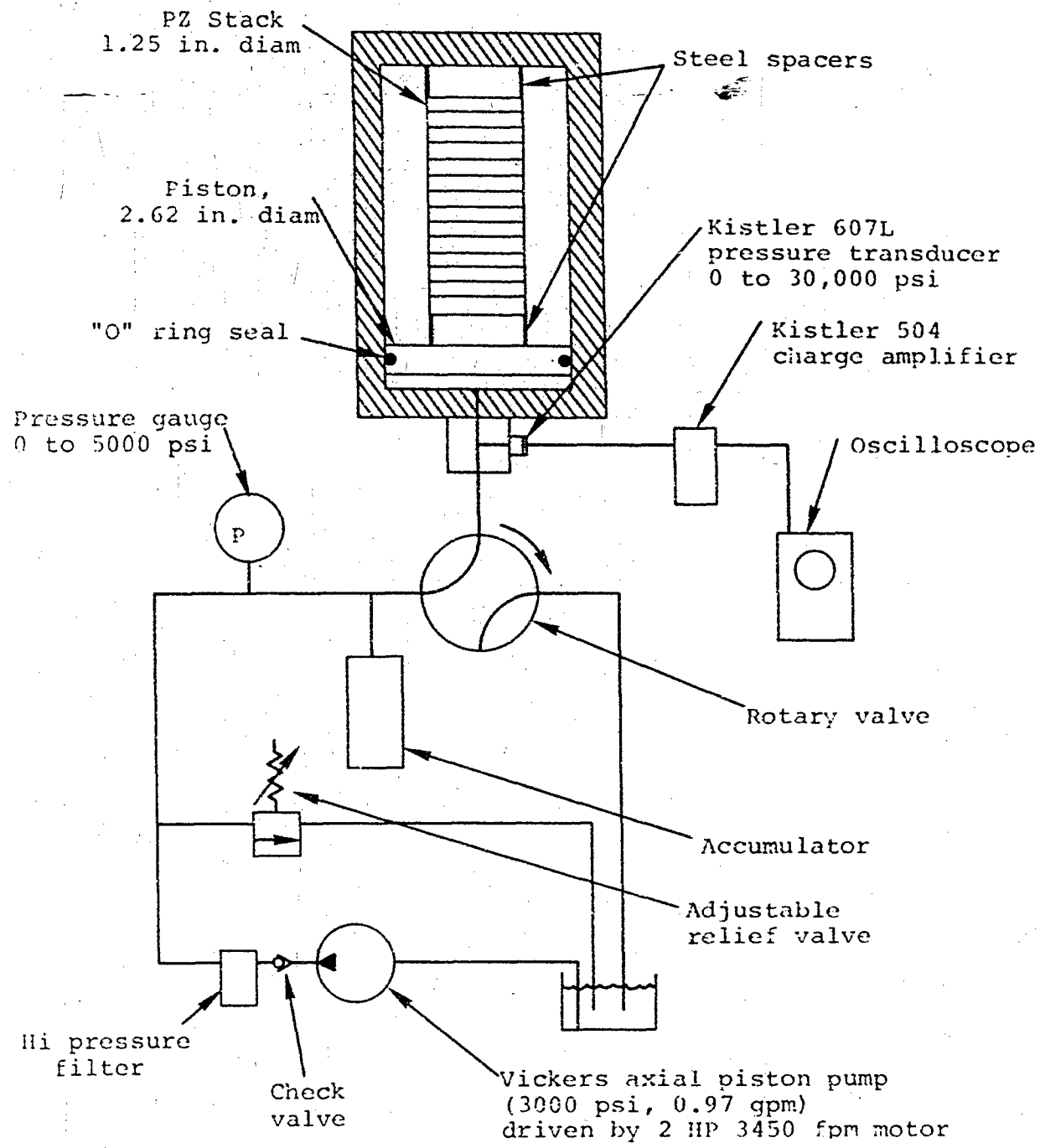


Figure 2 Schematic of PZ generator and hydraulic driving system.

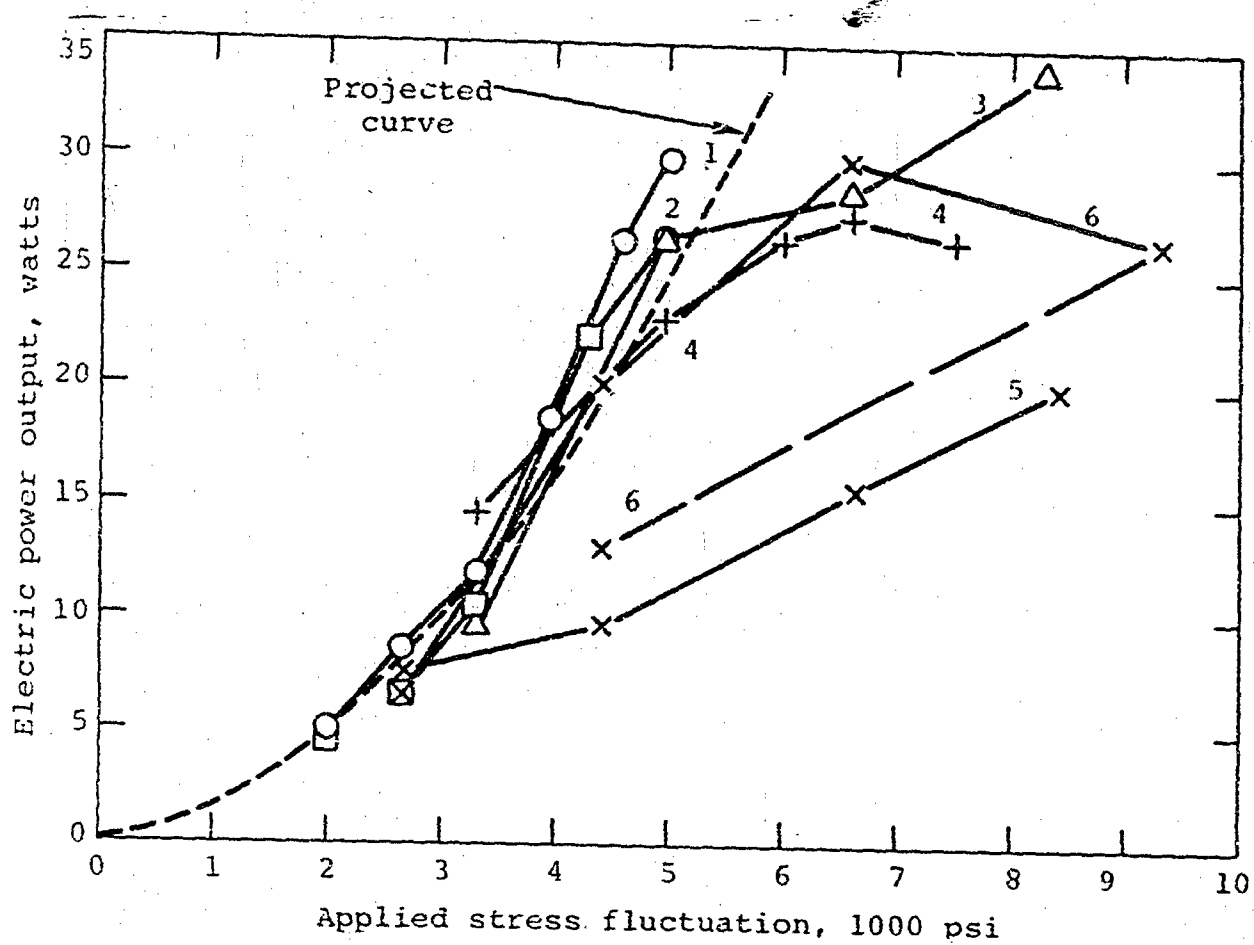


Figure 3 Output power of PZT 5H generator, volume of material: 5 in.³.

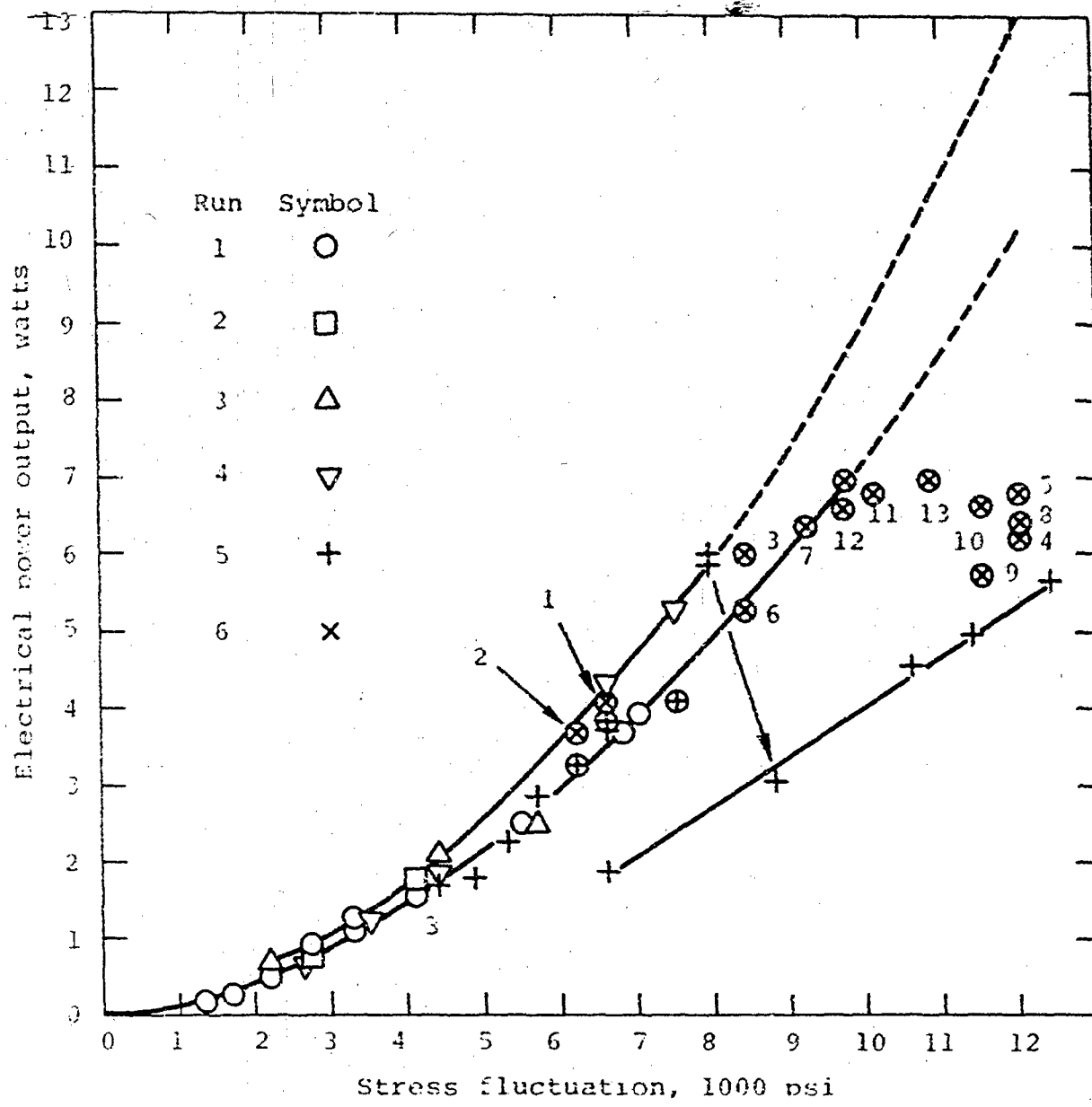


Figure 4 Output power of LTZ1 generator, volume of material: 0.8 in³.

PROPERTIES OF ELEMENTS IN THE PERIODIC TABLE
IN RELATION TO THEIR POSITION

TABLE I

Element	Electro-magnetic		Electro-chemical	
	Electro-magnetic	Electro-chemical	Electro-magnetic	Electro-chemical
Hydrogen	1.00	1.00	1.00	1.00
Helium	1.00	1.00	1.00	1.00
Lithium	1.00	1.00	1.00	1.00
Boron	1.00	1.00	1.00	1.00
Carbon	1.00	1.00	1.00	1.00
Nitrogen	1.00	1.00	1.00	1.00
Oxygen	1.00	1.00	1.00	1.00
Fluorine	1.00	1.00	1.00	1.00
Neon	1.00	1.00	1.00	1.00
Sodium	1.00	1.00	1.00	1.00
Magnesium	1.00	1.00	1.00	1.00
Aluminum	1.00	1.00	1.00	1.00
Silicon	1.00	1.00	1.00	1.00
Phosphorus	1.00	1.00	1.00	1.00
Sulfur	1.00	1.00	1.00	1.00
Chlorine	1.00	1.00	1.00	1.00
Argon	1.00	1.00	1.00	1.00
Calcium	1.00	1.00	1.00	1.00
Strontium	1.00	1.00	1.00	1.00
Boron	1.00	1.00	1.00	1.00
Phosphorus	1.00	1.00	1.00	1.00
Sulfur	1.00	1.00	1.00	1.00
Chlorine	1.00	1.00	1.00	1.00
Argon	1.00	1.00	1.00	1.00
Barium	1.00	1.00	1.00	1.00
Radium	1.00	1.00	1.00	1.00
Thorium	1.00	1.00	1.00	1.00
Uranium	1.00	1.00	1.00	1.00

APPENDIX

PZ GENERATOR EQUIVALENT CIRCUIT

An equivalent circuit for the PZ generator is shown in Figure A-1. If the value of the load resistor on the output is small compared to R_p , the circuit can be simplified to that shown in Figure A-2. Assuming the generator output is sinusoidal, the circuit equation in the frequency domain is:

$$V_G = I (R_L + R_S + Z_C)$$

$$\text{where } Z_C = X_C \tan \omega t = \frac{1}{\omega C} \tan \omega t$$

or

$$V_G = \frac{V_O}{R_L} (R_L + R_S + Z_C)$$

The output voltage, V_O , can be measured for two different values of load resistor, R_L . The load resistor must be small compared to R_p . The equation can be written as follows:

$$\frac{V_{O_1}}{R_{L_1}} (R_{L_1} + R_S + Z_C) = \frac{V_{O_2}}{R_{L_2}} (R_{L_2} + R_S + Z_C)$$

The internal series resistor, R_S , is now given by:

$$R_S = \frac{\frac{R_{L_1}}{R_{L_2}} \frac{V_{O_2}}{R_{L_2}} - \frac{V_{O_1}}{R_{L_1}}}{\frac{V_{O_1}}{R_{L_2}} - \frac{V_{O_2}}{R_{L_1}}} - Z_C$$

If the generator is driven at the frequency ω_1 , the ~~magnitude~~ ^{value} of z_C can be inserted into the equation. Therefore:

$$R_S = \frac{R_{L_1} R_{L_2} (V_{O_2} - V_{O_1})}{V_{O_1} R_{L_2} - V_{O_2} R_{L_1}} - \frac{1}{\omega_1 C_S} \tan \omega_1 t \quad (5)$$

If the generator is excited at frequency, ω_2 , R_S can again be expressed in ~~two~~ ^{an} equations in terms of z_C . Since the value of R_S is independent of frequency, the two equations can be solved for R_S and C_S .

For maximum power transfer from the generator, the load resistance R_L must be equal to the internal resistance, R_S , and the capacitive reactance must be balanced by the addition of an inductive reactance of the same magnitude.

Power from a PZ Generator With a Resistive Load. Referring to Diagram ~~1~~, the maximum power from a PZ generator with resistive load is given by:

$$W = \frac{\left(F_{avg} g_{33} \frac{t}{A} \right)^2}{4 R_L} *$$

and

$$\frac{1}{\omega C_0} = R_L = \frac{1}{2\pi f C_0}$$

* Gulton Industries Catalog.

therefore,

$$W = \frac{2\pi f C_0 (F_{avg} g_{33} \frac{t}{\lambda})^2}{4}$$

Since

$$\frac{F_{avg}}{A} = \frac{F_{peak}}{2A} = \frac{\sigma}{2}$$

This is true only if
 $F_{min} = 0$, otherwise

$$F_{peak} \neq F_{peak to peak}$$

and

$$C_0 = \frac{K_3 \epsilon_0 A}{t}$$

then

$$W = \frac{\pi f K_3 \epsilon_0 A (\sigma g_{33} t)^2}{8t}$$

However,

$$d_{33} = K_3 \epsilon_0 g_{33}$$

so

$$W = \frac{\pi f}{8} d_{33} g_{33} \sigma^2 At$$

or

$$W = \frac{\pi f}{8} d_{33} g_{33} \sigma^2 v_{pz}$$

or

$$W = \frac{\pi f}{16} d_{33} g_{33} \sigma^2 v_{pz}$$

where: W = power delivered to load (watts) (for a single disc)

f = frequency (hertz)

R_L = load resistance (ohms)

t = thickness of the disc (meters)

A = area of the disc (meters²)

C_0 = capacitance of generator

F = ^{peak} applied force (Newtons)

σ = applied stress (Newtons/meter²)

g_{33} = PZ voltage coefficient

d_{33} = PZ charge coefficient

K_3 = dielectric constant

V_{p3} = volume of disc (meter³)

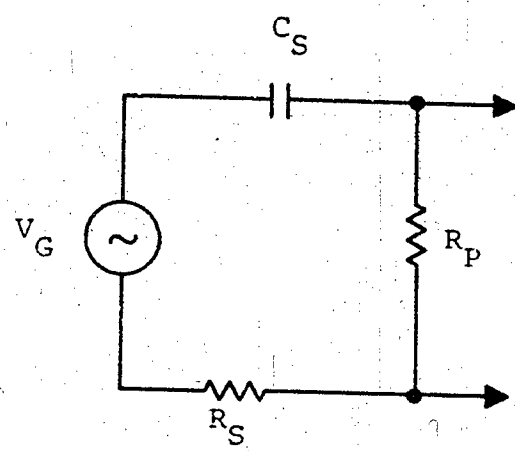


Figure A.1

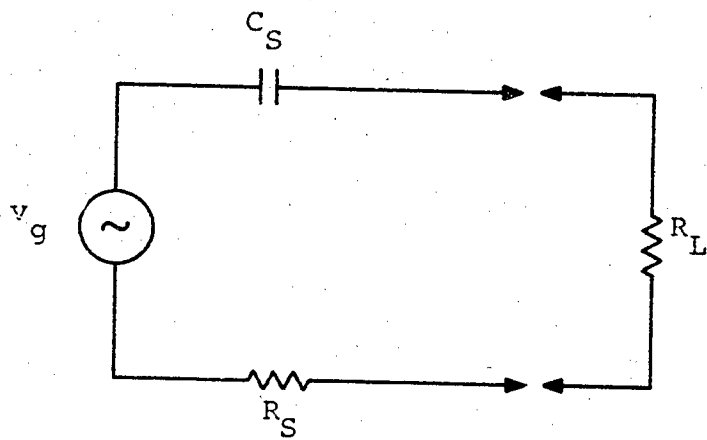


Figure A.2

SUPPLEMENTARY REPORT TO PIFR-355

Report PIFR-355, issued January 1972, presented data on the design, fabrication, and testing of a piezoelectric generator intended to be driven by a Stirling engine developed by McDonnell-Douglas Astronautics Company.

The following supplementary information is submitted relating to tests on PZT 5H and LTZ 2H generator materials.

1. A description of the effort to build and debug a hydraulic driving system for the generator.
2. A discussion of temperature measurement of the PZ generator.
3. A calculation of theoretical power generated for comparison with actual power measured.
4. A consecutive tabulation of the test data.
5. A calculation of circuit constants (i.e., series inductance and load resistance) required to match the impedance of the PZT 5H generator.
(The circuit constants for the LTZ 1 generator were determined experimentally, see tabulation data.)
6. A list of expenditures according to task and date.

PZ GENERATOR, DRIVING SYSTEM

In order to provide data to establish the feasibility of a high power/density generator it was necessary to perform tests upon a stack of piezoelectric discs to determine its performance at high driving pressures and to validate the extrapolation that has been made from limited available data.

Since the proposed generator concept employed hydraulic coupling between the prime mover and the generator, a system was designed to provide an approximately sinusoidal hydraulic output for application to an existing FZ housing.

A rotary valve was designed to connect a hydraulic pressure source with the generator twice for each revolution of the driveshaft. The design work was performed with P.I. funds before the start of the contract.

Fabrication of the rotary valve started about July 1, 1971. The rotary valve, the generator, and the hydraulic system were assembled during the first 3 weeks of August 1971. The PZT 5H stack and most of the components for the hydraulic driving system were available in-house. Testing of the system began on August 18, 1971.

The rotary valve was a first experimental model and the subject of some development itself. The pump output required was determined by calculating the volumetric displacement necessary to compress the stack plus the volumetric compliance of the hydraulic fluid. However, it was found that hydraulic compliance exceeded estimates and leakages occurred in the rotary valve. Consequently the output of the pump was inadequate to raise pressure to the desired value. The driving system was modified several times in order to increase the driving pressure.

attainable. First the pressure was controlled by a 1/4-in. direct acting relief valve (Manatrol 1/4-RA400-4), which was found to be of inadequate capacity and sensitivity to control the pressure accurately. It was replaced with a 3/8-in. pilot operated relief valve (Parker Hannifin MRFN-06-PIAA) which was found to be adequate. However the output from the pump (Vickers axial piston) was limited when driven at 1800 rpm and consequently drive speed was increased to 3600 rpm. Foaming of the hydraulic fluid and excessive noise indicated that the pump inlet was restricted causing cavitation. Therefore the inlet tube was increased to 1/2-in. diameter and the reservoir was elevated to about 2-ft. above the pump.

The needle valve and a 0.062-in. diameter passage between the rotary valve and generator restricted the flow and caused heating locally. The valve was replaced with a ball valve and the passage was drilled out to 0.125-in. diameter. The passage was in a brass block (on hand) employed to hold the Kistler pressure transducer. Evidently the block was weakened by the larger drilling or was damaged during installation. Consequently it broke during one of the first runs and was replaced with a steel part.

The driving system was limited in the pressure delivery capability to approximately 1700 psi (7500 psi on stack) and most of the hydraulic power was dissipated as heat.

The last three runs on the LTZ 1 generator were performed with a gas/hydraulic accumulator in the system to boost the pressure capability of the driving system for short durations.

It was found that friction in the rotary valve made the valve hard to start at pressures above 2000 psi despite having balanced pressure ports.

During the test program it was found that much more effort than expected was required to develop the driving system. Consequently this diversion reduced the amount of testing and analysis that could be performed within the limited budget.

If more testing of PZ stacks with a hydraulic driver is planned, more effort will be required to refine the hydraulic driving system.

TEMPERATURE MEASUREMENT

In the initial experiment and modification phase of testing the PZT 5H generator it was found that the insulating oil temperature rose to 96°F after a few minutes running time. (The temperature was measured with a mercury-glass thermometer.) A cooling coil, 2-in. in diameter with 26 turns of 1.8-in. O.D. copper tubing, was inserted in the oil. With water running through the coil the temperature of the oil increased from 75°F to 76°F with 7 minutes running time on the generator.

In six days of testing and modifying the apparatus after the cooling coil was installed it was found that the temperature variation of the oil did not exceed 7°F (71 - 78°F) or approximately the same as the room temperature variation. The cooling coil was led through the same hole that was used for the thermometer. Consequently the fit around the thermometer was snug. The thermometer was removed after the first power run to avoid breakage due to vibration.

It was noted that the insulating oil temperature does not represent the bulk temperature of the PZ stack. However the effort required to place thermocouples in special PZ discs and incorporate them into the stack was not allowed for in the budget.

POWER CALCULATION

The expression for power from a piezoelectric generator as derived in the appendix of the report is

$$W = \pi f d_{33} g_{33} \sigma^2 V_{pz}$$

where W = power delivered to the load in watts

f = frequency of applied stress (hertz)

d_{33} = piezoelectric voltage coefficient (volts meters/newton)

g_{33} = piezoelectric charge coefficient (coulombs/meter²)

σ = applied stress fluctuation (newton/meter²)

V_{pz} = volume of piezoelectric material (meters³).

It is assumed that the generator is matched for maximum power transfer to the load (see page 18).

The volume of the PZT 5H stack is

$$V_{pz} = \frac{\pi}{4} (3.18)^2 \times 10.12 = 80 \text{ cc or } 8 \times 10^{-5} \text{ m}^3$$

Using values from the Vernitron catalog:

$$W = \frac{\pi}{8} (6.0 \times 10^{-12}) (10.7 \times 10^{-3}) \sigma^2 (8 \times 10^{-5})$$

$$2.2 \times 10^{-14} \sigma^2 \text{ for } \sigma \text{ in newton/m}^2$$

$$(2.2 \times 10^{-14}) (6895)^2 \sigma^2 \text{ watts}$$

$$W = 1.05 \times 10^{-6} \sigma^2 \text{ watts (for } \sigma \text{ in psi).}$$

This agrees very well with the projected curve in Figure 3.

— Similarly the power for the LTZ 1 generator is:

$$W = \frac{\pi 60}{8} (284 \times 10^{-12}) (29.2 \times 10^{-3}) (6895)^2 \sigma^2 (1.26 \times 10^{-5})$$

$$W = 0.117 \times 10^{-6} \sigma^2 \text{ watts } (\sigma \text{ in psi})$$

The actual power from the LTZ 1 generator falls below this theoretical relationship. However, this generator was made up of ten 1.25-in. diameter discs, 0.040-in. thick and one 0.125-in. thick disc on each end. Ignoring the two thick end discs the power is

$$W = 0.074 \times 10^{-6} \sigma^2 \text{ watts.}$$

This expression falls on the 2nd curve from the top in Figure 4. Since several points fall between the two curves it is apparent that the effective volume of PZ material lies intermediate the full stack volume and the full volume less the thick end discs. The thick discs were included to reduce the end effects on the short 10 disc stack (i.e., shear stresses on the ends generated by the steel end pieces and the Poisson effect). If a similar stack were tested again it is recommended that the end discs be shorted and left out of the generator circuit.

It must also be considered that the series inductance was not truly optimized. However it is estimated that the increase in power with optimum inductance would be less than 2% neglecting re-optimization of the load resistor to suit the larger inductor (see page 11).

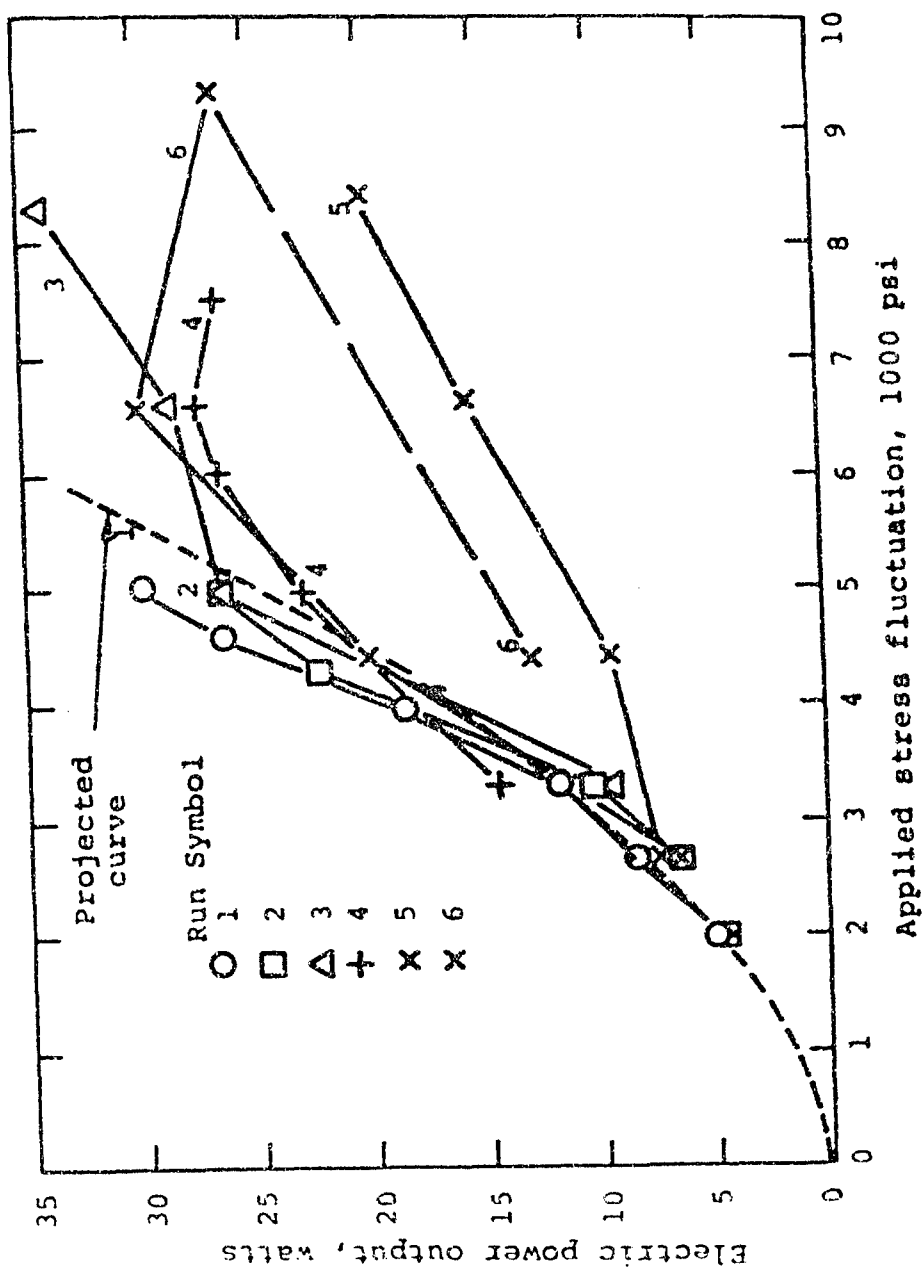


Figure 3 Output power of PZT 5H generator, volume of material: 5 in. ³.

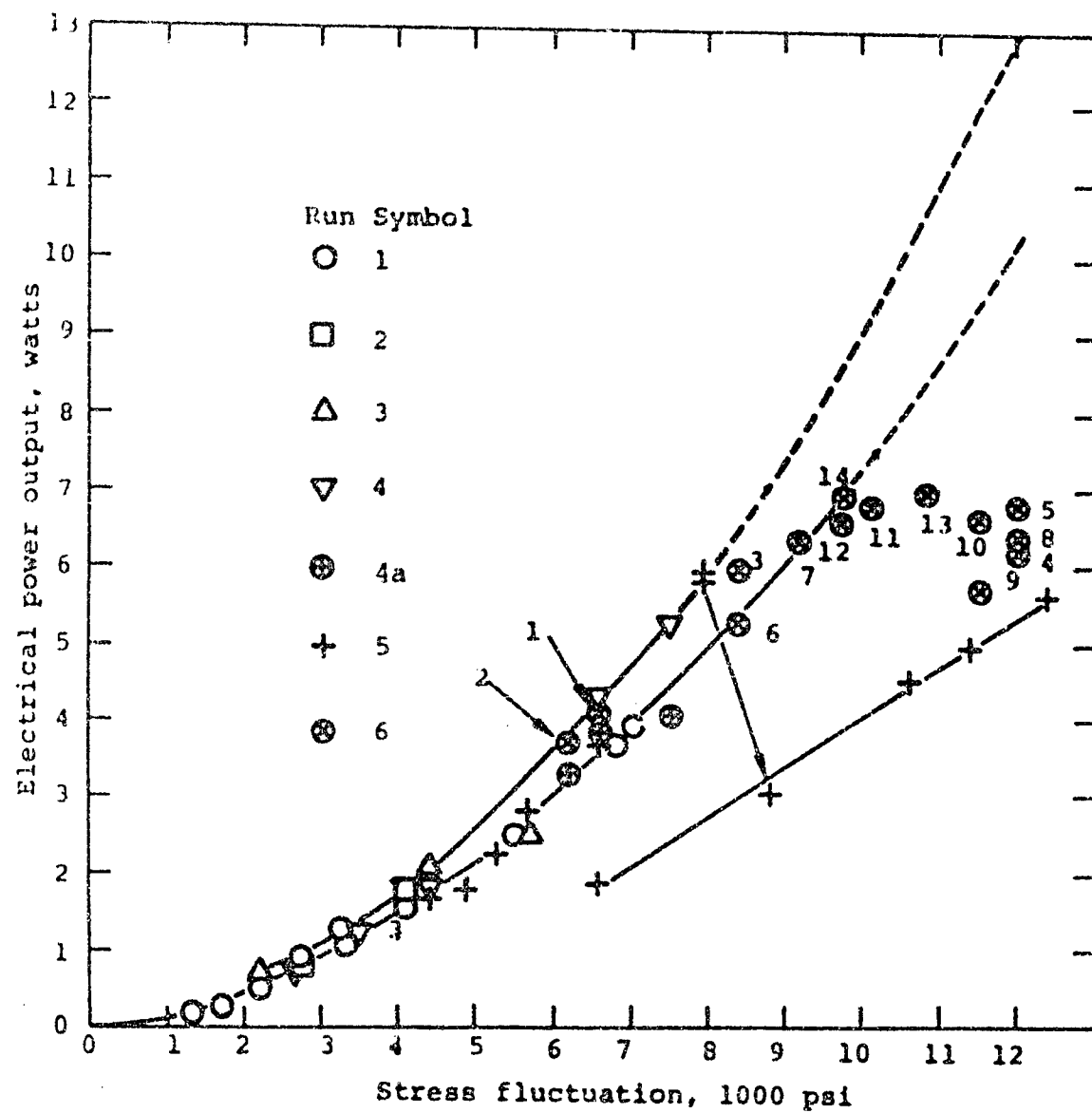


Figure 4 Output power of LTZ1 generator, volume of material: 0.8 in³.

PZT 5H GENERATOR

Power Runs

Load resistance: 425Ω

Series inductance: 1.4 Henries

Δp = hydraulic pressure fluctuation, psi

$\Delta \sigma$ = stress fluctuation = $4.4 \Delta p$

V_L = peak to peak voltage across resistor

P = power, watts

Ambient temperature $72 - 78^{\circ}\text{F}$

<u>Δp</u>	<u>$\Delta \sigma$</u>	<u>V_L</u>	<u>P</u>
September 2, 1971			
Run No. 1			
450	1980	130	5.0
600	2640	170	8.5
750	3300	200	11.8
900	3960	250	18.5
1050	4600	300	26.5
1140	5000	320	30.0 - insul. oil temp. 78°F

September 3, 1971

Run No. 2

450	2000	120	4.25
600	2650	150	6.6
750	3300	190	10.6
1150	4950	300	26.5
975	4300	275	22.2

<u>LP</u>	<u>$\Delta\sigma$</u>	<u>V_L</u>	<u>P</u>
-----------	----------------------------------	-------------------------	----------

September 7, 1971
Run No. 3

750	3300	180	9.5
1150	4950	235	16.2
1500	6600	310	28.4
1875	8300	340	34.0

September 8, 1971
Run No. 4

750	3300	220	14.3
1150	4950	280	23.2
1350	6000	300	26.5
1500	6600	305	27.5
1650	7250	300	26.5

September 9, 1971
Run No. 5

600	2640	125	7.3
1000	4400	180	9.5
1500	6600	230	15.4
1900	8400	260	20.0

Repoled stack to 50 V/mil DC pulse, 250 ms pulse at 2 Hz.
Run No. 6

600	2640	150	6.5
1000	4400	260	20.0
1500	6600	320	30.0
2100	9300	300	26.5
1000	4400	210	13.0

LTZ 1 GENERATOR

Selection of Load Resistor

Series inductance = 18 H

Stress fluctuation = 5500 psi

October 7, 1971	<u>R_L</u> (KΩ)	<u>V_L</u> (Volts)	Power $\left(\frac{V^2}{8R_L}\right)$ (Watts)
	7.0	350	2.2
	8.5	400	2.35 ← max.
	9.5	420	2.32
	10.0	430	2.31
	11.5	460	2.30

Selection of Series Inductance

R_L = 8.5 KΩ

Stress fluctuation = 5500 psi

	<u>L</u> (Henries)	<u>V_L</u> (Volts)	Power (Watts)	Δ Power (Watts)
October 7, 1971				
	16.6	380	2.22	0.13
	18.0	400	2.35	0.12
	20.0	410	2.47	0.06
	21.0	415	2.53 ← Use 21 H	0.03 est.*
	22.0	Higher inductances were not available in a time compatible with the schedule.		

*Increase in power with
larger inductance is estimated at < 2%

Power Runs

Load resistance $R_L = 8.5 \text{ k}\Omega$

Series Inductance $L = 21 \text{ Henries}$

Δp = hydraulic pressure fluctuation, psi

$\Delta\sigma$ = stress fluctuation = $4.4 \Delta p$

V_L = peak to peak voltage across resistor

P = Power, watts

Estimated running time: 2 min. per data point.

October 7, 1971

Run No. 1

<u>Δp</u>	<u>$\Delta\sigma$</u>	<u>V_L</u>	<u>P</u>
1250	5500	415	2.52
1560	6850	500	3.68
1600	7000	520	3.96
935	4100	330	1.60
625	2750	250	0.92
312	1375	120	0.21
750	3300	280	1.15
500	2200	200	0.59
500	2200	200	0.59
374	1650	160	0.25
625	2750	250	0.92
750	3300	290	1.24

	<u>Δp</u>	<u>$\Delta \sigma$</u>	<u>v_L</u>	<u>P</u>
October 8, 1971 Run No. 2				
	625	2750	240	0.85
	935	4100	350	1.80
October 8, 1971 Run No. 3				
	1000	4400	380	2.1
	500	2200	220	0.71
	1300	5700	490	3.5
October 11, 1971 Run No. 4				
	600	2650	220	0.71
	800	3500	290	1.25
	1000	4400	360	1.90
	1500	6600	540	4.30
	1700	7500	600	5.30
October 13, 1971 Run No. 4A				
	1400	6200	330	--- Odd pressure wave with 2 peaks
	1400	6200	470	3.25 Normal pressure wave
	1500	6600	510	3.85 Pressure falling with time, could not read
	1700	7500	530	4.15 scope accurately.

<u>Δp</u>	<u>$\Delta \sigma$</u>	<u>V_L</u>	<u>P</u>
October 14, 1971			
Run No. 5			
1100	4850	350	1.80
1200	5300	400	2.35
1300	5700	440	2.85
1500	6600	510	3.85
1800	7900	630	5.85
1800	7900	640	6.00
2000		460	3.10 Erratic behavior.
2800		620	5.65 " "
1800	7900	440	2.85 " "
1000	4400	360	1.9 " "
1500	6600	360	1.9 " "
2400	10600	560	4.6 " "
2600	11400	580	4.95 " "
1500	6600	350	1.8 " "

*These stress figures are in doubt because it is suspected that the "O"-ring extruded and jammed the piston.

<u>Δp</u>	<u>$\Delta\sigma$</u>	<u>V_L</u>	<u>P</u>
------------------------------	----------------------------------	-------------------------	----------

October 15, 1971

Run No. 6

10:00 A.M.

1500	6600	530	4.15		
1400	6200	500	3.7		
1900	8400	640	6.0		
2700	12000	650	6.2	Erratic behavior	
2700	12000	670	6.6	"	"
1900	8400	600	5.3	"	"
2100	9250	660	6.4	"	"
2700	12000	660	6.4	"	"
2600	11500	620	5.7	"	"
2600	11500	670	6.6	"	"

October 15, 1971

Run No. 6

2:30 P.M.

2300	10100	680	6.8	Erratic behavior	
2200	9700	670	6.6	"	"
2400	10600	690	7.0	"	"
2200	9700	690	7.0		

*These stress figures are in doubt because it is suspected that the "O"-ring extruded and jammed the piston.

IMPEDANCE MATCHING

A knowledge of the behavior of piezoelectric materials was used to postulate the equivalent circuit (shown in Figure A1) of a PZ generator.¹ The voltage source shown in the equivalent circuit represents an ideal voltage generator. Since a PZ stack is capacitive, a capacitor, C_S , has been included in the equivalent circuit. The resistor, R_S , represents the internal losses of the PZ generator while R_P is the shunt resistance present in all PZ stacks. This shunt resistance causes an initial voltage on a stack to decay and is included in the circuit. The series capacitance C_S is not equal to the capacitance of the stack, but is calculated as shown below.

If the value of the load resistor on the output is small compared to R_P , the circuit can be simplified to that shown in Figure A2. If it is also assumed that the impedance due to C_S and R_S are small compared to R_P , then the generated voltage, V_G , can be assumed equal to the open circuit voltage measured at the output of the generator. Assuming the generator output is sinusoidal, the circuit equation in the frequency domain is

$$V_G = I (R_L + R_S + Z_C) \quad \text{Eq. (1)}$$

or

$$V_{OC} = \frac{V_O}{R_L} (R_L + R_S + Z_C) \quad \text{Eq. (2)}$$

If the generated voltage, V_G , is independent of frequency then, by

1. A circuit similar to this is shown on page 17 in Piezoelectric Technology Data for Designers, by the Piezoelectric Division of Clevite Corp.

assumption V_{OC} is also. Hence the output at two frequencies can be equated:

$$\frac{V_{O_1}}{R_L} (R_L + R_S + Z_{C_1}) = \frac{V_{O_2}}{R_L} (R_L + R_S + Z_C) \quad \text{Eq. (3)}$$

Therefore R_S is

$$R_S = \frac{\frac{V_{O_2}}{R_L} (Z_C) - V_{O_1} - \frac{V_{O_1}}{R_L} (Z_C)}{\frac{V_{O_1} - V_{O_2}}{R_L}} \quad \text{Eq. (4)}$$

or

$$R_S = \frac{\left[V_{O_2} - V_{O_1} + \frac{V_{O_2}}{R_L w_2 C} - \frac{V_{O_1}}{R_L w_1 C} \right] R_L}{V_{O_1} - V_{O_2}} \quad \text{Eq. (5)}$$

$$R_S = \frac{\left(V_{O_2} - V_{O_1} \right) R_L + \left(\frac{V_{O_2}}{w_2} - \frac{V_{O_1}}{w_1} \right) \frac{1}{C}}{V_{O_1} - V_{O_2}} \quad \text{Eq. (6)}$$

Substituting:

$$R_S = \frac{(3.9 - 5.7) \cdot 100 + \left(\frac{3.9}{197} - \frac{5.7}{377} \right) \frac{1}{C}}{(5.7 - 3.9)} \quad \text{Eq. (7)}$$

$$R_S = \frac{2.61 \times 10^{-3}}{C} - 100 \quad \text{Eq. (8)}$$

Using Eq. (8) and the experimental values for the PZT 5H generator shown in Table 3A for Eq. (2) yields:

$$60.1 = \frac{5.7}{100} \cdot 100 + \frac{2.61 \times 10^{-3}}{C} = 100 + \frac{1}{377C} \quad \text{Eq. (9)}$$

or

$$C = \frac{5.7}{6.01} \cdot (5.26) \cdot 10^{-6} = 5.01 \mu\text{f} \quad \text{Eq. (10)}$$

Therefore:

$$R_S = \frac{2.61 \times 10^{-3}}{5.01 \times 10^{-6}} = 100 = 421 \Omega \quad \text{Eq. (11)}$$

The capacitive impedance is:

$$Z_{C_{60 \text{ Hz}}} = \frac{1}{377 (5.01 \times 10^{-6})} = 532 \Omega \quad \text{Eq. (12)}$$

For maximum power transfer from the generator, the load resistance must be equal to the internal resistance, R_S , and the capacitive reactance must be balanced by the addition of an inductive reactance of the same magnitude. Therefore:

$$L_{60 \text{ Hz}} = \frac{532}{377} = 1.41 \text{ h} \quad \text{Eq. (13)}$$

It is necessary that the voltage measurements used to calculate the equivalent circuit be accurate to prevent errors. For instance, if

V_{O_1} was measured 5% high (6.0 volts instead of 5.7) and V_{O_2} was measured 5% low (3.7 volts instead of 3.9) the series capacitance, C_S , increases 10%.

$$R_S = \frac{(3.7 - 6.0) 100 + \frac{3.7}{197} - \frac{6.0}{377} \frac{1}{C}}{6.0 - 3.7}$$

$$\frac{2.87 \times 10^{-3}}{C} = 100\Omega$$

Therefore:

$$C = 5.52 \times 10^{-6} \text{ f}$$

Although the induction calculation above produced a value that worked very well in tests, later calculations on different stacks produced values that were not realistic. Another method was used to determine the circuit values which worked fairly well in actual tests. However further work is necessary to characterize PZ generators. A vital part of this is to determine what relationship the stack capacitance has to the equivalent series capacitance.

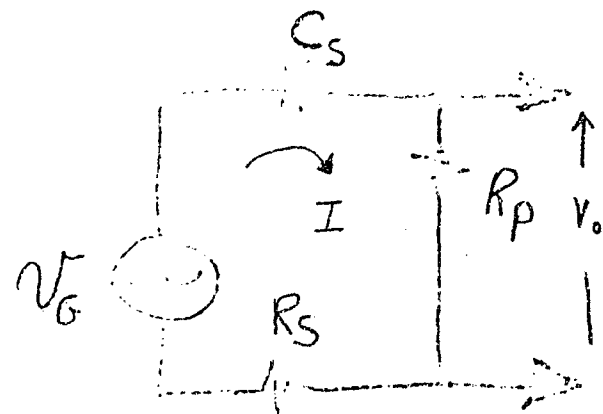


Figure A1

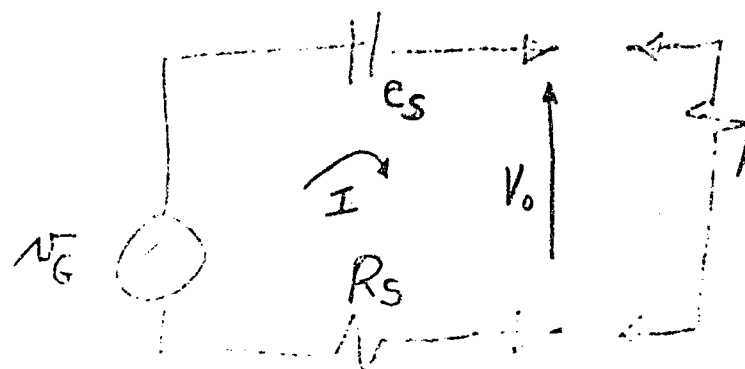


Figure A2

$$(R_L < R_P)$$

Figure A3

$\omega_1 = 377 \text{ (60 Hz)}$	$\omega_2 = 197 \text{ (31.1 Hz)}$
$V_{o1} = 5.7 \text{ V. (rms)}$	$V_{o2} = 3.9 \text{ V. (rms)}$
$R_L = 100 \Omega$	$V_{oc} = 60.1 \text{ V (rms)}$

EXPENDITURES

<u>Task</u>	<u>Date</u>	<u>\$ Expended</u>	<u>Increment</u>	<u>Accumulated</u>	<u>% Expended</u>
Fabricate and assemble hydraulic driver, PZ generator, and test apparatus	7/2/72 to 8/13/72	3,461	3,461	3,461	49
Test and modify apparatus	8/16/72 to 8/27/72	657	4,118	4,118	58
Test PZT 5H generator	8/30/72 to 9/10/72	1,307	5,425	5,425	77
Fabricate LTZ-1 Gen- erator	9/13/72 to 9/24/72	706	6,131	6,131	87
Test LTZ-1 Generator	9/27/72 to 10/15/72	926	7,057	7,057	100

Appendix B
 INDEPENDENT DEVELOPMENT OF PIEZOELECTRIC
 GENERATOR TECHNOLOGY USING CYCLE
 AVERAGED FORMALISM

This appendix discusses the analytical closed solution formalism associated with continuous and pulsed operation of the piezoelectric generator. For both modes of operation, two cases are considered: (1) the purely resistive load, and (2) the load with inductance added to compensate for the capacitance of the piezoelectric stack. For continuous operation, an analytical correlation with the PZT-5H data presented in Appendix A is also made.

B.1 CASE I - CONTINUOUS-POWER OPERATION WITH RESISTIVE LOAD

This case is shown in Figure B-1 where the following conditions apply.

Mechanical Input: Sinusoidal Compression

Load: Resistive; no matching inductance

2238

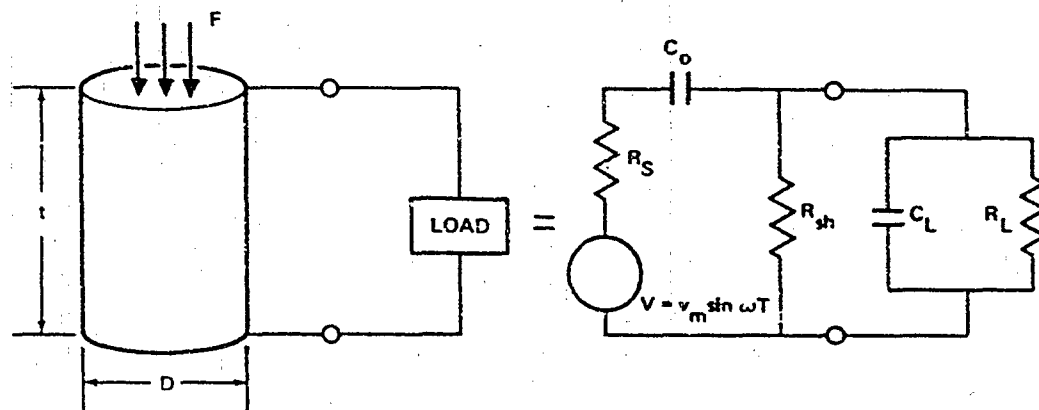


Figure B-1. Mechanical and Electrical Equivalent Circuits

The shunt resistor, R_{sh} , for crystals of useful sizes is on the order of 10^{10} ohms; C_L is the capacitance of the leads and load. For this case, C_L is very small, e.g., a few picofarads; therefore, X_{CL} is also very large (10^{10} ohms). The electrical equivalent circuit can then be simplified as in Figure B-2.

With sinusoidal compression as the mechanical input, the instantaneous voltage is

$$v = V_m \sin \omega T$$

and at steady state, the instantaneous current is

$$i = I_m \sin(\omega T + \phi)$$

Where the peak current I_m , and peak voltage, V_m , are related by

$$I_m = \frac{V_m}{\sqrt{(R_L + R_S)^2 + X_C^2}} = \frac{V_m}{Z}$$

with

R_L : Load resistance

R_S : Internal stack series resistance

X_C : Stack capacitive reactance

Z : Circuit impedance

2239

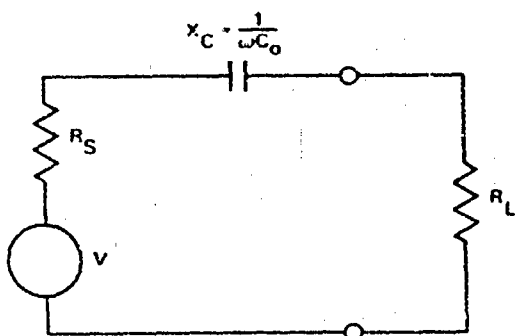


Figure B-2. Simplified Electrical Equivalent Circuit

and the phase angle, ϕ , is given by

$$\phi = \tan^{-1} \frac{X_C}{R_L + R_S}$$

Straightforward mathematical manipulation leads to the following expression for power W , delivered to the load

$$W = \frac{V_m I_m}{Z} \frac{R_L}{Z}$$

By definition and from typical piezoceramic property data,

$$\frac{R_S}{X_C} \ll \tan \delta \ll 1$$

The maximum power transferred, therefore, occurs very nearly at $R_L = X_C$. For this case

$$W = \frac{V_m^2}{4R_L} = \frac{V_{rms}^2}{2R_L}$$

where

$$V_{rms} = \frac{V_m}{\sqrt{2}}$$

As was discussed in Section 2.1.3

$$V_{rms} = \left(F_{rms} / A \right) \text{ gt}$$

Therefore

$$W = \frac{\left[\left(F_{rms} / A \right) \text{ gt} \right]^2}{2 R_L}$$

But

$$F_{rms} = \frac{F_m}{\sqrt{2}}$$

and

$$F_{\text{peak-peak}} = 2 F_m$$

and it also equals $2 F_{\text{avg}}$

Thus, the maximum power transferable is

$$W = \frac{[F_{\text{avg}}/A]_g t]^2}{4 R_L}$$

This is the equation utilized in Appendix A.

B.2 CASE II - CONTINUOUS-POWER OPERATION WITH MATCHING INDUCTANCE

Mechanical Input: Sinusoidal Compression

Load: Resistive with Matching Inductance

The equivalent electric circuit for the case is shown in Figure B-3.

When $X_L = X_C$, this circuit reduces to the form of Figure B-4, where $X_L = \omega L$ = inductive reactance.

Power transferred to the load resistance, R_L , is

$$W = \frac{V^2 R_L}{(R_S + R_L)^2}$$

2240

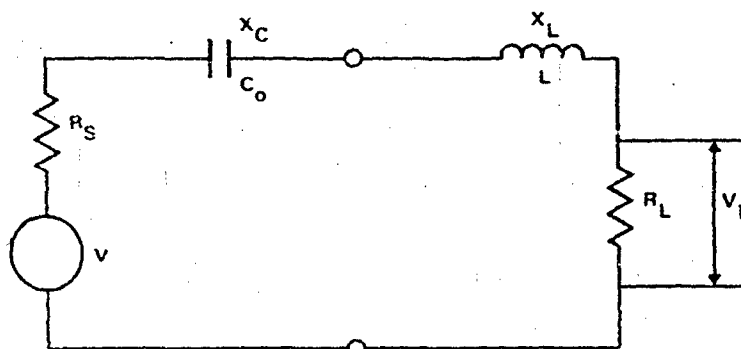
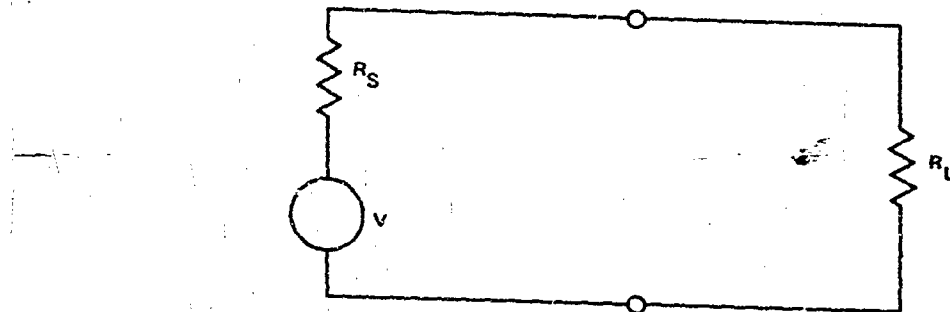


Figure B-3. Simplified Electrical Equivalent Circuit with Inductance



2241

Figure B-4. Simplified Resonant Circuit with $X_L = X_C$

When $R_L = R_s$, the power transfer is a maximum and is given by

$$W = \frac{V^2 R_s}{4 R_s^2} = \frac{V^2}{4 R_s}$$

where

$$R_s = R_L$$

This is not a desirable operating condition because half of the power generated is dissipated in the stack. In practice, R_L is normally chosen somewhere between this value and the optimum value for no inductance, depending on the desired tradeoff between efficiency and power density.

B.3 CASE III - PULSED-POWER OPERATION WITH RESISTIVE LOAD

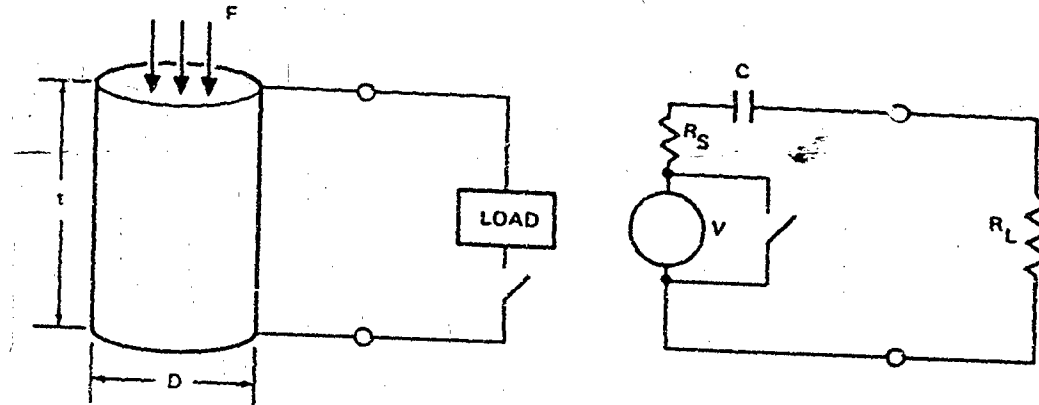
This case is shown in Figure B-5 where the following conditions apply.

Mechanical Input: Periodic Compression, Frequency ω

Load: Resistive/No Inductance

At the instant the switch is closed, instantaneous current is zero and the voltage across the capacitor is the peak voltage of the capacitor

$$V_{AC} = [(F/A) g t]$$



2242

Figure B-5. Mechanical and Electrical Equivalent Circuits

Current as a function of time after the switch is closed is

$$i = \frac{V_{oc}}{R_s + R_L} e^{-T/(R_s + R_L)C_0}$$

This leads to an average current over a half cycle of

$$I_{avg} = \frac{1}{1/2f} \int_0^{1/2f} idT = \frac{1}{1/2f} \int_0^{1/2f} \frac{V_{oc}}{R_s + R_L} e^{-T/(R_s + R_L)C_0} dT$$

Integration and evaluation at the limits leads to

$$I_{avg} = 2f V_{oc} C_0 \left[1 - e^{-1/(2f C_0 (R_L + R_s))} \right]$$

The average power, W , delivered to the load can now be determined

$$W = I_{avg}^2 R_L = (2f V_{oc} C_0)^2 R_L \left[1 - 2e^{-1/2f\tau} + e^{-1/f\tau} \right]$$

where

$$\tau = (R_L + R_s)C_0$$

In this equation for average power, there is also an optimum value of R_L to produce the maximum power. This is demonstrated by the following argument: When R_L is very small, the quantity outside

the brackets is very small; when R_L is very large, the quantity inside the brackets is very small.

B.4 CASE IV - PULSED-POWER OPERATION WITH INDUCTANCE

This case is shown in Figure B-6 with the following conditions.

Mechanical Input: Periodic Compression, frequency ω

Load: Resistive plus Inductance

This case is a little more difficult mathematically. The solution for instantaneous current depends on the relative values of

$$(R_L + R_s), L, \text{ and } C$$

Case IV-A:

$$\left(\frac{R}{2L}\right)^2 > \frac{1}{LC} \text{ Normal Damping}$$

$$i = \frac{V_{oc}}{2L\delta} e^{-RT/2L} e^{\delta T} - e^{-\delta T}$$

2243

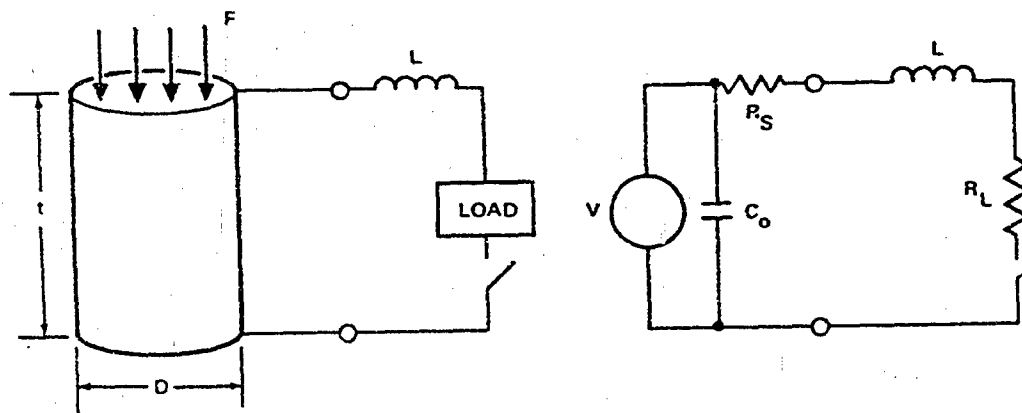


Figure B-6. Mechanical and Electrical Equivalent Circuits

where

$$\begin{aligned} R &= R_L + R_S \\ \delta &= \left\{ (R/2L)^2 + 1/LC \right\}^{0.5} \end{aligned}$$

Case IV-B:

$$\left(\frac{R}{2L}\right)^2 = \frac{1}{LC}, \text{ Critical Damping}$$

$$i = \frac{V_{oc}}{L} e^{-RT/2L}$$

Case IV-C:

$$\left(\frac{R}{2L}\right)^2 < \frac{1}{LC} \quad \text{Oscillatory}$$

$$i = \frac{V_{oc}}{\eta L} e^{-RT/2L} \sin \eta T$$

where

$$\eta = \left\{ \left(\frac{1}{LC}\right)^2 - \left(\frac{R}{2L}\right)^2 \right\}^{0.5}$$

As in Case III, average currents can be calculated for Case IV-A, B, and C:

$$I_{avg} = \frac{1}{1/2i} \int_0^{1/2i} idT$$

Again, average power delivered to the load is

$$W = I_{avg}^2 R_L$$

For a given stack capacitance C_s , an R_L and L can be found to produce the maximum power. Again, R_L would normally be increased above this value for the best tradeoff between power density and efficiency.

B.5 CORRELATION OF EXPERIMENTAL DATA WITH THEORY

Calculations were performed utilizing the formalism for continuous operation presented in Cases I and II. The particular example given here is for a PZT-5H stack consisting of 100 discs connected electrically in parallel. Each disc is 0.040 in. thick x 1.25 in. dia. Such a stack was used in the experiments reported in Appendix A. Figure B-7 presents the results of applying this formalism to the operating conditions of Run No. 1, 9-2-71, described in Appendix A. Also shown are the experimental data points gathered on that run.

The calculations of PZT-5H stack performance make use of materials parameters provided in Clevite Catalog No. 695. Generally, low signal parameters were used with some corrections for high stress and high field made to the dielectric constant and dissipation factor. Data for these corrections are only strictly valid to 2000 psi, and these corrections should be considered qualitative at higher stresses. This is especially true because a linear dependence of each correction was assumed for extrapolation which is not necessarily correct. Series resistances (internal, lead, and inductor) are disregarded in all power calculations using this formalism. Even though there are these limitations on the analysis, some correlations and dependencies are worth examination. In Figure B-7, calculated power exhibits the same general dependence on applied stress as the experimental data. These calculated values tend to be higher than the data. When a low field relative dielectric constant of 3200 is used instead of 3400, this difference disappears. Such a difference in dielectric constant could result from the temperature of the material or time after poling.

Figure B-8 shows the calculated dependence of the PZT-5H stack output power on load resistance at a given stress fluctuation (2640 psi). With respect to power, the calculated optimum circuit resistance of about 700 ohms with the given inductance ($X_C - X_L = 700\Omega$) and the experimental optimum load resistance of 425 ohms imply as much as 275 ohms of series resistance elsewhere in the circuit, if the calculations are correct. Such resistance would probably be primarily in the stack with a small amount in the inductor and leads. Increasing stack temperature leads to an almost exponential rise in $\tan \delta$ and increases the effective series resistance. Such a rise without cooling could lead to rapid stack deterioration; any temperature increase causes more self heating and more temperature rise.

This same analytical formalism also provided good agreement for power vs stress and power vs load for data gathered at DWDL. However, with both Physics International and DWDL data, the dependence on inductance was in error. While the power versus inductance dependence was qualitatively correct, the optimum inductance calculated was over 50% higher than measured. By reformulating the equations on an instantaneous rather than time-averaged basis, and accounting for the charge on the stack throughout a given cycle, this

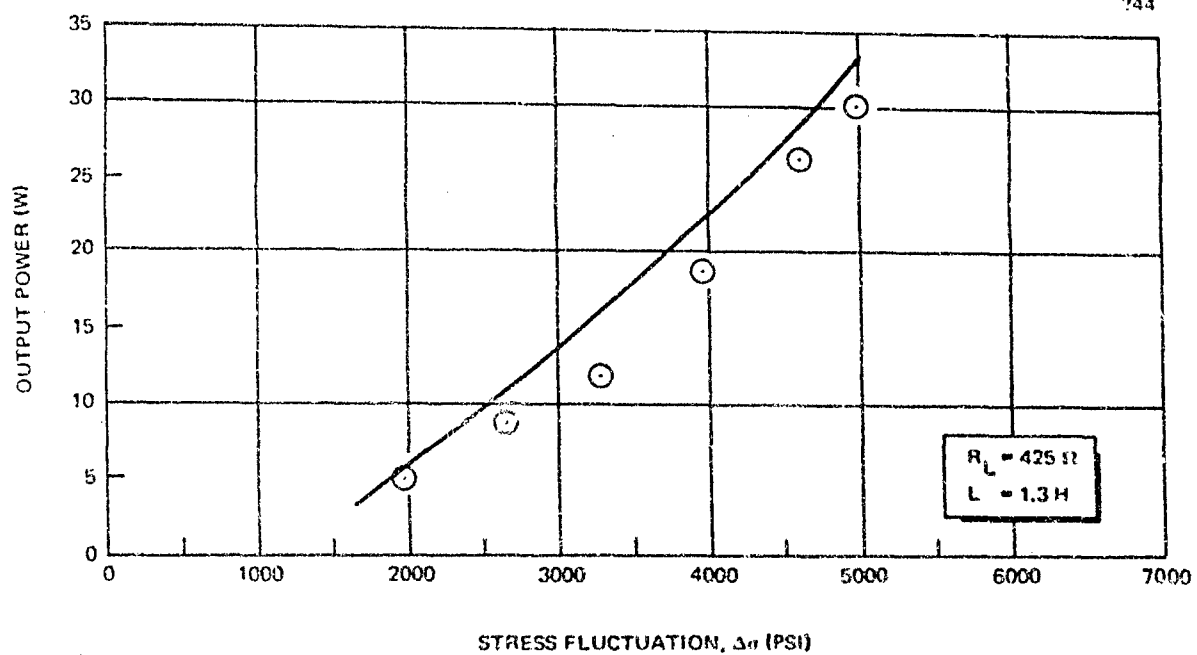


Figure B-7. PZT-5H Stack Output Power Dependence Upon Stress

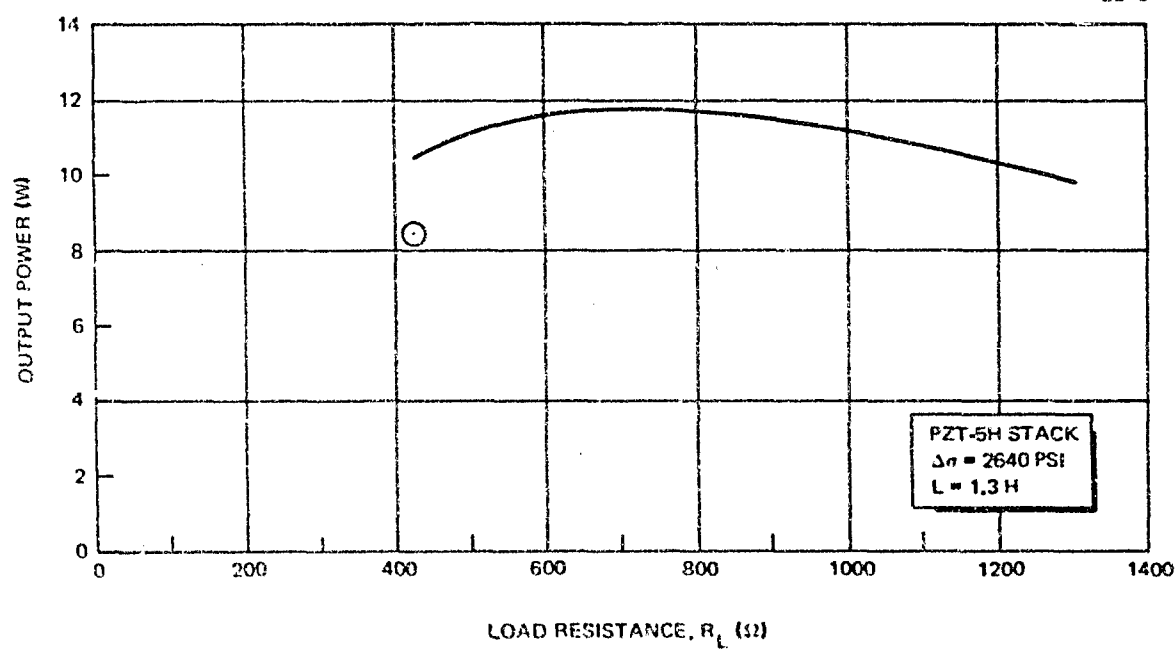


Figure B-8. PZT-5H Stack Output Power Dependence Upon Load

discrepancy was eliminated. This latter formulation is described in more detail in Appendix C and applied to Physics International and DWDL data.

A sample set of calculations for obtaining the curve in Figure B-7 is given in Section B.6. Symbols used are defined in Table B-1.

B.6 SAMPLE CALCULATION

PZT-5H Stack:

100 discs, 0.040 in. thick x 1.25 in. dia (connected in parallel)

$$D = 1.25 \text{ in.} = 0.03175 \text{ m}$$

$$A = \frac{\pi}{4} D^2 = 1.227 \text{ in.}^2 = 0.000792 \text{ m}^2$$

$$t = 0.040 \text{ in.} = 0.001016 \text{ m}$$

$$\text{PZ volume/disc} = At = 0.0491 \text{ in.}^3 = 0.804 \times 10^{-6} \text{ m}^3$$

$$\text{PZ stack volume} = 100 At = 4.91 \text{ in.}^3 = 0.804 \times 10^{-4} \text{ m}^3$$

$$\epsilon_{33}^T = \epsilon_0 \epsilon_r = (8.85 \times 10^{-12}) (3400) [1 + 0.04 (\Delta\sigma)/2000]$$

Assume $\Delta\sigma = 1980 \text{ psi}$

$$\epsilon_{33}^T = 0.289 \times 10^{-7}$$

$$C_0 = \epsilon_{33}^T A/t = 0.225 \times 10^{-7} \text{ farad/disc}$$

$$\text{Stack capacitance} = (100)(0.225 \times 10^{-7}) = 0.225 \times 10^{-5} \text{ farads}$$

$$X_C = \frac{1}{2\pi f C_0} = 1/(2\pi 60)(0.225 \times 10^{-5}) = 1178 \Omega$$

Assume $R_L = 425 \Omega$, $L = 1.3 \text{ henries}$

$$X_L = (2\pi f L) = 490 \Omega$$

$$(X_C + X_L) = 688 \Omega$$

$$Z = \sqrt{(R_L^2 + (X_C + X_L)^2)} = \sqrt{425^2 + 688^2} = 808 \Omega$$

All circuit resistance except the load is disregarded.

$$\cos\theta = \frac{R_L}{Z} = \frac{425}{808} = 0.526$$

(also $\sin\theta$ regarding all circuit resistance except the load)

Table B-1
SYMBOLS USED IN SAMPLE CALCULATION

Symbol	Definition
A	Area
t	Thickness
D	Diameter
f	Frequency
E	Electric field, (v/m)
F	Force
Vol	Volume
G_{33}	Piezoelectric coefficient (volts/applied stress)
R_L	Load resistance
ϵ_{33}	Relative dielectric constant, (free)
F_p	Peak force
F_{pp}	Peak-to-peak force
F_{rms}	Rms force
F_{avg}	Average force
Z	Impedance
X_c	Capacitive reactance
C_o	Capacitance
I	Current
P	Power
L	Inductance
X_L	Inductive reactance
$\tan \delta$	Dissipation factor, $(R_{series})_{effective} / (X_{c\ series})_{effective}$
V_{rms}	Rms voltage
V_{oc}	Open circuit voltage
V_{pp}	Peak-to-peak voltage
V_L	Voltage across the load
H	Heat generated
η	Efficiency

$$(F/A)_{MAX} = 1980 \text{ psi} \quad (1980)(6895) = 0.1365 \times 10^6 \text{ N/m}^2$$

$$(F/A)_P = (F/A)_{AVG} = 990 \text{ psi} = 0.683 \times 10^7 \text{ N/m}^2$$

$$(F/A)_{RMS} = \frac{(F/A)_P}{\sqrt{2}} = 700 \text{ psi} = 0.483 \times 10^7 \text{ N/m}^2$$

$$V_{RMS} = (F/A)_{RMS} G_{33} t = (0.483 \times 10^7) (0.0197)(0.001106) = 96.6 \text{ v}$$

$$V_{oc} = V_{RMS} = 96.6 \text{ v}$$

$$V_L = V_{oc} \cos \theta = (96.6)(.527) = 50.9 \text{ v}$$

$$V_{pp} = 2\sqrt{2} V_L = 143 \text{ v}$$

$$I = \frac{V_{oc}}{Z} = \frac{96.6}{808} = 0.1195 \text{ amp}$$

$$P = V_L I = (50.9)(0.1195) = 607 \text{ w}$$

$$\tan \delta = (\tan \delta)_{\text{low signal}} + \frac{\Delta (\tan \delta)}{\Delta E} E$$

$$\frac{0.02 + (0.04 - 0.02)(0.483 \times 10^7)(0.0197)}{(0.3)} = 0.0834$$

$$(R_{\text{series}})_{eff} = X_c \tan \delta = (1178 \Omega)(.0834) = 98 \Omega$$

$$H = I^2 (R_{\text{series}})_{eff} = (0.1195)^2 (98) = 1.40 \text{ w}$$

$$\eta = \frac{P}{P + H} = \frac{6.07}{6.07 + 1.40} = 0.81 = 81\%$$

This value of efficiency disregards all mechanical losses, lead, and inductor losses.

Appendix C

INDEPENDENT DEVELOPMENT OF PIEZOELECTRIC GENERATOR TECHNOLOGY USING TIME-STEP NUMERICAL INTEGRATION FORMALISM

This appendix discusses the time step numerical integration formalism for piezoelectric generator analysis which was developed at DWDL. This formalism permits system studies when integrated with the dynamic engine simulation and now provides better correlation with experimental data than the techniques described in Appendix B. Using this formalism, the LTV-1 data gathered by Physics International and reported in Appendix A is analyzed. Data gathered at DWDL is also analyzed together with a discussion of the related experimental measurements.

C. 1 COMPUTER PROGRAM

The technique of segmenting a given stress fluctuation cycle of the piezoelectric stack into a number of discrete time steps (e. g. 100) is analogous to segmenting the Stirling engine cycle into a number of time steps as is done in the dynamic Stirling engine simulation program. In the case of the piezoelectric stack, this enables the computer to instantaneously monitor the charge on the stack. Charge is continually generated by the stress fluctuation while it leaks off either through the load or through the stack shunt resistance. The equivalent circuit utilized in the computer program is given in Figure C-1. The letters "a" through "e" indicate reference points which are used in describing the circuit. Symbols used in this discussion are defined in Table C-1.

The basic charge balance on the capacitor is:

$$Q = \text{charge generated} - \text{charge lost}$$
$$= (\text{capacitance}) (\text{voltage generated})$$
$$- (\text{average current}) (\text{time increment})$$
$$= \left(\frac{n \cdot t \cdot A}{t} \right) \left(\frac{gt \cdot F}{A} \right) - \bar{I} \cdot DT$$

Preceding page blank

where the dielectric constant used is field dependent:

$$\epsilon = \epsilon_0 \epsilon_r \left(1 - \frac{PC |V_{ab}|}{t E_{MAX}} \right)$$

The average current, \bar{I} , is determined by an iterative process of calculating voltage on the stack and average impedances in the circuit at each time instant in the cycle. All current values for a cycle are then used to calculate an average current. Work delivered to the load is the average (rms) current squared times the load resistance. While all calculations and experiments to date have involved sinusoidally applied force, the computer program is capable of utilizing whatever time dependence is input. For forces requiring more rapid changes within a time frame than the 60 Hz sine wave utilized, the only modification necessary is reducing the computer time step increment which results in additional computer running time for each case.

The work input calculation also utilizes the charge balance to determine the instantaneous compliance of the stack.

Mechanical work input = Sum of all $F(DX)$ over a cycle

where

$$DX = \frac{gt}{A} Q$$

$$X = \frac{nFt}{A} \quad SSC = DX$$

2246

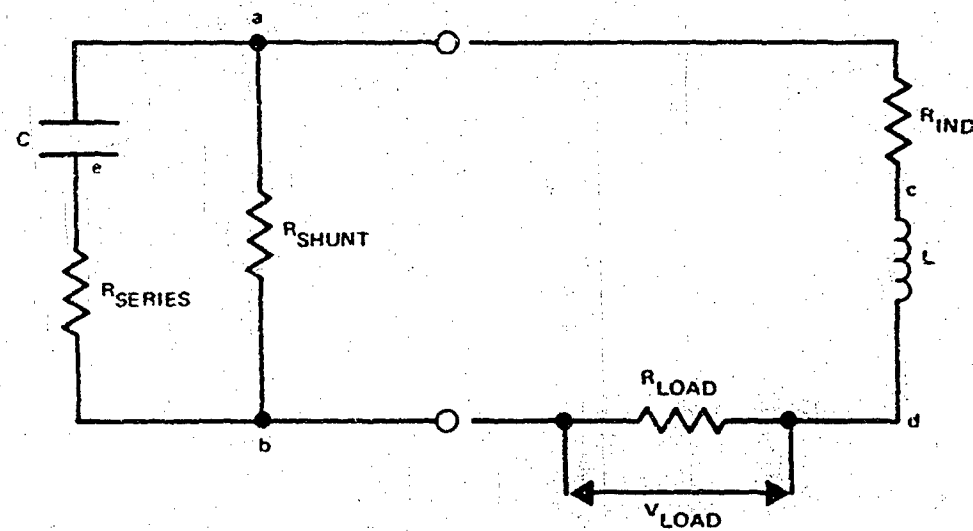


Figure C-1. Piezoelectric Stack Equivalent Circuit

Table C-1
DEFINITION OF SYMBOLS

Symbol	Definition
A	Cross sectional area of disc
t	Thickness of disc
f	Frequency
n	Number of discs in stack
g	Piezoelectric coefficient (volts/applied stress)
ϵ	Dielectric constant
ϵ_0	Dielectric constant of free space
ϵ_r	Low field relative dielectric constant
PC	Fractional increase in dielectric constant at E_{MAX} electric field
E_{MAX}	Electric field for a dissipation factor $\tan \delta = 0.4, 25^\circ C$
$\tan \delta$	Dissipation factor R_{series}/X_c
$\tan \delta_{in}$	Dissipation factor at low field
R_{Series}	Effective internal resistance of stack
R_{Shunt}	Effective shunt resistance of stack
C	Capacitance of stack
X_c	Capacitive reactance of stack
L	Inductance of load inductor
R_{ind}	Resistance of load inductor
P	Power to load
V_{ab}	Voltage across stack terminals
V_L	Voltage across load
F	Force: $F = F(time)$
I	Average current over time increment DT
DT	Time increment of computer step
DX	Change in length of the stack over time increment DT
X	Net displacement of stack at time T
SSC	Compliance (strain/stress) of stack at short circuit
η	Efficiency

The net electrical efficiency of the generator is then given by

$$\eta_{\text{work to load}} = \frac{I^2 R_{\text{load}}}{\text{mechanical work input}} = \frac{I^2 R_{\text{load}}}{f F (\Delta x)}$$

Alternately, the efficiency of the stack alone can be determined by including the work dissipated in the inductor, although this definition was not used for any of the efficiency numbers reported here.

$$\eta = \frac{I^2 (R_{\text{load}} + R_{\text{ind}})}{f F (\Delta x)}$$

C.2 CORRELATION WITH PHYSICS INTERNATIONAL LTZ-1 DATA

The formulation developed in Section C.1 was utilized in analyzing LTZ-1 stack performance. Because LTZ-1 material is essentially identical with PZT-4, the materials parameters for the latter (Reference C-1) were used in the computer program.

These parameters include:

$$\epsilon_r = 1300$$

$$\text{PC} = 0.17$$

$$E_{\text{MAX}} = 300,000 \text{ volt/meter}$$

$$g = 0.0261 \text{ volt/meter/Newton}$$

$$\text{So that } \epsilon = 1300 \epsilon_0 \left(1 + \frac{0.17 |V_{\text{ab}}|}{300,000 t}\right)$$

$$\text{and } \tan \delta = 0.004 + \left(\frac{0.04 + 0.004}{300,000}\right) (0.0261) \frac{F}{A}$$

The LTZ-1 stack consisted of 10 discs each 0.040 in. thick x 1.25 in. dia with all discs electrically connected in parallel. Calculations were run for a variety of stress fluctuations, load resistances, and series inductance. All calculations were for a frequency of 60 Hz.

Figure C-2 shows the results of these power versus stress calculations superimposed on the Physics International figure previously presented Appendix A. Particularly good agreement occurs for stress fluctuations at or below 6000 psi. At higher stress levels, calculated values are mostly higher than measured performance. This may result from ϵ and $\tan \delta$ having a nonlinear field dependence. The linear dependence of these two quantities was assumed based on two points of data provided in Reference C-1: the low field values

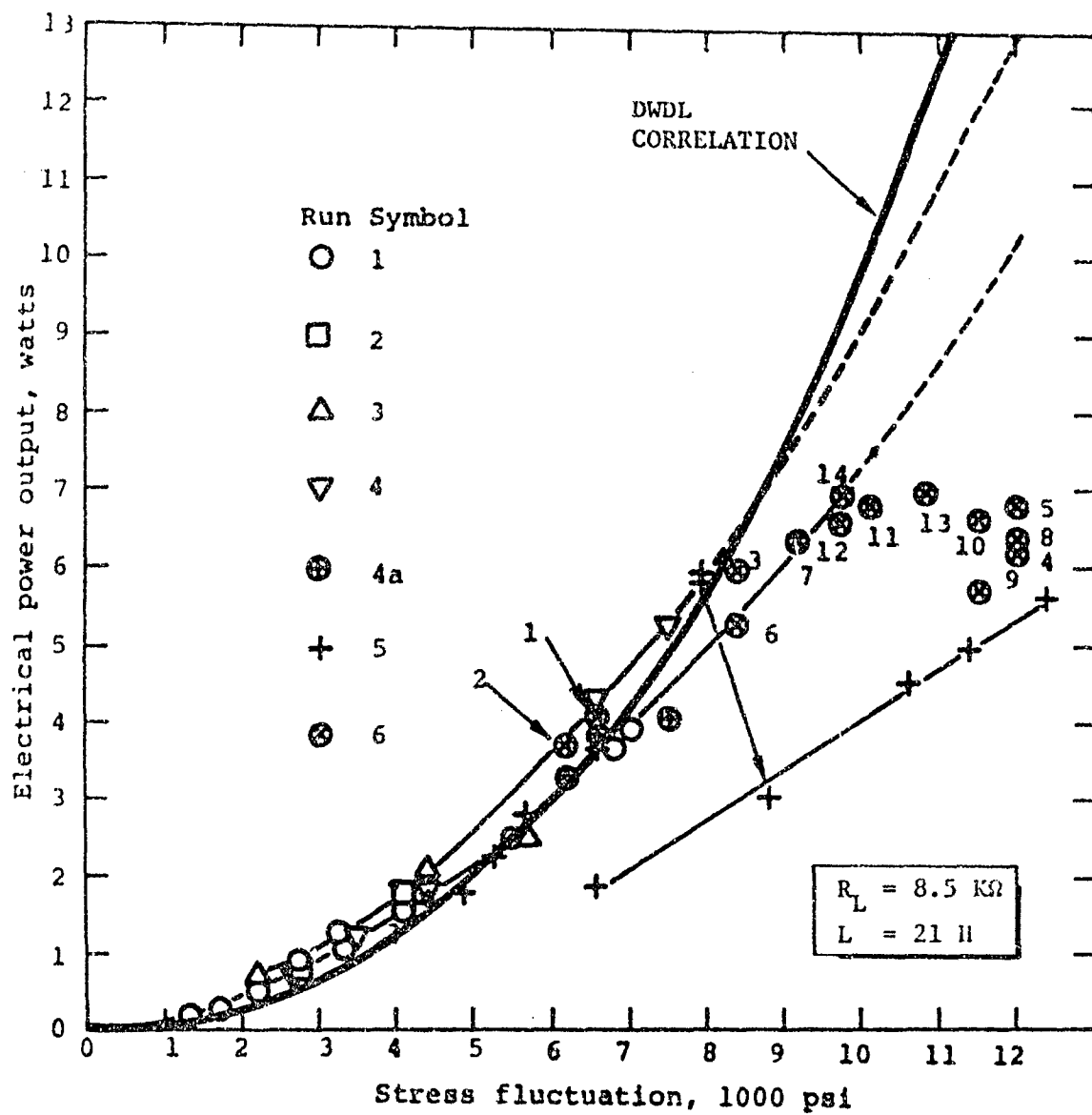


Figure C-2. DWDL Analytical Correlation with Physics International LTZ-1 Generator Performance

of $\tan\delta$ and ϵ , the electric field for $\tan\delta = 0.04$ ($E_{MAX} = 390,000$ v/m), and the corresponding change in ϵ for that field (PC = 0.17).

Figure C-3 shows the dependence of output power on series load inductance for the experimental conditions where inductance was varied. The agreement between experiment and theory appears close. Experimentally, output power continued to increase gradually as inductance was added. The largest inductor available was 21 henries. Calculations indicate that increasing the inductance further would have resulted in a maximum output power for an inductance of over 50 henries (where X_L effective X_L). This maximum of over 10 watts at 50 henries is over 4 times the measured value at 21 henries.

Figure C-4 presents the dependence of output power on load resistance for both the 18 henry experimental case and 55-henry calculated case. For the calculated case, lowering the load resistance increases output power even further. With all circuit reactance minimized, a load resistor equal to the effective internal resistance of the stack produces maximum obtainable output power for a given stress fluctuation.

Disadvantages of operating at this increased power density include reduced efficiency and increased heat generation per unit volume of stack. Provisions for removing this heat without allowing the stack to overheat would be required, especially in applications where power density is more important than efficiency.

C.3 PIEZOELECTRIC MEASUREMENTS

C.3.1 Test Equipment

Tests were carried out by DWDL to establish practical operation parameters for electrical power generation and to verify analytical predictions of performance. All tests were performed using the electrohydraulic materials loading system at Battelle Pacific Northwest Laboratories in Richland, Washington. This unit, Model 312.21 (12.5/25 KIP), was manufactured by MTS Systems, Inc. Loads were applied sinusoidally at 60, 90, or 120 Hz with a minimum of 1000 psi compression and up to 13,000 psi maximum compression. At each compressive loading, the electrical load on the stack was changed by varying load resistance and inductance.

Equipment utilized in these piezoelectric tests experiments is shown in Figure C-5; however, none of the MTS System control equipment is shown. Included in the electrohydraulic system are control, loading, and hydraulic power subsystems. The control loop utilized a load cell in series with the test specimen, together with the necessary electronic signal conditioning, comparator, and readout modules. A pump maintained hydraulic fluid pressure in a servo valve controlled

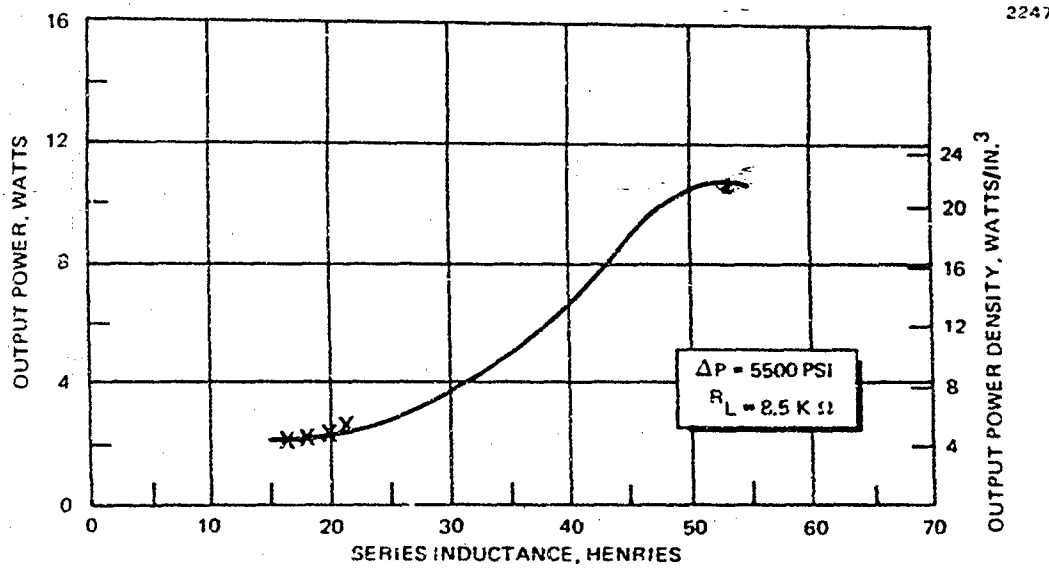


Figure C-3. LTZ-1 Stack Output Power Dependence on Inductance

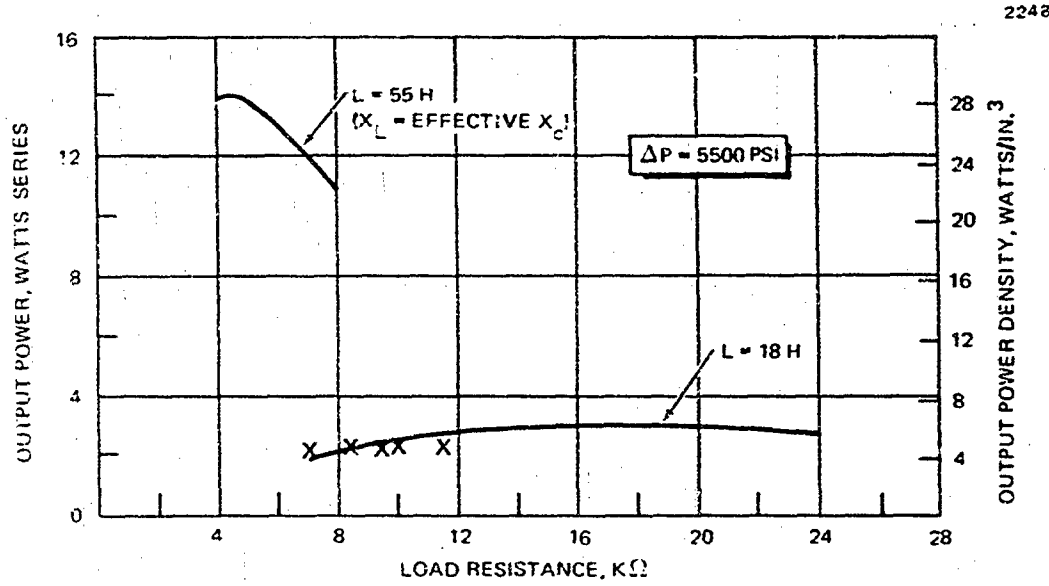


Figure C-4. LTZ-1 Stack Output Power Dependence on Load Resistance

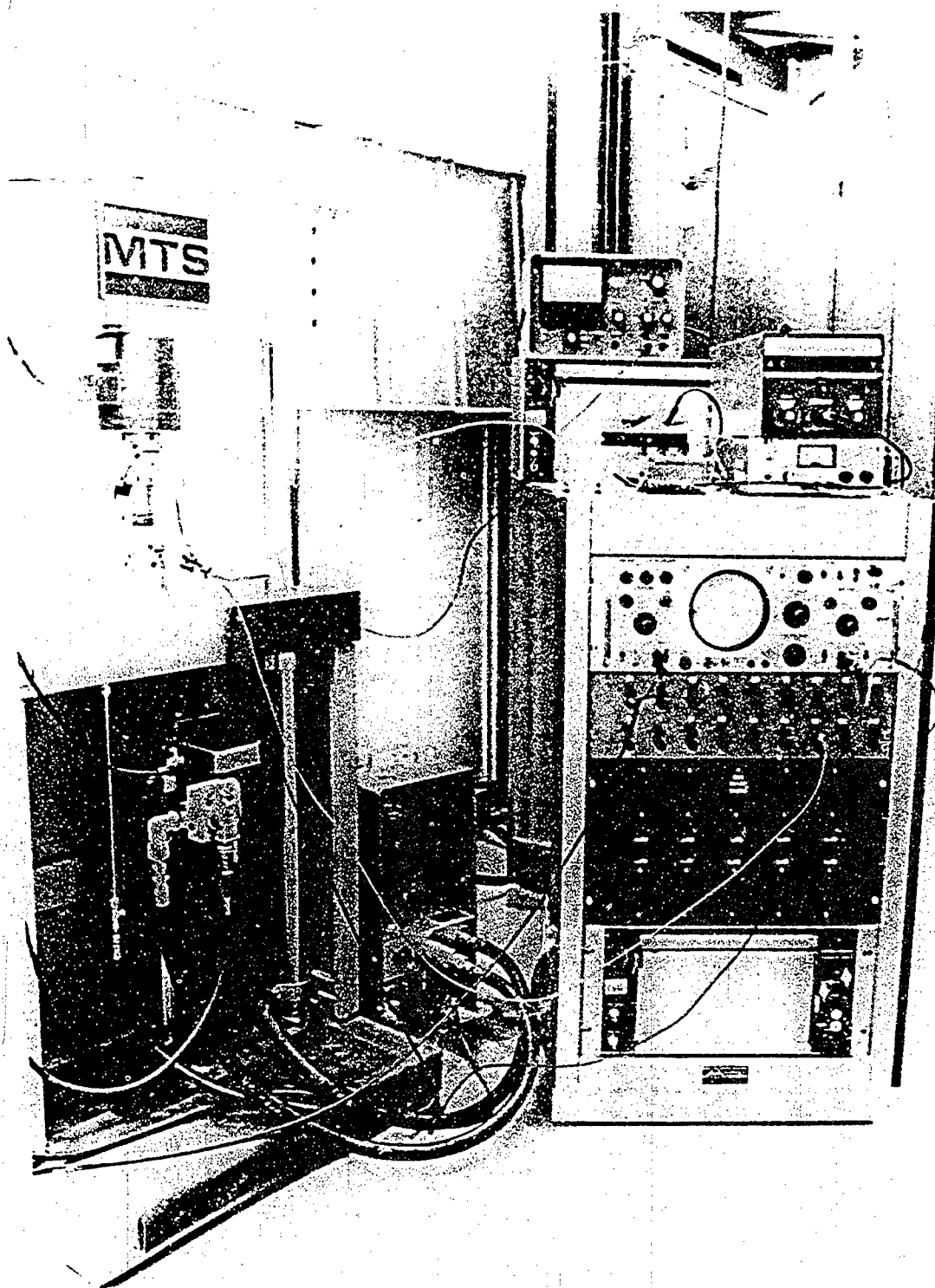


Figure C-5. Apparatus for Testing Piezoelectric Stack

by the servo controller. In all tests, a sinusoidally varying force was maintained on the loading piston by the servo valve. The piezoelectric stack under test was mounted on top of the piston, just below the load cell, all within the load frame shown.

Mechanical work input to a piezoelectric stack under test was determined as the area within the force versus displacement loop displayed on a Tektronix Model 503 X-Y oscilloscope. The force signal was obtained from the MTS system load cell. The signal of 1 volt/1000 lb provided to the oscilloscope was displayed on the Y axis. Displacement was measured using a Bently Nevada Model 302L30 proximity measuring system consisting of a proximitator (probe excitation source) and probe (sensing element). Displacement is measured by the non-contacting, eddy current probe with an output signal of the proximitator supplied to the X axis of the oscilloscope. With the Model 316L probe used in displacement measurements, the gain was 0.20 volt/mil displacement ($\pm 10\%$) according to manufacturer specifications. This unit was capable of measurements over 0 to 120 Hz without significant phase lag or amplitude attenuation. Displacement variation under static load conditions could be verified with a Bendix Indi-Ac A.T. Gaging System Model AT-1 with a Type T-220 gage head. However, this unit with a head operating on the LVDT (linear voltage differential transformer) principle could not produce accurate results at operating frequencies.

Figure C-6 shows a piezoelectric stack on the MTS System with the Bendix probe on the left and the Bently Nevada probe on the right. The electrical leads from the piezoelectric stack are also shown. Electrical power output was measured as $P = V_L^2/R_L$, where V_L was the voltage across the load resistor R_L . This voltage was detected with a Ballantine Model 355 digital voltmeter ($\pm 0.1\%$ accuracy with sine waves; this meter does not indicate true rms voltage for non-sinusoidal input). In later tests, all load resistors were Dale wire-wound 1% power resistors each with 25-w heat dissipation capability. Inductors were Triad filter chokes Model C-7X (90 ma, 10 h, 270 ohms). Overnight recording of stack output voltage was made on a Moseley Model 7100B strip chart recorder.

C.3.2 Test Results

Initial testing was done on a 16-disc unbonded stack (each disc 0.10 in. thick x 0.5 in. dia) consisting of unbonded HDT-31 (equivalent to PZT-4) material supplied by Gulton Industries, Inc. Both stress level and load resistance were varied. A stress fluctuation of 8000 psi (1000 to 9000 psi) produced 4.25 watts (13.5 w/in.³) with a load resistance of 175 K Ω . The load resistance for maximum power decreased from 180 K at 5100 psi to 170 K at 8200 psi stress fluctuation, suggesting a stress or field dependence of the piezoelectric properties. Table C-2 summarizes test results for all tests performed by DWDL.

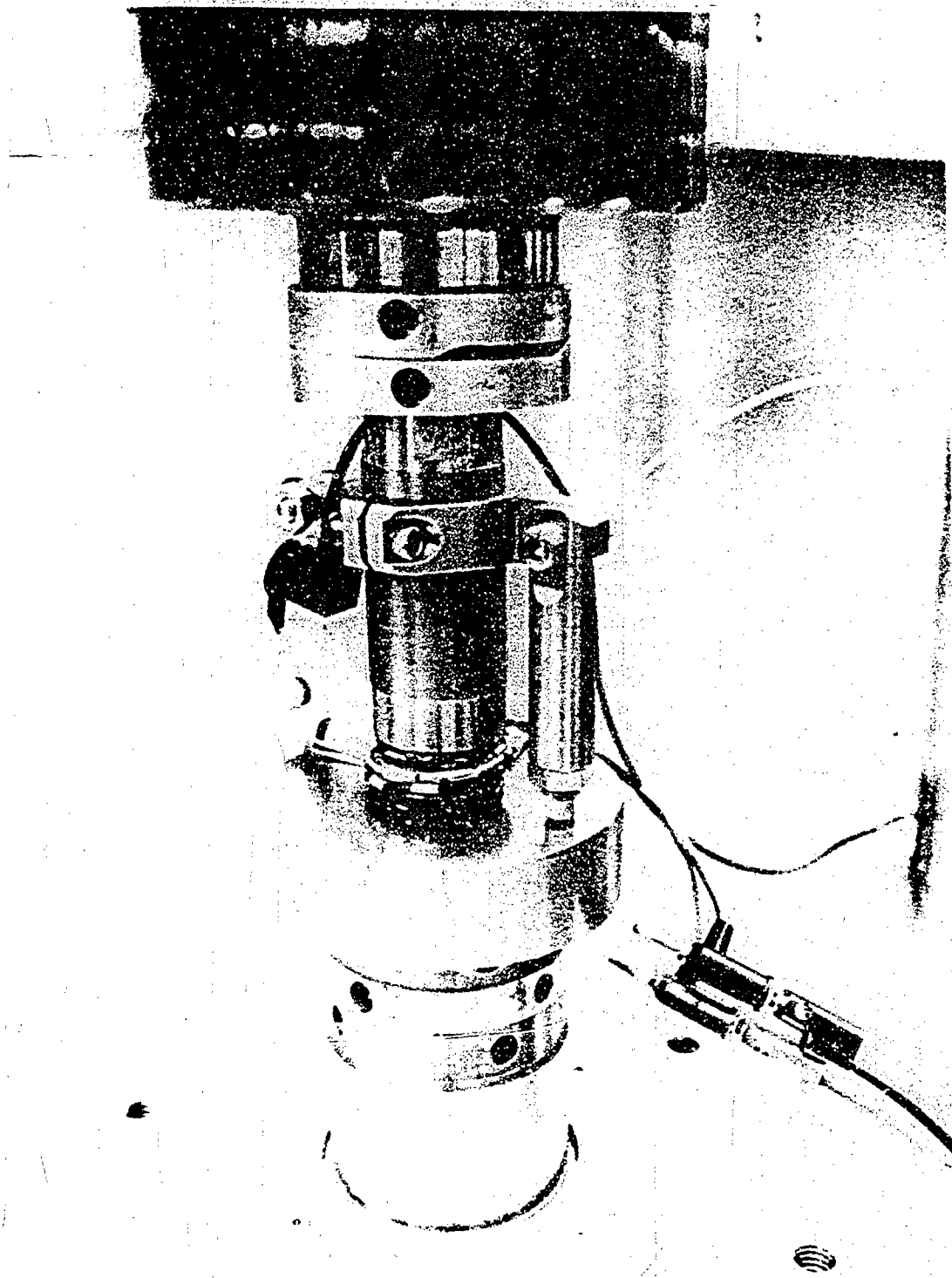


Figure C-6. Piezoelectric Stack Test Fixture

Table C-2
PIEZOELECTRIC TESTS CARRIED OUT BY DWDL

Material	Stack Dia. (in.)	Disc Thick (in.)	No. of Discs	Frequency (Hz)	Stress Level (psi)	Induc- tance (h)	Operating Time (hr)	Continuous Density (w/in. ³)	Max. Power
Gulton HDT-31	0.5	0.10	8	60	1000-5000	0	1	1.75	
			16		1000-9200	0	1	13.5	
			20		1000-9200	0	2	10.7	
					1000-13300	0	20	18.8	
					1000-7140	45	20	7.2	
					1000-10200	45	1	11.3	
					1000-7140	45	16	6.0	
					1000-7140	0	2	8.0	
					1000-7000	0	0.1	1.7	
Linden Lab PZT-4 Equiv.	1.25	0.040	10						
Gulton HDT-31	0.5	0.0165	20		1000-7000	40	1	8.3	
	0.10	14	60		1000-7000	100	1	6.5	
			120		1000-7000	100	0.5	16.6	
			120		1000-7000	30	2	31.0	

Many tests were then conducted on a 20-disc unbonded stack of the same material with each disc 0.016 in. thick \times 0.5 in. dia. This stack had a much lower capacitive reactance. By varying the load resistance and measuring output power at various stress levels, a dependence of stack capacitive reactance on stress was experimentally determined. This dependence is shown in Figure C-7. Later analysis, particularly the time dependent formalism, related this dependence to the electric field dependence of the dielectric constant as previously stated. This stack was tested at 60 Hz and stress fluctuations to 8000 psi at various loads. These data are plotted in Figure C-8. The stack was then held at 8000 psi and $R_L = 20$ K for over one hour. At these conditions, output power dropped 7% during the hour. This decrease in performance during the initial few hours of testing occurred on all subsequent tests as well. For stress fluctuations to and including 8000 psi (1000 to 9000 psi) the decrease is reversible; that is, the stack returns to its undegraded condition when allowed to relax. For a stress fluctuation of 12,000 psi (1000 to 13,000 psi), an additional, permanent degradation occurred. This degradation was observed when the stack was stressed overnight at 12,000 psi and 60 Hz. Output power across the 20-K resistive load decreased from an initial value of 1.14 watts (18.2 w/in.³) to 0.79 watts (12.8 w/in.³). The resistive load was not detectably warmer to the touch, nor had the equipment changed in temperature. These results are also shown in Figure C-8.

Work input measurements attempted on these tests were not valid because the Bendix displacement measuring unit was not able to perform satisfactorily at 60 Hz. Both signal attenuation and phase lag

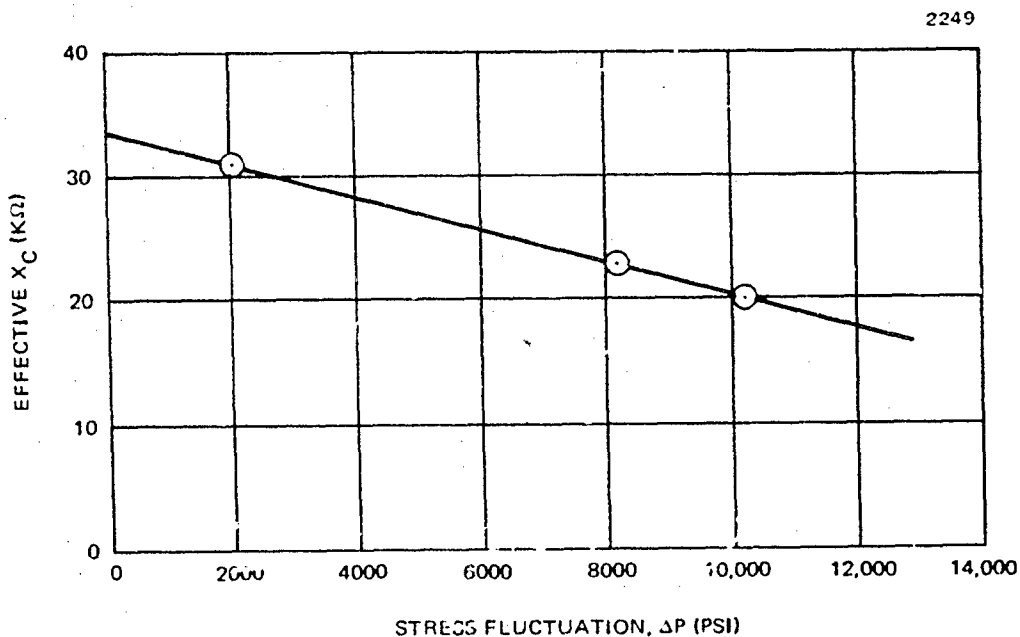


Figure C-7. Effective Capacitive Reactance of Piezoelectric Stack as a Function of Applied Stress

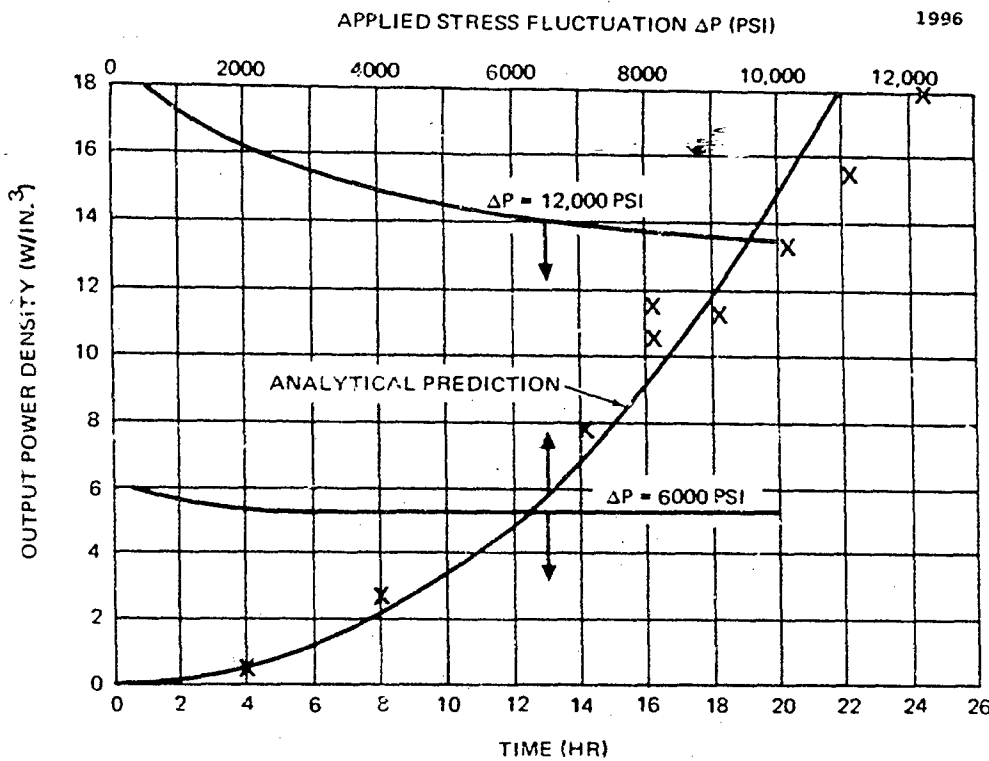


Figure C-8. Test Results for Twenty-Disc Piezoelectric Stack

were introduced; subsequently the Bently Nevada proximitron and another type of LVDT (linear voltage differential transformer) transducer were ordered. The latter did not arrive in time to be used on tests described in this report.

When the inductors were available, the same stack was again tested as a function of stress, load resistance and series inductance. The strong dependence of output power on series inductance is shown in Figure C-9. While the analytical prediction of optimum series inductance (X_L = effective X_C) was 70 henries with the time-averaged formulation described in Appendix B, the prediction was 50 h with the time-dependent formalism described in this appendix. Figure C-9 shows the experimental optimum value was 45 h.

This stack was then tested overnight at a stress fluctuation of 6000 psi at 60 Hz with a 20-K load and 40-h series inductance. The results of this test are also plotted on Figure C-8. Coincidentally, the time = 0 operating point for this test with 40-h inductance on the stack, which had degraded during the test at 12,000 psi stress fluctuation, corresponded with the original short test at 6000 psi stress fluctuation and no inductance prior to stack degradation.

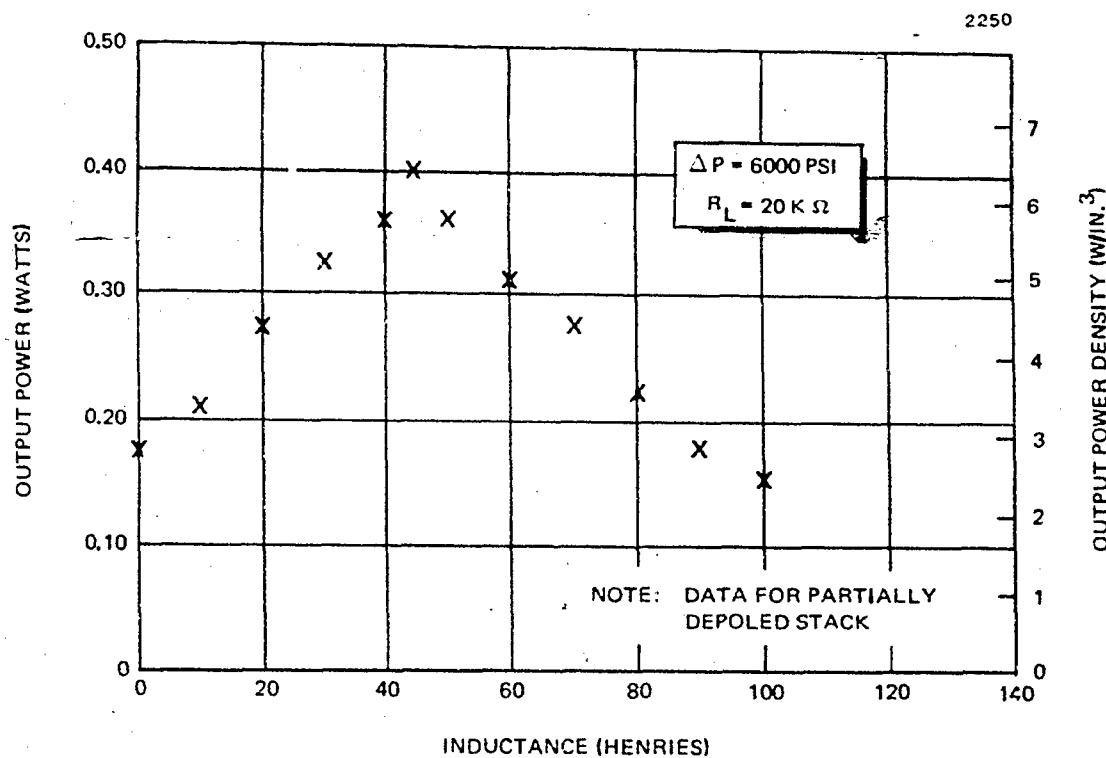


Figure C-9. Dependence of Output Power Upon Inductance

With the stack at an optimum inductance, the load resistance was then reduced until the maximum power density of 8.0 w/in.³ was achieved. This is shown in Figure C-10.

The next stacks tested were 10 disc (1.25 in. dia x 0.040 in. thick disc) stacks of PZT-4 equivalent piezoelectric ceramic supplied by Linden Laboratories, State College, Pennsylvania. The discs in these stacks were bonded together with conducting epoxy. During the first few minutes of testing on each of these stacks, arcing occurred in the epoxy on the sides of the stacks. This occurred at stress fluctuations of 6000 psi as series inductance was added to the load (thereby increasing voltage across the stack). Prior to breakdown, output power was only 25% of the predicted value for one stack and 50% for the second stack. As load resistance was varied with no inductance, maximum power occurred at the predicted load resistor value. The probable cause of the low power output was a relatively low shunt resistance path provided by the epoxy. After continued arcing on both stacks at stress fluctuations of 3000 psi, all testing of these bonded 1.25-in. dia stacks was terminated.

Testing resumed on the 20- disc (0.5 in. dia x 0.016 in. thick disc) stack of HDT-31 material previously tested; Figure C-11 shows this stack. For this series of runs, the Bently Nevada probe was utilized to make accurate displacement measurements. From

these measurements, an efficiency can be calculated. Figure C-12 is a typical force versus displacement photograph from the XY oscilloscope. The operating conditions for this case were:

$$f = 60 \text{ Hz}$$

$$F_{\min} = 196 \text{ lb (1000 psi)}$$

$$F_{\text{mean}} = 783 \text{ lb}$$

$$F_{\max} = 1370 \text{ lb (7000 psi)}$$

$$L = 40 \text{ h (} X_L \approx \text{effective } X_c \text{)}$$

$$R_L = 30 \text{ K (} R_L \approx \text{optimum for } X_L = 0 \text{)}$$

$$V_L = 108.5 \text{ v}$$

$$P_{\text{out}} = \frac{V_L^2}{R_L} = \frac{(108.5)^2}{30000} = 0.394 \text{ w}$$

X scale on scope 0.02 v/cm

Y scale on scope 0.2 v/cm

The photograph was cut up to obtain the area with the force displacement loop. The area was weighed; a section of the grid display 2 cm x 4 cm on the same scope picture xerox copy was then weighed.

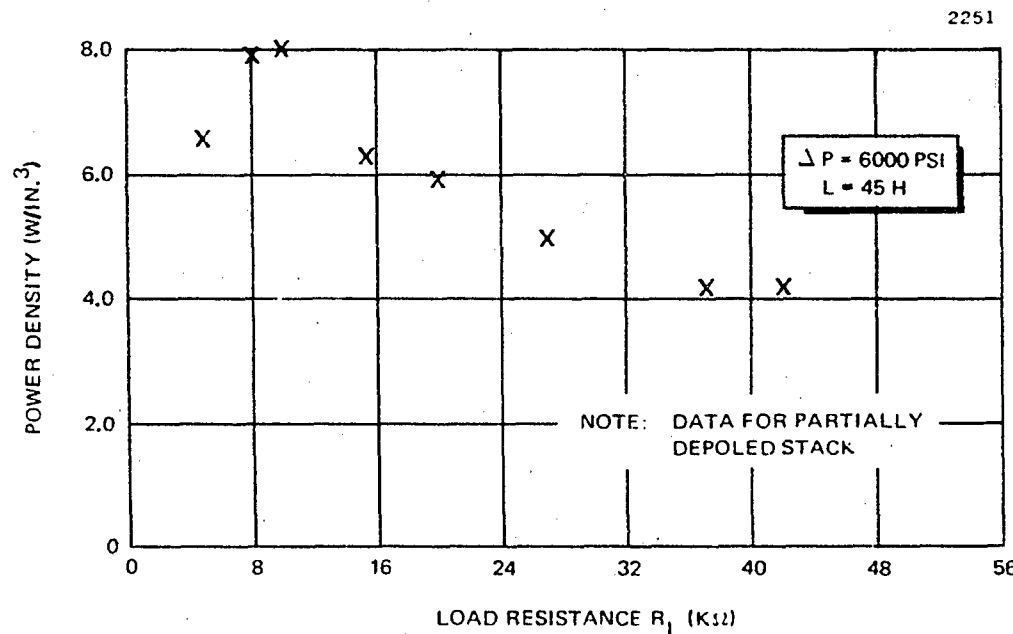


Figure C-10. Power Density Dependence Upon Load Resistance

71-1897



Figure C-11. Piezoelectric 20-Disc Test Stack

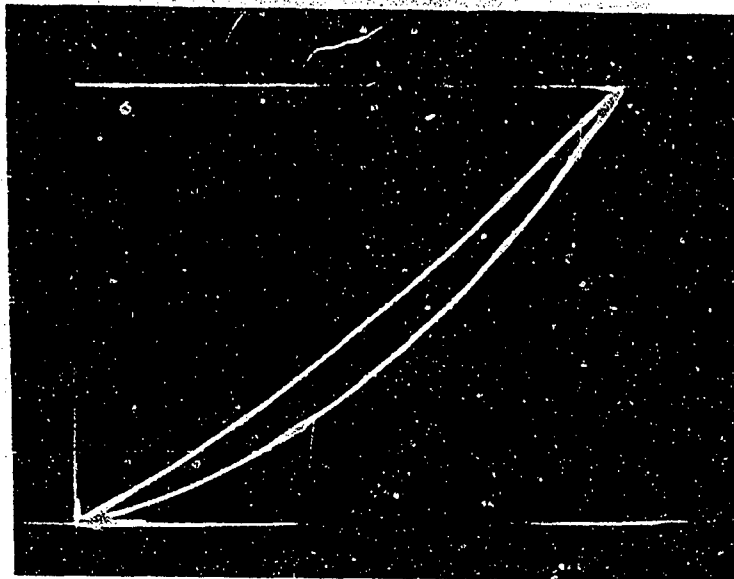


Figure C-12. Typical Force-Displacement Experimental Curve for Twenty-Disc Piezoelectric Stack

From these two weights, the true area of the loop was established. Input power was then determined:

$$\begin{aligned}
 P_{in} &= (3.87 \text{ cm}^2) \left[\left(\frac{0.2 \text{ v}}{\text{cm}} \right) \left(\frac{1000 \text{ lb}}{\text{v}} \right) \left(\frac{4.448 \text{ newtons}}{1 \text{ lb}} \right) \right] \\
 &\quad \left[\left(\frac{0.02 \text{ v}}{\text{cm}} \right) \left(\frac{1 \text{ mil}}{0.2 \text{ v}} \right) \left(\frac{9.001 \text{ in.}}{\text{mil}} \right) \left(\frac{1 \text{ meter}}{39.37 \text{ in.}} \right) \right] \times (60 \text{ sec}^{-1}) \\
 &\approx 0.525 \text{ watts}
 \end{aligned}$$

$$\text{Efficiency } \eta = \frac{0.394}{0.525} \times 100 = 75.2\%$$

Current uncertainty in these measurements includes (1) $\pm 10\%$ uncertainty in the 0.2 v/mil calibration factor for the Bently Nevada displacement transducer, and (2) $\pm 2\%$ in determining the area. The latter was estimated from three attempts to determine the area of the same curve where one measurement utilized the inside of the scope trace line, the second used the middle of the scope trace line and the third used the outside of the line. Other uncertainties which appear to be small compared to these include oscilloscope calibration of X and Y axes, the load cell calibration factor (1000 lb/volt), and the imperfect sine wave affecting voltage measurement as indicated on the Ballantine voltmeter. Incorporating these uncertainties, efficiency becomes

$$\eta = 75 \pm 12\%$$

In the near future, this uncertainty should be reduced as the actual calibration of the displacement transducer is established.

Figure C-13 presents the efficiency and output power of the same 20-disc stack as a function of inductance. The load resistance of 30 K gave maximum power with no inductance in the circuit. Stress fluctuation was again 6000 psi and frequency was 60 Hz. For the same operating conditions, load resistance was then varied while holding load inductance near optimum ($X_L = \text{effective } X_c$). These results are given in Figure C-14.

Testing then began on 14-disc unbonded stack (0.50 in. dia x 0.10 in. thick disc) of HDT-31 material at 60 Hz. This particular configuration resulted in a stack capacitive reactance for which neither optimum load resistors nor series inductance was available. At 60 Hz and 6000 psi stress fluctuation, the stack produced the following results:

1.42 watts (5.2 w/in.³) at $L = 0$, $R_L = 163$ K; $\eta = 57\%$

1.8 watts (6.5 w/in.³) at $L = 100$, $R_L = 163$ K; $\eta = 57\%$

After running 16 hours at these conditions, stack output had stabilized at 2.0 watts (7.2 w/in.³) with the stress fluctuation drifting and eventually stabilizing at 6300 psi. Returning to the original stress fluctuation of 6000 psi reduced the output power to 1.6 watts (5.7 w/in.³). This decrease from the initial 6.5 w/in.³ is qualitatively and quantitatively consistent with the results shown in Figure C-8 for the small stack.

A second unbonded stack of 12 identical discs was then placed on top of the 14 discs to produce a 26-disc unbonded stack with an overall height of 2.67 in. As in all unbonded stack tests, the interdisc electrode leads were 0.002 in. copper sheet. Plexiglas sleeves aided in maintaining alignment during set up; these were not removed during testing. Testing was carried out at 120 Hz and 6000 psi stress fluctuation for various load conditions. With $X_L \approx$ effective X_c , the load resistance was reduced to maximize output power. These results are shown in Figure C-15.

C.3.3 Thermal Effects

These were the first tests to establish apparent thermal effects. For those tests producing more than 10W, output power drifted gradually upward over a few minutes. For example, at $R_L = 10$ K at $t = 0$, $V_L = 375$ v; at $t = 1$ min, $V_L = 385$ v; at $t = 2$ min, $V_L = 397$ v. The stack may have been heating as a result of the increase in power, or the load resistor might have been heating.

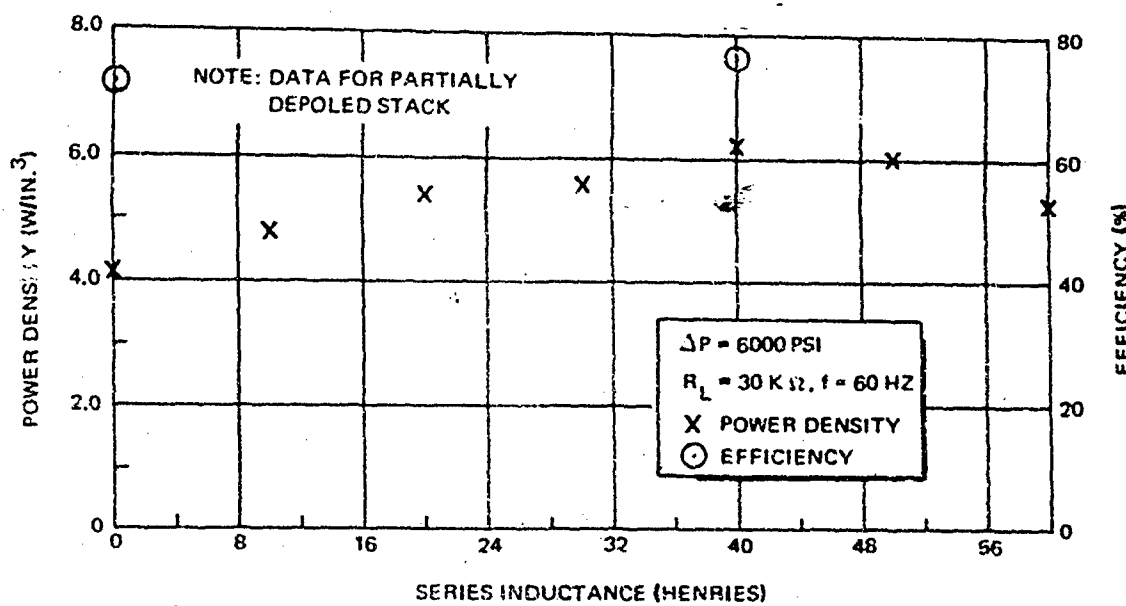


Figure C-13. Power Density Dependence Upon Inductance

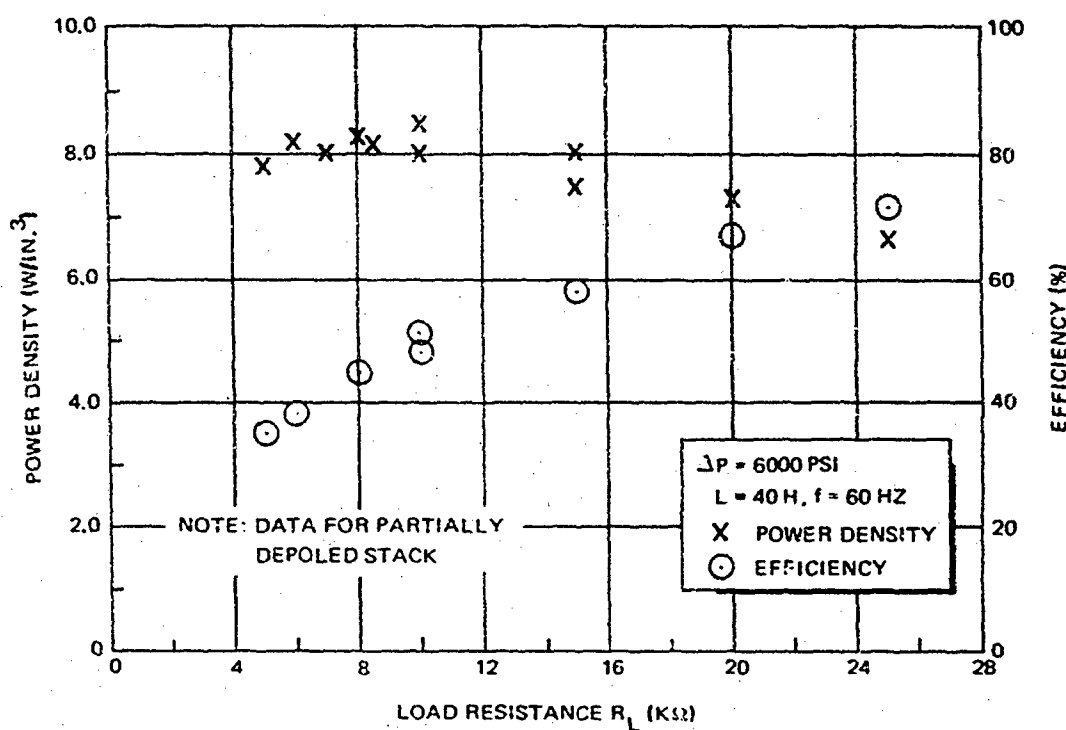


Figure C-14. Power Density Dependence Upon Load Resistance

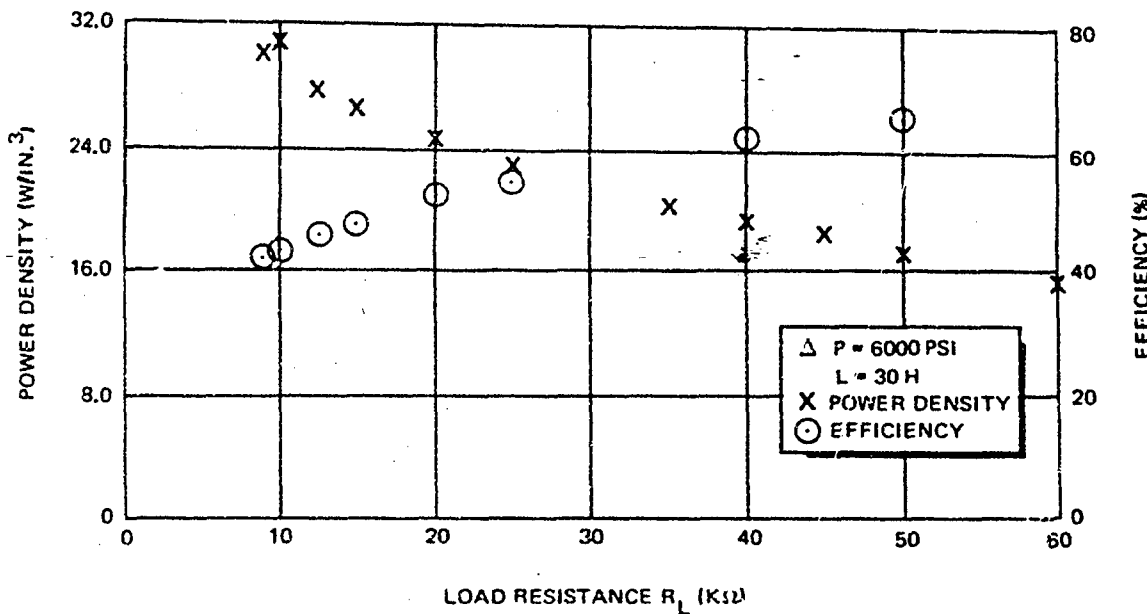


Figure C-15. Power Density Dependence on Load Resistance for 26-Disc Stack

At a power level of 7 w (14 w/in.³), the stack was tested for an hour with a 1% increase in power in contrast to previous observations at lower power densities (about a 7% decrease).

Temperatures were measured only on the 1.25-in. dia stacks. All stacks were positioned between the piston and load cell of the MTS system. While the load cell remained essentially at ambient temperature, piston temperatures increased because the hydraulic oil is maintained at 125°F by a water-cooled heat exchanger in the system. The top of the piezoelectric stack was 72°F and the bottom was 98°F. After stress fluctuation at 6000 psi and 60 Hz with 1 watt output for several minutes, the top of the stack was still at 72°F, but the bottom had warmed to 98.5°F. This agreed with analytical predictions based on calculated electrical losses for those operating conditions.

The Plexiglas sleeves of the 26-disc stack were warm to the touch during these high power density tests, but never became objectionably hot. These tests included maximizing power with a resultant efficiency decrease to 42%. This is a worst heating condition which would not normally be used in practice. Because of the small diameter discs, relatively large copper leads which could also act as heat conductors, and the Plexiglas sleeves, no thermocouples were attached to the stacks during these tests.

Suppliers literature (References C-1 and C-2) provided materials property data as a function of temperature. The relative dielectric constant increases as the temperature rises. This change appears

to dominate in performance calculations; therefore, power is expected to increase with temperature. However, the maximum stress allowable drops from 12,000 psi at 25°C to 6000 psi at 100°C. If 6000 psi had been chosen for long-term operation at 25°C, then a much lower value should be chosen for 100°C operation. This interaction between stack operating conditions and thermal design considerations remains critical to successful system operation. Furthermore, long-term testing with accurate temperature measurements under varied conditions will be required to unequivocally determine allowable operating conditions. Temperature effects under realistic operating conditions have been negligible to date as predicted by a simplistic thermal analysis assuming all heat is generated at the center of the stack. Should a temperature problem with full-size stacks arise in the future, stack cooling is a technically feasible alternative, as previously discussed.

C.4 REFERENCES

- C-1. Clevite Catalog No. 695. Piezoelectric Technology Data for Designers. Clevite Piezoelectric Division, Bedford, Ohio, 1965.
- C-2. Gulton Catalog No. H-700. Glennite Piezoceramics. Gulton Industries, Inc., Fullerton, California.

Appendix D

DETERMINATION OF HEAT TRANSFER COEFFICIENTS AND REGENERATOR PERFORMANCE IN THE STEPZ ENGINE

The heat exchangers and regenerator in the STEPZ engine are quite different from those typically used in Stirling engines. A partial cross section of the annular flow passage between the cylinder and displacer walls is shown in Figure D-1. Different regions of the annulus serve as heater, cooler, and regenerator in this approach. There is a lower surface-to-volume ratio and less heat transfer area than for conventional Stirling engines. This imposes a power density limitation in exchange for decreased gas dead volume and less mechanical complexity.

Heat exchanger performance is readily analyzed for the STEPZ engine geometry. An excellent treatment of all essential aspects of STEPZ heat exchanger analysis is given in Reference D-1, especially chapters 2 and 6. Heat transfer coefficients are determined on the basis of laminar flow with fully developed velocity and temperature profiles. These are, in general, valid assumptions which in any case give conservative results if they are not precisely true during transient conditions. Specifically, for the reference design case, the Reynold's number varies from zero to 5600, with a mean value of 1600. Turbulent flow may possibly, but not necessarily, be established for momentary Reynold's numbers above 2000. If turbulent flow at a high Reynold's number does occur, the heat transfer coefficient will momentarily be increased by up to a factor of three. Similarly, near the ends of the displacer where velocity and temperature profiles are not fully established, the heat transfer coefficient is higher by a factor of two to three. This length is typically 10 to 100 flow widths or 0.05 to 0.5 in. in the reference engine. A third area where a conservative heat transfer assumption is made is in the end regions. Stagnant gas conduction is assumed, although substantial mixing certainly occurs. This approach gives confidence that the heat exchanger model will not indicate unrealistically high performance.

Mathematical Relationships:

The Nusselt number Nu is defined as

$$Nu = \frac{h D_h}{K} = \frac{2hG}{K} \quad (D-1)$$

where

h = heat transfer coefficient

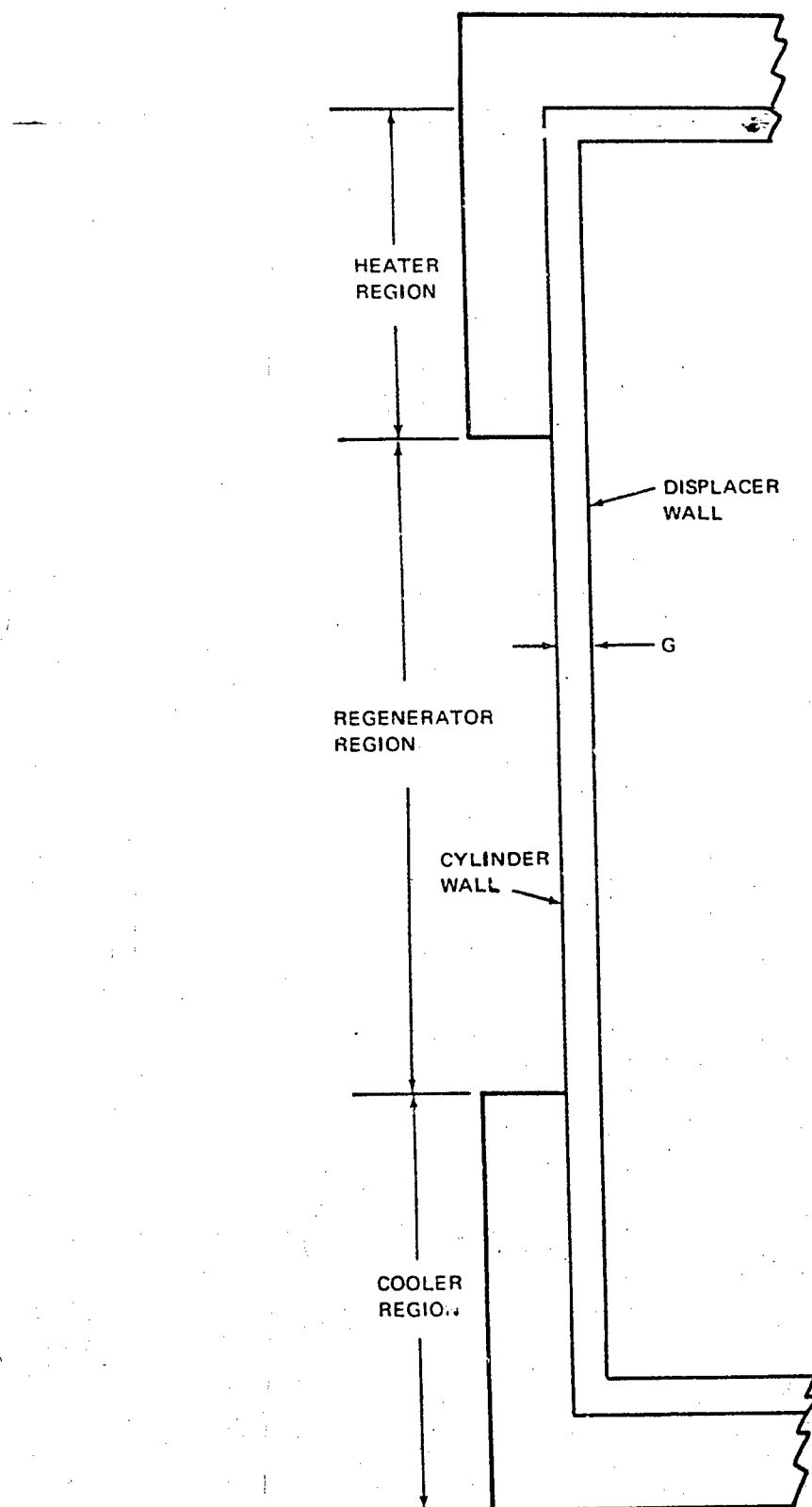


Figure D-1. Heat Exchanger Geometry

D_h = hydraulic diameter = $2G$ for a narrow annulus
 G = radial clearance between displacer and cylinder
 K = thermal conductivity of gas

In practice, it is the heat transfer coefficient that is required because the Nusselt number is constant for a given region under the assumed operating conditions. The equation of interest is, therefore,

$$h = \frac{Nu \cdot K}{2G} \quad (D-2)$$

Thermal conductivity of the working fluid is a strong function of temperature and must be separately determined for each region or node. The Nusselt number is dependent on geometrical and thermal characteristics of the heat exchangers. The annular gap, which is very small compared with the diameter, is essentially identical with flow between infinitely wide parallel plates separated by a distance G . In the heater and cooler regions, boundary conditions are essentially isothermal on the outside of the gap and adiabatic on the inside. From Figure 6-1 of Reference D-1, this leads to a Nusselt number of 4.86 for heater and cooler. In the regenerator region, a large amount of heat transfer to and from the gas occurs regeneratively on each cycle, although the spatial temperature profile remains essentially constant. This condition represents a constant heat transfer rate per unit of length on both inner and outer surfaces, for which the Nusselt number is 8.24.

This approach yields conservative heat transfer coefficients for the STEP% engine. These coefficients are then used to determine engine thermal performance as outlined in the paragraphs which follow. Heat transfer rate, Q , in the heater or cooler is given by

$$Q = h A \Delta T \quad (D-3)$$

where

A = heater or cooler area on the outside of the annulus
 ΔT = temperature difference between the heater or cooler and adjacent gas

Heat transfer in the hot end is given by the sum of all nonparasitic heat requirements for the engine, while in the cooler it is this value less the mechanical work output. Equation (D-3) can then be solved for the gas temperature in the heater and cooler regions. These temperatures then affect the work output, Carnot heat input, and reheat losses, such that heat transfer requirements are revised and new gas temperatures determined on an iterative basis until a convergence criterion is satisfied.

Regenerator performance is determined using an effectiveness approach as in Reference D-1, Chapter 2 and more directly in Reference D-2. The regenerator analysis is again conservative, in that, gas specific heat at constant pressure, c_p , is used to calculate reheat loss. The effective specific heat is some intermediate value between c_p and c_v (specific heat at constant volume). This true specific heat varies in an indeterminate manner over a cycle. Using the larger c_p at all times yields a larger reheat loss which provides for some analytical performance margin.

The STEP% regenerator is a periodic counterflow type with alternating flow of the same gas in opposite directions. For these conditions, the following relationships are valid.

$$(h_r A_r)_c = (h_r A_r)_h = h_r A_r \quad (D-4)$$

and

$$(\dot{m}_r c_p)_c = (\dot{m}_r c_p)_h = \dot{m}_r c_p \quad (D-5)$$

where

h_r = heat transfer coefficient in regenerator region

A_r = total surface area in regenerator region

\dot{m}_r = mass flow rate through regenerator

c_p = working gas specific heat at constant pressure

and the subscripts c and h refer respectively to the gas flowing from the cold region and the hot region. Relationships needed to evaluate regenerator effectiveness are found in Reference D-2 as follows.

$$NTU_c = \frac{h_r A_r}{\dot{m}_r c_p} \quad (D-6)$$

$$NTU_o = NTU_c \left[1 + \frac{(h_r A_r)_c}{(h_r A_r)_h} \right]^{-1} = \frac{1}{2} NTU_c \quad (D-7)$$

where the last equality results from applying equation (D-4). Further,

$$\epsilon = \frac{NTU_o}{1 + NTU_o} \quad (D-8)$$

where

NTU_c = number of transfer units for cold flow

NTU_o = overall number of transfer units

ϵ = regenerator effectiveness

The effectiveness may also be expressed as

$$\epsilon = \frac{\Delta T_o - \Delta T_h}{\Delta T_o} \quad (D-9)$$

where

ΔT_o = overall temperature difference between hot region gas and cold region gas

ΔT_h = temperature difference between hot region gas and gas entering the heater from the regenerator

ΔT_h is the temperature rise which must be accomplished in the heater as a result of regenerator ineffectiveness, which gives rise to the main reheat loss. The two expressions for regenerator effectiveness may be equated and solved for ΔT_h .

$$\Delta T_h = \frac{\Delta T_o}{1 + NTU_o} \quad (D-10)$$

Using Equations (D-6) and (D-7) in (D-10) reduces ΔT_h to an expression in more basic quantities,

$$\Delta T_h = \frac{2 \dot{m}_r c_p \Delta T_o}{2 \dot{m}_r c_p + h_r A_r} \quad (D-11)$$

The reheat power which must be added to achieve this temperature rise is

$$P_{rh} = \frac{1}{2} \dot{m}_r c_p \Delta T_h \quad (D-12)$$

where the factor of 1/2 is included because the gas is only flowing toward the hot region half the time as opposed to the continuous flow case in Reference D-2. Combining Equations (D-11) and (D-12) gives the final result for main reheat loss.

$$P_{rh} = \frac{(\dot{m}_r c_p)^2 \Delta T_o}{2 \dot{m}_r c_p + h_r A_r} \quad (D-13)$$

The basic heat exchanger and regenerator analysis summarized here is common to both the isothermal and nonisothermal computer programs. The method of implementing the analysis differs, and the isothermal program typically indicates significantly lower reheat losses and temperature drops. This is shown in Table 2-2. The reason for the reheat loss discrepancy is that the isothermal program calculates it from time averaged flow, temperature drop, and heat transfer coefficient in

Equation (D-13) while the nonisothermal simulation uses a numerical integration of Equation (D-13) over a cycle. The average hot gas temperature is much lower in the nonisothermal case, partly because more heat must be transferred and probably also because most heat is transferred at times when the temperature difference is unfavorable. The only explanation for the close correlation of average cold gas temperature given in Table 2-2 for the two models is that most heat transfer occurs under favorable conditions.

In summary, the mechanically simple but unconventional heat exchanger and regenerator approach used in the STEP% engine can be readily characterized by the experimentally verified analysis given in Reference D-1. Where any question exists relative to appropriate parameters or conditions, the most conservative approach is taken. While the application of the results to the isothermal program is necessarily limited in accuracy by assumptions in the isothermal model, the nonisothermal simulation should offer a high degree of confidence in the results.

REFERENCES

- D-1 W. M. Kays and A. L. London. *Compact Heat Exchangers*. McGraw-Hill Book Company, New York, 1964.
- D-2 J. E. Coppage and A. L. London. *The Periodic-Flow Regenerator - A Summary of Design Theory*. Trans ASME, Vol 75 pp 779-787, 1953.

Appendix E
SAMPLE DESIGN OF A LINEAR ELECTROMAGNETIC
DISPLACER ACTUATOR

A dynamic coil linear electromagnetic displacer actuator has been designed at DWDL for a 66 w(m) STEPZ engine module for space applications. The configuration of the actuator is shown in Figure E-1. A weight analysis indicated that the magnetic circuit containing Alnico-9 was lighter than one with samarium-cobalt, as a result of flux concentration in the center pole. Advantageous use of SmCo₅ is anticipated for higher windage engine modules. The actuator for the 66 w(m) engine module produces 1 w(m) at 60 Hz with an efficiency of 27%. The actuator weighs 0.5 lb and requires 1.9 amperes (rms) excitation for rated output. The impedance of the coil is 2.0 Ω with a lagging phase angle of 59°.

E. 1 DESIGN PHILOSOPHY

For space applications, reliability of the STEPZ displacer drive must be of the same order as that of the displacer suspension and other engine components. The intrinsically high reliability of flexural mounting may be more than an order of magnitude superior to that of couplings involving rotating motors and mechanical linkages. The

2257

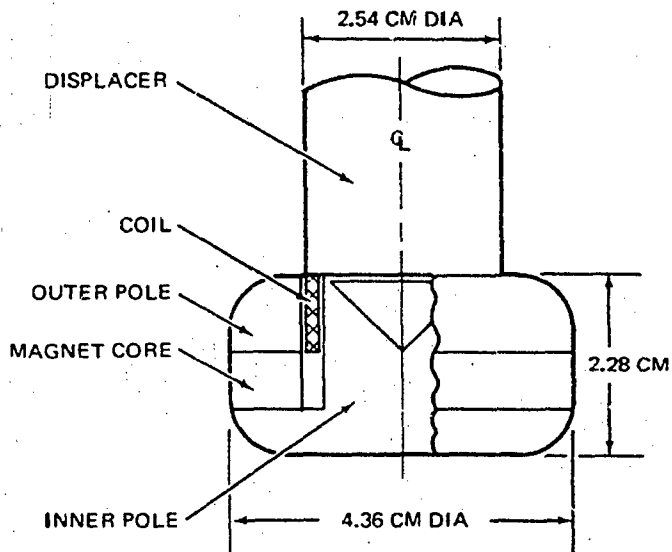


Figure E-1. Displacer Actuator for STEPZ Engine

oscillatory displacer motion suggests the use of a linear motion electromechanical actuator, such as a solenoid or a dynamic coil (loudspeaker) motor system. Both devices permit the suspension of the oscillating component directly on the displacer and require no seals or mechanical leadthroughs to function.

Oscillating linear motion is produced by the interaction of alternating currents and/or magnetic fields. The most efficient use of magnetic material in a solenoid is achieved with direct-current excitation of the field coil. With ac excitation (Reference E-1), the magnetic circuit is used only one half as effectively as that of a dc system to produce the same average force on the armature. As the armature is a component of the magnetic circuit, its mass reflects this inefficiency and contributes a several-fold increase in the weight of the displacer. The force acting on a solenoid armature is a monodirectional force of attraction. Use of a solenoid, therefore, also necessitates incorporation of a spring or double solenoid to provide the restoring force for oscillatory motion.

The dynamic coil linear motor depends on the interaction of an alternating electric field and a permanent magnetic field for its action. The instantaneous force (F) on a coil system carrying a sinusoidally varying current is given by

$$F = (B \times I_m) \ell \sin \omega t \quad (E-1)$$

where

B = flux density in permanent magnet gap

I_m = maximum coil current

ℓ = length of coil winding

ω = angular frequency of coil current

Oscillatory motion of the coil results from the sinusoidal force function. This response is significantly superior to that of the solenoid. The dynamic coil also follows complex excitation waveforms which permit nonsinusoidal excitation if desired to effect sophisticated control functions. For these reasons, therefore, a dynamic coil drive is considered the prime choice to activate the displacer.

E. 2 DESIGN ASSUMPTIONS AND CONSTRAINTS

The design of the displacer actuator was based on the following assumptions.

1. Actuator power supplies the displacer windage loss in an otherwise dynamically resonant mechanical system.
2. Coil mass added to the displacer has negligible influence on the displacer resonant response.

3. Magnetic flux fringing the motor gap is the same order as the flux between pole faces.
4. The internal field energy of the magnet provides the gap energy and fringe field; magnetization of the pole pieces is neglected.
5. The engine working fluid absorbs the Joule heating produced by the coil current.

Assumed characteristics of the displacer were:

1. Windage loss: 1 w(m) at 60 Hz
2. Stroke: 1.27 mm (0.05 inch)
3. Diameter: 2.54 cm (1 inch)

The mechanical work done by the displacer in one half cycle is the product of average force (F_{av}) and stroke (s). From Equation E-1,

$$F_{av} = \frac{|B I_m| \ell}{\pi} \int_0^{\pi} \sin \theta d\theta \quad (E-2)$$

$$= 0.637 B I_m \ell \quad (E-3)$$

where θ is the angle in radians from the instant of zero current.

At 60 Hz, there are 120 half cycles per second; therefore, mechanical power of the displacer (P_d) is given by

$$P_d = 120 F_{av} s \text{ Joules/sec} \quad (E-4)$$

$$= 76.38 I_m B \ell s \text{ w(m)} \quad (E-5)$$

With $s = 1.27 \text{ mm}$ and $P_d = 1 \text{ w(m)}$ Equation E-5 leads to an expression of $I_m \ell$ in terms of B

$$I_m \ell = \frac{10.31}{B} \quad (E-6)$$

Joule heating (P_c) in the dynamic coil is expressed by

$$P_c = \frac{I^2 m}{2} \rho \frac{\ell}{a} \quad (E-7)$$

where ρ is the resistivity of coil material and a is the cross sectional area.

With reference to Equation E-6, and for a given coil geometry,

$$P_c = \frac{K}{B^2} \quad (E-8)$$

In Figure E-2 Joule heating, P_c , is plotted versus gap flux density, B , in the range $0.1 < B < 1$ webers per square meter where permanent magnet materials of interest achieve their maximum energy product.

The flux density in the working gap was selected in the range 0.3 to 0.5 Wb/m^2 corresponding approximately to the range in which P_c is between 5 and 10% of its value where $B = 0.1 \text{ Wb/m}^2$. This does not provide an optimum configuration and was pursued on a quasi-intuitive basis to produce a compact magnetic circuit with acceptable weight and performance.

A major region of uncertainty occurs in estimating flux distribution in the working gap. Computer-aided mapping of this region is necessary to refine this effort. The fringing flux (i. e., flux not linking the dynamic coil) was considered equal to the useful flux. An aspect ratio of 5 was selected for the working gap to maintain the general validity of this assumption.

Two configurations of the magnetic circuit are shown in Figure E-3 consistent with a design which suspends the dynamic coil on an extension of the displacer. The placement of the permanent magnet shown in A, Figure E-3 is the more desirable. However, with gap dimensions shown in Figure E-1 and flux density in the gap approaching 0.5 Wb/m^2 , the geometry demands flux densities in the center pole greater than 1 Wb/m^2 . In Figure 1 of Reference E-2, 0.75 Wb/m^2 is the maximum flux density at which an acceptable energy product is achieved with available materials. For Alnico 9, this is in the region of its $[\text{BH}]_{\text{max}}$ point. However, for SmCo₅, $[\text{BH}]_{\text{max}}$ occurs at approximately 0.45 Wb/m^2 . The magnetic circuit design is forced, therefore, to that of the "outboard" magnet (B, Figure E-3) to permit sizing the magnet independent of displacer diameter. This geometrical constraint will be superimposed on both optimum and sub-optimum designs in all engines with a displacer diameter less than approximately 1.4 in.

Detailed calculations were performed of the Alnico 9 "outboard" magnet/coil configuration, and a similar design was completed for a SmCo₅ magnet/circuit to provide the same output. Table E-1 summarizes a weight comparison of the two systems.

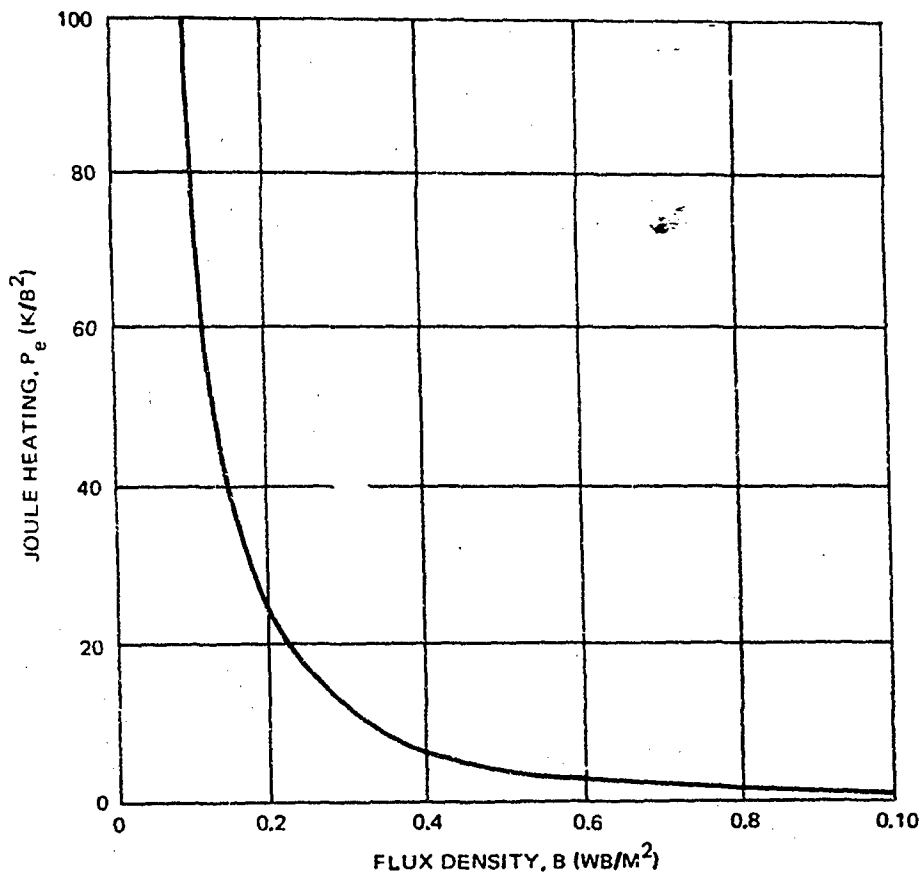


Figure E-2. Joule Heating as a Function of Magnet Gap Flux Density

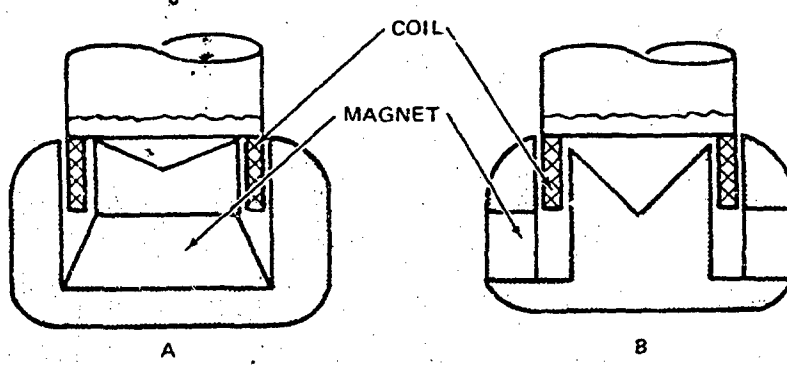


Figure E-3. Magnetic Circuit Configurations

Table E-1
WEIGHT SUMMARY OF DISPLACER ACTUATOR COMPONENTS

Component	Weight (g)	
	SmCo ₅ at 0.45 Wb/m ²	Alnico at 0.75 Wb/m ²
Magnet	34.0	52.5
Inner Pole (1) (2)	110.0	100.0
Outer Pole (2)	108.0	63.5
Coil	9.3	9.3
Displacer Extension	1.5	1.5
 Total	262.8	227.0

(1) With central conical void

(2) With ellipsoidal transitions from magnet element

The lighter magnet is achieved with the Alnico 9 despite its lower energy density as a result of $|BH|_{max}$ occurring at 0.75 Wb/m². The superior energy product of SmCo₅ would be reflected more favorably in a design for a larger displacer. Table E-2 summarizes characteristics of the Alnico 9 actuator.

E. 3 CONCLUSIONS

If the assumption of flux distribution is realistic, this design exercise provides encouragement for the application of electromechanical linear device actuation and control of the STEPZ engine. The particular engine investigated imposed an unscalable constraint by requiring the center pole to fit inside the extension of a small displacer. The resulting high flux density excludes the favored configuration of the magnetic circuit. Alnico 9 provides the lightest magnetic circuit of any available material working at its BH_{max} point. The superior energy product of SmCo₅ would benefit magnetic circuit designs for larger displacers. Its availability is established and it is considered both performance and cost competitive with Alnico materials.

Flux mapping of the working gap is necessary as a basis for optimizing the configuration of the linear actuator. In particular, flux concentration should be traded against increases in fringing flux for lower aspect ratio gaps.

Table E-2
ALNICO 9 DISPLACER ACTUATOR CHARACTERISTICS

Characteristic	Value
Weight (g)	227 (0.5 lb)
Mechanical Output (w_m)	1
Specific Mechanical Power (w_m /lb)	2
Coil Dissipation (w_e)	3.75
Efficiency (%)	27
Coil Impedance (Ω)	2.0 (1.0 + j 1.7)
Coil Phase Angle (°)	59

E. 4 REFERENCES

E-1. H. C. Roters. Electromagnetic Devices, 1967 John Wiley and Sons, Inc.

E-2. E. F. Hammond, Jr., et. al. Feasibility Study and Preliminary Design for a 100-Kw Permanent Magnet Generator. Westinghouse Electric Corporation, Report AD708-930, June 1970.